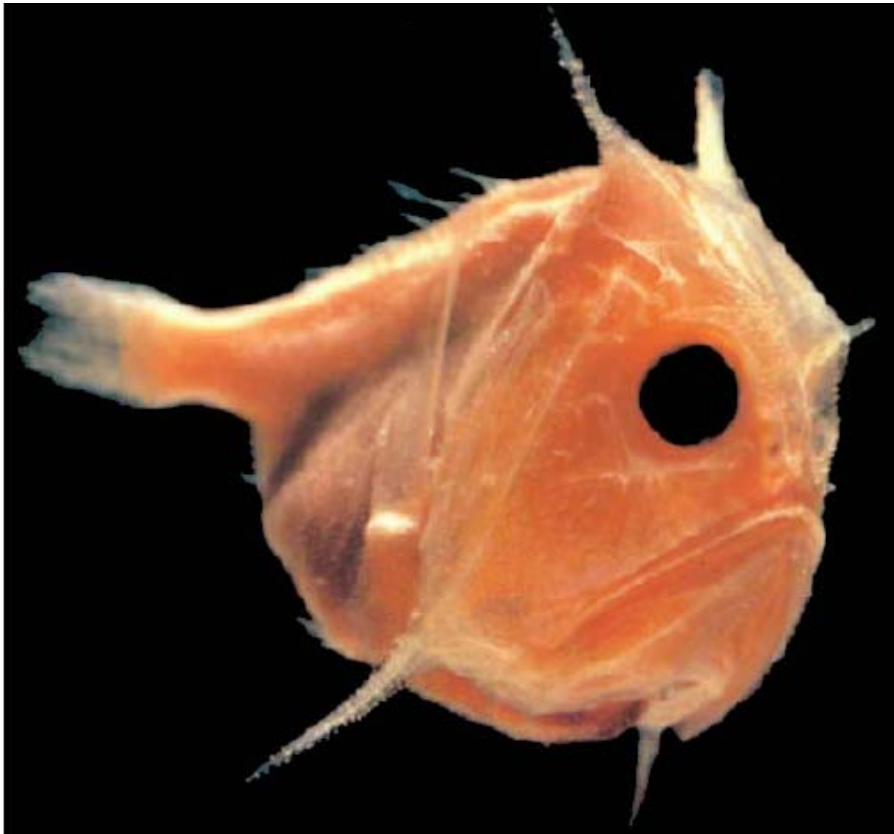


**GEOLOGICA ULTRAIECTINA**

Mededelingen van de  
Faculteit Aardwetenschappen  
Universiteit Utrecht

No. 168

**PELAGIC, HEMIPELAGIC AND TURBIDITE DEPOSITION  
IN THE ARABIAN SEA DURING THE LATE QUATERNARY**



**Unravelling the signals of eolian and fluvial sediment supply  
as functions of tectonics, sea-level and climate change  
by means of end-member modelling of siliciclastic grain-size distributions**

**Maarten A. Prins**

Front cover — *Dwellers of the Depths*

ISBN 90-5744-026-1

# **PELAGIC, HEMIPELAGIC AND TURBIDITE DEPOSITION IN THE ARABIAN SEA DURING THE LATE QUATERNARY**

**Unravelling the signals of eolian and fluvial sediment supply  
as functions of tectonics, sea-level and climate change  
by means of end-member modelling of siliciclastic grain-size distributions**

## **PELAGISCHE, HEMIPELAGISCHE EN TURBIDIET SEDIMENTATIE IN DE ARABISCHE ZEE GEDURENDE HET LAAT KWARTAIR**

Ontrafelen van eolische en fluviatiele sediment-aanvoer signalen  
als functie van tektoniek, zeespiegel- en klimaatveranderingen  
met behulp van eind-lid modellering van siliciklastische korrelgrootteverdelingen

(met een samenvatting in het Nederlands)

### **Proefschrift**

ter verkrijging van de graad van doctor  
aan de Universiteit Utrecht  
op gezag van de Rector Magnificus, Prof. Dr. H.O. Voorma  
ingevolge het besluit van het College voor Promoties  
in het openbaar te verdedigen  
op maandag 1 maart 1999 des middags te 4.15 uur

door

**Maarten Arnoud Prins**

geboren op 12 januari 1967, te Utrecht

**Promotoren:**

**Prof. Dr. D. Eisma *em.***

Netherlands Institute for Sea Research, Den Burg, The Netherlands;  
Faculty of Earth Sciences, Utrecht University, Utrecht, The Netherlands

**Prof. Dr. P.L. de Boer**

Faculty of Earth Sciences, Utrecht University, Utrecht, The Netherlands

**Co-promotoren:**

**Dr. G. Postma**

Faculty of Earth Sciences, Utrecht University, Utrecht, The Netherlands

**Dr. G.J. Weltje**

Department of Geo-Energy, Netherlands Institute of Applied Geoscience TNO,  
Haarlem, The Netherlands; Subfaculty of Applied Earth Sciences, Delft University of  
Technology, Delft, The Netherlands

Research was carried out at the Institute for Paleoenvironments and Paleoclimate Utrecht (IPPU) of the Netherlands Research School of Sedimentary Geology (NSG) in the framework of the Netherlands Indian Ocean Programme (NIOP).

*Aan mijn ouders  
Voor Jacqueline, Maaike en Frank*

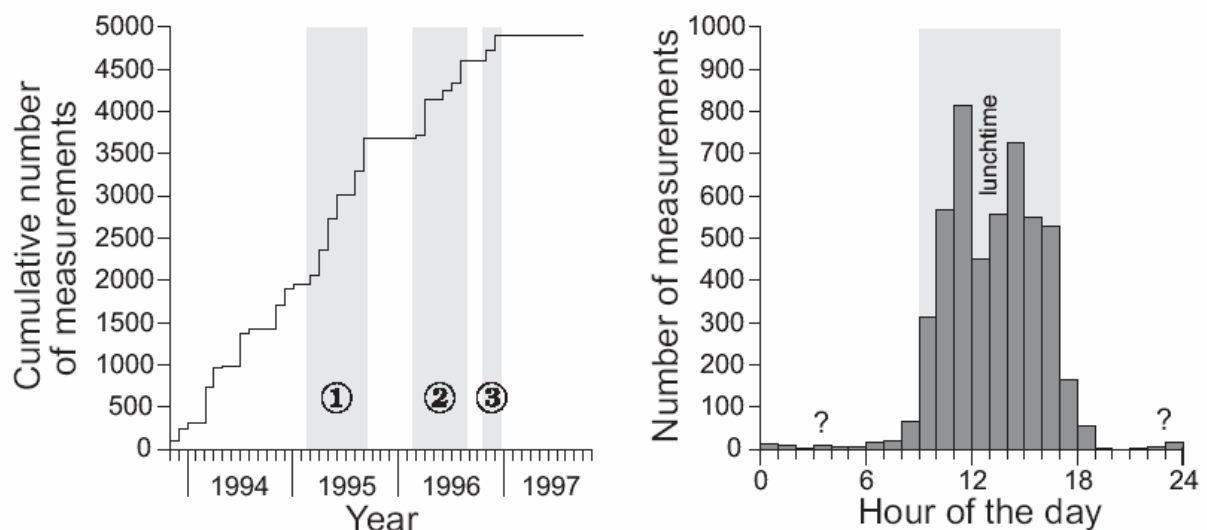


## DANKWOORD

Mijn promotoren, Doeke Eisma en Poppe de Boer, bedank ik voor hun opbouwende kritiek en wetenschappelijke ondersteuning bij de totstandkoming van dit proefschrift. Poppe de Boer wordt ook met name bedankt voor zijn redactionele hulp.

Voorts wil ik mijn eerste co-promotor, George Postma, bedanken voor het feit dat hij mij de mogelijkheid heeft gegeven om promotieonderzoek te doen. Zijn interesse voor turbidietafzettingen bleek besmettelijk tijdens mijn doctoraal veldwerk in de Noordelijke Appenijnen, dat ik onder zijn enthousiaste begeleiding heb verricht. Ik was dan ook blij verrast toen George mij vlak voor het behalen van mijn doctoraaldiploma voorstelde om mee te gaan naar de Indus Fan om daar marien-geologisch onderzoek te gaan doen. Naast het onderzoek aan de turbidieten, heb ik mij bezig gehouden met de – op het oog wat saaier – diepzeemodder in de Arabische Zee. In de vele korrelgrootteverdelingen die er gemeten zijn bleek echter heel wat informatie te zitten, die er ook werkelijk uitgehaald kon worden met behulp van de ‘black box’ van mijn tweede co-promotor, Gert Jan Weltje. Gert Jan heeft mij ervan weten te overtuigen dat sedimenten mengsels zijn van korrels met verschillende grootte en samenstelling, en dat er soms een verrassend verband is tussen die twee eigenschappen, maar soms ook helemaal niet maar toch ook weer wel, of zoiets. Gert Jan wordt hartelijk bedankt voor het beschikbaar stellen van de vele – nachtelijke – uren tijdens welke ik met hem heb mogen samenwerken.

Veel dank ben ik verschuldigd aan een aantal ex-studenten die mij hebben geassisteerd bij de vele duizenden korrelgroottemetingen, te weten Jan-Berend Stuu, Peter Paul Lebbink en Iwan de Lugt. Dat hun inspanning niet gering, doch ook niet overmatig is geweest valt af te leiden uit onderstaande figuur. Niet minder leuk en vruchtbaar was de samenwerking met Jelmer Cleveringa, mede dankzij het feit dat hij eigenlijk altijd bij de RGD aan het werk was.



**‘Timing’ of grain-size measurements. A: Individual contributions of M.Sc. students to the research described in this thesis is indicated by shaded bars: 1. Jan-Berend Stuu; 2. Peter Paul Lebbink; 3. Iwan de Lugt. B: Modal structure and ‘sorting’ of the distribution of grain-size measurements through the day is strongly indicative for a relaxed working atmosphere at the Sedimentology division of the Faculty of Earth Sciences of Utrecht University.**

De prettige sfeer op de Faculteit Aardwetenschappen heeft in belangrijke mate bijgedragen aan de vreugde die ik heb ervaren tijdens het werken en met name ook tijdens het pauzeren. Om verscheidene redenen gaat mijn dank dan ook uit naar een groot aantal collega's van wie ik in het bijzonder wil noemen, in min of meer willekeurige volgorde:

- mijn kamergenoten: Henk de Haas, Johan ten Veen, Gert Jan Weltje, Jelmer Cleveringa en Jan-Berend Stuut;
- mijn overige collega's van de Afdeling Sedimentologie: Albert Oost, Jaco Baas, Hans Zijlstra, Niek Molenaar, Wout Nijman, Max van Heijst, Bastiaan van Dijck, Xander Meijer, Quintijn Clevis, Marjan Reith, Ton Zalm, en Paul Anten;
- al mijn collega's van de Afdeling Stratigrafie/Paleontologie, in het bijzonder Michiel van der Meulen, Jan van Dam, Natasja Jannink, Ivo Duijnstee, Tanja Kouwenhoven en Lucas Lourens;
- mijn NIOP collega's: Gert Jan Reichart, Hendrik Jan Visser, Maryke den Dulk, Jan-Willem Zachariasse, Cees van der Weijden, Willem van der Linden;
- Thea Broers, Arnold van Dijk, Geert Ittmann, Gerrit van 't Veld, en Helen de Waard;
- Jeroen de Graaff;
- Paul van Oudenallen, Fred Trappenburg;
- Marnella van der Tol, Boudewijn 't Hart;
- alle overige collega's die naarstig op zoek zijn geweest naar hun naam in bovenstaande lijst maar er helaas – om géén enkele reden – niet in te vinden zijn.

De leden van de leescommissie – Prof. Dr. C.H. van der Weijden, Prof. Dr. J.E. van Hinte, Prof. Dr. J.F. Vandenberghe en Dr. Tj.C.E. van Weering – dank ik hartelijk voor hun getoonde belangstelling voor mijn promotieonderzoek.

Mijn familie, schoonouders, vrienden en kennissen wil ik hartelijk bedanken voor hun voortdurende belangstelling in mijn onderzoek (“wat is het nut van jouw onderzoek?”) en mijn wel en wee (“wanneer ben je nou eindelijk klaar?”).

Mijn overtollige energie kon ik gelukkig altijd probleemloos botvieren onder muzikale begeleiding van Huig Bergsma, Arno Hanssen, Sjoerd Wortelboer, Dustbin Dogs, Miquel Agerkop, Annemiek Harreman, Four Granted en natuurlijk Johan ten Veen, Jan van Dam, Michiel van der Meulen en – niet te vergeten – Frank Koornwinder. Ik dank hen hiervoor hartelijk.

Veel dank ben ik verschuldigd aan mijn ouders voor hun liefde, interesse en hun niet aflatende steun. Het verdriet dat ik heb om het overlijden van mijn vader komt bij het schrijven van deze alinea in alle hevigheid terug, aangezien mijn vader – mijn belangrijkste inspiratiebron om promotieonderzoek te gaan doen – nooit dit ‘blauwe boekje’ in ontvangst zal kunnen nemen.

Jacqueline, Maaike en Frank ..... krijg ik nu eindelijk een cavia?

# CONTENTS

<b>Samenvatting</b>		<b>11</b>
<b>Chapter 1</b>	Introduction and summary	<b>19</b>
<b>Chapter 2</b>	Evaluation of the Malvern 2600 laser-diffraction size analyser for use with fine-grained sediments	<b>25</b>
<b>Chapter 3</b>	End-member modelling of grain-size distributions of sediment mixtures	<b>47</b>
<b>Chapter 4</b>	Late Quaternary eolian and fluvial sediment supply to the Arabian Sea and its paleoclimatic significance: an application of end-member modelling of siliciclastic grain-size distributions	<b>69</b>
<b>Chapter 5</b>	Teleconnections between the Asian monsoons and the North Atlantic climate during the late Quaternary	<b>97</b>
<b>Chapter 6</b>	Controls on late Pleistocene-Holocene sedimentation on the Indus Fan	<b>121</b>
<b>Chapter 7</b>	Controls on late Pleistocene-Holocene sedimentation on the Makran continental slope	<b>145</b>
<b>Chapter 8</b>	Sea-level and climate signatures in turbidite successions along the tectonically active and passive northern margin of the Arabian Sea	<b>173</b>
<b>References</b>		<b>184</b>
<b>Curriculum vitae</b>		<b>192</b>



# **SAMENVATTING**

## **PROBLEEMSTELLING**

Tektoniek, zeespiegel- en klimaatveranderingen zijn de belangrijkste factoren die, over lange tijdschalen, de aanvoer van terrigene (van het land afkomstige) sedimenten naar oceanische bekkens bepalen en beïnvloeden. Twee belangrijke mechanismen bepalen met name de ‘timing’ van hoogfrequente veranderingen in mariene sedimentaire opeenvolgingen van het laat Kwartair: glacio-eustatische zeespiegelveranderingen en klimaatveranderingen. Verlaging van de zeespiegel gedurende ijstijden bevordert het transport van sediment naar de diepzee door het vergroten van de instabiliteit van sedimenten op de continentale helling, door het vergroten van drainagebekkens van rivieren als gevolg van het droogvallen van shelfzeeën, en door het verhogen van de erosiecompetentie van rivieren als gevolg van een ‘base-level’ verlaging. De overgang van een relatief droog klimaat naar een relatief nat klimaat zal resulteren in een stijging van rivierwaterafvoer en daarmee samenhangend in een toename van transport van fijnkorrelige riviersedimenten naar de diepzee. Aan de andere kant, een verdroging van het klimaat kan resulteren in woestijnvorming. Dit leidt tot een toename van eolisch (door de wind) sedimenttransport naar de oceaan. Deze mechanismen voor verhoogd sedimenttransport naar de diepzee zijn ‘eindleden’ van een breed spectrum, waarbij zeespiegelverlaging en verhoogde rivierafvoer gedurende natte klimaatcondities aan de ene kant, en verhoogd eolisch sedimenttransport gedurende droge klimaatcondities aan de andere kant, in fase of uit fase kunnen plaatsvinden.

Het doel van het onderhavige onderzoek was een ‘massabalans’ (‘timing’, herkomst, volume, distributie) op te stellen van het terrigene sediment in de Arabische Zee, afgezet gedurende het laat Kwartair (de laatste 20,000-200,000 jaar). De gereconstrueerde veranderingen in de onderzochte sedimentaire systemen worden gerelateerd aan glacio-eustatische zeespiegelveranderingen, aan de klimatologische evolutie van de omringende continenten en aan de tektonische configuratie van de sedimentaire bekkens. De uitkomsten van het onderzoek verschaffen een beter inzicht in de relatie tussen zeespiegel- en klimaatveranderingen en hun effecten op de distributie van terrigene sedimenten in de Arabische Zee.

## **DE ARABISCHE ZEE**

### *Regionale Setting*

De Arabische Zee beslaat de noordwestelijke Indische Oceaan en wordt omringd door de Somalische en Arabische schiereilanden in het westen, Iran en Pakistan in het noorden, en het Indische schiereiland in het oosten. De oost-west gelinieerde Makran gebergtegordel in Iran en zuidwest Pakistan vormt de noordelijke begrenzing van de Arabische Zee. De subductie (onderschuiving) van de oceanische korst van de meest noordwestelijke hoek van de Arabische Zee (Oman Bekken), dat onderdeel uitmaakt van de Indische tektonische plaat, onder het Aziatische continent zorgt voor de gebergtevorming in de Makran (tektonisch ‘actieve’ continentrand) en heeft een kustparallele onderzeese topografie gevormd van gelinieerde opgeheven gebergten (‘ruggen’) en tussenliggende laagten (mariene sedimentbekkens). Het meest markante geologische fenomeen in de Arabische Zee is wellicht de onderzeese puinwaaier van de Indus Rivier (‘Indus Fan’) die vrijwel geheel het centrale

deel van de Arabische Zee (Arabische Bekken) vult. De ‘Indus Fan’ heeft een noord-zuid lengte van maximaal 1600 kilometer en een west-oost breedte van maximaal 1000 km en is daarmee de op één na grootste onderzeese puinwaaier op de wereld. De puinwaaier heeft zich ontwikkeld langs de tektonisch ‘passieve’ continentrand van zuidoost Pakistan en India, en wordt begrensd door enkele hoge onderzeese gebergtekets, de Chagos-Laccadiven Rug in het oosten, de Owen-Murray Rug in het westen, en de Carlsberg Rug in het zuiden.

#### *Tegenwoordige Distributiepatronen van Eolische en Fluviaatiele Sedimenten*

Het huidige Aziatische moessonklimaat beïnvloedt in belangrijke mate de huidige distributiepatronen van terrigene sedimenten in de Arabische Zee. Gedurende de winter resulteren de verschillen in opwarming van het Aziatische continent (‘koud’) en de Indische Oceaan (‘warm’) in een lagedrukgebied boven de zuidelijke Indische Oceaan en een hogedrukgebied boven het Aziatische continent (gecentreerd rond het Tibetaanse Plateau). Deze noordoost-zuidwest georiënteerde atmosferische drukgradient is de motor achter de wintermoessoncirculatie welke zich manifesteert in noordoostelijke winden over de Arabische Zee. De wintermoesson transporteert kleine hoeveelheden eolisch stof vanuit Pakistan en India, onder andere vanuit de Thar woestijn, naar de noordoostelijke Arabische Zee. Gedurende het voorjaar, wanneer het Aziatische continent begint op te warmen, ontwikkelt zich een atmosferisch circulatiesysteem met dominant westelijke tot noordwestelijke winden boven de Arabische Zee. Dit windsysteem is verantwoordelijk voor het transport van grote hoeveelheden eolisch stof vanuit de Arabische woestijn en relatief kleine hoeveelheden eolisch stof vanuit Pakistan naar de westelijke-noordwestelijke Arabische Zee. Gedurende de zomer, wanneer het Aziatische continent warmer wordt dan de Indische Oceaan en de drukgradient tegengesteld is aan de wintersituatie, ontwikkelt zich een sterke zuidwestelijke wind; de zomermoesson. De zomermoesson transporteert relatief kleine hoeveelheden eolisch stof vanaf het Somalische schiereiland naar de westelijke Arabische Zee. Tevens vervoert de zomermoesson grote hoeveelheden waterdamp die de belangrijkste bron van neerslag vormt voor het Aziatische continent. Deze sterk seizoensgebonden neerslag vormt de dominante bron van water voor de Aziatische rivieren, waaronder de Indus Rivier welke uitstroomt in de noordelijke Arabische Zee (zuid Pakistan). De diepzeesedimenten in de Arabische Zee zijn dus mengsels van eolische en fluviatiele sedimenten met daarbij sediment dat in de open zee door organismen wordt geproduceerd (kalk, silica). De verhouding tussen de twee typen sediment (eolisch, fluviatiel) is onder meer afhankelijk van de nabijheid van sedimentleverende brongebieden (woestijn, rivier) en dus afhankelijk van de locatie in het sedimentbekken. Tevens zal op elke locatie in de Arabische Zee de aanvoer van de eolische en fluviatiele sedimenten door de tijd hebben gevarieerd als functie van zeespiegel- en klimaatveranderingen.

#### *Pelagische, Hemipelagische en Turbidiet Sedimentatie Gedurende het Laat Kwartair*

Bemonstering van diepzeesedimenten met behulp van sedimentkernen levert ongestoorde monsters van laat-Kwartaire sedimentaire opéénvolgingen, die relatief éénvoudig en nauwkeurig kunnen worden gedateerd. De terrigene fractie van deze sedimenten weerspiegelt de aanvoer van sedimenten die op het nabijgelegen continent zijn geproduceerd. Dergelijke sedimentkolommen bevatten mogelijk de sleutel voor de reconstructie van het klimaat in het geologische verleden (‘paleoklimaat’). De verwachting en aanname is dat het totale volume aan fijnkorrelig sediment (klei, silt), dat door rivieren naar de Arabische Zee wordt getransporteerd, toeneemt met een toenemende snelheid en volume van waterafvoer. Veranderingen in de accumulatiesnelheid van fluviatiele modder op een bepaalde locatie in de

diepzee kunnen dan worden gebruikt als indicatie voor veranderingen in de hoeveelheid neerslag in het stroomgebied van de rivier. Analyse van de eolische fractie van diepzeesedimenten kan op deze wijze inzicht verschaffen in veranderingen in ariditeit in het brongebied van het eolische stof. Veranderingen in de intensiteit (windsterkte) van het sediment-transporterende windsysteem kunnen worden gereconstrueerd aan de hand van korrelgroottemetingen van het eolische stof.

Verschillende onderzoekers hebben gesuggereerd dat variaties in accumulatiesnelheid van terrigeen materiaal in de pelagische en hemipelagische sedimenten ('diepzeemodder' afgezet uit suspensie) in de westelijke en noordelijke Arabische Zee (op de continentale helling van Arabië, Owen Rug, Murray Rug) kan worden gebruikt om veranderingen in ariditeit in de Arabische woestijn te reconstrueren. Zo zijn de temporele variaties in korrelgrootte van het terrigene sediment op de Owen Rug gebruikt om veranderingen in de sterkte van de zomerwoestijn te reconstrueren. Dit is echter alleen mogelijk indien het terrigene sediment uitsluitend uit eolisch stof bestaat. De aanwezigheid van zowel eolische als fluviatiele sedimentbronnen, dat wil zeggen grote woestijnen en grote riviersystemen, sluit uit dat in het verleden ooit slechts één van beide actief geweest is.

Dit 'mengprobleem' is slechts door een enkeling herkend. Het probleem werd dan 'opgelost' door op basis van een arbitraire korrelgroottegrens onderscheid te maken tussen eolische ('siltige') en fluviatiele ('kleiige') sedimenten. Op die manier is getracht het geografisch distributiepatroon van eolisch stof in de Arabische Zee te reconstrueren. De aldus geobserveerde noordwest-zuidoost gradient in het percentage eolisch silt (t.o.v. fluviatiele modder) suggereert dat noordwestelijke winden het belangrijkste transport medium zijn. De geografische verspreiding van eolisch stof werd tevens gebruikt om de positie van het front tussen de noordwestelijke winden en de zuidwestelijke zomerwoestijn, een fysische barrière voor oostwaarts transport van eolisch stof, te benaderen. Veranderingen in de positie van dit front gedurende het geologische verleden werden aldus afgeleid uit veranderingen van korrelgrootte en mineralogie van de sedimenten in de westelijke Arabische Zee.

Het is waarschijnlijk dat veranderingen in de intensiteit en richting van de zomerwoestijn in het geologische verleden ook de neerslagpatronen op het Aziatische continent hebben beïnvloed. Echter, een duidelijk beeld van eventuele laat Kwartaire veranderingen in waterafvoer en transport van fluviatiel sediment naar de Arabische Zee ontbreekt tot op heden. De variaties in samenstelling van de terrigene fractie in de diepzeesedimenten in de Arabische Zee worden in de bestaande literatuur met name uitgelegd in termen van variaties in eolisch sedimentaanvoer. Echter, gedetailleerde kennis van laat Kwartaire veranderingen in het distributiepatroon van eolisch sediment afkomstig uit het Indische-Pakistaanse aride achterland ontbreekt in zijn geheel. Sedimentaire opéénvolgingen die hoogst waarschijnlijk de signaturen bevatten over veranderingen in zowel de fluviatiele sedimentaanvoer als de winterwoestijn-gestuurde eolische sedimentaanvoer zijn te verwachten op de Pakistaanse continentale helling en op de puinwaaier van de Indus rivier. Dit proefschrift beoogt de ontbrekende paleoklimatologische informatie aan te dragen door de eolische en fluviatiele signalen in bovengenoemde sedimenten te ontrafelen.

Op de bodem van het continentale plat en op de continentale helling voor de delta van de Indus rivier bevindt zich een diep ingesneden trog, de 'Indus Canyon'. Deze trog fungeert als doorvoerkanal van fluviatiel sediment dat wordt aangevoerd door de Indus rivier. In het geologische verleden zijn enorme hoeveelheden sediment als troebelingsstroom (onderzeese sedimentstromen) via de trog en grote geulsystemen (onderzeese 'rivieren') naar de diepzee getransporteerd en afgezet in de Indus puinwaaier. Een recente studie aan de trog bracht naar voren dat de laatste fase van insnijding heeft plaats gevonden tijdens de laatste ijstijd toen de zeespiegel zo'n 125 meter lager stond. Verschillende onderzoekers hebben gesuggereerd dat met name de veranderingen in de stand van de zeespiegel een belangrijke sturende factor is

achter het sedimenttransport naar de puinwaaier. Echter, deze studies hebben allen nagelaten om harde bewijzen aan te dragen die hun beweringen ondersteunen: goede dateringen van de sedimenten en de verschillende geulsystemen op de puinwaaier ontbreken tot op heden. Dit proefschrift beoogt deze leemte in kennis op te vullen.

## **INDELING EN SAMENVATTING VAN DIT PROEFSCHRIFT**

De ‘kwaliteit’ van paleoklimaatreconstructies (windsterkte, ariditeit op land) gebaseerd op de analyse van terrigene sedimenten in de Arabische Zee hangt af van de mogelijkheid om de verschillende types sediment –fluviaal en eolisch– te onderscheiden. In dit proefschrift is een nieuwe onderzoeksmethode onderzocht (Hoofdstuk 2, 3) die het mogelijk maakt om een onderscheid te maken tussen eolische en fluviatiele sedimenten op basis van de korrelgrootteverdeling van de terrigene sediment fractie. De methode maakt het mogelijk om mengsels van deze en eventueel andere sedimenttypen (bijvoorbeeld troebelingsstroomafzettingen: turbidieten) te ontmengen (Hoofdstuk 4, 7). Aldus maakt deze methode het mogelijk om veranderingen in sedimentsamenstelling te interpreteren in termen van continentale ariditeit en windsterkte: de verhouding tussen het fluviatiele en eolische aandeel in diepzeesedimenten is een maat voor de ariditeit in het brongebied terwijl de korrelgrootte van het eolische stof een maat is voor de transportcapaciteit van het windsysteem (intensiteit van de zomer- en wintermoesson) dat het eolische stof heeft getransporteerd (Hoofdstuk 4, 5, 7). De ‘timing’ van turbidietsedimentatie op twee tektonisch-contrasterende diepzee puinwaaier systemen –langs de passieve continentale plaat (Indus Fan) en langs de actieve continentale plaat (Makran)– wordt gerelateerd aan laat-Pleistocene en Holocene zeespiegel- en klimaatveranderingen (Hoofdstuk 6, 7). Een synthese van de resultaten wordt gepresenteerd in Hoofdstuk 8.

### ***Hoofdstuk 2 — Evaluatie van een korrelgroottemeetinstrument voor de toepassing op fijnkorrelige sedimenten***

Korrelgrootteverdelingen van sedimenten bevatten informatie over het betreffende sedimentaire milieu en de daarin afspelende afzettingsprocessen. Variaties in de korrelgrootte in een sedimentair bekken zijn meestal te relateren aan twee soorten processen: (1) menging van sedimenten met verschillende korrelgrootteverdelingen; (2) selectieve processen gedurende transport en afzetting. Daardoor ontstaan sedimenten met korrelgrootteverdelingen die systematisch veranderen met de afstand tot het brongebied en/of de transportcapaciteit van het medium (water, lucht) waarin het sediment wordt vervoerd. De betrouwbaarheid van paleoklimaatreconstructies die zijn gebaseerd op korrelgroottegegevens hangt, naast andere factoren, af van de kwaliteit van de korrelgroottemetingen. De kwaliteiten van het meetinstrument dat is gebruikt voor dit onderzoek, een Malvern Instruments Laser Particle Sizer Type 2600, worden daarom in dit hoofdstuk geëvalueerd. Speciaal voor dit doel zijn kunstmatige sedimenten geprepareerd door standaarden met bekende korrelgrootteverdelingen in bekende massaverhoudingen te mengen. Analyse van deze mengsels staat toe om de capaciteiten van het meetinstrument te inspecteren. De experimenten brengen duidelijk naar voren dat het korrelgroottemeetinstrument goed te gebruiken is om ‘subpopulaties’ in natuurlijke sedimentmengsels te herkennen en ook dat de korrelgroottegegevens goed zijn te gebruiken om dergelijke mengsels te ‘ontmengen’.

### ***Hoofdstuk 3 — Eindlid modellering van korrelgrootteverdelingen van sediment mengsels***

Een set computer programma's –invers-numerieke, statistische eindlid modellerings algoritmen– worden in dit hoofdstuk getest op hun bruikbaarheid voor het ontrafelen van de samenstelling van natuurlijke sedimenten afkomstig uit meerdere bronnen ('mengsels'). De korrelgroottegegevens van de kunstmatige sedimentmengsels beschreven in het vorige hoofdstuk worden gebruikt als 'testcase'. Het ultieme doel van eindlid modellering is om de aanwezige variatie in sedimentsamenstellingen (in dit geval de variatie in de korrelgrootteverdelingen) zo goed mogelijk te benaderen en te verklaren als gevolg van menging van 'extreme' samenstellingen (eindleden) zonder voorkennis van het geologische systeem waaruit de monsters zijn genomen. Een eindlid model beschrijft de samenstelling (korrelgrootteverdelingen) van de eindleden en de mengverhoudingen van deze eindleden in de gemodelleerde sedimentmengsels. Een onafhankelijke vergelijking van gemodelleerde eindleden en mengverhoudingen van deze eindleden enerzijds en de 'echte' eindleden (de sediment standaarden) en de 'echte' mengverhoudingen anderzijds, maakt het mogelijk een objectieve inschatting te maken van de geldigheid van de ontmengings uitkomst. De vergelijking geeft aan dat eindlid modellering een zeer krachtig gereedschap is voor het analyseren van korrelgroottegegevens in die gevallen waar de geobserveerde variatie in de samenstellingen veroorzaakt zijn door menging van materiaal uit verschillende bronnen.

***Hoofdstuk 4 — Transport van eolische en fluviatiele sedimenten naar de Arabische Zee gedurende het laat-Kwartair en de paleoklimatologische betekenis daarvan: een toepassing van eindlid modellering van korrelgrootteverdelingen van siliciklastische sedimenten***

De algoritmen voor eindlid modellering worden gebruikt om de variatie in een grote dataset van korrelgrootteverdelingen van een grote hoeveelheid monsters van terrigene diepzeemodder uit de Arabische Zee te modelleren. De korrelgrootteverdelingen van sedimenten van de continentale helling van Oman, de Owen Rug, de continentale helling van Pakistan en van de Indus Fan kunnen goed worden beschreven als mengsels van drie eindleden. De geografische variatie in de verhouding van de drie eindleden wordt geïnterpreteerd in termen van herkomst (brongebied) en transportprocessen. De eindleden representeren grof-siltig eolisch stof, fijn-siltig eolisch stof en fijn-siltig/kleiïg fluviatiele modder. De temporele variaties in de mengverhoudingen van de eindleden kunnen, op elke willekeurige locatie in de Arabische Zee, worden geïnterpreteerd in termen van klimaatveranderingen. De mengverhouding van de twee eolische eindleden, ofwel de korrelgrootteverdeling van het eolische stof, wordt gebruikt als maat voor de sterkte van het stof-transporterende windsysteem. De mengverhouding van de eolische en fluviatiele eindleden wordt gebruikt als maat voor continentale ariditeit. De reconstructie van het moessonklimaat rond de Arabische Zee gedurende het laat Kwartair (ongeveer de laatste 200,000 jaren) geeft tijdseries van continentale ariditeit, de sterkte van de zomer-moesson en de sterkte van winter-moesson.

***Hoofdstuk 5 — Teleconnecties tussen het moesson klimaat van Azië en het klimaat van de Noord Atlantische Oceaan gedurende het laat Kwartair***

Additionele tijdseries van de in het vorige hoofdstuk geïntroduceerde, op korrelgroottegegevens gebaseerde, klimaatsindicatoren worden gepresenteerd. Het doel van deze studie is te analyseren of er een correlatie bestaat tussen veranderingen in de mariene eolische-fluviatiele moddersequenties in de noordoostelijke Arabische Zee en de terrestrische (op land afgezette) sedimentsequenties in centraal China. De laatste bestaan uit afwisselingen

van löss (eolisch sediment) en fossiele bodems. Voorts wordt een vergelijking gemaakt tussen de laat-Kwartaire klimaatveranderingen rond de Arabische Zee en de Noord Atlantische Oceaan. Overeenkomsten tussen de klimaatreconstructies van deze regio's laten zien dat in het geologische verleden de veranderingen in het moessonklimaat rond de Arabische Zee en in Oost-Azië gelijktijdig hebben plaats gevonden met tegelijkertijd belangrijke klimatologische veranderingen rond de Noord Atlantische Oceaan.

### **Hoofdstuk 6 — Sedimentatie op de Indus Fan gedurende het laat Pleistoceen en het Holoceen**

Sedimentkernen genomen in de Indus Canyon en op de Indus Fan worden bestudeerd met het doel een reconstructie te maken van zand- en moddersedimentatie op de puinwaaier gedurende de laatste ~35,000 jaar. De geochemische, mineralogische en korrelgroottekaracteristieken van de modderafzettingen op de Indus Fan worden geanalyseerd om temporele veranderingen in de accumulatiesnelheid en de herkomst van het terrigene sediment te bepalen. De 'timing' van sedimentatie en de evolutie van de geulsystemen op de puinwaaier worden gerelateerd aan interne (door het systeem zelf gecontroleerde) sedimentaire processen en externe mechanismen, met name zeespiegelveranderingen. Een vergelijking wordt gemaakt tussen de geschiedenis van puinwaaierontwikkeling (geulontwikkeling, turbidiet sedimentatie) op de Indus Fan en de erosie- en sedimentatiegeschiedenis in de Indus Canyon en op de omringende shelf en continentale helling. De geologische gegevens laten zien dat de cyclische veranderingen in erosie en sedimentatie in de 'canyon' en op de 'fan' in belangrijke mate worden bepaald door veranderingen in de stand van de zeespiegel.

### **Hoofdstuk 7 — Sedimentatie op de Makran continentale helling gedurende het laat Pleistoceen en het Holoceen**

De sedimentatiepatronen van terrigene sediment op de continentale helling van zuidwestelijk Pakistan, dus langs de tektonisch-actieve Makran continentale plaatrand, wordt bestudeerd aan de hand van een aantal sedimentkernen. Numeriek-statistische algoritmen worden gebruikt om de eindleden van de korrelgrootteverdelingen van de diepzeemodder- en turbidietafzettingen te modelleren. De geochemische en mineralogische samenstelling van de modderige sedimenten geven aan dat het eolische stof met name afkomstig is van het noordelijke Arabische schiereiland en de regio rond de Perzische Golf, en dat de fluviatiele sedimenten afkomstig zijn van de Makran. De mengverhouding van de eolische en fluviatiele sedimenten in de modderige intervallen wordt gebruikt als indicator voor continentale ariditeit, welke weer is gerelateerd aan de sterkte van de zomermoesson. Geografische en temporele variatie in sedimentsamenstelling, sedimentatiesnelheid en frequentie van turbidietafzetting gedurende het laat Pleistoceen en het Holoceen (laatste 20,000 jaar) wordt bediscussieerd en gerelateerd aan veranderingen in klimaat en zeespiegel en tektonische setting en activiteit (aardbevingen).

### **Hoofdstuk 8 — Zeespiegel- en klimaatsignaturen in turbidietafzettingen langs de tektonisch actieve en passieve noordelijke sectoren van de Arabische Zee**

De 'timing' van modder- en turbidiet sedimentatie langs een tektonisch passieve plaatrand, d.w.z. op de Indus Fan, en langs een tektonisch actieve plaatrand, d.w.z. op de Makran continentale helling, worden bediscussieerd. Het unieke aan deze vergelijking is dat beide turbidiet systemen in het zelfde sedimentaire bekken liggen, in de Arabische Zee. Dit

impliceert dat beide systemen dezelfde veranderingen in klimaat en zeespiegel hebben ervaren, maar in verschillende tektonische regimes. De vergelijking maakt het mogelijk om de individuele effecten van klimaatveranderingen, zeespiegelveranderingen en tektonische activiteit op sedimentaanvoer- en distributiepatronen in de Arabische Zee te onderzoeken.



## INTRODUCTION AND SUMMARY

### GENERAL

Tectonics, sea-level changes and variations in climate are the major controlling factors on the input of terrigenous sediments in ocean basins over long periods of time. Two important mechanisms define the timing of high-frequency changes in the sedimentary record of the late Quaternary: glacio-eustatic sea-level change and climate change. Lowering of sea level enhances sediment transport by slope instability processes, by enlargement of the drainage basin through exposure of the shelf and by increasing the river's competence through base-level lowering. Climate change from an arid into a humid climate may result in an increase in river discharge and thus in an increased fluvial sediment transport into deep-sea fan systems. On the other hand, a change into a dry climate may increase the eolian transport of fine-grained terrigenous material. These mechanisms for increased sediment transport are 'end members' of a spectrum, in which sea-level lowstand and high river discharge during favourable humid-climate periods on the one hand, and enhanced eolian activity during favourable arid-climate periods on the other hand can be in phase or out of phase.

The main objectives of this project are to unravel late Quaternary Arabian-Sea records of fine-grained terrigenous sediments, and to reconstruct the flux and provenance of these sediments. The reconstructed 'mass balance' (origin, timing, volume and distribution) of the terrigenous sediments deposited in the Arabian Sea during the late Quaternary will be related to glacio-eustatic sea-level changes, to the paleoclimate evolution of the surrounding continental areas and to the tectonic setting of the sedimentary systems. The outcome of the project will allow insights into the phase relationship of glacio-eustatic sea-level changes and climate changes and their effects on terrigenous sediment distribution in the Arabian Sea.

### THE ARABIAN SEA

#### *Regional Setting*

The Arabian Sea constitutes the north-western Indian Ocean and is enclosed by the Somalian and Arabian Peninsulas in the west, Iran and Pakistan in the north, and the Indian Peninsula in the east. The northern margin of the Arabian Sea (Iran, south-western Pakistan) is the offshore extension of the Makran subduction complex. In this region, the subduction process has produced a topography of uplifted ridges and intervening basins delineated parallel to the coast (White, 1982). The most conspicuous geological feature in the Arabian Sea is the Indus Fan which occupies the complete central part of the basin. The Indus Fan, with a length of 1600 km and a maximum width of 1000 km, is the second-largest deep-sea fan in the world (McHargue and Webb, 1986; Kolla and Coumes, 1987). The fan developed off the passive continental margin of Pakistan-India, and is bounded by the Chagos-Laccadive Ridge in the east, by the Owen-Murray Ridges in the west, and in the south by the Carlsberg Ridge.

*Modern Eolian and Fluvial Sediment-Supply Patterns*

At present the Asian monsoon climate strongly influences terrigenous sediment supply patterns into the Arabian Sea. Differential heating during the northern-hemisphere winter leads to low surface pressure over the southern Indian Ocean and high surface pressure over the high elevations of the Indian-Asian continent. This NE-SW pressure gradient drives the winter-monsoon circulation which produces north-easterly monsoon winds over the Arabian Sea. The winter-monsoon winds transport minor amounts of eolian dust from Pakistan and northern India, e.g. from the Thar Desert, towards the Arabian Sea. During spring when the Indian-Asian continent starts to heat up, westerly to north-westerly winds prevail over the Arabian Sea. The north-westerly winds transport large quantities of eolian dust from the Arabian Peninsula, and only minor amounts from Pakistan. During peak summer, when the continent becomes warmer than the ocean and the pressure gradient reverses, strong south-westerly monsoon winds develop. The summer-monsoon winds supply minor amounts of eolian dust from Somalia. Moreover, the summer-monsoon winds carry large amounts of water vapour which is released as precipitation over the Indian-Asian continent. This precipitation provides the runoff for river systems draining the Indian-Asian continent, including the Indus River which flows into the Arabian Sea. The above observations indicate that the Arabian Sea sediments are mixtures of eolian dust and fluvial/hemipelagic mud. The relative proportion of the two types of sediment depends on the location in the basin. At any given location, the relative contributions of materials from both sources is likely to vary through time.

*Pelagic, Hemipelagic and Turbidite Deposition during the Late Quaternary*

Cores of late Quaternary deep-sea sediments provide continuous records which can be dated accurately. The terrigenous fraction of deep-sea sediments reflects the supply of sediments produced on the continents surrounding the basin. Such records potentially hold the key to the reconstruction of paleoclimate. The flux of river-derived fine-grained siliciclastics is expected to correlate with continental runoff, and thus would provide a proxy of continental humidity. Analysis of eolian dust in deep-sea sediments allows estimates of the past aridity of eolian source regions, through flux determinations, and of the intensity of the transporting winds through grain-size measurements. These two parameters, the grain size and the mass flux of eolian dust, may vary independently (Rea, 1994).

Several studies suggested that the analysis of pelagic-hemipelagic sediment records from the western and northern Arabian Sea (Oman continental slope, Owen Ridge, Murray Ridge) allows estimation of past aridity on the Arabian Peninsula (most important eolian source region) through determinations of the terrigenous sediment flux (Clemens and Prell, 1990; Shimmield *et al.*, 1990; Clemens and Prell, 1991; Clemens *et al.*, 1991; Shimmield and Mowbray, 1991; Clemens *et al.*, 1996; Reichart *et al.*, 1998). Clemens and Prell (1990, 1991) and Clemens *et al.* (1991, 1996) used the median grain size of terrigenous sediments on the Owen Ridge as an indicator of the summer-monsoon strength. Above proposed indicators of continental aridity and wind strength, i.e., the flux and the grain size of the terrigenous fraction within deep-sea sediments, are only valid, however, if the terrigenous fraction is exclusively of eolian origin. The presence of major eolian and fluvial sources around the Arabian Sea makes it highly unlikely that this prerequisite is fulfilled in many (if any) parts of the basin.

Sirocko (1991) and Sirocko *et al.* (1991) recognised this 'mixing problem' and used a somewhat arbitrary size cut-off to partition eolian and fluvial sediments, in order to map the distribution pattern of eolian dust in the marine sediment record of the Arabian Sea. They

observed a NW to SE gradient in eolian dust content from which they inferred that eolian dust is supplied mainly from the Arabian Peninsula by the northwesterlies. The extent of the eolian dust distribution pattern over the ocean was used to approximate the position of the front between the northwesterlies and the SW summer monsoon. Shifts of the position of this front are inferred from changes in grain-size parameters and mineralogy of western Arabian Sea sediments (Sirocko *et al.*, 1991; Sirocko and Lange, 1991; Sirocko *et al.*, 1993).

The changes in intensity and direction of the summer monsoon, inferred from the eolian dust mineralogy and grain-size records of the western Arabian Sea (see above), must have influenced the pattern of precipitation over the landmasses bordering the Arabian Sea to the west (Arabian Peninsula), north (Pakistan) and the east (India). Changes in precipitation within the drainage basins of Indian-Pakistan rivers are expected to have controlled the water discharge and the sediment load of these rivers. However, late Quaternary changes in continental runoff and associated fluvial suspended sediment supply to the Arabian Sea have not been documented. Similarly, a clear picture of the late-Quaternary history of the winter monsoon in the Arabian Sea area is at present lacking. Sedimentary records likely to contain the signatures of winter-monsoon strength and continental runoff are expected to be found on the Pakistan continental slope and the Indus Fan.

In the shelf and slope area near the Indus Delta, several canyon complexes have been recognised which served as conduits for sediments supplied by the Indus River. Several large channel-levee systems radiate from each canyon complex, forming a channel-levee complex. The youngest complex comprises the recently active Indus Canyon (McHargue and Webb, 1986; Kolla and Coumes, 1987; Droz and Bellaiche, 1991). Von Rad and Tahir (1997) presented a very detailed survey, including high-resolution seismic data and sediment cores, of the outer shelf and slope off the Indus Delta, including the Indus Canyon. They indicated that the Indus Canyon experienced maximum erosion and funnelled turbidity currents to the Indus Fan during the last glacial sea-level lowstand. The two youngest large channel-levee systems of the youngest channel-levee complex have been mapped in detail with long-range side-scan sonar (GLORIA) (Kenyon *et al.*, 1995). The study of Kenyon *et al.* (1995) resulted in a new scheme for labelling the Indus Fan channels on the basis of their relative age. Although it has been suggested that changes in sea level are the dominant factor controlling turbidite deposition on the Indus Fan (McHargue and Webb, 1986; Kolla and Coumes, 1987; Kolla and Macurda, 1988; McHargue, 1991; Kenyon *et al.*, 1995), no well-constrained data on the absolute ages of the channel-levee systems of the Indus Fan are available to support this hypothesis.

## ORGANISATION AND SUMMARY OF THIS THESIS

The quality of paleoclimate reconstructions (wind strength, continental aridity) on the basis of Arabian Sea terrigenous records depends primarily on the possibility of distinguishing between sediments of eolian and fluvial origin. In this thesis I have investigated a research methodology (Chapters 2, 3) which allows the distinction and unmixing of eolian and fluvial sediments on the basis of the grain-size distribution of the terrigenous sediment fraction (Chapter 4). This methodology allows temporal variations in sediment composition to be explicitly interpreted in terms of variations in continental aridity and intensity of both the summer and winter monsoons (Chapter 4, 5, 7). Furthermore, I will present results on the timing of turbidite deposition on the Indus Fan (Chapter 6) and, moreover, on the Makran continental slope (Chapter 7). A synthesis of the results is presented in Chapter 8.

**Chapter 2** — Analysis of grain-size distributions provides information about sedimentary environments and depositional processes. Variations in grain-size distribution within basin-

fill sediments may reflect two kinds of processes: (1) physical mixing of sediment populations with different grain-size distributions; (2) selective mechanisms operating during unidirectional transport and deposition, producing sediments whose grain-size distributions change systematically with distance from the source and/or capacity of the transporting process. Successful reconstructions of paleoclimate from grain-size data depend, therefore, among other factors, on the quality of the grain-size determinations. The performances of a laser-diffraction size analyser, the Malvern Instruments Laser Particle Sizer Type 2600, are evaluated in this chapter. For this purpose, artificial samples were prepared by mixing a series of microsphere standards as well as a series of natural sediment standards with known grain-size distributions. Measurements of these mixtures allow evaluation of the ability of the Malvern laser-diffraction size analyser to ‘recognise’ subpopulations within sediment mixtures. The mixing experiments indicate that the Malvern grain-size distributions can be used for the recognition of subpopulations by ‘unmixing’ of polymodal grain-size distributions.

**Chapter 3** — Inverse numerical-statistical end-member modelling algorithms are tested on grain-size data of microsphere and natural sediment mixtures to evaluate their usefulness for unravelling natural multi-sourced basin fills. The ultimate objective of end-member modelling is to provide the ‘simplest possible and least dramatic’ explanation of compositional variation in the absence of *a priori* knowledge of the geological system under study. An outstanding quality of end-member modelling is the great intuitive appeal of the resulting mixing models, which are formulated in the same units as the input data. The independent comparison between the modelled end members and mixing coefficients and the ‘true’ end members (microsphere and sediment standards) and ‘true’ mixing coefficients allows for an objective assessment of the validity of the unmixing solution. The comparison indicate that end-member modelling is a powerful tool for analysing grain-size distribution data in cases where the observed variation among compositions is the result of mixing.

**Chapter 4** — End-member modelling algorithms are used to model grain-size distribution end members of pelagic and hemipelagic siliciclastic sediments of the Arabian Sea. The grain-size distributions of sediments from the Oman continental slope, the Owen Ridge, the Pakistan continental slope and the Indus Fan can be adequately described as mixtures of three end members. The spatial variation in relative contribution of the end members is interpreted in terms of provenance and transport processes. The end members represent ‘proximal’ and ‘distal’ eolian dust, and fluvial mud. At any given location, the temporal variations in the relative contribution of the end members are interpreted in terms of climate change. The ratio of contributions of the two eolian end members (i.e., the grain-size distribution of the eolian dust) reflects the strength of the dust-transporting wind system. The ratio of contributions of eolian and fluvial sediment reflects continental aridity. A reconstruction of late Quaternary (~200-0 ka BP) variations in Arabian Sea monsoon climate is presented, comprising proxy records of continental aridity, summer-monsoon strength and winter-monsoon strength.

**Chapter 5** — Additional climate-indicator records based on the grain-size distribution of hemipelagic siliciclastic muds from the north-eastern Arabian Sea are presented in Chapter 5. The objectives are to demonstrate a correlation between marine eolian-fluvial mud sequences of the north-eastern Arabian Sea and terrestrial loess-paleosol sequences of central China, and to present a correlation between the summer and winter-monsoon indicator records of the Arabian Sea and the climate-indicator records of the North Atlantic region. Correlations between these records provide evidence for atmospheric teleconnections between the

Arabian-Sea monsoonal climate, the East-Asian monsoonal climate and the North Atlantic climate.

**Chapter 6** — Sediment cores from the Indus Canyon and the middle Indus Fan are studied in order to reconstruct the timing of (hemi-) pelagic and turbidite sedimentation on the fan (~35-0 ka BP). The geochemical, mineralogical and grain-size characteristics of the (hemi-) pelagic sediments on the middle Indus Fan are analysed to determine temporal variations in the flux and the provenance of the terrigenous sediment fraction. The timing and pattern of channel-levee system evolution will be discussed in relation to autocyclic and allocyclic (e.g. sea-level fluctuations) mechanisms. Moreover, a comparison of the timing of active growth of the Indus Fan, and erosion and deposition in the Indus Canyon and on the adjacent outer shelf and continental slope is made. It appears that erosional and depositional cycles on the Indus Fan are strongly controlled by changes in sea level.

**Chapter 7** — The input of terrigenous sediment along the tectonically active Makran continental margin off south-western Pakistan (Gulf of Oman, northern Arabian Sea) is studied on the basis of sediment cores along a transect from the upper slope to the abyssal plain. Numerical-statistical algorithms are used to model end-member grain-size distributions of the hemipelagic and turbidite sediments on the Makran continental slope. The geochemical and mineralogical composition of the hemipelagic sediments indicates that the eolian dust was dominantly supplied from the northern Arabian Peninsula and the Persian Gulf region, and that the fluvial input is from the Makran. The ratio of contributions of eolian and fluvial sediment in the hemipelagic intervals is used as an indicator of continental aridity, i.e., summer-monsoon intensity. Spatial and temporal variations in sediment composition, sedimentation rate and turbidite frequency in the late Pleistocene-Holocene (~20-0 ka BP) will be discussed, and related to changes in sea level and climate, and tectonic activity.

**Chapter 8** — The timing of hemipelagic and turbidite deposition along a passive margin, i.e., on the Indus Fan and along an active margin, i.e., on the Makran continental slope will be discussed in the last chapter. The importance of the comparison is that the studied turbidite systems are located in the same sedimentary basin (Arabian Sea). This implies that they were subject to similar changes in climate and sea level, but to different tectonics. The comparison allows the assessment of the individual contribution of sea-level change, climate change and tectonic activity to the controls on sediment supply to the Arabian Sea.



## EVALUATION OF THE MALVERN 2600 LASER-DIFFRACTION SIZE ANALYSER FOR USE WITH FINE-GRAINED SEDIMENTS

M.A. Prins<sup>1</sup> and J.-B.W. Stuut<sup>1, 2</sup>

### ABSTRACT

The qualities of a laser-diffraction size analyser, the Malvern Instruments Laser Particle Sizer Type 2600, are evaluated on certified polystyrene microsphere standards and natural sediment samples. Accuracy and precision (reproducibility) of measurements on discrete microsphere standards and precision of results on natural sediments are very good. Binary mixtures were prepared by mixing a series of microsphere standards as well as a series of natural sediment standards with known grain-size distributions. Measurements of these mixtures allow evaluation of the ability of the Malvern laser-diffraction size analyser to ‘recognise’ subpopulations within sediment mixtures. Resolution of measurements on mixtures of microsphere standards is poor. All measured grain-size distributions of the natural sediment mixtures are fitted closely by a calculated grain-size distribution of a hypothetical sediment mixture. Approximation of the measured grain-size distribution by the ‘best-fit’ grain-size distribution provide the apparent mixing proportions of the sediment standards as seen by the Malvern laser-diffraction size analyser. The mixing experiments indicate that the Malvern grain-size distributions can be used for the tracing of subpopulations by ‘unmixing’ of polymodal grain-size distributions. Deviations exist between the known mixing proportions (by weight) and the Malvern mixing proportions of the sediment standards. Explanations and implications of these observations for geological studies are discussed.

### INTRODUCTION

The objective of many studies of records of deep-sea terrigenous sediments is to interpret the composition and fluxes of these sediments in terms of paleoclimate evolution of the surrounding continental source areas. Analysis of grain-size distributions provide information about sedimentary environments and depositional processes. Variations in grain-size distribution within basin-fill sediments may reflect two kinds of processes: (1) physical mixing of sediment populations with different grain-size distributions; (2) selective mechanisms operating during unidirectional transport and deposition producing sediments whose grain-size distributions change systematically with distance from the source. Successful reconstructions of paleoclimate from grain-size data depend, therefore, among other factors, on the performances of the particle size instrument used.

Many techniques have been developed to obtain grain-size distributions of sediments from various physical methods: sieving, sedimentation rate, image analysis, X-ray attenuation,

---

<sup>1</sup> Institute for Paleoenvironments and Paleoclimate Utrecht (IPPU), Faculty of Earth Sciences, Utrecht University, P.O. Box 80021, 3508 TA Utrecht, The Netherlands

<sup>2</sup> Netherlands Institute for Sea Research (NIOZ), Department of Marine Chemistry and Geology, P.O. Box 59, 1790 AB Den Burg, The Netherlands

electrical resistance, light scattering, and light diffraction. An overview and discussion of these techniques and associated instruments is given in Syvitski (1991a). In general it appears that automated particle size instruments are far superior to the classical sieving and pipette gravitational sedimentation methods as these latter techniques are imprecise and very dependent on the laboratory and the operator error. Inter-instrument calibration experiments pointed out that the results obtained with different types of particle size instruments may deviate significantly (Syvitski *et al.*, 1991; Bischof *et al.*, 1993). These deviations are largely due to the fact that each technique defines the size of a particle in a different way and thus produces different property measurements of the same material.

The theoretical effects of particle shape and density on particle size measurements were discussed by Matthews (1991). Ideally, the established size of an object should be independent of such attributes as grain shape and density. This is not true for assemblages of sedimentary particles that are of mixed shapes and densities. Therefore, it is unreasonable to expect that a single length value describes completely the size of an irregularly shaped sediment grain. The reduction of the multitude of information needed to describe the size of an irregular grain to a single value is accomplished through the use of a reference shape such as a sphere or circle. As we are obliged to define the size of a particle by a single value, it is clear that the different methods of measurement will only correlate with spherical particles. Results will diverge as we move away from sphericity, highlighting the importance of shape in particle size determination. The effect of particle density on size measurements is similar.

The inability to accurately describe the size of a sediment grain uniquely by a single value forces us to choose the size analysis method that benefits the purpose of the study. If the purpose is to describe the hydraulic conditions of the depositional environment, a settling technique should be chosen, because depositional processes associated with suspension fall-out is important. Alternatively, traction might be considered important and an area-based technique chosen, emphasising drag at the water-sediment interface; or a volume-based technique may be chosen, believing the inertia of the particle to be important (Matthews, 1991). Grain-size data presented in this thesis are obtained on the Malvern Instruments Laser Particle Sizer Type 2600 at hand at the Department of Geology of Utrecht University. Laser-diffraction size analysis is a volume-based technique as the diameter of a particle is expressed as the diameter of a sphere having the same volume as the particle (equivalent volume diameter). Decisive for the selection of a laser-diffraction size analyser is its ability to analyse a wide range of sizes in a single measurement and the speed with which these analyses are performed.

### *Laser-Diffraction Size Analysis*

The construction of commercial laser-diffraction size analysers started in the 1970's after several authors had suggested to define size distributions of suspended particles from the angular distribution of forward-scattered light (see Agrawal *et al.*, 1991). These methods are now widely used but with several different designs and based on different hardware and software principles. A brief description of the principles of the Malvern laser-diffraction size analyser is given below. It is largely taken from McCave *et al.* (1986). See Agrawal *et al.* (1991) for a more extensive discussion.

Laser-diffraction size analysis is based on the principle that particles of a given size diffract light through a given angle, the angle increasing with decreasing size. A narrow pulsating beam of monochromatic light from a He-Ne laser,  $\lambda = 633 \text{ nm}$ , is passed through a suspension and the diffracted light is focused by a lens onto a detector, which measures at time intervals the angular distribution of scattered light. The lens placed between the illuminated sample with the detector at its focal point focuses the undiffracted light to a point

at the centre of the detector and leaves only the surrounding diffraction pattern. A stream of particles has to be passed through the beam to generate a statistically stable diffraction pattern. The size distribution is then determined from the angular distribution of the light intensity. Malvern Instruments (U.K.) developed a series of instruments which employ the principles set out by Swithenbank *et al.* (1977).

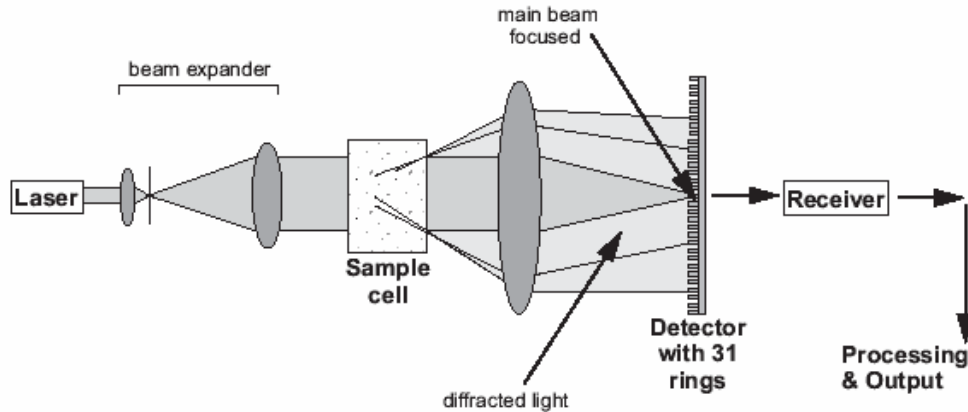


**Fig. 2.1** — Schematic diagram showing the arrangement of a Malvern laser-diffraction size analyser (after McCave *et al.*, 1986).

The set-up of the Malvern laser-diffraction size analyser involves a laser source, beam expander, sample cell, focusing lens and ring detector with associated electronics, and a computer (Fig. 2.1). The size range detected by the instrument depends upon the focal length of the focusing lens. A total range of 0.5 to 1880  $\mu\text{m}$  (equivalent volume diameter) is claimed by the manufacturers. Six lenses are available, and each one resolves sizes into 32 size classes with an overall 100-fold size range. The detection limit is 0.5  $\mu\text{m}$ . This is the size at which particles do not diffract light in the manner required for valid application of Fraunhofer diffraction theory because their diameter ( $d$ ) approaches the wavelength of light ( $\lambda$ ) (de Boer *et al.*, 1987). In fact, this approximation becomes increasingly poor below  $\sim 7 \mu\text{m}$  or  $d \approx 10 \lambda$  (Bayvel and Jones, 1981), and the full Mie scattering theory should be used (Agrawal *et al.*, 1991).

### Previous Work

Comparison between data obtained with laser-diffraction size analysers and other sizing techniques has been reported by Cooper *et al.* (1984), McCave *et al.* (1986), Singer *et al.* (1988), Syvitski *et al.* (1991), Loizeau *et al.* (1994) and Konert and Vandenberghe (1997). Some aspects of laser-diffraction size analysis will be summarised below.

McCave *et al.* (1986) showed that the Malvern Instruments Laser Particle Sizer Type 3600 E produces very high precision results by checking the reproducibility of results in a series of multiple subsamples taken from a single sediment sample. However, the analyses of a set of samples showed pronounced sets of modes on the grain-size distribution with constant position depending on the lens used. These recurring modes in the grain-size distributions made comparison with other techniques difficult. According to McCave *et al.* (1986), these analytical problems are caused by the clay-sized particles. In their experiments, a high clay content in samples is partly responsible for a large and almost entirely false mode at 3  $\mu\text{m}$  as well as several progressively smaller modes at higher sizes (6, 11, 20 and 50  $\mu\text{m}$  for the 100 mm lens). These analytical problems are related mainly to dispersion of light by the clay particles (Singer *et al.*, 1988). Moreover, McCave *et al.* (1986) indicated that replicate

analyses of samples using different lenses produced poorly comparable results.

Singer *et al.* (1988) found that the Malvern laser-diffraction size analyser shows broadening of individual modes of polymodal standards indicating poor resolution ability. The clear modal structure seen by some other analysers in polymodal standards, is discernible but blurred. Consequently, McCave *et al.* (1986) and Agrawal *et al.* (1991) concluded that the Malvern grain-size distributions can better not be used for the tracing of subpopulations by dissection of polymodal grain-size distributions. On the other hand, interinstrument comparison of size spectra of polymodal glass-sphere standards presented by Syvitski *et al.* (1991) showed that the performance of the Malvern laser-diffraction size analyser is comparable with other techniques and that the Malvern laser-diffraction size analyser used in our laboratory gives results which nicely are at about the mean of the results of a group of laboratories which participated.

Studies by McCave *et al.* (1986), Loizeau *et al.* (1994), and Konert and Vandenberghe (1997) showed that certain laser-diffraction size analysers underestimate the fraction of clay particles  $<2 \mu\text{m}$  as compared to determinations with the pipette gravitational sedimentation method. Konert and Vandenberghe (1997) indicated that the differences between pipette and laser measurements are caused by the non-sphericity (platy form) of clay minerals in the clay fraction. It appeared that the  $<2 \mu\text{m}$  grain size defined by the pipette method corresponds with a grain size of  $<8 \mu\text{m}$  defined by their laser-diffraction size analyser. Cooper *et al.* (1984) concluded that their instrument 'sees' more clay and fine silt particles than the pipette method in the 1.9 to 3.9  $\mu\text{m}$  size range. They argued that besides particle shape also clay mineralogy influences the determination of particle size.

Loizeau *et al.* (1994) checked the ability of laser-diffraction size analysis to detect clay particles by analysing samples composed of two standards ('clay' and 'coarse silt') mixed in various, accurately known proportions. Results showed that the amount of clay detected by their instrument is underestimated in inverse proportion to the actual clay content. The modes of both standards are correctly reported except for samples with low clay content. This 'internal' comparison showed that small amounts of clay are overlooked in clayey silt by the mixing of particles of different grain size.

Hence, to evaluate the appropriateness of the Malvern laser-diffraction size analyser we have to carefully reflect on our needs which are set by our research goals. In this chapter an evaluation of the Malvern Instruments Laser Particle Sizer Type 2600 is presented focusing therefore on two different issues. Firstly, the accuracy and precision of the laser-diffraction size analyser is examined, by analysis of certified polystyrene microsphere standards, and by analysis of multiple replicates of these standards as well as of natural sediment samples. Secondly, the ability of the Malvern laser-diffraction size analyser to 'recognise' polymodal sediment mixtures is tested. Two kinds of artificial mixtures were prepared and analysed: mixtures of two polystyrene microsphere standards and mixtures of two 'natural' sediment standards with different grain-size distributions.

## MATERIAL AND METHODS

Prior to analysis, the carbonate was removed from the sediment samples by treatment with an excess 1M HCl solution. Grain-size analyses therefore provide the grain-size distribution of the siliciclastic sediment fraction. The sample is dispersed in a beaker in distilled water by stirring. While stirring, a subsample is taken with a pipette and dispersed in the sample tank of the Malvern laser-diffraction size analyser. Total dispersion of the sample is ensured by using a sonic dismembrator attached to the tank containing the suspended subsample. The analysis time in the sample chamber itself is only a few seconds, while the data (hardcopy and on file) are obtained in about five minutes. To avoid problems associated with the use of different lenses (McCave *et al.*, 1986) all analyses were performed with a lens with a focal length of 100 mm. This lens sizes material between 0.5 and 188  $\mu\text{m}$ , and records the data in 32 classes whose size boundaries are given in Table 2.1.

**TABLE 2.1 — SIZE RANGE FOR MALVERN LASER-DIFFRACTION SIZE ANALYSER**

Size class	Lower boundary ( $\mu\text{m}$ )	Upper boundary ( $\mu\text{m}$ )	Size class	Lower boundary ( $\mu\text{m}$ )	Upper boundary ( $\mu\text{m}$ )
1	0.50	1.93	17	17.67	20.50
2	1.93	2.23	18	20.50	23.83
3	2.23	2.60	19	23.83	27.50
4	2.60	3.02	20	27.50	32.00
5	3.02	3.48	21	32.00	37.00
6	3.48	4.05	22	37.00	43.00
7	4.05	4.68	23	43.00	49.83
8	4.68	5.43	24	49.83	57.67
9	5.43	6.30	25	57.67	66.83
10	6.30	7.30	26	66.83	77.50
11	7.30	8.47	27	77.50	89.83
12	8.47	9.82	28	89.83	104.17
13	9.82	11.37	29	104.17	120.67
14	11.37	13.18	30	120.67	140.00
15	13.18	15.28	31	140.00	162.17
16	15.28	17.67	32	162.17	188.00

Size range indicated for lens with 100 mm focal length. First class indicates amount of particles between detection limit (0.5  $\mu\text{m}$ ) and analysed range (1.93-188  $\mu\text{m}$ ).

## RESULTS

### *Polystyrene Microsphere Standards*

#### *Accuracy and precision.—*

Accuracy of the Malvern laser-diffraction size analyser was tested with calibrated polystyrene microsphere standards. Four standards were analysed with nominal mean grain sizes of 5.3, 10.2, 21.7, and 51.1  $\mu\text{m}$  (Duke Scientific Corporation standards #7505, #7510, #7520, #7550; see Table 2.2). These standards cover largely the size range of the fine-grained pelagic and hemipelagic siliciclastic sediments obtained in the Arabian Sea (see Chapter 4).

**TABLE 2.2 — STATISTICS OF POLYSTYRENE MICROSPHERE STANDARDS**

Polystyrene microsphere standard:	#7505	#7510	#7520	#7550
Nominal mean diameter ( $\mu\text{m}$ )	5.3	10.2	21.7	51.1
Nominal standard deviation ( $\mu\text{m}$ )	1.2	1.5	3.2	7.0
Number of measurements	5	5	2	2
Measured mean diameter $\pm 1\sigma$ ( $\mu\text{m}$ )	$5.4 \pm 0.049$	$10.4 \pm 0.004$	22.6	51.3
Measured standard deviation $\pm 1\sigma$ ( $\mu\text{m}$ )	$0.9 \pm 0.021$	$1.5 \pm 0.015$	3.0	8.9
Deviation (%) between measured and nominal mean diameter	1.4	1.8	4.2	0.4

Standards #7520 and #7550 were measured twice from the same suspension and standards #7505 and #7510 were measured five times from different suspensions. The laser measurements appear to be very precise and accurate. The high precision (reproducibility) of the measurements is demonstrated by small variations in the mean diameter and the standard deviation of the size distributions (Table 2.2): e.g. measurements of standard #7505 give a mean diameter of  $5.4 \pm 0.049 \mu\text{m}$  (0.9 % variation) and a standard deviation of  $0.9 \pm 0.021 \mu\text{m}$  (2.3 % variation). Laser measurements of standard #7510 provided even more precise results as indicated by the 0.04 % variation in the mean diameter ( $10.4 \pm 0.004 \mu\text{m}$ ) and the 1 % variation in the standard deviation ( $1.5 \pm 0.015 \mu\text{m}$ ). Because of the high precision, only the average grain-size distributions of the multiple analyses are shown in Figure 2.2 and Table 2.3. Relative departures from the nominal mean diameter, which is indicative of the accuracy of the measurements, vary between 0.4 to 4.2 % (Table 2.2), corresponding to absolute deviations between 0.1 to 0.9  $\mu\text{m}$ . The recorded standard deviations of the size distributions also match the nominal values closely. Thus, the Malvern laser-diffraction size analyser produces precise and accurate measurements of the calibrated polystyrene microsphere standards.

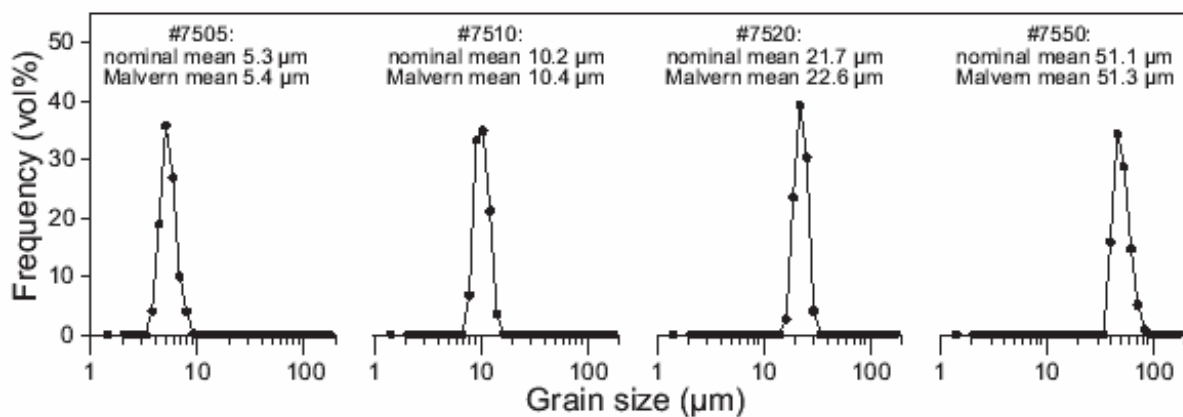


**Fig. 2.2 — Grain-size distributions of four polystyrene microsphere standards (Duke Scientific Corporation standards #7505, #7510, #7520, #7550) measured with the Malvern laser-diffraction size analyser. Certified nominal and Malvern mean grain sizes are indicated. Data are listed in Tables 2.2 and 2.3.**

**TABLE 2.3 — GRAIN-SIZE DISTRIBUTIONS OF POLYSTYRENE MICROSPHERE STANDARDS**

Size class	#7505	#7510	#7520	#7550	Size class	#7505	#7510	#7520	#7550
1	0.00	0.00	0.00	0.00	17	0.00	0.00	23.55	0.00
2	0.00	0.00	0.00	0.00	18	0.00	0.00	39.45	0.00
3	0.00	0.00	0.00	0.00	19	0.00	0.00	30.40	0.00
4	0.00	0.00	0.00	0.00	20	0.00	0.00	4.05	0.00
5	0.00	0.00	0.00	0.00	21	0.00	0.00	0.00	0.00
6	3.98	0.00	0.00	0.00	22	0.00	0.00	0.00	15.95
7	18.96	0.00	0.00	0.00	23	0.00	0.00	0.00	34.50
8	35.90	0.00	0.00	0.00	24	0.00	0.00	0.00	28.85
9	27.00	0.00	0.00	0.00	25	0.00	0.00	0.00	14.75
10	9.96	0.00	0.00	0.00	26	0.00	0.00	0.00	5.10
11	4.00	6.78	0.00	0.00	27	0.00	0.00	0.00	0.85
12	0.14	33.36	0.00	0.00	28	0.00	0.00	0.00	0.00
13	0.02	34.96	0.00	0.00	29	0.00	0.00	0.00	0.00
14	0.00	21.38	0.00	0.00	30	0.00	0.00	0.00	0.00
15	0.00	3.50	0.00	0.00	31	0.00	0.00	0.00	0.00
16	0.00	0.00	2.60	0.00	32	0.00	0.00	0.00	0.00

**TABLE 2.4 — MIXING COEFFICIENTS OF POLYSTYRENE MICROSPHERE MIXTURES**

Mixtures #7505 + #7510			Mixtures #7510 + #7520			Mixtures #7520 + #7550		
Sample	Fraction #7510 (wt%)	Fraction #7510 (LSF*)	Sample	Fraction #7520 (wt%)	Fraction #7520 (LSF*)	Sample	Fraction #7550 (wt%)	Fraction #7550 (LSF*)
A	0.09	0.06	N	0.03	0.02	1	0.04	0.13
B	0.16	0.19	O	0.04	0.05	2	0.06	0.18
C	0.25	0.28	P	0.08	0.07	3	0.11	0.21
D	0.33	0.35	Q	0.14	0.17	4	0.20	0.18
E	0.49	0.49	R	0.22	0.24	5	0.29	0.36
F	0.66	0.66	S	0.30	0.32	6	0.38	0.46
G	0.75	0.78	T	0.46	0.50	7	0.55	0.60
H	0.83	0.86	V	0.72	0.72	8	0.71	0.75
I	0.91	0.93	W	0.81	0.79	9	0.79	0.82
J	0.94	0.87	X	0.89	0.93	10	0.86	0.88
K	0.95	0.88	Y	0.94	0.94	11	0.92	0.93
L	0.97	0.91	Z	0.96	0.98	12	0.96	0.93
M	0.98	0.92				13	0.97	0.94

\* LSF: mixing coefficients according to least-squares fit approximation (see text for discussion)

*Resolution.—*

To test the resolution of the Malvern laser-diffraction size analyser, the grain-size distributions of various polystyrene microsphere mixtures were measured. Three series of samples were prepared by mixing two standards with adjacent modal grain size in various, accurately known weight proportions (Table 2.4). Samples A-M are mixtures of microsphere standards #7505 and #7510 (nominal mean grain sizes 5.3 and 10.2  $\mu\text{m}$ ; Fig. 2.4), samples N-Z are mixtures of standards #7510 and #7520 (10.2 and 21.7  $\mu\text{m}$  spheres; Fig. 2.5), and samples 1-13 are mixtures of standards #7520 and #7550 (21.7 and 51.1  $\mu\text{m}$  spheres; Fig. 2.6).

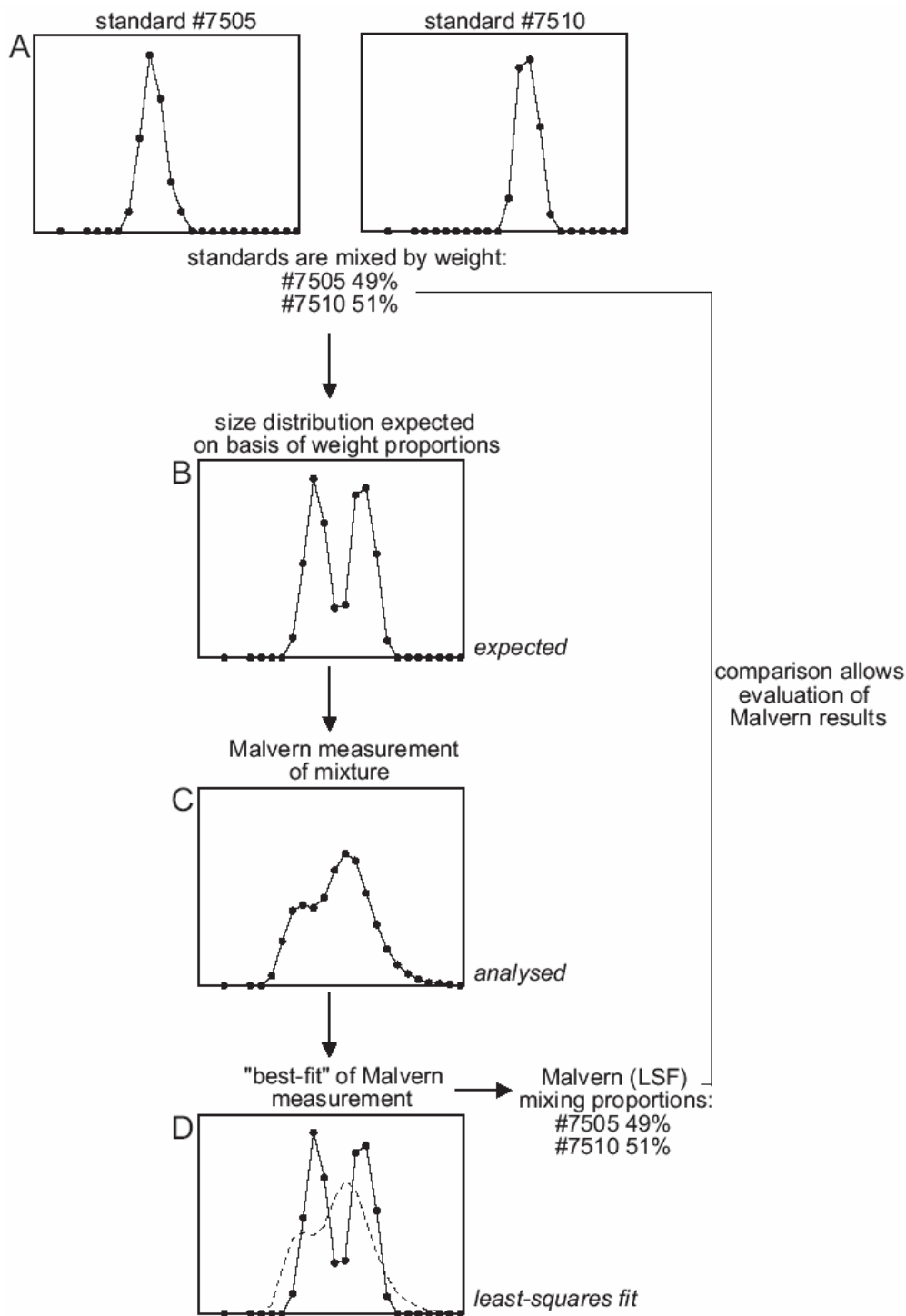


Fig. 2.3 — Schematic presentation of different types of grain-size distributions used in this study; results of sample E (see also Fig. 2.4) are shown as an example. A: Size distributions of microsphere standards #7505 and #7510 measured with the Malvern laser-diffraction size analyser. B: Calculated size distribution of sample E expected on basis of the weight proportions of standards #7505 and #7510; the *expected* size distribution. C: Malvern laser-diffraction measurement of sample E; the *analysed* size distribution. Note the large deviations between the *expected* and the *analysed* size distributions. D: Calculated size distribution (heavy line) which fits the *analysed* (dashed line) size distribution as close as possible according to the method of least-squares: the *least-squares fit* size distribution. Note the close correspondence between the *expected* and *least-squares fit* size distributions. The mixing proportions by weight (wt%) are compared with the Malvern least-squares fit (LSF) mixing proportions in Fig. 2.7.

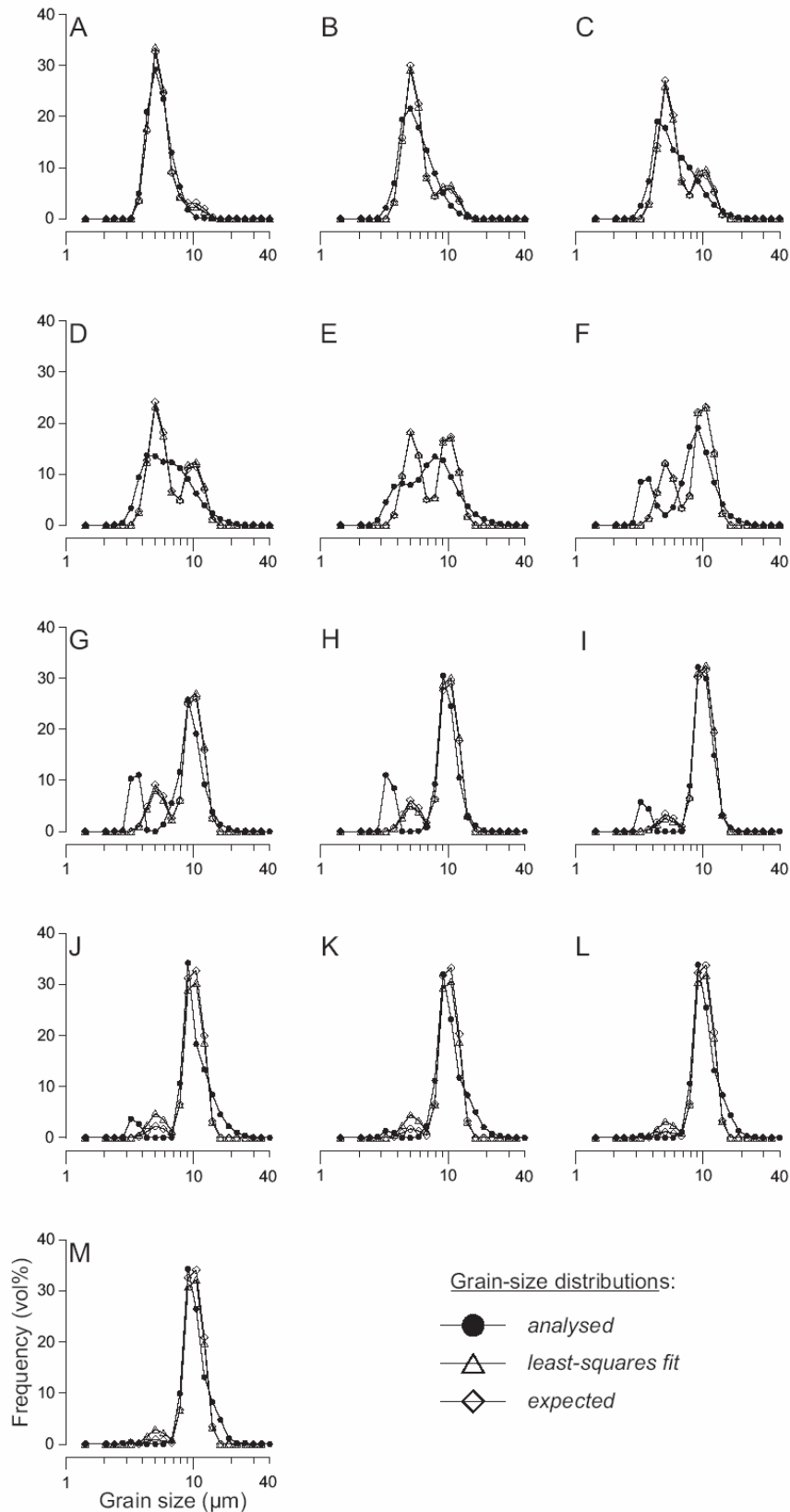


Fig. 2.4 — Samples A-M are composed of various proportions of standards #7505 and #7510 (Table 2.4). For each mixture the *analysed*, *least-squares fit*, and *expected* grain-size distributions are shown. Note that the *expected* and *least-squares fit* distributions are very similar.

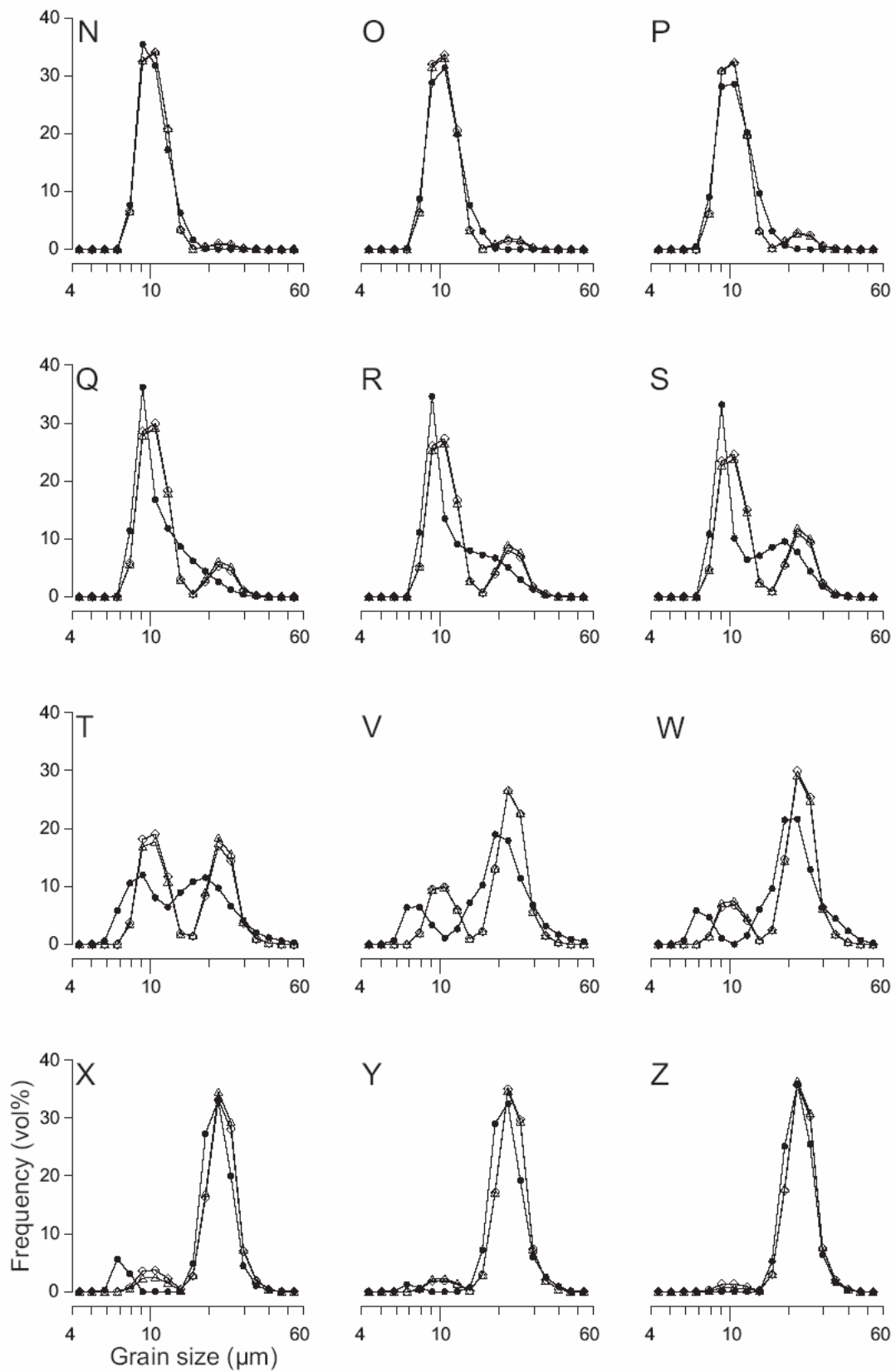


Fig. 2.5 — Samples N-Z are composed of various proportions of standards #7510 and #7520 (Table 2.4).

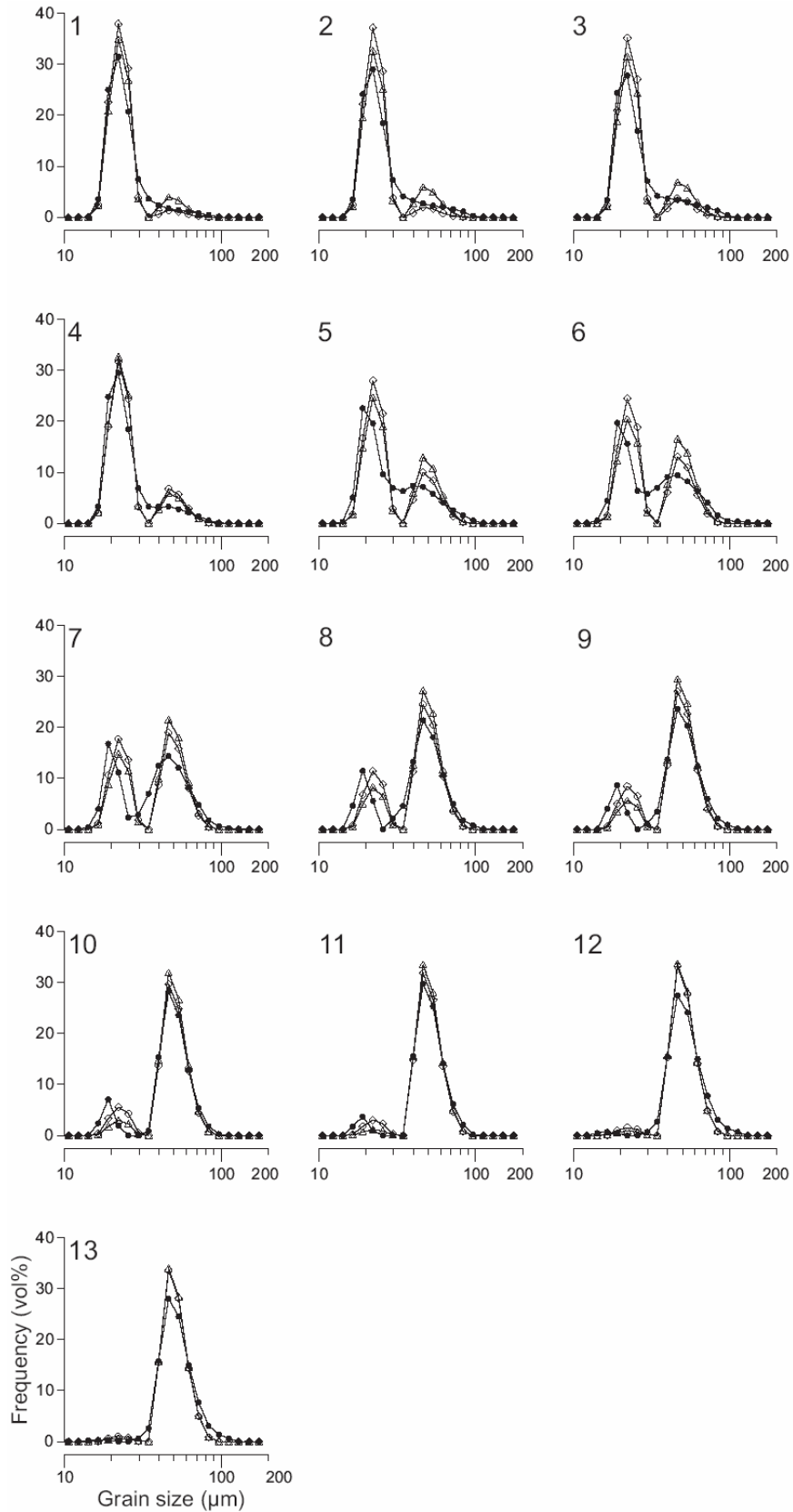
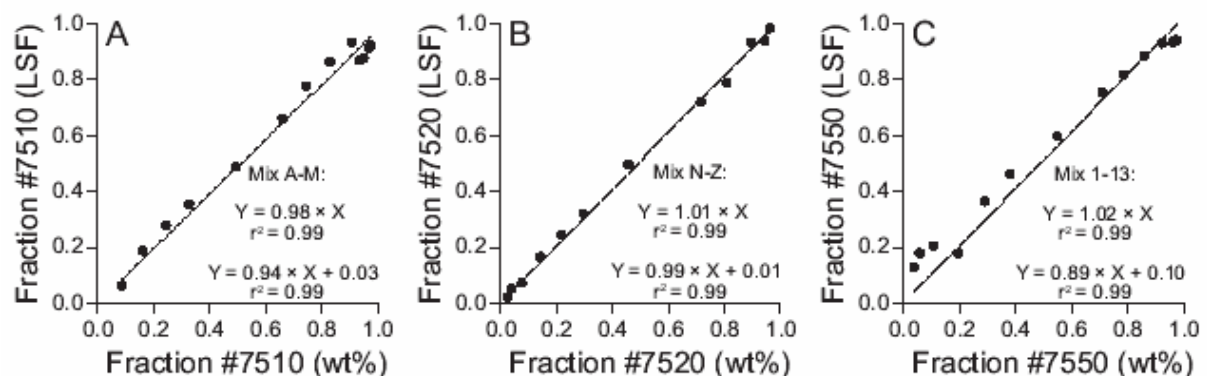


Fig. 2.6 — Samples 1-13 are composed of various proportions of standards #7520 and #7550 (Table 2.4).

In Figures 2.4, 2.5 and 2.6, the measured grain-size distribution (*analysed* distribution; Fig. 2.3) of each microsphere mixture is compared to two calculated grain-size distributions. Firstly, the *expected* distribution (Fig. 2.3) is calculated by summing the grain-size distributions of two standards (as listed in Table 2.3) in relative proportions according to the mixing weight proportions listed in Table 2.4. The *expected* distribution is what one should ‘expect’ when the Malvern laser-diffraction size analyser produces accurate measurements of the mixtures. Secondly, the *analysed* distribution was approximated as close as possible by a calculated grain-size distribution referred to as the *least-squares fit* distribution (Fig. 2.3). The approximation was performed with the method of least squares (Davis, 1986): for each sample the apparent (‘best-fit’) mixing ratio of the standards was calculated for which the absolute deviation between the *analysed* and *least-squares fit* distribution is minimum.

Resolution appears to be poor because the subpopulations in the *analysed* distributions are not clearly separated from each other as one should expect on basis of the weight proportions (*expected* distributions). In general the mode of the most abundant subpopulation in the two-component mixtures is correctly defined. However, if the expected secondary mode is to be found on the ‘coarse side’ of the main mode it first results in bulging of the flank of the main mode instead of appearing as a discrete peak. If the expected secondary mode is to be found on the ‘fine side’ of the main mode it does appear as a discrete peak although shifted considerably to smaller sizes (up to four size classes). The considerable deviations between the *analysed* and *expected* grain-size distributions indicate that the bimodal structure of the samples is not reproduced accurately.



**Fig. 2.7** — Correlation diagrams of known weight fractions and calculated (*least-squares fit*; LSF) fractions of the coarse-grained standard in the binary microsphere mixtures. Regression equations of form  $y=ax$  (also shown as regression lines) and  $y=ax+b$  are shown with associated correlation coefficients ( $r^2$ ). A: Samples A-M, mixtures of 5.3 and 10.2  $\mu\text{m}$  spheres. B: Samples N-Z, mixtures of 10.2 and 21.7  $\mu\text{m}$  spheres. C: Samples 1-13, mixtures of 21.7 and 51.1  $\mu\text{m}$  spheres. Results are listed in Table 2.4.

The approximation of the *analysed* grain-size distributions with the method of least-squares results into *least-squares fit* distributions which match closely the *expected* grain-size distributions. The known weight proportions (wt%) and the approximated (*least-squares fit*; LSF) proportions of the standards in the two-component mixtures correlate very well with one another (Fig. 2.7; data are listed in Table 2.4). For all sample series the regression equations, correlating the known and approximated proportional contributions of the standards with each other, are very close to  $y=x$  with very high correlation coefficients of 0.99.

## Natural Sediments

## Precision.—

Multiple analyses were conducted on a single natural sediment sample, by analysing the same suspension repeatedly, to assess the reproducibility (precision) of the measurement. The measurements of a coarse silt sample ( $n=20$ ) show a variability (coefficient of variation) of the median grain size ( $50.8 \pm 0.1 \mu\text{m}$ ) of 0.2 % and a variability of the mean grain size ( $53.3 \pm 0.2 \mu\text{m}$ ) of 0.4 %. Reproducibility of results thus is excellent.

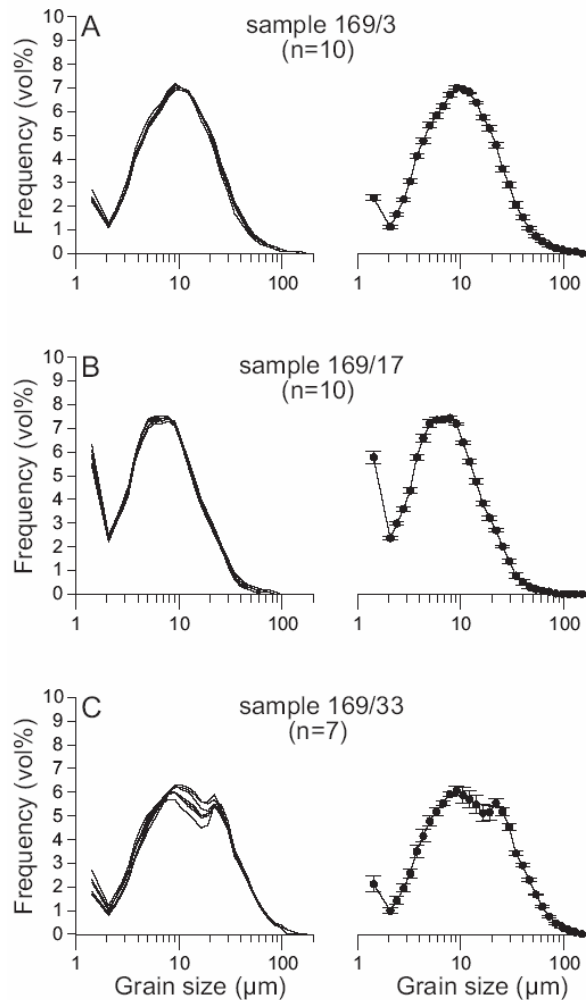


**Fig. 2.8** — Replicate analyses of three Arabian Sea hemipelagic mud samples from core SO90-169KL. Grain-size distributions of the replicates are shown in the left diagrams, and the average of these replicates and corresponding error bars ( $\pm 1\sigma$ ) are shown in the right diagrams. A: Ten subsamples of sample 169/3. B: Ten subsamples of sample 169/17. C: Seven subsamples of sample 169/33. See also Table 2.5.

Subsequently, measurements were carried out on several subsamples taken from three Arabian Sea hemipelagic mud samples to check the influence of sampling and processing errors. Three samples from core SO90-169KL (see Chapters 4 and 5) were selected and analysed repeatedly (169/3,  $n=10$ ; 169/17,  $n=10$ ; 169/33,  $n=7$ ). Results are shown in Figure 2.8 and Table 2.5. The measured grain-size distributions of the unimodal samples (169/3 and 169/17) are analysed precisely as the individual measurements resulted in similar grain-size distributions (Fig. 2.8A, B). The variability of the median grain size (169/3 - 2.3 %; 169/17 -

1.8%) and the variability of the mean grain size (169/3 - 2.9 %; 169/17 - 3.1 %) are small. The replicate analyses of bimodal sample 169/33 show considerable more variability in the central portion of its grain-size distribution (Fig. 2.8C). The variability of the median grain size (3.9 %) and the variability of the mean grain size (1.7 %) are still small.

TABLE 2.5 — MEASUREMENTS OF ARABIAN SEA HEMIPELAGIC MUD SAMPLES

SO90-169KL samples:	169/3		169/17		169/33	
	Median	Mean	Median	Mean	Median	Mean
Grain size ( $\mu\text{m}$ )	9.7	13.6	6.8	9.2	11.3	16.8
Standard deviation $\sigma$ ( $\mu\text{m}$ )	0.2	0.4	0.1	0.3	0.4	0.3
Coefficient of variation (%)	2.3	2.9	1.8	3.1	3.9	1.7

Finally, two certified reference materials (BCR No. 67 and 69) were analysed independently by Mrs. M. Reith in January 1993 and by us in July 1997 with the same Malvern laser-diffraction size analyser. The analyses by Mrs. M. Reith were part of an inter-laboratory, inter-instrument calibration experiment (Bischof *et al.*, 1993). The grain-size distributions of the BCR samples obtained by our analyses are compared with the certified values as listed in the certification report (BCR information, 1980). The laser measurements of the BCR samples appear to indicate a slightly coarser grain size than the certified values (Fig. 2.9). As BCR samples are to be used to calibrate the pipette gravitational sedimentation method and sieving, it is not very surprising and disturbing that the laser measurements do not fit perfectly the certified values. What gives confidence in the Malvern laser-diffraction size analyser are the highly comparable results of the measurements performed by different operators in 1993 and 1997 despite the period of four years in between during which the instrument was used intensively.

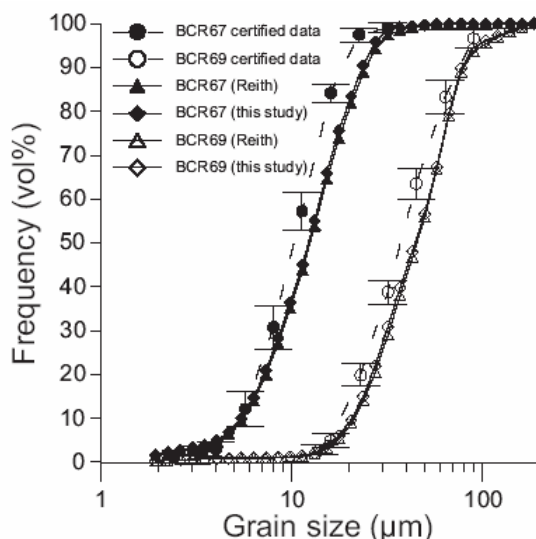


Fig. 2.9 — Cumulative grain-size distributions of the certified data (dots) and the laser measurements of BCR samples 67 and 69 performed by Mrs. M. Reith (triangles) and the authors (diamonds).

#### *Sediment mixtures.*—

Mixtures of natural sediments were prepared and analysed to provide insight in the ability of the Malvern laser-diffraction size analyser to ‘recognise’ mixtures of natural sediment populations with different compositions. Three sediment standards were extracted from a

sand sample (Assenzand), a silty loess sample (Limburg, The Netherlands) and a turbidite mud sample from the Indus Fan (core NIOP489, section 1, section depth 62-72 cm: see Chapter 4 and 6). Appropriate fractions were extracted from the sediment samples by dry sieving and settling in small settling tubes. Standard S1 was extracted from the mud sample taken from core NIOP489. Standard S2 is a mixture of fine-grained loess and the coarse-grained fraction of the sample taken from NIOP489. Standard S3 is a mixture of coarse-grained loess and a sieve fraction (53-75  $\mu\text{m}$ ) of Assenzand. The grain-size distributions of the sediment standards are shown in Figure 2.10 and Table 2.6. The standards were constructed such that the grain-size distributions of these artificial ‘end members’ resemble the grain-size distributions of the modelled end members of the Arabian Sea pelagic and hemipelagic siliciclastic sediments (see Chapter 4; Prins and Weltje, 1999) as close as possible.

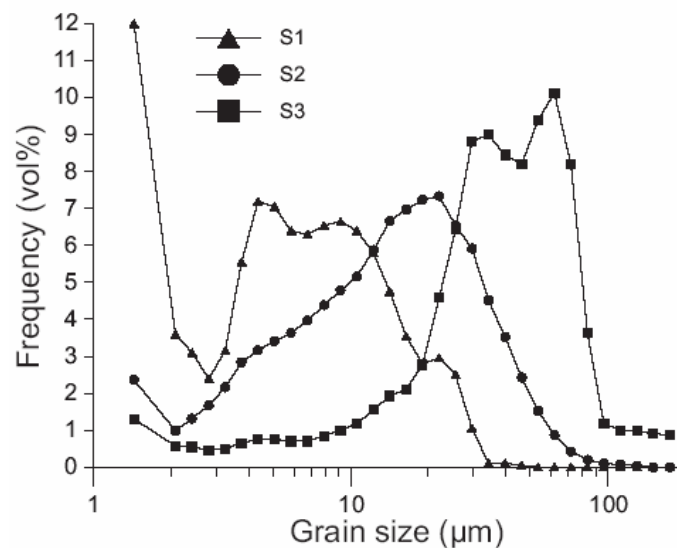


Fig. 2.10 — Grain-size distributions of sediment standards (S1, S2, S3) used to construct sediment mixtures. Data are listed in Table 2.6.

The shape of a sediment particle is largely determined by its mineralogy: clay minerals are highly non-spherical (‘platy’), whereas other minerals (quartz, feldspars) are relatively spherical (‘blocky’): see e.g. SEM photographs in Konert and Vandenberghe (1997). The particle shape characteristics of the sediment standards (S1, S2, S3) differ therefore markedly as two fractions (loess, Assenzand) consist predominantly of quartz and feldspar grains whereas another (Indus Fan sediments) consists mainly of clay minerals.

Three series of samples were prepared by mixing two standards by weight in various, accurately known proportions. In total 61 samples were assembled of which 19 are mixtures of standards S1 and S2, 21 are mixtures of S2 and S3 and 21 are mixtures of S1 and S3. The *analysed* grain-size distributions of the mixtures are approximated by *least-squares fit* distributions compiled on the basis of the separate distribution curves of the standards in the same way as described for the polystyrene microsphere mixtures (Fig. 2.11). The approximated (*least-squares fit*, LSF) mixing proportions of the standards are compared with the actual known weight proportions in Figure 2.12 (data are listed in Table 2.7). Important to notice here is that, because the Malvern laser-diffraction size analyser expresses sediment ‘mass’ in units of volume, the *least-squares fit* mixing proportions are expressed in volume percentages. In contrast, the *expected* mixing proportions are expressed in weight percentages, as the sediment standards were mixed by weight.

**TABLE 2.6 — GRAIN-SIZE DISTRIBUTIONS OF SEDIMENT STANDARDS**

Size class	S1	S2	S3	Size class	S1	S2	S3
1	12.00	2.37	1.30	17	2.80	7.23	2.78
2	3.60	0.98	0.58	18	2.95	7.33	4.58
3	3.10	1.31	0.55	19	2.50	6.55	6.43
4	2.40	1.67	0.45	20	1.05	5.92	8.83
5	3.15	2.16	0.50	21	0.10	4.52	9.00
6	5.55	2.84	0.65	22	0.10	3.53	8.45
7	7.20	3.16	0.75	23	0.05	2.43	8.20
8	7.05	3.41	0.75	24	0.00	1.52	9.40
9	6.40	3.63	0.70	25	0.00	0.87	10.13
10	6.30	3.97	0.70	26	0.00	0.43	8.20
11	6.55	4.38	0.85	27	0.00	0.20	3.63
12	6.65	4.78	1.00	28	0.00	0.10	1.18
13	6.40	5.16	1.18	29	0.00	0.07	1.00
14	5.80	5.88	1.55	30	0.00	0.03	0.98
15	4.75	6.67	1.93	31	0.00	0.00	0.90
16	3.55	6.98	2.10	32	0.00	0.00	0.88

Frequency expressed in volume percent (vol%)

**TABLE 2.7 — MIXING COEFFICIENTS OF SEDIMENT MIXTURES**

Mixtures S1 + S2			Mixtures S2 + S3			Mixtures S1 + S3		
Sample	Fraction S2 (wt%)	Fraction S2 (LSF*)	Sample	Fraction S3 (wt%)	Fraction S3 (LSF*)	Sample	Fraction S3 (wt%)	Fraction S3 (LSF*)
A2	0.91	0.90	C1	0.15	0.09	D1	0.27	0.11
A3	0.84	0.86	C2	0.26	0.14	D2	0.40	0.21
A4	0.78	0.82	C3	0.38	0.24	D3	0.53	0.39
A5	0.73	0.79	C4	0.47	0.33	D4	0.58	0.45
A6	0.68	0.71	C5	0.55	0.40	D5	0.65	0.52
A7	0.64	0.67	C6	0.59	0.43	D6	0.70	0.59
A8	0.60	0.64	C7	0.65	0.50	D7	0.73	0.62
A9	0.57	0.62	C8	0.68	0.53	D8	0.77	0.64
A10	0.54	0.58	C9	0.72	0.60	D9	0.79	0.68
A11	0.51	0.55	C10	0.75	0.63	D10	0.81	0.69
A12	0.55	0.55	C11	0.77	0.65	D11	0.82	0.75
A13	0.52	0.54	C12	0.80	0.70	D12	0.84	0.77
A14	0.48	0.51	C13	0.82	0.73	D13	0.86	0.80
A15	0.44	0.47	C14	0.86	0.77	D14	0.89	0.82
A16	0.40	0.45	C15	0.88	0.81	D15	0.90	0.85
A17	0.35	0.37	C16	0.91	0.85	D16	0.92	0.88
A18	0.29	0.32	C17	0.93	0.88	D17	0.94	0.91
A19	0.21	0.22	C18	0.95	0.92	D18	0.96	0.94
A20	0.12	0.14	C19	0.98	0.96	D19	0.98	0.97
			C20	0.18	0.11	D20	0.18	0.10
			C21	0.08	0.05	D21	0.13	0.05

\* LSF: mixing coefficients according to least-squares fit approximation (see text for discussion)

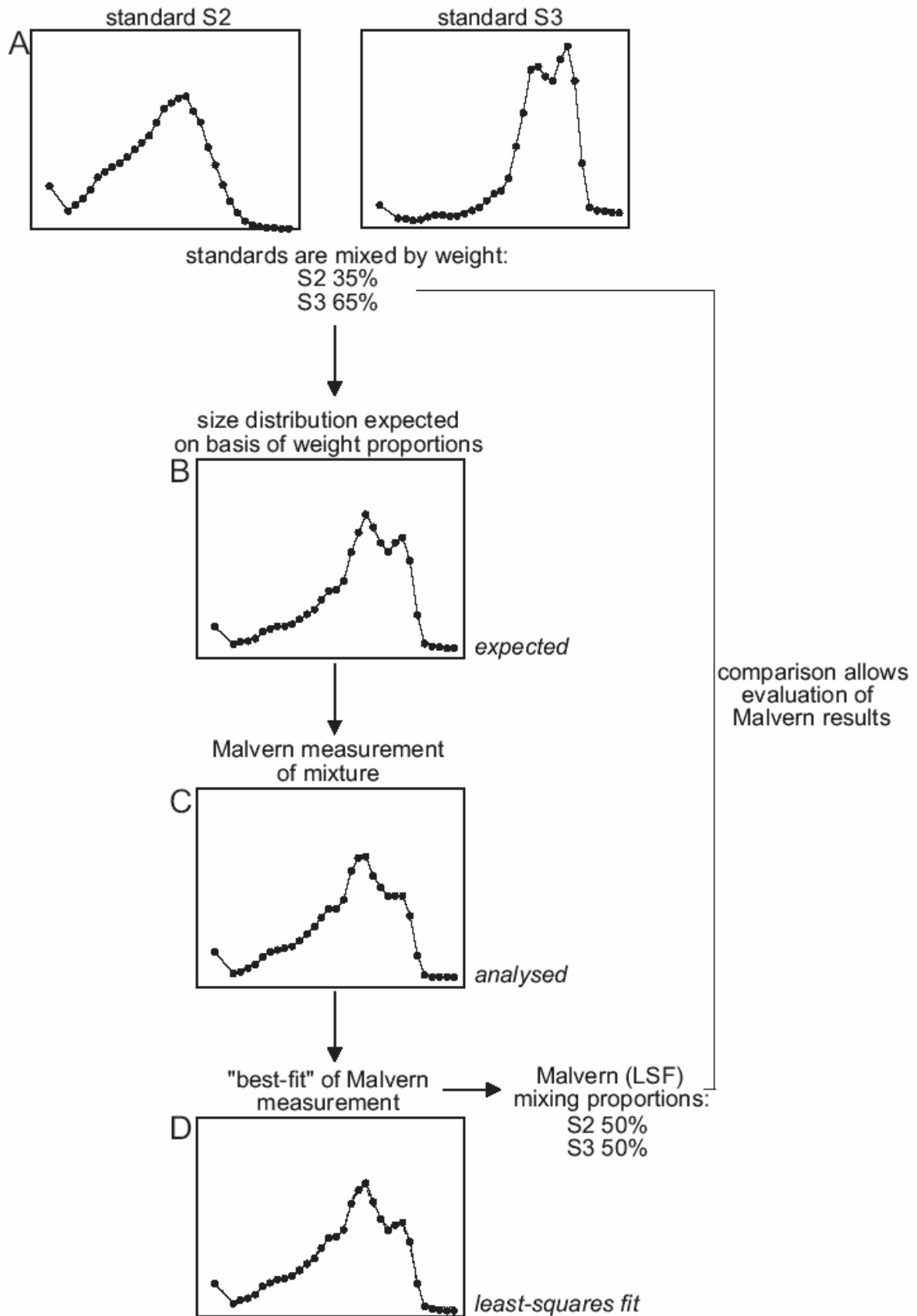


Fig. 2.11 — Schematic presentation of different types of grain-size distributions used in this study; results of sample C7 (see also Fig. 2.13) are shown as an example. A: Size distributions of sediment standards S2 and S3 measured with the Malvern laser-diffraction size analyser. B: Calculated size distribution of sample C7 expected on basis of the weight proportions of standards S2 and S3; the *expected* size

**distribution. C: Malvern laser-diffraction measurement of sample C7; the *analysed* size distribution. Note the small deviations between the *expected* and the *analysed* size distributions. D: Calculated size distribution (heavy line) which fits the *analysed* (dashed line) size distribution as close as possible according to the method of least-squares: the *least-squares fit* size distribution. Note the close correspondence between the *analysed* and *least-squares fit* size distributions. The mixing proportions by weight (wt%) are compared with the Malvern least-squares fit (LSF) mixing proportions in Fig. 2.12.**

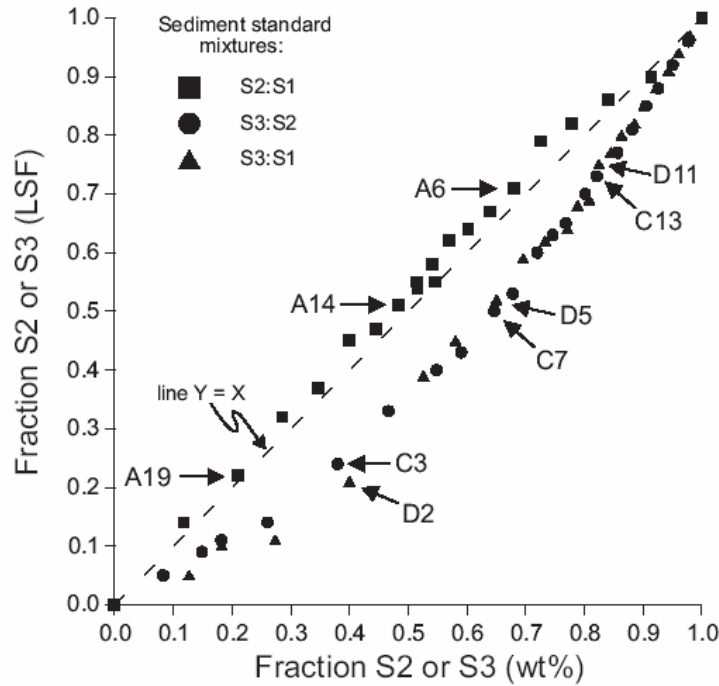
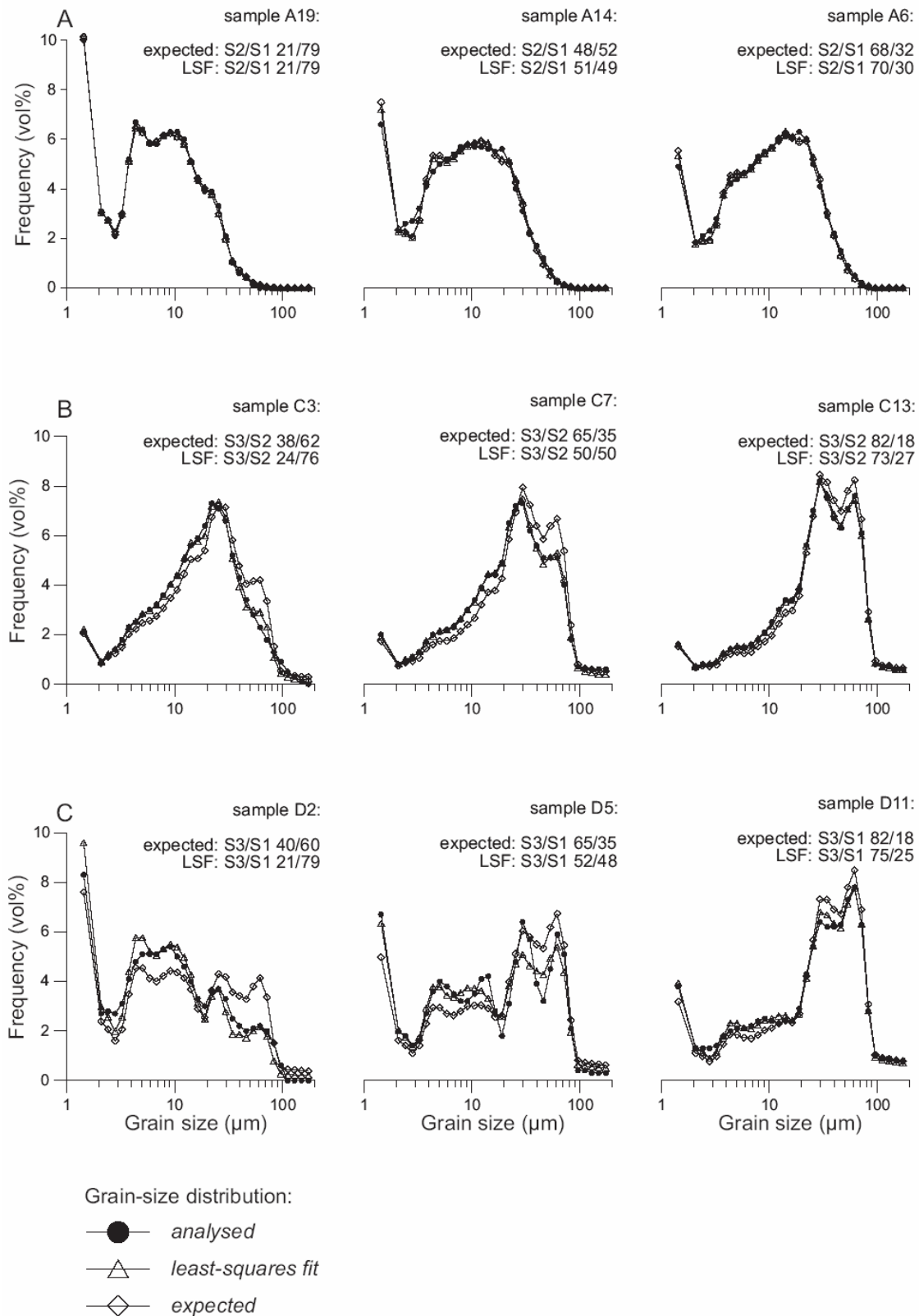


Fig. 2.12 — Correlation diagrams of known weight fractions and calculated (*least-squares fit*) fractions of the coarse-grained standard in the binary sediment mixtures. For comparison the ‘expected’ line  $y=x$  is shown. Significant deviations from the line  $y=x$  are observed in the mixtures composed of S3 and S1 or S2. Mixtures of S1 and S2 are ‘accurately’ measured. A few measured grain-size distributions are shown in Fig. 2.13. Data are listed in Table 2.7.

A nearly linear relation is observed between the known and calculated (LSF) mixing proportions of the standards in the mixtures of standards S1 and S2. For these mixtures only a very small offset can be seen from line  $y=x$ , the relation one expects when the Malvern produces perfectly ‘accurate’ results. A considerable non-linear deviation from this line is observed for the other two series of mixtures (S2:S3 and S1:S3 mixtures). In the latter mixing experiments the proportion of S3 is systematically underestimated by the Malvern laser-diffraction size analyser (and consequently S1 and S2 are systematically overestimated).

Grain-size distributions of a few sediment mixtures are shown in Figure 2.13. For each mixture the *analysed*, *least-squares fit*, and *expected* grain-size distributions are shown. The underestimation of the coarse fraction in mixtures containing S3 is evidenced by the deviations between the *expected* and *analysed* grain-size distributions (Fig. 2.13B, C). In general the *analysed* grain-size distributions are approximated closely by the *least-squares fit* distributions, indicating that the underestimation of S3 is systematic. The mixtures containing S1 and S2 are ‘accurately’ measured by the Malvern laser-diffraction size analyser (Fig. 2.13A). In these mixtures the *analysed*, *least-squares fit*, and *expected* grain-size distributions are almost identical.



**Fig. 2.13** — Grain-size distributions of a few binary mixtures: for each mixture the *analysed*, *least-squares fit*, and *expected* grain-size distributions are shown. A: Samples A6, A14 and A19 are mixtures of S1 and S2. B: Samples C3, C7 and C13 are mixtures of S2 and S3. C: Samples D2, D5 and D11 are mixtures of S1 and S3. Note the systematic overestimation of the ‘coarse fraction’ in mixtures containing S3. In general the *analysed* grain-size distributions are approximated closely by the *least-squares fit* distributions. The mixtures of S1 and S2 are ‘accurately’ measured by the Malvern laser-diffraction size analyser.

## DISCUSSION

### *Measurements of Microsphere Standards*

The Malvern laser-diffraction size analyser produces accurate measurements of the four discrete polystyrene microsphere standards. The mean particle sizes and the standard deviations (widths) of the size distributions are correctly measured. This was to be expected because the microsphere standards represent the ideal samples as particles are truly spherical, as postulated in diffraction theory.

Less encouraging results appear from the analyses of the polystyrene microsphere mixtures. Although small variations in the size distributions are recorded very precisely, the accuracy of these measurements appears to be poor as the 'expected' bimodal structure of the binary mixtures could not be reproduced accurately. The poor resolution ability is likely the result of the problems associated with the analytical inversion of the light intensity distribution function to obtain the size distribution function (for details see Agrawal *et al.*, 1991). Hirleman (1987) found that for a dynamic range in angles of 100 (100:1 size range), between ten and twelve size classes were the maximum that could be recovered by the analytical inversion, with log spacing of size bins. The size data of an overall 100-fold size range (with 100 mm lens, 1.93-188  $\mu\text{m}$ : Table 2.1) produced by the Malvern laser-diffraction size analyser is moulded into 31 size classes. Conformably to the findings by Hirleman (1987), a division into 31 size classes may be much too 'optimistic'. Agrawal *et al.* (1991) further pointed out that some inversion methods which aim at achieving higher-resolution results, produce smoothing of the size distribution function. Detailed discussion on possible causes for the poor resolution ability of the Malvern laser-diffraction size analyser is beyond the scope of this study, and possibly beyond the reach of the scientific community as the algorithm used by Malvern Instruments is generally regarded a 'black box' (Agrawal *et al.*, 1991).

The mixture results indicate that the relative contributions of the microsphere standards within the mixtures can be discerned accurately from the *analysed* distributions if the grain-size distributions of the subpopulations (standards) are known *a priori*. Thus, the 'composite' grain-size distributions of mixtures can be 'unmixed' very accurately despite the inaccurate, blurred bimodal structure of the measurements themselves. These 'surprising' results indicate that the Malvern laser-diffraction size analyser produces systematically distorted results for the polystyrene microsphere mixtures.

### *Measurements of Natural Sediments*

Crucial for geological studies is the ability of the Malvern laser-diffraction size analyser to measure small variations in the grain-size distribution of natural sediments accurately and precisely. However, an 'accurate' grain-size measurement of natural sediment may be regarded as an unrealisable desire as the 'size' of a grain is dependent on its shape and density, and the size analysis method used. Matthews (1991) and Jonasz (1991) discussed these 'problems' from a theoretical point of view. Konert and Vandenberghe (1997) compared the results obtained with two size-analysis methods based on different principals: the pipette method which is based on the 'Stokes' sedimentation rates, and laser-diffraction size analysis which is based on the diffraction of light. They clearly pointed out that the non-sphericity of clay minerals has large effects on size measurements. Given these inevitable 'problems' with the accuracy of a size measurement of natural sediments, the best what can be examined is the precision of the grain-size measurements.

Replicate analyses of 'natural' sediment samples (coarse silt sample, SO90-169KL

samples and BCR samples) indicate that the Malvern laser-diffraction size analyser produces very precise measurements. The results indicate that the variability between measurements of a series of subsamples (SO90-169KL samples) is larger than between measurements of the same subsample (coarse silt sample). Thus the sediment sample preparation procedure is responsible for greater variation than the laser-diffraction measurement itself. Nevertheless, careful handling of samples and a systematic preparation procedure result in highly comparable results, as indicated by the replicate analyses of the BCR samples.

The ability of the Malvern laser-diffraction size analyser to identify polymodal grain-size distributions correctly was questioned by McCave *et al.* (1986) and Singer *et al.* (1988). The occurrence of spurious modes on the grain-size distributions (McCave *et al.*, 1986), and broadening of individual modes with respect to other sizing techniques (Singer *et al.*, 1988) let Agrawal *et al.* (1991) to conclude that if one's goal is dissection of polymodal size distributions and the tracing of populations through modal structure, it may be worth waiting for the 'next generation' of laser-diffraction size analysers. The results with the sediment mixtures presented in this chapter indicate that the conclusion drawn by Agrawal *et al.* (1991) is not fully correct.

The experiments with the sediment mixtures indicate that the Malvern laser-diffraction size analyser is able to determine very small variations in mixing coefficients of sediment standards S1-S3. The measured grain-size distributions of the sediment mixtures (*analysed*) could be approximated closely by the computed grain-size distributions (*least-squares fit*) of hypothetical mixtures composed of the sediment standards. These observations indicate that laser-diffraction size measurements of sediments known to be mixtures of a number of different components can potentially be 'unmixed' correctly, in other words, the mixing proportions and 'end-member' grain-size distributions can potentially be estimated correctly. An inversion algorithm for end-member modelling of compositional data (Weltje, 1994 and 1997a), especially developed for 'unmixing' of multi-sourced basin fills in the absence of prior knowledge of the sediments, will be tested on the sediment mixture grain-size data in Chapter 3.

The mixing experiments also pointed out that in two series of samples (series C and D) the calculated mixing proportions, inferred from the *least-squares fit* approximation of the *analysed* grain-size distributions, do not correspond accurately with the mixing proportions as determined by weight (*expected*). In these samples the Malvern laser-diffraction size analyser underestimated systematically the proportion of sediment standard S3 with respect to standards S1 or S2. The solution for this apparent problem must be sought in the units in which the mixing proportions are expressed. The Malvern laser-diffraction size analyser expresses sediment 'mass' in units of volume, whereas the sediment standards were mixed by weight. This means that the *least-squares fit* (volume-based) and *expected* (weight-based) mixing proportions will only be similar when the particle characteristics (density, shape) of the standards are similar. Concerning the effect of particle shape on size analysis, Jonasz (1991) stated that the projected area of a non-spherical particle averaged over the different particle orientations is larger than that of a sphere with equal volume. This implies that, if grain densities are equal, mixing experiments will indicate that standards consisting of relatively spherical or 'blocky' particles (e.g. quartz) will be underestimated with respect to standards being relatively enriched in non-spherical or 'platy' particles (e.g. clay minerals).

Following this line of reasoning, the systematic deviations in mixing coefficients as 'observed' by the Malvern laser-diffraction size analyser can be explained by the effect of differences in particle shape. Standard S3, which appeared to be underestimated in the mixing experiments, indeed contains predominantly quartz grains (loess, Assenzand), which are relatively spherical. Standards S1 and S2, which appeared to be overestimated in the mixing experiments, indeed consist of mainly clay minerals (Indus Fan sediments), which are highly

non-spherical. Mixtures containing S1 and S2 are ‘accurately’ measured by the Malvern laser-diffraction size analyser as the type of sediment present in both standards is highly comparable.

## **CONCLUSIONS**

1. Certified microsphere standards are very precisely and accurately measured by the Malvern laser-diffraction size analyser.
2. Mixtures composed of microspheres are not measured accurately and resolution of the measurements is poor.
3. If the grain-size distributions of the microsphere standards are known *a priori*, the ‘composite’ grain-size distributions of microsphere mixtures can be unmixed very accurately despite the inaccurate, blurred bimodal structure of the measurements themselves.
4. Replicate analyses of natural sediment samples indicate that the Malvern laser-diffraction size analyser produces very precise measurements.
5. The grain-size distributions of sediment mixtures can be approximated closely by calculated grain-size distributions of hypothetical mixtures composed of the sediment standards.
6. Sediment standards consisting of relatively spherical or ‘blocky’ particles (e.g. quartz) are underestimated by the Malvern laser-diffraction size analyser with respect to sediment standards consisting of relatively non-spherical or ‘platy’ particles (e.g. clay minerals).
7. Grain-size distribution data of sediment mixtures analysed with the Malvern laser-diffraction size analyser can be ‘unmixed’ correctly, in other words, the apparent mixing proportions and ‘end-member’ grain-size distributions can be estimated correctly.

## **ACKNOWLEDGEMENTS**

Mrs. M. Reith of the Sedimentology Laboratory of Utrecht University is thanked for the analyses of the BCR samples.



## END-MEMBER MODELLING OF GRAIN-SIZE DISTRIBUTIONS OF SEDIMENT MIXTURES

M.A. Prins<sup>1</sup> and G.J. Weltje<sup>2</sup>

### ABSTRACT

The ultimate objective of end-member modelling is to provide the ‘simplest possible and least dramatic’ explanation of compositional variation in the absence of *a priori* knowledge of the geological system under study. An outstanding quality of end-member modelling is the great intuitive appeal of the resulting mixing models, which are formulated in the same units as the input data. The end-member modelling algorithm of Weltje (1994, 1997a) is tested on grain-size data of microsphere and natural sediment mixtures to evaluate their usefulness for unravelling of natural multi-sourced basin fills. The independent comparison between the modelled end members and mixing coefficients and the ‘true’ end members (microsphere and sediment standards) and ‘true’ mixing coefficients allows for an objective assessment of the validity of the unmixing solution. The sediment mixture experiments indicate that end-member modelling is a powerful tool for analysing grain-size distribution data in cases where the observed variation among compositions is believed to be the result of linear mixing.

### INTRODUCTION

Variations in grain-size distributions within basin-fill sediments may reflect two kinds of processes: (1) physical mixing of sediment populations with different grain-size distributions; (2) selective mechanisms operating during unidirectional transport and deposition producing sediments whose grain-size distributions change systematically with distance from the source. In many geological applications of grain-size analysis, no *a priori* knowledge is available to distinguish above subpopulations of sediments. Indeed, reconstruction of provenance and dispersal patterns is the very objective of most studies. The best way to proceed in such cases would be to use an inverse method which does not require detailed assumptions about the geological system being studied. One such method is the inversion algorithm for end-member modelling of compositional data of Weltje (1994, 1997a), especially developed for ‘unmixing’ of multi-sourced basin fills in the absence of prior knowledge.

The end-member modelling algorithm has been tested on petrographic data of modern beach sands to evaluate its usefulness for unravelling multi-sourced basin fills in the absence of prior knowledge (Weltje, 1995). In this experiment, modern coastal sands of the Adriatic Sea were used to infer the compositional signatures of fluvial input and the locations of the major drainage basins. Several independent comparisons with the actual situation, through

---

<sup>1</sup> Institute for Paleoenvironments and Paleoclimate Utrecht (IPPU), Faculty of Earth Sciences, Utrecht University, P.O. Box 80021, 3508 TA Utrecht, The Netherlands

<sup>2</sup> (a) Department of Geo-Energy, Netherlands Institute of Applied Geoscience TNO, P.O. Box 6012, 2600 JA Delft, The Netherlands; (b) Subfaculty of Applied Earth Sciences, Delft University of Technology, P.O. Box 5028, 2600 GA Delft, The Netherlands

additional information on the fluvial basins and marine dispersal patterns, allowed for an objective assessment of the validity of the unmixing solution. The experiment showed that the end-member modelling algorithm provides fairly accurate estimates of the end-member compositions in the absence of prior knowledge.

In this study Weltje's end-member modelling algorithm will be tested on two data sets of grain-size distributions: Malvern laser-diffraction size measurements of synthetic mixtures composed of (1) polystyrene microsphere standards and (2) sediment standards. Each data set includes three series of binary mixtures which were prepared by mixing a series of standards with known composition in accurately known proportions (see Chapter 2). End-member modelling of these data allows verification of the correctness of the modelled end members and of the mixing coefficients as they can be compared with the actual 'source compositions', c.f. the grain-size distributions of the standards, and the proportional contributions of these standards in the mixtures.

## DISCRIMINATION OF GRAIN-SIZE SUBPOPULATIONS

### *Parametric Approaches*

Doeglas and Brezesinska Smithuysen (1941) and Doeglas (1946) observed that many cumulative grain-size distributions drawn on arithmetic probability paper appear to be composed of two or more practically straight line segments. They argued that such curves are caused by the mixing of materials of different origins, which possess Gaussian (normal) distributions. Visher (1969) followed a similar line of reasoning by stating that grain-size distributions do not follow a simple lognormal law, but are composed of several lognormal subpopulations each with a different mean and standard deviation. He distinguished at least three subpopulations produced by three modes of sediment transport: surface creep/rolling, saltation, and suspension. A theoretical basis for the existence of different 'transport populations' was provided by the hydraulic models of Middleton (1976) and Bridge (1981). Curray (1960) plotted grain-size distributions on a logarithmic scale ( $\phi$  units), and manually decomposed polymodal frequency distributions into a series of Gaussian (lognormal) distributions. An automated version of Curray's method was developed by Sheridan *et al.* (1987).

The sequential fragmentation-transport (SFT) theory of Wohletz *et al.* (1989) is another parametric method for interpretation of polymodal grain-size distributions. It is based on the assumption that observed grain-size distributions have been produced by a sequence of repeated steps of breakage and selective transport, represented by a series of SFT subpopulations with variable skewness. Decomposition into unimodal SFT distributions has been applied to volcanic ash and pyroclastic grain-size distributions by Wohletz *et al.* (1989) and Lirer *et al.* (1996).

All of the above methods are parametric in the sense that they require *a priori* specification of the end-member grain-size distributions. This may not be desirable in many cases, in view of our incomplete understanding of the mechanisms governing the grain-size distribution of natural sediments and because it may not be possible to define end members beforehand. In the worst case, such a parametric approach could even hamper the recognition of subpopulations with grain-size distributions differing markedly from the adopted model (Gaussian, log-Gaussian, or SFT). The existence of subpopulations which do not fit one of the theoretical grain-size distributions is likely, in view of the potentially unlimited number of combinations of initial and acquired characteristics of sediments (e.g. parent material,

weathering history, mode of transport). Another disadvantage of the above methods is that the decomposition is performed on individual grain-size distributions. The information contained in the covariance structure of the data is not used at all. Large data sets cannot be easily analysed with any of the above techniques, as exemplified by Curray (1960), who manually formed groups of subpopulations with similar modes in order to simplify the results of his analysis.

### *Non-Parametric Approaches*

A different view on grain-size distributions is to regard the proportion of mass in each size class as an attribute of a multivariate measurement, i.e., to consider each grain-size distribution as consisting of as many components as there are size classes. Proportions of mass in two or more size classes may be negatively or positively correlated across a series of grain-size distributions. Such variation among individual measurements is contained in the covariance structure of a data set. The non-parametric methods discussed below all make use of this source of information to group samples with similar overall characteristics. In contrast with the previous methods, the functional forms of the groups, clusters, or end members do not have to be specified *a priori*. Non-parametric approaches to the recognition of subpopulations in grain-size data include methods such as cluster analysis (Zhou *et al.*, 1991) and multivariate entropy analysis (Forrest and Clark, 1989). However, the family of multivariate techniques used most extensively for this purpose comprises principal component analysis (e.g. Davis, 1970; Chambers and Upchurch, 1979; Driscoll *et al.*, 1985; Lirer and Vinci, 1991; Zhou *et al.*, 1991) and factor analysis (e.g. Klován, 1966; Solohub and Klován, 1970; Allen *et al.*, 1971, 1972; Dal Cin, 1976; Sarnthein *et al.*, 1981; Syvitski, 1991b).

The aim of principal component analysis (PCA) and factor analysis (FA) is to decompose the data matrix into two matrices: (1) a matrix of ‘components’ or ‘factors’ from which inferences may be drawn about the shapes of the grain-size distributions of each of the groups recognised in the data, and (2) a matrix representing the extent to which each of the input grain-size distributions matches each of these ‘components’ or ‘factors’ (Jöreskog *et al.*, 1976; Davis, 1986). Thus, interpretation of the subpopulations is based on the properties of the first matrix, and classification of the observations is based on the properties of the second matrix. A major problem with both techniques is that the units in which the output is cast are difficult to interpret because they cannot be expressed in physical terms (for instance, a typical input variable for grain-size analysis, a weight proportion, may have been ‘miraculously’ transformed to a negative value in a component or factor matrix). This is unfortunate because the predominant application of PCA and FA in sedimentology has been in the field of ‘unmixing’ of polymodal grain-size distributions.

Specialist techniques are required if the analytical objective is to unravel grain-size distributions subject to strict physicality (i.e., non-negativity and constant-sum) constraints. End-member modelling algorithms are aimed at construction of physical mixing models which express the input data as mixtures (non-negative contributions) of a limited number of end members with realistic (i.e. non-negative) compositions. The techniques of Klován and Miesch (1976), Full *et al.* (1981, 1982), Renner (1993, 1995) and Weltje (1994, 1997a) have been developed with this objective in mind. Fillon and Full (1984) and Wohletz *et al.* (1989) applied the techniques of Full *et al.* (1981, 1982) to grain-size distribution data. The modelled end members of Fillon and Full (1984) and Wohletz *et al.* (1989) have varying skewness and are of no simple mathematical form, supporting the idea that parametric decomposition into predefined end members (Gaussian, log-Gaussian, or SFT) may not be the best approach towards an understanding of variation among grain-size distributions.

## END-MEMBER MODELLING

### *Linear Mixing Model*

Linear mixing models of compositional data have been developed in various branches of the earth sciences (e.g. geochemistry, petrology, mineralogy, sedimentology) for the purpose of summarising variation among a series of observations in terms of proportional contributions of (theoretical) end members (Klovan and Miesch, 1976; Jöreskog *et al.*, 1976; Full *et al.*, 1981, 1982; Renner, 1993, 1995; Weltje, 1994, 1997a). Compositional variation among a series of genetically related geological specimens (e.g. rock samples) can often be attributed to physical mixing or mathematically analogous processes, such as fractional crystallisation or selective transport and deposition. Data sets which conform to a linear mixing model can be expressed as mixtures of a fixed number of end members. The end members represent a series of fixed compositions, which can be regarded as distinct subpopulations within the data set being analysed. The linear mixing model is formulated as follows.

Compositional data are generally cast into the form of an  $(n \times p)$  matrix  $X$ , with  $n$  rows representing observations, and  $p$  columns representing variables. By definition, compositional variables are non-negative and sum to a constant  $c$ , usually 1, 100, or  $10^6$  (for measurements recorded as proportions, percentages, or parts per million, respectively):

$$\sum_{j=1}^p x_{ij} = c, \text{ where } x_{ij} \geq 0$$

(1)

If compositional variation among a series of measured specimens results from a physical mixing process, each row of the matrix of compositional data  $X$  is a non-negative linear combination of the  $q$  rows of  $B$ , a matrix of end-member compositions. The matrix  $M$  represents the proportional contributions of the end members to each observation. In matrix notation, this perfect mixing can be expressed as:

$$X = MB$$

(2)

subject to the following non-negativity and constant-sum constraints:

$$\sum_{k=1}^q m_{ik} = 1, \text{ where } m_{ik} \geq 0$$

(3)

$$\sum_{j=1}^p b_{kj} = c, \text{ where } b_{kj} \geq 0$$

(4)

Although this representation is acceptable from an algebraic point of view, it fails to account for the fact that perfect mixing cannot be demonstrated in practice, due to sampling and measurement errors in  $X$ . Therefore, it is more realistic to assume that the data matrix  $X$  is made up of a systematic part  $X'$ , attributable to perfect mixing, and a matrix of error terms  $E$ , representing non-systematic contributions to  $X$ :

$$X = X' + E \quad (5)$$

It is assumed that the errors are relatively small and  $X'$  closely resembles  $X$ . By definition, the rows of  $X'$ , the estimated matrix of perfect mixtures, consist of non-negative linear combinations  $M$  of  $q$  end-member compositions  $B$ :

$$X' = MB \quad (6)$$

The range of each variable in  $X'$  cannot exceed that of the corresponding variable in the end members  $B$ , due to the non-negativity constraints on  $M$ . By definition, the rows of  $X'$  are also compositions:

$$\sum_{j=1}^p x'_{ij} = c, \text{ where } x'_{ij} \geq 0 \quad (7)$$

and therefore:

$$\sum_{j=1}^p e_{ij} = 0 \quad (8)$$

The above considerations lead to the following mathematical formulation of the general mixing model:

$$X = MB + E \quad (9)$$

subject to the constraints listed above.

In many cases where compositional variation is believed to have been produced by mixing, the parameters of the mixing process are unknown. Recasting the observed compositional variation into a linear mixing model in the absence of *a priori* knowledge about the number and composition of end members requires a solution of the bilinear (or explicit) mixing problem. This problem may be solved in two stages.

#### *Estimating the Number of End Members*

In the first modelling stage, the mixing space is defined by partitioning the data into  $X'$  and  $E$  ('signal' and 'noise') for each possible number of end members by means of numerical algorithms rooted in fundamental concepts of vector analysis and linear algebra. The dimensionality (shape) of the data in  $p$ -space reflects  $q$ , the number of linearly independent end-member vectors needed to span the mixing space. This implies that the number of end members can be estimated before their compositions have been calculated. The requirement of linear independence limits the number of end members in inverse models of a mixing process to  $p$ , the number of variables measured.

Estimates of  $X'$  for various numbers of linearly independent end members ( $2 \leq q \leq p$ ) are obtained from constrained weighted least-squares approximations to the singular value decomposition of  $X$  (see Weltje, 1994, 1997a). Because the true number of end members and the errors associated with  $X$  are unknown,  $q$  can only be estimated by a comparison of the constrained linear approximations  $X'$  for different values of  $q$  to the original data  $X$ . In general, the goodness-of-fit increases as the number of end members is increased. The principle of parsimony is a useful guideline to the choice of  $q$  in view of the main objective of unmixing, i.e., to 'explain' the observed compositional variation with a minimum number of end members. The minimum number of dimensions (end members) required for a satisfactory approximation of the data is estimated by calculating the coefficients of determination. The coefficients of determination represent the proportions of the variance of each variable (e.g. grain-size class) that can be reproduced by the approximated data. This proportion is equal to the squared correlation coefficient ( $r^2$ ) of the input variables and their approximated values. In view of the principle of parsimony the number of end members required for a satisfactory approximation of the data is fixed at  $q$  associated with the inflection point on the ( $q$  - mean  $r^2$ ) curve.

### *Estimating the End-Member Compositions*

The problem to be solved in the second modelling stage consists of expressing  $X'$ , the matrix of perfect mixtures, as the product of two matrices  $M$  and  $B$  (both of rank  $q$ ). This is a constrained bilinear minimisation problem, which may be solved by means of co-ordinate transformation. The bilinear unmixing solution is intrinsically non-unique. Commonly, an exact solution does not exist and the number of approximate solutions is infinite. In other cases, there may be an infinite number of exact solutions. A unique solution thus requires specification of additional constraints.

A practical strategy is to provide additional constraints based on formalisation of the notion of 'geological reasonableness.' In the absence of prior knowledge, such a rule would allow the reconstruction of the 'optimal' set of end-member compositions from which the observed variation could have been generated. Weltje (1994, 1997a) proposed that the 'optimal' solution of the bilinear mixing problem should be based on the trade-off between two apparently contradictory, but equally desirable requirements: a fully non-negative mixing proportions matrix  $M$  and a conservative estimate of the end-member matrix  $B$ . The latter is non-negative by definition, so that the optimal solution can be regarded as a compromise between mathematical and geological feasibility. In other words: the optimal solution of the bilinear mixing problem (for a given value of  $q$ ) consists of a set of end members that encloses as many of the data points as tightly as possible.

The preferred strategy for solving the bilinear mixing problem is an iterative estimation procedure, which does not require that all of the non-negativity constraints are taken into account at the same time (Full *et al.*, 1981, 1982; Renner, 1993, 1995; Weltje, 1994, 1997a). A commonly adopted approach is to provide an initial guess of the end-member compositions, based on the properties of  $X'$ . Robust initial end-member estimates for a given value of  $q$  may be defined with non-hierarchical Q-mode cluster analysis (c.f. Full *et al.*, 1982; Davis, 1986). The compositions represented by the cluster centres are projected into the mixing space to provide a starting point for iterative procedures aimed at locating a set of 'optimal' end members (Fig. 3.1A).

The mixing proportions matrix  $M$  corresponding to a set of trial end members  $B$  is generated by means of co-ordinate transformation, after which discrepancies between an ideal (e.g. fully non-negative)  $M$  and the current  $M$  are evaluated in order to define improvements

to  $M$ . The end-member matrix  $B$  corresponding to the improved  $M$  is then calculated and optionally adjusted to comply with the non-negativity constraints. This procedure is iterated until the constraints on an optimal  $M$  are satisfied (Figs. 3.1B, 1C). The end-member modelling algorithm proposed by Weltje (1994, 1997a) is guaranteed to converge if compositional variation in the estimated data reflects mixing of  $q$  linearly independent end members, because each successive set of end members encloses those generated in the previous iteration cycle.

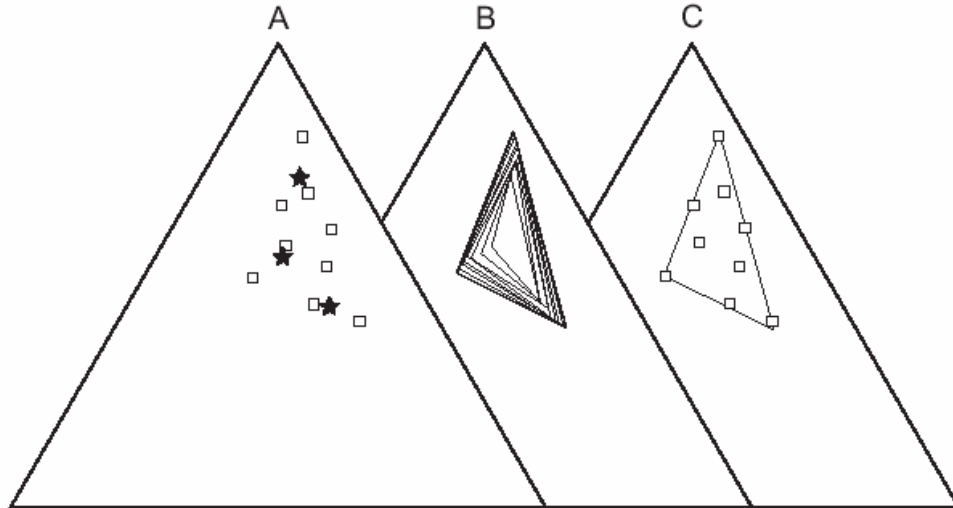


**Fig. 3.1** — Illustration of the numerical end-member modelling algorithm. Construction of a ternary mixing model for a synthetic data set composed of three variables. Data set includes the true end members from which the mixtures were generated. **A:** Initialisation phase, showing data points (squares) and cluster centres (stars). **B:** A series of iterations (initial model and cycles no. 1 to 5, 7, 10, and 20 are shown). **C:** Convergence is reached after 22 iterations. The modelled end members (vertices of the mixing space) closely approximate the true end members.

## MATERIAL AND METHODS

Two data sets are used as input data for the end-member modelling algorithm of Weltje (1994, 1997a). The first data set includes the grain-size distributions of polystyrene microspheres standards #7505, #7510, #7520 and #7550 (certified by Duke Scientific Corporation), and the grain-size distributions of 38 binary mixtures of these standards. The second data set includes 7 measurements of sediment standards S1, S2 and S3, and the grain-size distributions of 61 binary mixtures of these sediment standards. The preparation procedure of the standards and mixtures is presented in Chapter 2. The grain-size distributions were measured on a Malvern 2600 laser-diffraction size analyser using a lens with 100 mm focal length. This configuration provides measurements in 32 discrete size classes between 0.5 and 188  $\mu\text{m}$  (equivalent volume diameter; see Table 2.1 in Chapter 2). The four finest and six coarsest size classes of the polystyrene microsphere mixtures contain on average a very small proportion of the total mass. These classes were amalgamated into single classes ('1/4', '27/32') to reduce the number of variables to 24.

## MODELLING RESULTS — POLYSTYRENE MICROSPHERE MIXTURES

*Goodness-of-Fit Statistics*

Figure 3.2A illustrates how the coefficients of determination are distributed across the individual grain-size classes for different numbers of end members. Many size classes are poorly reproduced ( $r^2 < 0.7$ ) by the models with two or three end members. The four-end-member model produces poor results only for size classes 1/4-6, 15-16, and 21. All of the 24 variables, except size classes 1/4 and 21, are adequately reproduced by a six-end-member model, as indicated by their coefficients of determination which exceed 0.7. The mean coefficient of determination for a two-end-member model is 0.34, i.e., on average 34% of the variance in each grain-size class can be reproduced (Fig. 3.2B). A three end-member model reproduces on average 58% of the variances ( $r^2 = 0.58$ ), and a four-end-member model produces on average 79% of the variances ( $r^2 = 0.79$ ). The mean coefficient of determination increases only slightly for models with more than four end members. In view of the contradictory requirements of parsimony on the one hand (i.e., a minimal number of end members) and reproducibility on the other hand, the goodness-of-fit statistics suggest that a four-end-member model provides a reasonable choice.

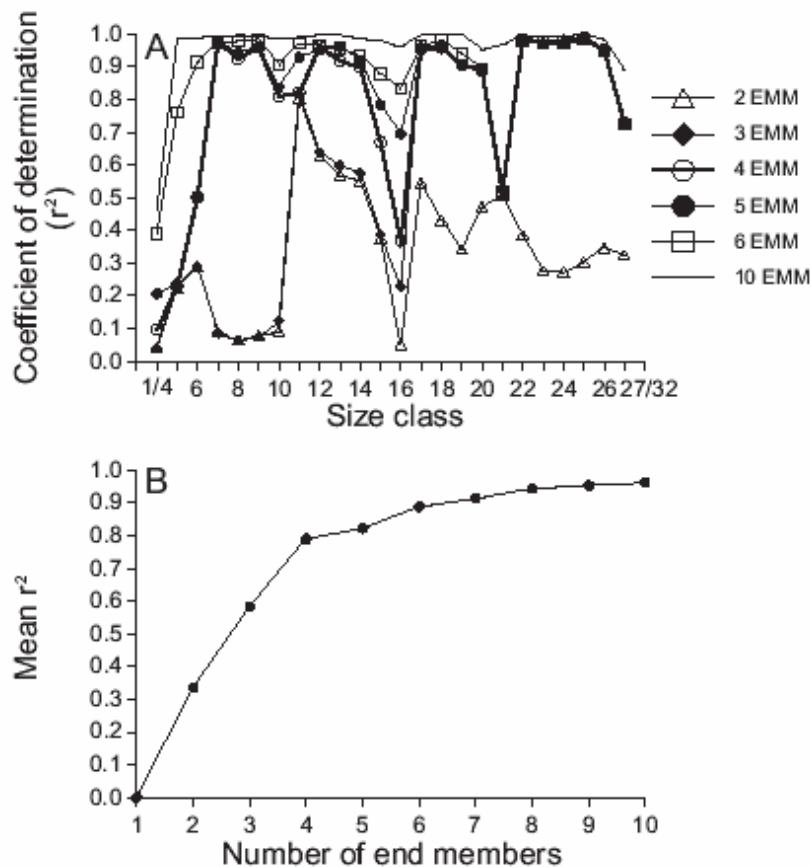
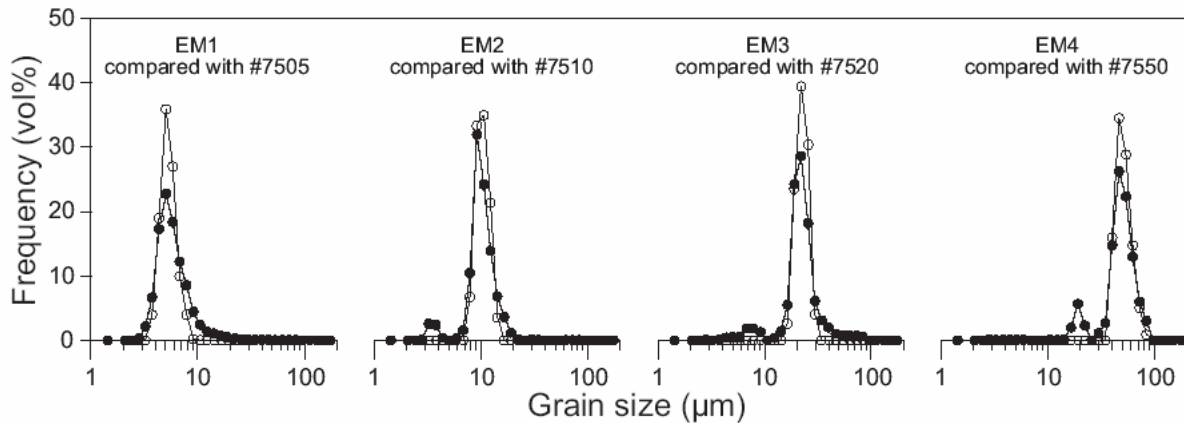


Fig. 3.2 — Goodness-of-fit statistics used to estimate the number of end members of the polystyrene microsphere mixtures. A: Coefficients of determination for each size class. At least four end members are needed to reproduce most variables adequately; a two or three end-member model shows distinct lack of fit in several size ranges. Use of five or more end members hardly improves the goodness-of-fit relative to a four-end-member model. B: Mean coefficient of determination suggests that four end members are needed to closely approximate the data.

### Four-End-Member Model

#### Grain-size distributions of end members.—

The modelled end-member grain-size distributions for the four-end-member model are shown in Figure 3.3 and the data are listed in Table 3.1. All end members have a clearly defined dominant mode: end member EM1 at  $\sim 5 \mu\text{m}$  (size class 8), end member EM2 at  $\sim 9 \mu\text{m}$  (size class 12), end member EM3 at  $\sim 22 \mu\text{m}$  (size class 18), and end member EM4 at  $\sim 46 \mu\text{m}$  (size class 23). End members EM2, EM3 and EM4 have an additional small mode at  $\sim 3\text{-}4 \mu\text{m}$  (size class 5-6),  $\sim 7 \mu\text{m}$  (size class 10-11), and  $\sim 19 \mu\text{m}$  (size class 17), respectively.



**Fig. 3.3** — Grain-size distributions of the modelled end members (filled circles) and the standards (open circles) of the polystyrene microsphere mixtures. The modelled end members closely approximate the standards, c.f., the ‘true’ end members. Note additional small modes in end members EM2, EM3 and EM4. Data of end members are listed in Table 3.1.

#### Comparison between end members and polystyrene microsphere standards.—

The grain-size distributions of the modelled end members are compared with the grain-size distributions of the polystyrene microsphere standards in Figure 3.3. This comparison allows for an objective assessment of the validity of the end-member compositions (Fig. 3.4). An immediate similarity is observed between standard #7505 and EM1, #7510 and EM2, #7520 and EM3, #7550 and EM4. The position of the main modes of the end members correspond well with the position of the modes of the standards. The minor modes occurring in the end members (at  $\sim 3\text{-}4 \mu\text{m}$  in EM2, at  $\sim 7 \mu\text{m}$  in EM3, and at  $\sim 19 \mu\text{m}$  in EM4) are not present in the standards. Similar ‘mysterious’ modes, however, are present in the grain-size distributions of the microsphere mixtures as a result of the inability of the Malvern laser-diffraction size analyser to analyse these mixtures accurately (see Chapter 2).

#### Variations in mixing coefficients.—

Variations among grain-size distributions are expressed as variations among the relative abundances of the four end members. The modelled end-member contributions in the polystyrene microsphere mixtures are listed in Table 3.2. Each microsphere standard is closely approximated by one of the modelled end members (as indicated in Figure 3.3). Samples A-M are mixtures of standards #7505 and #7510 and are represented by essentially binary mixtures of EM1 and EM2. The contributions of EM3 and EM4 are very small

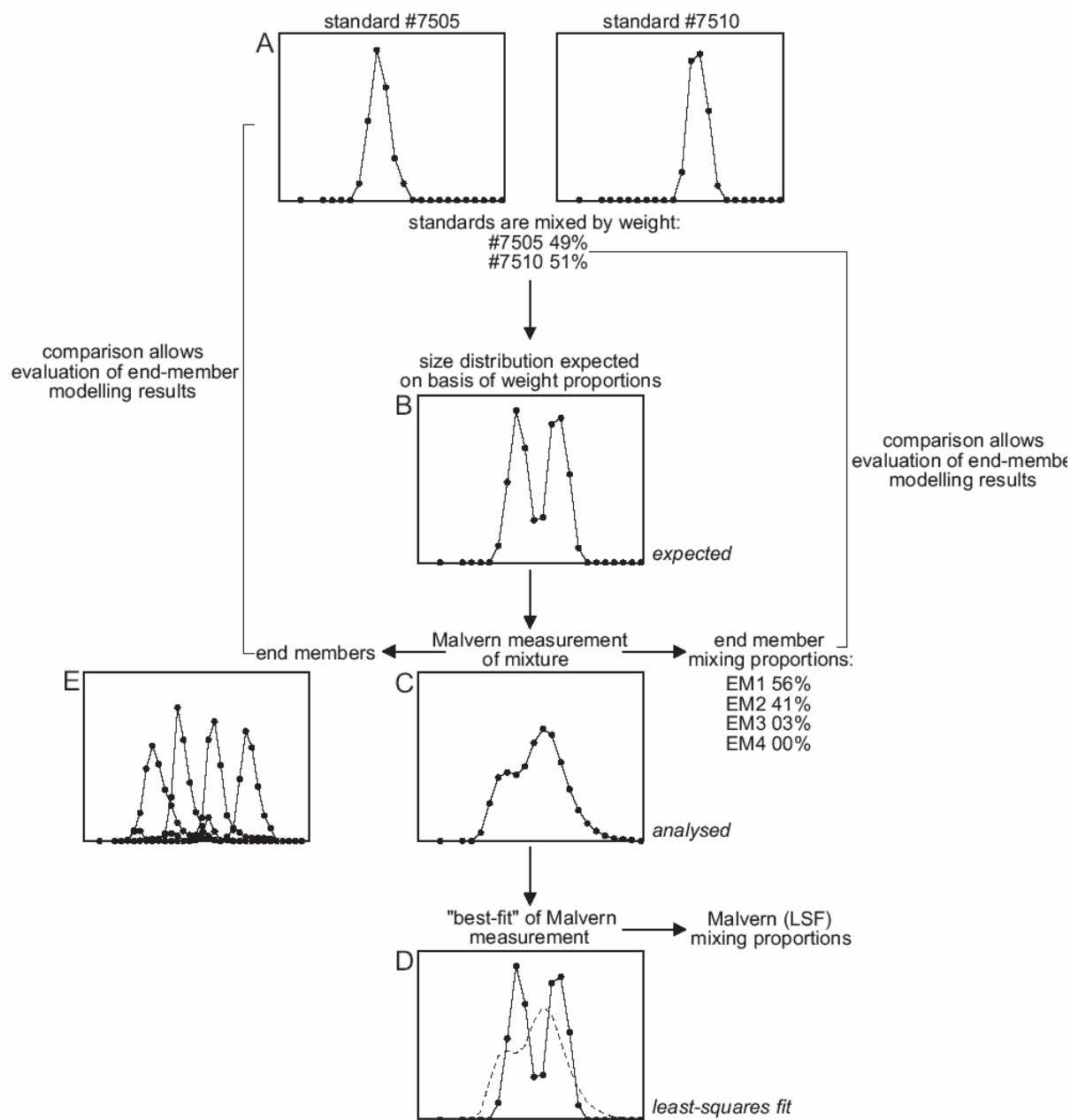


Fig. 3.4 — Schematic representation of different types of grain-size distributions used in this study; results of sample E are shown as an example. A: Size distributions of microsphere standards #7505 and #7510 measured with the Malvern laser-diffraction size analyser. B: Calculated size distribution of sample E expected on basis of the weight proportions of standards #7505 and #7510; the *expected* size distribution. C: Malvern laser-diffraction measurement of sample E; the *analysed* size distribution. D: Calculated size distribution (heavy line) which fits the *analysed* (dotted line) size distribution as close as possible according to the method of least-squares: the *least-squares fit* size distribution. E: Size distributions of the modelled end members. The mixing proportions by weight (wt%) are compared with the proportional contributions of the end members in Figure 3.5.

**TABLE 3.1 — GRAIN-SIZE DISTRIBUTIONS OF POLYSTYRENE MICROSPHERE END MEMBERS**

Size class	EM1	EM2	EM3	EM4	Size class	EM1	EM2	EM3	EM4
1/4	0.22	0.12	0.07	0.10	16	0.75	3.63	5.52	2.00
5	2.21	2.61	0.00	0.06	17	0.53	1.19	24.22	5.64
6	6.67	2.41	0.11	0.07	18	0.29	0.17	28.62	2.31
7	17.29	0.39	0.40	0.09	19	0.15	0.00	18.18	0.00
8	22.79	0.00	0.51	0.11	20	0.16	0.14	6.12	1.10
9	18.41	0.29	0.54	0.09	21	0.10	0.01	3.14	2.68
10	12.25	1.56	1.83	0.00	22	0.06	0.00	2.00	14.81
11	8.56	10.50	1.80	0.00	23	0.04	0.00	1.01	26.24
12	4.45	31.96	1.29	0.00	24	0.03	0.00	0.78	22.38
13	2.43	24.18	0.00	0.07	25	0.03	0.01	0.81	13.01
14	1.43	13.95	0.36	0.05	26	0.03	0.01	0.70	6.03
15	1.10	6.83	1.45	0.14	27/32	0.03	0.02	0.58	3.03

Frequency expressed in volume percent (vol%)

**TABLE 3.2 — END-MEMBER CONTRIBUTIONS IN POLYSTYRENE MICROSPHERE MIXTURES**

Sample	EM1	EM2	EM3	EM4	Sample	EM1	EM2	EM3	EM4
#7505	1.00	0.00	0.00	0.00	R	0.00	0.84	0.16	0.00
#7510	0.00	1.00	0.00	0.00	S	0.00	0.76	0.24	0.00
#7520	0.00	0.00	1.00	0.00	T	0.07	0.46	0.46	0.01
#7550	0.00	0.00	0.00	1.00	V	0.06	0.14	0.79	0.01
A	1.00	0.00	0.00	0.00	W	0.05	0.05	0.90	0.00
B	0.93	0.00	0.00	0.06	X	0.01	0.00	0.99	0.00
C	0.83	0.11	0.00	0.06	Y	0.00	0.00	1.00	0.00
D	0.78	0.22	0.00	0.00	Z	0.00	0.00	1.00	0.00
E	0.56	0.41	0.03	0.00	1	0.00	0.00	0.98	0.02
F	0.30	0.69	0.01	0.00	2	0.00	0.00	0.93	0.07
G	0.13	0.86	0.00	0.01	3	0.00	0.00	0.91	0.09
H	0.02	0.98	0.00	0.00	4	0.00	0.00	0.91	0.09
I	0.00	1.00	0.00	0.00	5	0.00	0.00	0.73	0.27
J	0.00	0.97	0.03	0.00	6	0.00	0.00	0.55	0.45
K	0.00	0.98	0.02	0.00	7	0.00	0.00	0.38	0.62
L	0.00	0.99	0.01	0.00	8	0.00	0.00	0.19	0.81
M	0.00	1.00	0.00	0.00	9	0.00	0.00	0.08	0.92
N	0.00	1.00	0.00	0.00	10	0.00	0.00	0.00	1.00
O	0.00	1.00	0.00	0.00	11	0.00	0.00	0.00	1.00
P	0.00	1.00	0.00	0.00	12	0.00	0.00	0.00	1.00
Q	0.00	0.92	0.08	0.00	13	0.00	0.00	0.00	1.00

( $\leq 6\%$ ). Samples N-Z (mixtures of #7510 and #7520) and samples 1-13 (mixtures of #7520 and #7550) are represented by essentially binary mixtures of EM2:EM3 and EM3:EM4, respectively. Contributions of the other two end members (EM1:EM4 or EM1:EM2) in these mixtures are less than  $\leq 7\%$ .

As the modelled compositions are essentially composed of two end members ( $\geq 92\%$ ), it is appropriate to compare the proportional contributions of one of these end members with the contributions (wt%; see Table 2.4 in Chapter 2) of one of the two microsphere standards present in the samples (Fig. 3.5). This comparison allows for an objective assessment of the validity of part of the unmixing solution (Fig. 3.4). The modelled relative contributions of

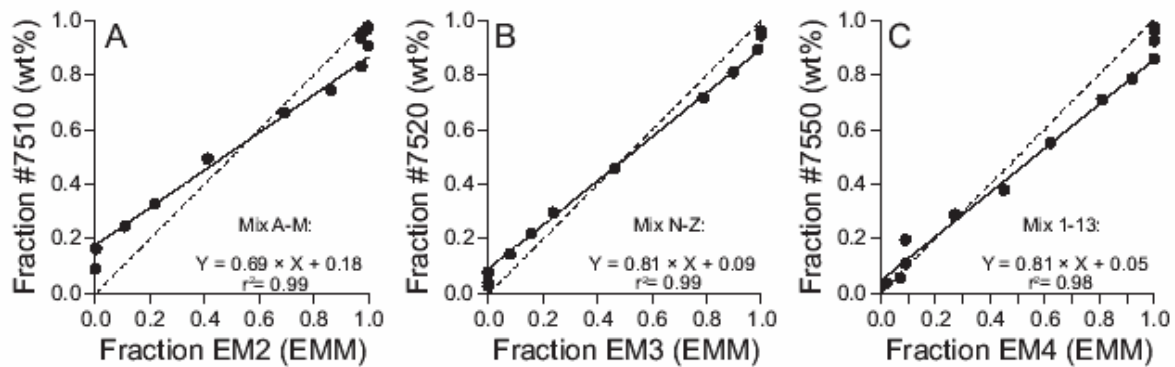


**Fig. 3.5 — Correlation diagrams of modelled mixing proportions of end members and mixing proportions by weight of polystyrene microsphere standards in the three series of binary mixtures composed of standards #7505 and #7510 (A), standards #7510 and #7520 (B), and standards #7520 and #7550 (C). Regression lines (solid) and line  $y=x$  (dashed) are drawn. Regression equations and correlation coefficients are indicated. Calculation of the regressions is based on data points with ‘fraction EMx’  $> 0$  and  $< 1$ . Data are listed in Table 3.2.**

EM2 show a very good correlation ( $r^2 > 0.99$ ) with the known relative contribution of #7510 in samples A-M. In these samples the proportional contributions of EM2 and #7510 deviate, however, significantly from unity ( $y=x$ ), as the regression equation is  $y=0.69x + 0.18$  (Fig. 3.5A). Similar results are obtained for the other two series of mixtures, e.g., samples N-Z (Fig. 3.5B) and 1-13 (Fig. 3.5C). The regression equations between proportional contributions of the end members (EM3, EM4) and the standards (#7520, #7550) are  $y=0.81x + 0.09$  ( $r^2 > 0.99$ ; Fig. 3.5B) and  $y=0.81x + 0.05$  ( $r^2 > 0.98$ ; Fig. 3.5C).

## MODELLING RESULTS — NATURAL SEDIMENT MIXTURES

### *Goodness-of-Fit Statistics*

Figure 3.6A illustrates how the coefficients of determination are distributed across the individual grain-size classes for different numbers of end members. Two size ranges are poorly reproduced ( $r^2 < 0.8$ ) by a two-end-member model: classes 1-3 and 15-19. All of the 32 variables are adequately reproduced by a three-end-member model, as indicated by their coefficients of determination which exceed 0.9 (equivalent to a correlation coefficient of 0.95). The mean coefficient of determination for a two-end-member model is 0.81, i.e., on average 81% of the variance in each grain-size class can be reproduced (Fig. 3.6B). A three end-member model already reproduces on average 96% of the variances ( $r^2=0.96$ ), indicating that the input data can be reproduced almost perfectly in three dimensions. The mean coefficient of determination increases only slightly for models with more than three end members (four-end-member model  $r^2=0.98$ ; five-end-member model  $r^2=0.99$ ). In conclusion, the goodness-of-fit statistics suggest that a three end-member model provides a very good choice in view of the contradictory requirements of parsimony on the one hand (i.e., a minimal number of end members) and reproducibility on the other hand.

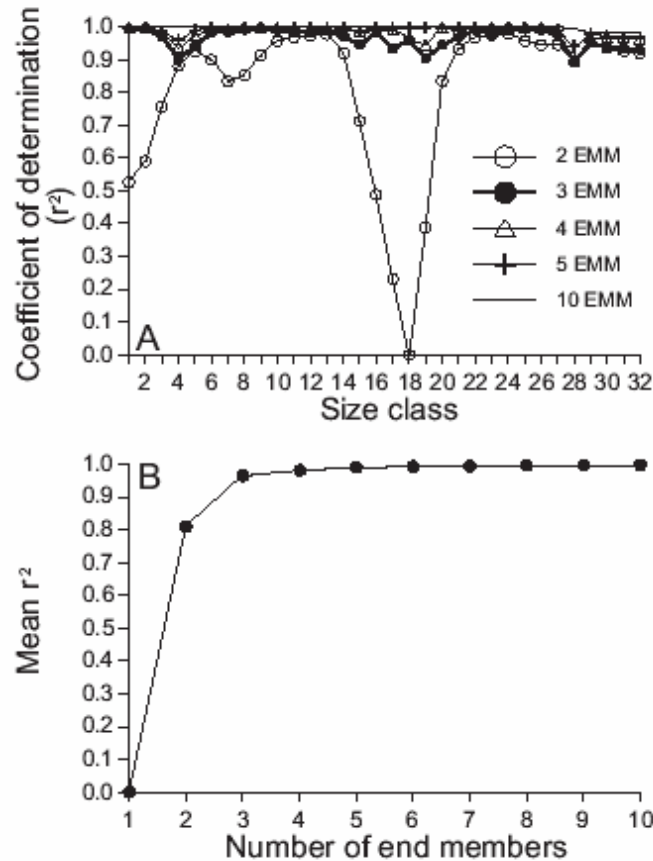


Fig. 3.6 — Goodness-of-fit statistics used to estimate the number of end members of the sediment mixtures. A: Coefficients of determination for each size class. At least three end members are needed to reproduce all variables adequately; a two end-member model shows distinct lack of fit in two size ranges. Use of four or more end members hardly improves the goodness-of-fit relative to a three-end-member model. B: Mean coefficient of determination suggests that three end members are needed to closely approximate the data.

### *Three-End-Member Model*

#### *Grain-size distributions of end members.—*

The modelled end-member grain-size distributions for the three-end-member model are shown in Figure 3.7 and the data are given in Table 3.3. All end members have a clearly defined dominant mode. End member EM1 has a main mode at  $\sim 5 \mu\text{m}$  (size class 8), and three smaller modes at  $\sim 9$ ,  $\sim 24$  and  $\sim 60 \mu\text{m}$  (size classes 12, 18-19, 25). EM1 has an excess of material in the fraction  $< 1.93 \mu\text{m}$  (size class 1). End member EM2 has a modal grain size of  $\sim 22 \mu\text{m}$  (size class 18). Small modes or shoulders can be seen at  $\sim 4$ ,  $\sim 9$  and  $\sim 95 \mu\text{m}$  (size classes 6, 12, 28). End member EM3 has two main modes around  $\sim 35$  and  $\sim 60 \mu\text{m}$  (size classes 21 and 25), and very small modes at  $\sim 5$  and  $\sim 14 \mu\text{m}$  (size classes 8 and 15).

#### *Comparison between end members and sediment standards.—*

The grain-size distributions of standards S1, S2 and S3 are shown together with the grain-size distributions of the modelled end members in Figure 3.7. This comparison allows for an objective assessment of the validity of the end-member compositions (Fig. 3.8). If the grain-size distributions of the standards and end members are compared, a close resemblance is

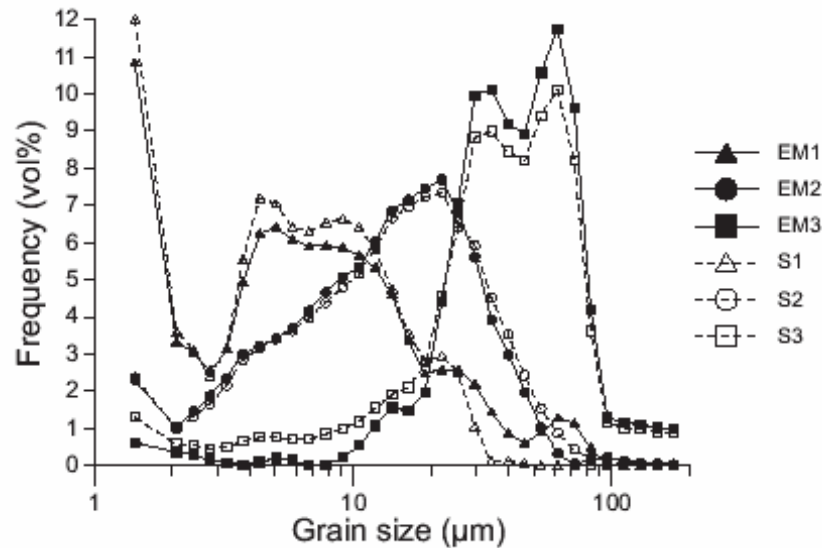


**Fig. 3.7** — Grain-size distributions of modelled end members and sediment standards of the sediment mixtures. The modelled end members closely approximate the sediment standards, c.f., the ‘true’ end members. Data of end members are listed in Table 3.3.

observed between S1 and EM1, S2 and EM2 and S3 and EM3. The main modes and most of the smaller modes present within the standards are very accurately reproduced by the modelled end members. In other words, within the 32-dimensional composition space the modelled end members approximate the ‘true’ end members (standards) very closely. However, some small deviations between the standards and the end members can be observed.

End member EM1 deviates from standard S1 in being ‘enriched’ in material  $>25 \mu\text{m}$  (size classes 19-32) with a clearly defined mode at  $\sim 60 \mu\text{m}$  (size class 25). This small mode is not present in S1. Compared to standard S2, end member EM2 is ‘depleted’ in material in the range  $>25 \mu\text{m}$  (size classes 19-32). The small mode at  $\sim 95 \mu\text{m}$  (size class 28) in end member EM2 is absent in standard S2. With respect to standard S3, end member EM3 is ‘depleted’ in material in the size range  $<22 \mu\text{m}$  (size class 1-18).

**TABLE 3.3** — GRAIN-SIZE DISTRIBUTIONS OF SEDIMENT END MEMBERS

Size class	EM1	EM2	EM3	Size class	EM1	EM2	EM3
1	10.84	2.31	0.61	17	2.48	7.44	1.96
2	3.33	1.04	0.36	18	2.58	7.69	4.40
3	3.07	1.45	0.29	19	2.58	6.78	7.04
4	2.57	1.88	0.14	20	2.20	5.62	9.94
5	3.13	2.36	0.06	21	1.45	3.91	10.12
6	4.95	2.99	0.02	22	0.87	2.98	9.19
7	6.25	3.20	0.09	23	0.61	1.96	8.90
8	6.42	3.41	0.19	24	0.91	1.02	10.56
9	6.09	3.69	0.14	25	1.28	0.33	11.73
10	5.90	4.16	0.00	26	1.14	0.04	9.62
11	5.92	4.66	0.02	27	0.48	0.15	4.18
12	5.86	5.06	0.22	28	0.03	0.22	1.28
13	5.67	5.34	0.55	29	0.00	0.13	1.15
14	5.34	6.03	1.07	30	0.02	0.06	1.10
15	4.60	6.86	1.55	31	0.02	0.04	1.02
16	3.37	7.14	1.47	32	0.03	0.03	1.00

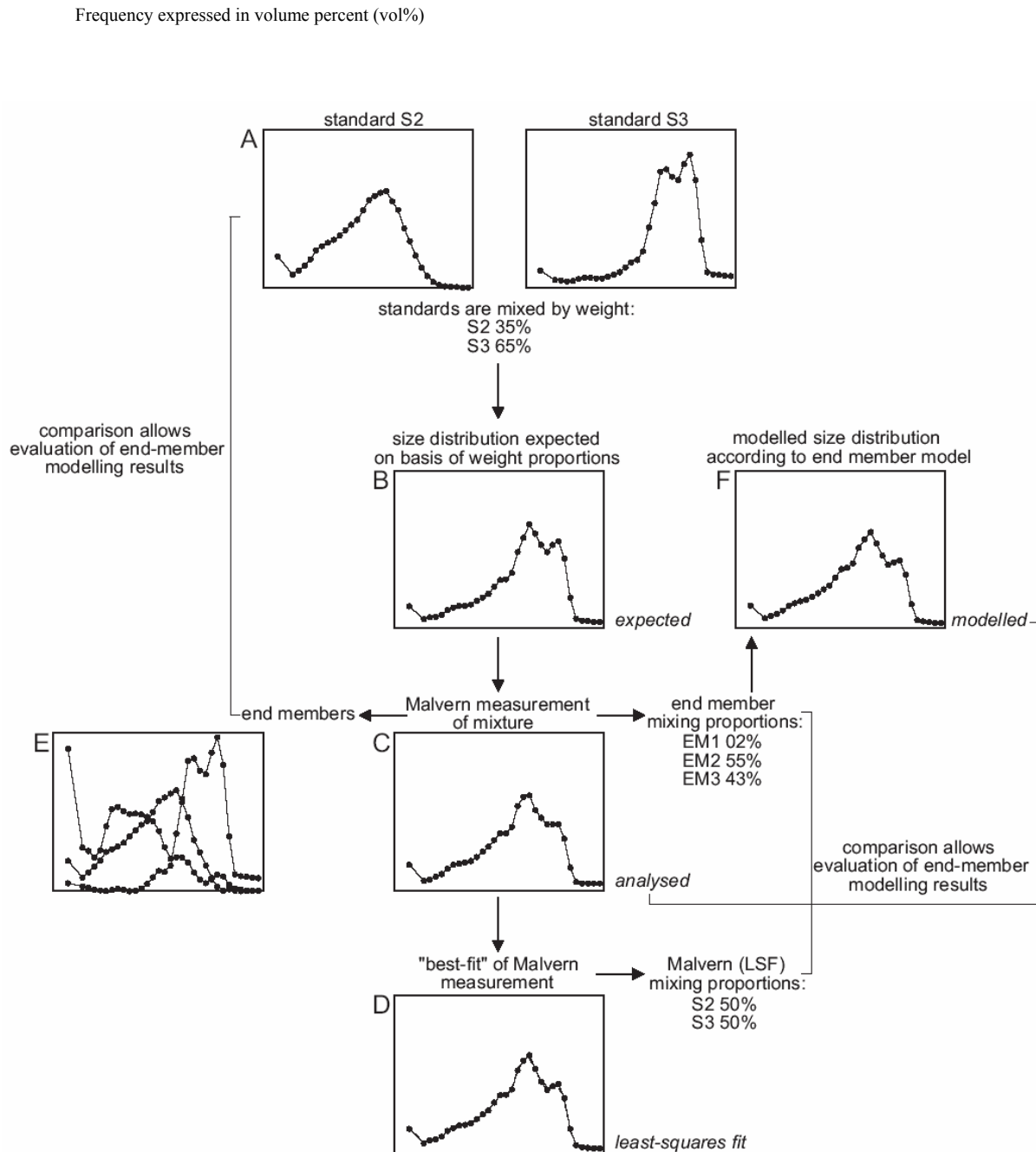


**Fig. 3.8** — Schematic representation of different types of grain-size distributions used in this study; results of sample C7 are shown as an example. A: Size distributions of sediment standards S2 and S3 measured with the Malvern laser-diffraction size analyser. B: Calculated size distribution of sample C7 expected on basis of the weight proportions of standards S2 and S3; the *expected* size distribution. C: Malvern laser-diffraction measurement of sample C7; the *analysed* size distribution. D: Calculated size distribution (heavy line) which fits the *analysed* (dotted line) size distribution of sample C7 as close as possible according to the method of least-squares: the *least-squares fit* size distribution. E: Size distributions of the modelled end members. F: Modelled size distribution of sample C7 according to the end member model. Note the close correspondence between the *modelled* size distribution and the *analysed* and *least-squares fit* size distributions (see also Fig. 3.9). The Malvern mixing proportions (LSF) are compared with the proportional contributions of the end members in Figure 3.11.

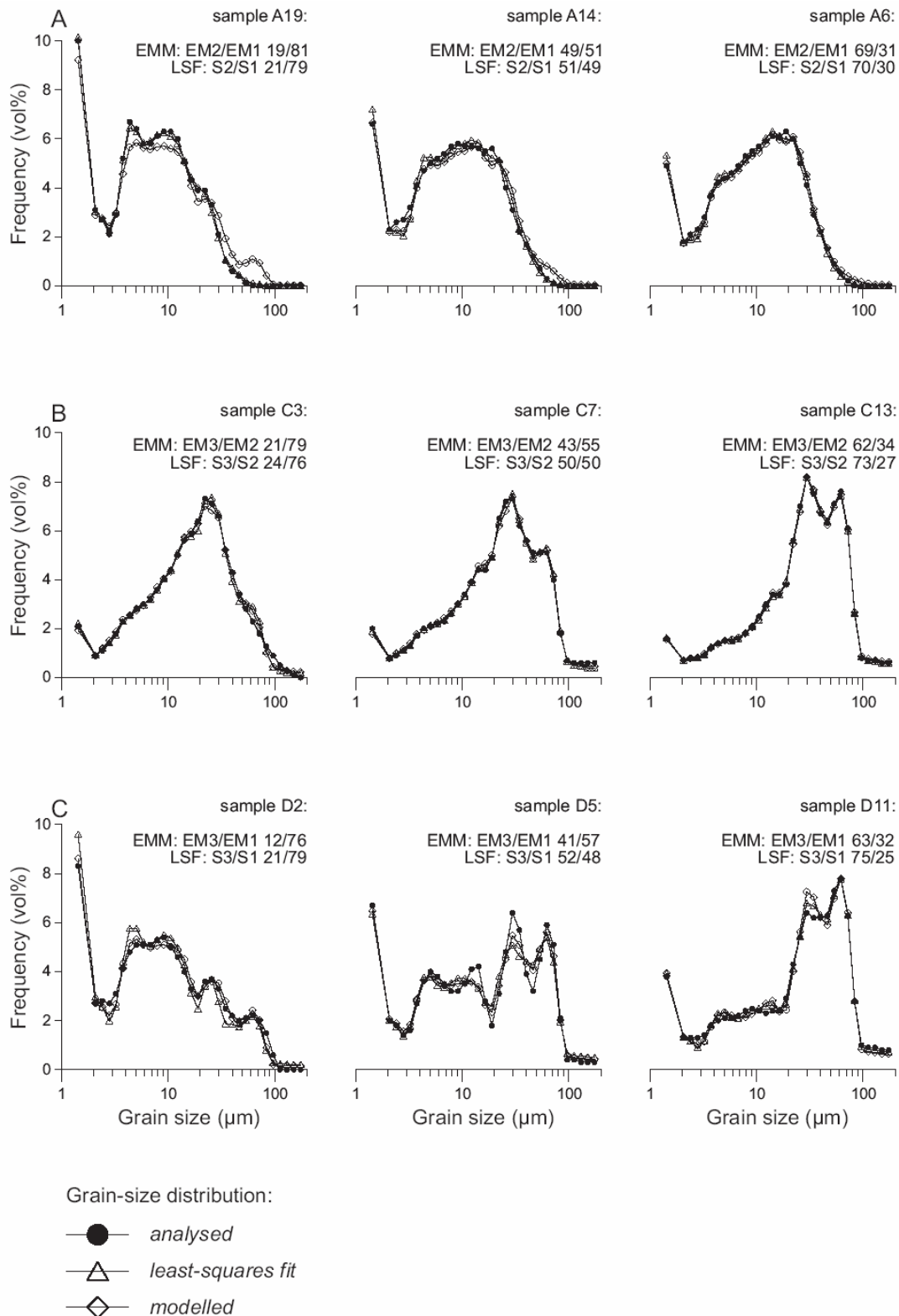


**Fig. 3.9** — Grain-size distributions of some binary mixtures: for each mixture the *analysed*, *least-squares fit*, and *modelled* grain-size distributions are shown. A: Samples A6, A14 and A19 are mixtures of S-1 and S-2. B: Samples C3, C7 and C13 are mixtures of S-2 and S-3. C: Samples D2, D5 and D11 are mixtures of S-1 and S-3. In general the *analysed* and *least-squares fit* grain-size distributions are approximated closely by the *modelled* grain-size distributions. Note the ‘false’ mode at 60  $\mu\text{m}$  in the *modelled* grain-size distributions of mixtures composed of S1 and S2 (e.g., sample A19).

The close similarities between the standards and the end members explain the very high percentage (96%) of the variances of the size classes reproduced by the three-end-member model. The fact that the three-end-member model reproduces the input data not completely (4% of the variances is not reproduced) is a consequence of the small deviations between the end members and the standards (and inevitable noise in the data). This point can be clarified by expressing the end members of the three-end-member model as mixtures of the standards, and vice versa. The least-squares mixing coefficients indicate that EM1 is closely approximated by a mixture of 89% S1 and 11% S3. Likewise, S3 is closely approximated by a mixture of 12% EM1 and 88% EM3. Above results indicate that a sample with an ‘extreme’ composition, e.g. composed of 100% S1, can not be approximated very accurately by the three-end-member model as the closest approximation of S1 is EM1.

*Comparison between analysed and modelled grain-size distributions.—*

In spite of the significant size reduction of the data set (compressing 32 size classes into three mixing coefficients), the complete grain-size distribution can still be reconstructed. The goodness-of-fit of each *modelled* grain-size distribution can be visualised by comparing it to the *analysed* grain-size distribution (Fig. 3.8). Figure 3.9 shows the modelling results of nine representative samples: samples A6, A14 and A19 are mixtures of standards S1 and S2 (Fig. 3.9A); samples C3, C7 and C13 are mixtures of standards S2 and S3 (Fig. 3.9B); samples D2, D5 and D11 are mixtures of standards S1 and S3 (Fig. 3.9C).

In general the *modelled* grain-size distribution approximates the *analysed* grain-size distribution very closely. It appears that deviations between observation and model are of the same order of magnitude as typical sampling and measurement errors for comparable material, which have been determined from replicate analyses (see Figure 2.8 in Chapter 2). Significant deviations between observation and model are only seen in samples with high relative abundances of S1. These S1-rich samples have compositions which are ‘too extreme’ to be approximated accurately by the three-end-member model (see discussion above). The *modelled* grain-size distributions of samples with high S1:S2 ratios have a small mode at ~60  $\mu\text{m}$  (e.g., sample A19; Fig. 3.9A), which is not present in the *analysed* grain-size distribution. The same is true for samples composed of S1 and S3 where the S1:S3 ratios  $> 8.1$  (approximated composition end member EM1; S1:S3=89:11=8.1). Nevertheless, it is apparent that most samples can be adequately described as mixtures of the three modelled end members.

*Variations in mixing coefficients.—*

In the ternary mixing model, changes in grain-size distributions are expressed as changes in the relative abundances of the three end members. The total range of compositional variation can be visualised in a ternary diagram of which the modelled end members form the three vertices. Binary mixtures are plotted on the sides of the ternary diagram, whereas ternary mixtures plot within the ternary diagram.

The individual data points of the estimated compositions of the sediment mixtures are shown in Figure 3.10 (data are listed in Table 3.4). Samples composed of standards S1 and S2 are translated into essentially binary mixtures of end members EM1 and EM2. The end-member model exceptionally assigned a small contribution of EM3 ( $\leq 2\%$ ) to only two samples composed of S1 and S2. Samples containing standards S2-S3 and S1-S3 are recognised as mixtures of essentially EM2:EM3 and EM1:EM3. Within the latter two series of mixtures, the contribution of the third end member (EM1 and EM2, respectively) is more

significant: within the S2:S3 samples the proportional contribution of EM1 is  $\leq 5\%$ , within the S1:S3 samples EM2 generally reaches values  $\leq 8\%$  (sample D2 exceptionally contains 12% EM2).

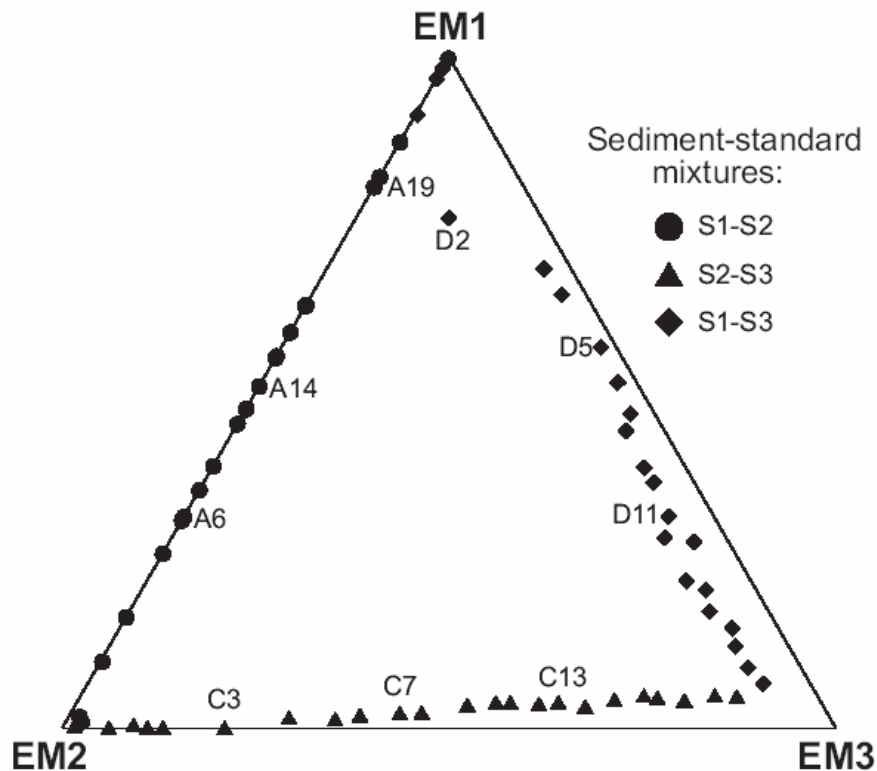


**Fig. 3.10** — Three-end-member mixing model of the sediment mixtures. The end members form the three vertices in the ternary diagram. Data are listed in Table 3.4.

The proportional contributions of the end members are compared with the calculated (*least-squares fit* (LSF): see Fig. 3.8) contributions of the sediment standards in Figure 3.11. The modelled relative contributions of EM2 show a very good correlation ( $r^2 > 0.99$ ) with the calculated relative contribution of S2 in samples composed of S1 and S2 (Fig. 3.11A). The mixing proportions of S1 and S2 are almost perfectly approximated by the modelled mixing proportions of EM1 and EM2 (EM3 is near zero: see Fig. 3.10). In these samples the proportional contributions of EM2 and S2 approaches unity ( $y=x$ ), as the regression equation is  $y=1.00x + 0.03$ .

Significant deviations from unity are detected for samples composed of S2:S3 and S1:S3. The regression equations between proportional contributions of EM3 and S-3 are  $y=1.19x - 0.02$  in mixtures composed of S2 and S3 (Fig. 3.11B), and  $y=1.03x + 0.10$  for mixtures composed of S1 and S3 (Fig. 3.11C). For both series, the modelled relative contributions of EM3 show a very good correlation ( $r^2 > 0.99$ ) with the known relative contribution of S3, indicating that the deviations from unity are systematic. The systematic deviations in mixing coefficients (standards versus end members) are obviously caused by the observed systematic differences in grain-size distributions of the modelled and ‘true’ end members.

**TABLE 3.4 — END-MEMBER CONTRIBUTIONS IN SEDIMENT MIXTURES**

Mixtures S1 + S2			Mixtures S2 + S3				Mixtures S1 + S3				
Sample	EM1	EM2	EM3	Sample	EM1	EM2	EM3	Sample	EM1	EM2	EM3
A1*	0.02	0.97	0.01	C1	0.00	0.91	0.09	D1	0.92	0.08	0.00
A2	0.10	0.90	0.00	C2	0.00	0.87	0.13	D2	0.76	0.12	0.12
A3	0.16	0.84	0.00	C3	0.00	0.79	0.21	D3	0.69	0.03	0.28
A4	0.22	0.78	0.00	C4	0.01	0.70	0.29	D4	0.65	0.03	0.32
A5	0.26	0.74	0.00	C5	0.01	0.64	0.35	D5	0.57	0.02	0.41
A6	0.31	0.69	0.00	C6	0.01	0.61	0.38	D6	0.52	0.02	0.46
A7	0.35	0.65	0.00	C7	0.02	0.55	0.43	D7	0.47	0.03	0.50
A8	0.39	0.61	0.00	C8	0.03	0.52	0.45	D8	0.44	0.05	0.51
A9	0.45	0.55	0.00	C9	0.03	0.46	0.51	D9	0.39	0.04	0.56
A10	0.48	0.52	0.00	C10	0.04	0.42	0.54	D10	0.37	0.05	0.58
A11	0.49	0.51	0.00	C11	0.04	0.40	0.56	D11	0.32	0.05	0.63
A12	0.49	0.51	0.00	C12	0.04	0.36	0.60	D12	0.28	0.08	0.64
A13	0.48	0.52	0.00	C13	0.04	0.34	0.62	D13	0.28	0.04	0.68
A14	0.51	0.49	0.00	C14	0.03	0.31	0.66	D14	0.22	0.08	0.70
A15	0.55	0.45	0.00	C15	0.04	0.26	0.70	D15	0.21	0.06	0.73
A16	0.59	0.41	0.00	C16	0.05	0.22	0.73	D16	0.18	0.07	0.75
A17	0.69	0.31	0.00	C17	0.04	0.21	0.75	D17	0.15	0.06	0.79
A18	0.73	0.27	0.00	C18	0.04	0.17	0.79	D18	0.12	0.07	0.81
A19	0.81	0.19	0.00	C19	0.05	0.13	0.82	D19	0.09	0.07	0.84
A20	0.88	0.12	0.00	C20	0.00	0.89	0.11	D20	0.97	0.03	0.00
A21*	1.00	0.00	0.00	C21	0.00	0.94	0.06	D21	0.99	0.01	0.00
A22*	0.01	0.97	0.02	C22*	0.00	0.99	0.01	D22*	1.00	0.00	0.00
				C23*	0.05	0.10	0.85	D23*	0.06	0.06	0.88

\* samples consisting of 100% S1, S2 or S3

## DISCUSSION

In this paper the end-member modelling algorithms of Weltje (1994, 1997a) are tested on grain-size data of sediment mixtures to evaluate their usefulness for unravelling of natural multi-sourced basin fills in the absence of prior knowledge. The independent comparison between the modelled end members and the 'true' end members (standards) allowed for an objective assessment of the validity of the unmixing solution.

In both experiments the goodness-of-fit increases systematically when the number of end members increases. However, beyond a certain number of end members  $q$  the rate of improvement of the goodness-of-fit, indicated by the mean coefficient of determination  $r^2$ , decreases sharply. This is shown by the inflection point on the ( $q$  - mean  $r^2$ ) curves (Fig. 3.2A and Fig. 3.6A). In view of the principle of parsimony the number of end members required for a satisfactory approximation of the data was fixed at  $q$  associated with the inflection point on the ( $q$  - mean  $r^2$ ) curves. Following this approach, the number of end members of the synthetic mixtures was estimated correctly in both experiments as the number of end members corresponded with the number of standards present in the samples.

A conspicuous result of the unmixing procedure is that all modelled end members have clearly defined dominant modes on their grain-size distributions, whereas none are truly unimodal or of simple analytical form. This shows that end-member modelling allows the extraction of subpopulations with fairly 'natural' and 'sensible' grain-size distributions. None of the alternative approaches discussed above would have been capable of resolving such end members.

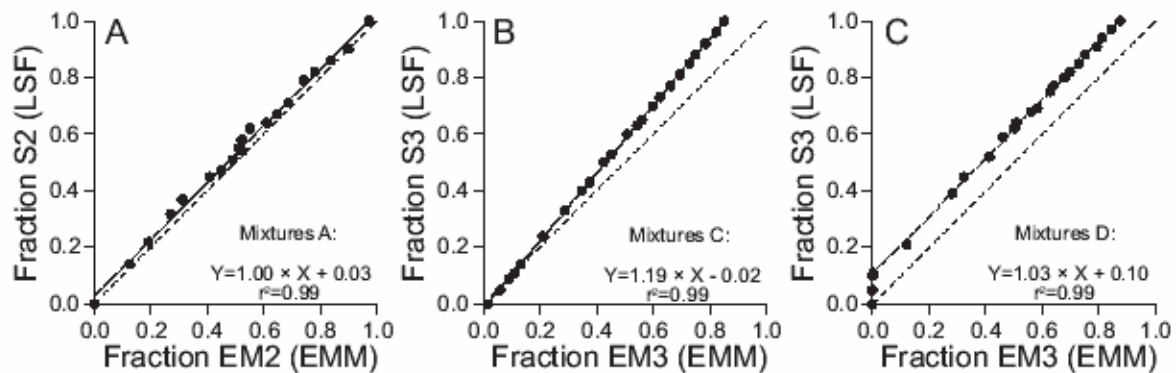


**Fig. 3.11** — Correlation diagrams of modelled mixing proportions of end members and calculated mixing proportions (*least-squares fit*) of sediment standards in the three series of binary mixtures composed of standards S1 and S2 (A), standards S2 and S3 (B), and standards S1 and S3 (C). Regression lines (solid) and line  $y=x$  (dashed) are drawn. Regression equations and correlation coefficients are indicated. Calculation of the regression equation for mixtures composed of S1 and S3 (C) is based on data points with ‘fraction EM3’ > 0. Data are listed in Table 3.4.

Reconstruction of the ‘optimal’ sets of end member grain-size distributions appeared to be successful for both series of artificial mixtures as the modelled end members are very similar to the ‘corresponding’ standards. Nevertheless, some dissimilarities are observed between grain-size distributions of the end members and the standards. These dissimilarities are partly due to ‘inaccuracies’ in the Malvern grain-size data of the microsphere mixtures and partly due to the conservative estimates of the end members.

The additional minor modes (‘inaccuracies’) of the grain-size distributions of polystyrene microsphere end members EM2, EM3 and EM4 are not present in the grain-size distributions of the polystyrene microsphere standards (Fig. 3.3). However, these modes do occur in the binary mixtures of the polystyrene microsphere standards (see Figures 2.4, 2.5 and 2.6 in Chapter 2). Although the secondary modes do truly reflect the presence of a second population of microspheres in the mixtures, the modes are shifted considerably to smaller sizes due to the inability of the Malvern laser-diffraction size analyser to analyse these mixtures accurately (see discussion in Chapter 2). One may conclude that as a consequence of the ‘inaccuracies’ in the data set, the ‘shifted modes’ were assigned to the ‘wrong’ end member. From a mathematical point of view the dissimilarities between the end members and standards are inevitable as the model is based on erroneous data. Compositional variation among the polystyrene microsphere mixtures cannot be attributed to mixing solely, because it also reflects the measurement artefacts.

The end-member grain-size distributions of the sediment mixtures are very similar to the grain-size distributions of the sediment standards S1-S3 (Fig. 3.7). Small systematic deviations between the end members and the standards reflect a systematic ‘deformation’ of the modelled mixing space with respect to the original data set (Fig. 3.10). Due to this systematic departure it appears that small contributions of sediment standard S3 are accidentally assigned to the ‘wrong’ end member EM1. The composition of end member EM3 appears to be ‘too extreme’ as it is not present in the data set. Due to the conservative estimate of the modelled end members, which encloses as many of the data points as tightly as possible, some samples fall outside the modelled mixing space (e.g. standard S1). In view of the intrinsically non-unique solution of the iterative estimation procedure, the test performed here gives very promising results.

An advantage of the end-member modelling approach is that it reduces the size of a data set significantly, e.g. in case of the sediment standard mixtures 32 size classes are compressed

into three mixing coefficients. In spite of the significant size reduction of the data, the complete grain-size distributions of the observations can still be reconstructed, in contrast with a ‘traditional’ description in terms of three graphic or moment measures. The disadvantage of using descriptive statistics to summarise variations in grain-size distributions of the pelagic and hemipelagic siliciclastic sediments of the Arabian Sea are discussed in Chapter 4 (see e.g. Fig. 4.17).

For all six series of binary mixtures of polystyrene microspheres (Fig. 3.5) and sediment standards (Fig. 3.11), a very strong linear correlation ( $r^2 > 0.98$ ) is observed between the proportional contributions of the end members and the proportional contributions of the standards. This indicates that small variations in grain-size distributions are translated efficiently into variations in mixing coefficients by the end-member modelling algorithm. The fact that all regression equations deviate significantly from unity ( $y=x$ ), except maybe the regression equation of the sediment mixtures S1:S2 (Fig. 3.11A), is due to the systematic ‘deformation’ of the end members with respect to the sediment standards.

In case of the sediment mixtures, the proportional contributions of the end members are compared with the calculated proportions (*least-squares fit*) instead of the actual weight proportions (*expected*) of the sediment standards. The deviations between *least-squares fit* and *expected* proportions of the sediment are likely due to the influence of particle shape on laser-diffraction size analysis (see Chapter 2 for details). Given the inescapable particle-shape effects on laser-diffraction measurements it makes only sense to compare the end-member model results with the *least-squares fit* results. In most geological applications of grain-size analysis no *a priori* knowledge is available about the composition and proportional contribution of potential subpopulations (‘end members’) in the sediment. Instead, reconstruction of these subpopulation is the very objective of these studies. The results presented in this paper indicate that end-member modelling of grain-size distributions allows the distinction of subpopulations present within a basin fill. If one is interested in the absolute weight proportions of the modelled end members (e.g. for determination of flux records) one should extract the appropriate sediment fractions from the sediment samples similar to the modelled end members. Mixing experiments like presented in Chapter 2 with these sediment fractions would allow one to calibrate the modelling results. Ideally, calibration of the end-member modelling results must be established individually for sediments of different provenance.

## CONCLUSIONS

1. End-member modelling of grain-size distributions allows the distinction of subpopulations within mixtures of either polystyrene microsphere standards or sediment standards.
2. The number of end members  $q$  required for satisfactory approximation of the two synthetic mixture data sets is accurately estimated by fixing it at  $q$  associated with the inflection point on the ( $q$  - mean  $r^2$ ) curve.
3. All modelled end members have clearly defined modes on their grain-size distributions, whereas none are truly unimodal or of simple analytical form.
4. Modelled end members are very similar to the ‘true’ end members, c.f. the polystyrene microsphere standards and sediment standards.
5. Small systematic deviations between the end members and the standards reflect a systematic ‘deformation’ of the modelled mixing space with respect to the original data set.
6. Variations in the grain-size distributions of the artificial mixtures are translated efficiently into variations in proportional contributions of the end members.

7. Due to the inescapable particle-shape effects on laser-diffraction size analysis, variations in the proportional contributions of end members are only indicative of relative changes in composition.
8. Modelled proportional contribution of end members can potentially be calibrated towards absolute weight proportions via mixing experiments carried out with size fractions extracted from the sediment similar to the modelled end members.

**LATE QUATERNARY EOLIAN AND FLUVIAL SEDIMENT SUPPLY  
TO THE ARABIAN SEA AND ITS PALEOCLIMATIC SIGNIFICANCE:  
AN APPLICATION OF END-MEMBER MODELLING OF  
SILICICLASTIC GRAIN-SIZE DISTRIBUTIONS**

**M.A. Prins<sup>1</sup> and G.J. Weltje<sup>2</sup>**

**ABSTRACT**

Numerical-statistical algorithms are used to model end-member grain-size distributions of pelagic and hemipelagic siliciclastic sediments of the Arabian Sea. The grain-size distributions of sediments from the Oman continental slope, the Owen Ridge, the Pakistan continental slope and the Indus Fan can be adequately described as mixtures of three end members. The spatial variation in relative contribution of the end members is interpreted in terms of transport processes and provenance. In the western Arabian Sea deposition is dominated by two end members which represent ‘proximal’ and ‘distal’ eolian dust. A third end member, which dominates the deposits of the middle Indus Fan, represents fluvial mud deposited from low-density turbidity currents (lutite flows).

At any given location, the temporal changes in the relative contribution of the end members can be interpreted in terms of climate change. The ratio of contributions of the two eolian end members (i.e., the grain-size distribution of the eolian dust) on the Owen Ridge (NIOP492) reflects the strength of the summer monsoon. Deposition on the upper Indus Fan (NIOP458) is dominated by ‘distal’ eolian dust and fluvial mud. The ratio of contributions of eolian and fluvial sediment reflects continental aridity. The ratio of contributions of the two eolian end members (i.e., the grain-size distribution of the eolian dust) on the upper Indus Fan reflects the strength of the winter monsoon. Our reconstruction of the late Quaternary variations in Arabian Sea monsoon climate corresponds well with interpretations of the loess-paleosol sequences on the Chinese Loess Plateau.

**INTRODUCTION**

Cores of late Quaternary deep-sea sediments provide continuous records which can be dated accurately. The terrigenous fraction of deep-sea sediments reflects the supply of sediments produced on the continents surrounding the basin. Such records potentially hold the key to reconstruction of paleoclimatic evolution over geological time spans. In many cases, deep-sea siliciclastics are mixtures of a pelagic component brought in by the wind and a hemipelagic component supplied from the shelf by low-density turbidity currents. Hemipelagic sediment escaping from shelves by transport in semipermanent currents (exemplified by the plumes

---

<sup>1</sup> Institute for Paleoenvironments and Paleoclimate Utrecht (IPPU), Faculty of Earth Sciences, Utrecht University, P.O. Box 80021, 3508 TA Utrecht, The Netherlands

<sup>2</sup> (a) Department of Geo-Energy, Netherlands Institute of Applied Geoscience TNO, P.O. Box 6012, 2600 JA Delft, The Netherlands; (b) Subfaculty of Applied Earth Sciences, Delft University of Technology, P.O. Box 5028, 2600 GA Delft, The Netherlands

seen off deltas) is mainly deposited on the slope and rise. Volumetrically less important are wave and current-induced transport of sediments across the shelf. Most of the hemipelagic material is ultimately derived from fluvial sources, and stored in cones and fans off the major river deltas (McCave, 1972). The flux of river-derived fine-grained siliciclastics is expected to correlate with continental runoff, and thus provides a proxy for continental humidity. Analysis of eolian dust allows estimation of the past aridity of eolian source regions, via flux determinations, and of the intensity of the transporting winds, from grain-size measurements. These two parameters, the grain size and the mass flux of eolian dust, may vary independently (Rea, 1994). So clearly, the source of the sediments must be known before variations within the terrigenous fraction can be interpreted in terms of changes in paleoclimate.

Successful reconstructions of paleoclimate from siliciclastic deep-sea records depend primarily on the capability of distinguishing between sediments of eolian and fluvial origin. In certain cases, use can be made of *a priori* knowledge of the provenance and dispersal patterns to distinguish the two types of sediment input. For instance, Rea and Hovan (1995) characterised the grain-size distribution of 'typical' eolian dust and hemipelagic mud in the abyssal Pacific Ocean by selecting 'end-member samples' based on independent evidence. Eolian samples were selected from slowly accumulating pelagic clays deposited far from land and downwind from the Chinese Loess Plateau. The mineralogy and chemical composition of the samples were identical to the composition of 'local' atmospheric dust and Chinese loess. Hemipelagic mud samples were selected from sites closer to the shore, in settings characterised by moderate to high accumulation rates. Their mineralogy and chemical composition were identical to the composition of adjacent continental-margin sediments of presumed fluvial origin. Both types of 'end-member samples' have modes around 2  $\mu\text{m}$ , but differ strongly in the extent of sorting. Rea and Hovan (1995) argue that the very small grain size of the eolian dust in the Pacific Ocean is the result of the very distant location of the source area, the Chinese Loess Plateau. Eolian dust deposited closer to the source area is much coarser, as shown by Koopmann (1981) and Sarnthein *et al.* (1981, 1982) off north-western Africa and by Sirocko (1991) and Sirocko *et al.* (1991) off the Arabian peninsula. As marine sediments deposited close to an eolian source are likely to be mixtures of eolian dust and hemipelagic mud, Koopmann (1981), Sarnthein *et al.* (1981, 1982) and Sirocko *et al.* (1991) used a somewhat arbitrary cut-off of 6  $\mu\text{m}$  to partition eolian and hemipelagic sediments. They considered the fraction coarser than 6  $\mu\text{m}$  to be of predominant eolian origin, and the fraction smaller than 6  $\mu\text{m}$  to be of fluvial origin (hemipelagic mud).

In many geological applications of grain-size analysis, no *a priori* knowledge is available to distinguish subpopulations of sediments with different provenances. Indeed, reconstruction of provenance and dispersal patterns is the very objective of most studies. The best way to proceed in such cases would be to use an inverse method which does not require detailed assumptions about the geological system being studied. In this study, an inversion algorithm for end-member modelling of compositional data (Weltje, 1994; Weltje, 1997a), developed for 'unmixing' of multi-sourced basin fills in the absence of prior knowledge, is applied to a large data set of grain-size distributions of siliciclastics from the Arabian Sea (NW Indian Ocean). Experiments with artificial sediment mixtures indicate that the algorithm successfully estimates mixing proportions and end-member grain-size distributions in the absence of prior knowledge (see Chapter 3). Our objectives are (1) to unravel late Quaternary deep-sea records of fine-grained siliciclastics which were supplied by multiple sources, and (2) to demonstrate that the reconstructed fluxes and grain-size distributions of the sediments shed by each source provide valuable information about the paleoclimatic evolution of the surrounding continental areas.

*Regional setting.—*

The Arabian Sea constitutes the north-western Indian Ocean and is enclosed by the Somalian and Arabian peninsulas in the west, Iran and Pakistan in the north, and the Indian peninsula in the east (Fig. 4.1). The most conspicuous geological feature in the Arabian Sea is the Indus Fan which occupies the complete central part of the basin. The Indus Fan, with a length of 1600 km and a maximum width of 1000 km, covers an area of approximately 1.1-1.25 million km<sup>2</sup> (McHargue and Webb, 1986; Kolla and Coumes, 1987). It is the second-largest deep-sea fan in the world. The fan developed off the passive continental margin of Pakistan and India, and is bounded by the Chagos-Laccadive Ridge in the east, by the Owen-Murray Ridges in the west, and in the south by the Carlsberg Ridge, which is a portion of the Central Indian Ridge (mid-ocean spreading ridge).

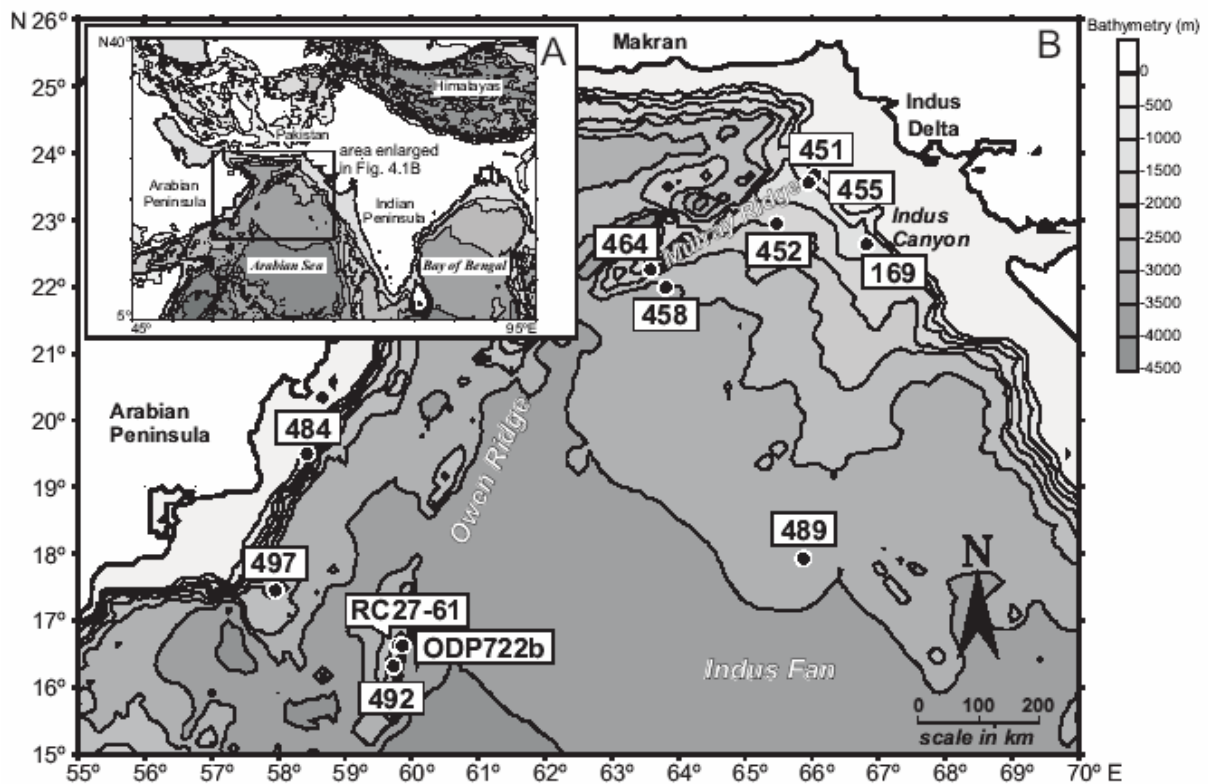


**Fig. 4.1** — Topographic maps of the Arabian Sea and adjacent landmasses. **A:** Inset map shows location of study area. Contour interval 1000 m. **B:** Study area with location of cores. Contour interval 500 m. Topographic data from U.S. National Geophysical Data Center/World Data Center A for Marine Geology and Geophysics.

*Monsoon-driven sedimentation patterns.—*

The Indian Ocean monsoon winds are driven by strong differential heating between the Indian Ocean and the Indian-Asian continents and by the availability of vast amounts of latent heat, collected over the Southern Hemisphere Indian Ocean, which is released over the high elevations of the Indian-Asian landmasses, the area of monsoon precipitation. Differential heating during the northern hemisphere winter causes low surface pressure over the southern Indian Ocean and high surface pressure over the high elevations of the Indian-Asian continents. This Northeast-Southwest pressure gradient is responsible for driving the winter monsoon circulation which results in relatively weak NE monsoon winds over the Arabian Sea. During spring, when the Indian-Asian continents start to heat up, W to NW winds prevail over the Arabian Sea. During peak summer, strong SW monsoon winds develop when the continents become warmer than the oceans and the pressure gradient reverses (Clemens and Prell, 1990; Clemens *et al.*, 1991; Sirocko, 1991).

At present the monsoon climate strongly influences sedimentation processes within the Arabian Sea. The north-westerly winds are responsible for the transport of large quantities of eolian dust from the Arabian peninsula, and minor amounts from Pakistan. The SW monsoon winds supply minor amounts of eolian dust originating from Somalia. The NE monsoon winds transport minor amounts of eolian dust from Pakistan and northern India (e.g. from the Thar desert) towards the Arabian Sea (Sirocko, 1991). Annually, 115-215 million tons of eolian dust is transported from adjacent continents to the Arabian Sea (Sirocko and Sarin, 1989).

The SW monsoon carries large amounts of water vapour which is released as precipitation over the Indian-Asian continent. This precipitation provides the runoff for river systems draining the Himalayas, including the Indus River which flows into the Arabian Sea. Before the Indus River was effectively dammed and channelled, which resulted in almost complete cessation of water and sediment discharge, the river was one of the world's largest in terms of both discharge and sediment load. Before dam construction, somewhat less than 250 million tons of suspended sediment reached the Indus Delta annually (Milliman *et al.*, 1982). Highest discharge coincides with the peak of the rainy season (July), and up to 80 % of the annual cumulative discharge occurs during the SW monsoon summer season (Beg, 1977).

The monsoons cause seasonal reversals in surface circulation of the Arabian Sea resulting in upwelling of nutrient-rich water along the coasts. Nair *et al.* (1989) recorded strong seasonality in particle flux at three sediment trap sites (western, central, eastern Arabian Sea) with peaks during the SW and NE monsoons. High primary productivity during the monsoons resulting from wind-induced mixed layer deepening and the associated nutrient injection into the euphotic zone appeared to be the main factor controlling the observed particle flux pattern. Highest terrigenous particle fluxes are recorded during the SW monsoon season. At the western sediment trap site 80 % of the annual cumulative terrigenous particle flux is recorded during this season. As the western trap site is close to the Arabian peninsula deposition is dominated by eolian dust blown in from the Arabian deserts. At the eastern site 67 % of the annual cumulative terrigenous particle flux is recorded during the summer season and it is dominated by input of Indus River muds.

*Eolian records.—*

During the last decade many studies concerning the marine sediment record in the Arabian Sea have concentrated on the faunal response to wind-induced upwelling (e.g., Clemens and Prell, 1990; Shimmiel *et al.*, 1990; Murray and Prell, 1991; Shimmiel and Mowbray, 1991; Reichert *et al.*, 1998) and on eolian dust transport in relation with the monsoonal climate

(e.g., Sirocko and Sarnthein, 1989; Clemens and Prell, 1990; Clemens and Prell, 1991; Clemens *et al.*, 1991; Krissek and Clemens, 1991; Sirocko, 1991; Sirocko *et al.*, 1991; Sirocko and Lange, 1991; Sirocko *et al.*, 1993; Reichart *et al.*, 1998).

Sirocko (1991) and Sirocko *et al.* (1991) used the percentage of sediment in the size fractions  $>20 \mu\text{m}$  and  $> 6 \mu\text{m}$  to map the distribution pattern of eolian dust in the marine sediment record of the Arabian Sea. The observed NW to SE gradient in eolian dust content indicates that eolian dust is supplied mainly from the Arabian peninsula by the north-westerly winds. The extent of the eolian dust distribution pattern over the ocean was used to approximate the position of the front (intertropical convergence zone) between the north-westerly winds and the SW monsoon. A southward shift of this front during the last glaciation is indicated by changes in grain size and mineralogy (Sirocko *et al.*, 1991; Sirocko and Lange, 1991; Sirocko *et al.*, 1993).

The median grain size and the mass-accumulation rate (MAR) of the terrigenous fraction in two sediment cores (RC27-61, ODP722; for location see Fig. 4.1) retrieved from the Owen Ridge were used as paleoclimatic indicators of SW monsoon wind strength and source-area aridity by Clemens and Prell (1990, 1991), Clemens *et al.* (1991), Murray and Prell (1991) and Clemens *et al.* (1996). Variations in lithogenic MAR appear to be associated with glacial-interglacial cycles with highest fluxes recorded during glacial periods indicating increased source-area aridity. The lithogenic grain size record, exhibiting higher frequency variability (23 ka), has no strong relationship to glacial-interglacial cycles. This suggests that the climate change associated with variability in global ice volume is not a primary factor in determining the strength and timing of the SW monsoon winds. Krissek and Clemens (1991) analysed the bulk mineralogy of the terrigenous fraction of sediments from ODP722 on the Owen Ridge, and concluded that temporal variations in mineralogical composition reflected climate-induced variations in weathering conditions during the late Quaternary.

#### *Fluvial records.—*

In the shelf and slope area near the Indus Delta, three canyon complexes have been recognised on seismics. They merge landward into one extensive erosional zone called the Indus Trough. The canyon complexes served as conduits for sediments supplied by the Indus River. Several large channel-levee systems radiate from each canyon complex, forming a channel-levee complex. The youngest complex comprises the recently active Indus Canyon (McHargue and Webb, 1986; Kolla and Coumes, 1987; Droz and Bellaiche, 1991). The two youngest large channel-levee systems of this complex have been mapped in detail by long range side-scan sonar (GLORIA) (Kenyon *et al.*, 1995). The study of Kenyon *et al.* (1995) resulted in a new scheme for labelling the Indus Fan channels on basis of their relative age. Von Rad and Tahir (1997) presented a very detailed survey, including high-resolution seismic data and sediment cores, of the outer shelf and slope off the Indus Delta, including the Indus Canyon.

Changes in sea level are thought to be the dominant factor controlling turbidite deposition on large deep-sea fan systems. Also for the Indus Fan such process-response is proposed (McHargue and Webb, 1986; Kolla and Coumes, 1987; Kolla and Macurda, 1988; McHargue, 1991; Kenyon *et al.*, 1995; Von Rad and Tahir, 1997; Prins and Postma, Chapter 6). Von Rad and Tahir (1997) indicated that due to the last glacial sea-level lowstand, the Indus Canyon experienced maximum erosion and funnelled turbidity currents to the Indus Fan. Accordingly, Prins and Postma (Chapter 6) concluded that the fall in sea level at  $\sim 25 \text{ }^{14}\text{C ka BP}$  initiated major lobe switching on the middle Indus Fan. The rise of sea level during the last deglaciation ( $\sim 11.5 \text{ }^{14}\text{C ka BP}$ ) cut off the Indus River as the main source of sediment for the middle fan.

#### *Interplay of eolian and fluvial sources.—*

The above observations indicate that the Arabian Sea sediments are mixtures of eolian and fluvial sediments, with the relative contributions of the two types of sediment depending on the location in the basin. At any given location, the relative contributions of materials from both sources are likely to have varied through time as well. Changes in continental aridity resulted in marked changes in the flux of eolian dust transported over the Arabian Sea. Changes in intensity and direction of the SW monsoon, inferred from the eolian dust records of the western Arabian Sea, must have influenced the pattern of precipitation over the landmasses bordering the Arabian Sea to the west (Arabian Peninsula), north (Pakistan) and the east (India). Changes in precipitation within the drainage basins of Indian-Pakistan rivers are expected to have controlled the water discharge and the suspended-sediment load of these rivers in the past as well. However, possible late Quaternary changes in continental runoff and associated fluvial suspended sediment supply to the Arabian Sea are sparsely documented. A suitable place to investigate changes in continental runoff and eolian dust supply by the NE monsoon is the continental margin of Pakistan. Results obtained by detailed analysis of sediment cores from the western, central and northern part of the Arabian Sea are presented in this study.

## MATERIAL AND METHODS

Sediment cores used in this study were collected during the Netherlands Indian Ocean Programme (NIOP) on RV *Tyro* (Van der Linden and Van der Weijden, 1994), and during the SO90 PAKOMIN Expedition on RV *Sonne* (Von Rad *et al.*, 1995). The cores, containing predominantly pelagic and hemipelagic sediments, were obtained from the Oman continental margin (NIOP484, 497), the Owen Ridge (NIOP492), the Pakistan continental slope between the Murray Ridge and the Indus Canyon (NIOP451, 452, 455 and 458) along a slope-perpendicular transect, the eastern levee of the major channel radiating from the Indus Canyon (SO90-169KL), and the levee of a small channel belonging to a large channel-levee system (system B, according to Kenyon *et al.*, 1995) on the middle Indus Fan (NIOP489). Figure 4.1 and Table 4.1 provide detailed information on the core locations.

Unsplit 1-m-sections of cores NIOP458 and NIOP492 were logged at 1-2 cm intervals with a Bartington Instruments MS2 pass-through loop sensor mounted on a GEOTEC automated multisensor corelogger in order to measure the bulk magnetic susceptibility. Samples were taken from the splitted 1-m-sections at approximately 5 to 10 cm intervals. Fixed volume samples were taken with a syringe, dried and weighted for measurement of dry-bulk density ( $\text{g/cm}^3$ ). One set of subsamples was washed and sieved to collect the fauna; another set of dried subsamples was used for analysis of the elemental chemical composition of the sediment (ICP). Wet subsamples were used for analysis of the grain size. The total carbonate content (biogenic and detrital) was calculated from the total Ca concentration (obtained from ICP analyses), using a correction for clay-derived Ca which works well for carbonate-rich sediments:  $\text{CaCO}_3 = 2.5(\text{Ca}_{\text{tot}} - (\text{Ca}/\text{Al}_{\text{clay}} \times \text{Al}_{\text{tot}}))$ , where  $\text{Ca}/\text{Al}_{\text{clay}}$  is 0.345 (Turekian and Wedepohl, 1961; Shimmiel *et al.*, 1990).

Prior to the grain-size analysis, carbonate and organic carbon (only in organic-carbon-rich sediments) were removed from the sediment samples by treatment with excess HCl and H<sub>2</sub>O<sub>2</sub>. Total dispersion of the sample was ensured by using a sonic dismembrator attached to the tank containing the suspended sample. The grain-size distribution of the siliciclastic fraction of 1102 samples was measured on a Malvern 2600 laser-diffraction size analyser using a lens with 100 mm focal length. This configuration provided measurements in 32 discrete size classes between 0.5 and 188 µm (equivalent volume diameter; see Table 2.1 in Chapter 2). The three coarsest size classes contain on average a very small proportion of the total mass. They were amalgamated into a single class to reduce the number of input variables for the end-member modelling algorithms to 30. A brief summary of the end-member modelling technique of Weltje (1994, 1997a) is given in Chapter 3.

The δ<sup>18</sup>O curves of NIOP458 and NIOP492 are based on the analyses of 20 hand-picked specimens of the planktonic foraminifer *Neogloboquadrina dutertrei* (150-595 µm sieve fraction) per sample. The oxygen-isotopic composition of the carbonate shells was measured on a mass spectrometer. Age models have been constructed for cores NIOP458 and NIOP492 based on the correlation of the δ<sup>18</sup>O records with the δ<sup>18</sup>O record of core NIOP464 from the Murray Ridge (Fig. 4.1). The age model of core NIOP464 was taken from Reichart *et al.* (1997). Linear sedimentation rates (LSR, in cm/ka) were assumed between the age calibration points. Total mass accumulation rates (total MAR = LSR x DBD; MAR in g/cm<sup>2</sup>ka) were calculated using the dry-bulk density (DBD, in g/cm<sup>3</sup>) of the sediment. Fractionated MAR's, i.e., carbonate MAR and non-carbonate (siliciclastic) MAR, were determined by multiplying the total MAR with the carbonate fraction and with the siliciclastic fraction (1 - carbonate fraction).

**TABLE 4.1 — SEDIMENT CORES USED IN THIS STUDY**

Core number	Position (Lat. N, Long.E)	Area	Water depth (m)	Core length (m)	Number of samples
NIOP451	23°40'.5, 66°03'.0	upper Pakistan continental slope	542	17.06	163
NIOP452	22°56'.9, 65°28'.4	lower Pakistan continental slope	1992	12.96	91
NIOP455	23°33'.4, 65°57'.0	middle Pakistan continental slope	1002	14.50	117
NIOP458	21°59'.4, 63°48'.7	upper Indus Fan	3001	16.31	163
SO90-169KL	22°38'.5, 66°49'.3	channel levee, Indus Canyon	1283	11.65	114
NIOP489	17°56'.0, 65°52'.5	channel levee, middle Indus Fan	3375	10.24	85
NIOP484	19°29'.8, 58°25'.7	upper Oman continental slope	516	5.06+0.61	75
NIOP492	16°19'.0, 59°43'.6	Owen Ridge	2400	9.40	189
NIOP497	17°27'.0, 57°57'.6	middle Oman continental slope	1885	8.83	105

## RESULTS

*Estimating the Number of End Members*

The grain-size distributions of the pelagic and hemipelagic siliciclastic sediments ( $n=1102$ ) from the Arabian Sea were used as input data for the end-member modelling algorithms. The minimum number of dimensions (end members  $q$ ) required for a satisfactory approximation of the data is estimated by calculating the coefficients of determination. The coefficients of determination represent the proportions of the variance of each variable (i.e., grain-size class) that can be reproduced by the approximated data. This proportion is equal to the squared correlation coefficient ( $r^2$ ) of the input variables and their approximated values (see Chapter 3).

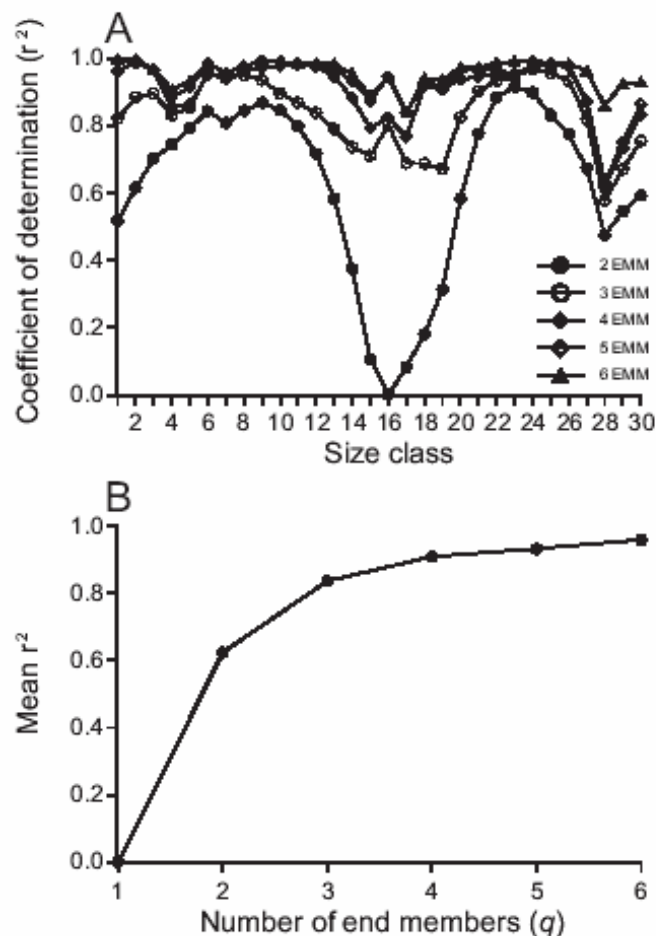


**Fig. 4.2** — Goodness-of-fit statistics used to estimate the number of end members (see text for discussion). **A:** Coefficients of determination for each size class. **B:** Mean coefficient of determination across size classes. At least three end members are needed to reproduce all variables adequately; a two-end-member model shows distinct lack of fit in several size ranges. Use of four or more end members hardly improves the goodness-of-fit relative to a three-end-member model.

Figure 4.2A illustrates the distribution of the coefficients of determination across the grain-size classes for different numbers of end members. Two size ranges are poorly reproduced by a two-end-member model: classes 13-20 and 27-30. The coefficients of determination for classes 27-30 are not weighted heavily in choosing the preferred end-member model, because the mass in the coarse tails of the grain-size distributions comprises only a small fraction of the total mass in the data set. Reproducibility of the other grain-size range (classes 13-20) by

the mixing model is considered to be of much greater importance, because this size range contains a considerable proportion of the total sediment mass. All of the 30 variables except size class 28 are adequately reproduced by a three-end-member model, as indicated by their coefficients of determination which exceed 0.6 (equivalent to a correlation coefficient of 0.77).

The mean coefficient of determination across the grain-size classes (Fig. 4.2B) increases when the number of end members is increased. The mean coefficient of determination for a three-end-member model is 0.83, i.e., on average 83% of the variance in each grain-size class can be reproduced. A four-end-member model reproduces on average 90% of the input variances. The mean coefficient of determination increases only slightly for models with more than four end members. In conclusion, the goodness-of-fit statistics suggest that a three or four-end-member model provides a reasonable choice in view of the contradictory requirements of parsimony on the one hand (i.e., a minimal number of end members) and reproducibility on the other hand.

### *Grain-Size Distributions of End Members*

Three and four-end-member solutions were constructed to provide more insight into the nature of compositional variation in the data. The modelled end-member grain-size distributions for both models are shown in Figure 4.3 and the data are given in Table 4.2. A conspicuous result of the unmixing procedure is that all end members have a clearly defined dominant mode, whereas none are truly unimodal or of simple analytical form. This shows that the covariance structure of the data allows the extraction of subpopulations with fairly 'natural' and 'sensible' grain-size distributions.

The first end members (EM1) of both models have a modal grain size of  $\sim 50 \mu\text{m}$  (class 24). End member 3 (EM3) of the three-end-member model is almost identical to end member 4 (EM4) of the four-end-member model. Both have a modal grain size of  $\sim 5 \mu\text{m}$  (class 8). End member 2 (EM2) of the three-end-member model has a bimodal grain-size distribution with modes around 14 and 22  $\mu\text{m}$  (classes 15 and 18). End members 2 and 3 (EM2 and EM3) of the four-end-member model have modes at 22 and 9  $\mu\text{m}$  (classes 12 and 18).

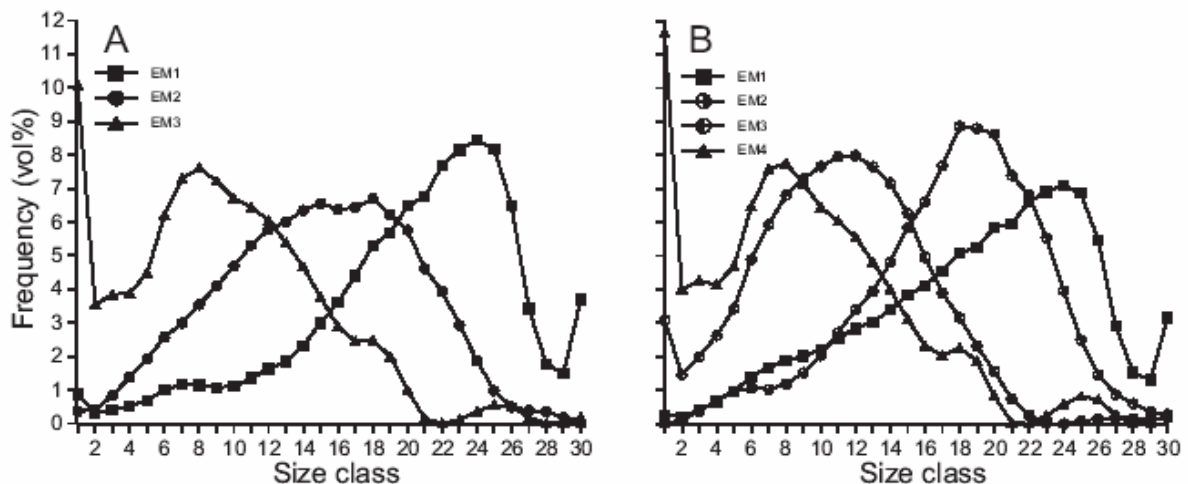


**Fig. 4.3** — Modelled end members of Arabian Sea pelagic and hemipelagic siliciclastic sediments (see also Table 4.2). **A:** three-end-member model. **B:** four-end-member model.

**TABLE 4.2 — MODELLED END MEMBERS OF ARABIAN SEA PELAGIC AND HEMIPELAGIC SILICICLASTIC SEDIMENTS**

Size class	Three-end-member model			Size class	Four-end-member model			
	EM1 (%)	EM2 (%)	EM3 (%)		EM1 (%)	EM2 (%)	EM3 (%)	EM4 (%)
1	0.86	0.36	10.07	1	0.26	0.00	3.09	11.64
2	0.32	0.41	3.54	2	0.21	0.11	1.46	4.01
3	0.40	0.83	3.84	3	0.40	0.36	2.00	4.25
4	0.51	1.38	3.88	4	0.66	0.70	2.62	4.14
5	0.69	1.92	4.48	5	0.96	0.96	3.43	4.69
6	1.01	2.57	6.21	6	1.41	1.07	4.89	6.48
7	1.16	2.98	7.30	7	1.68	1.02	5.94	7.59
8	1.15	3.54	7.61	8	1.88	1.18	6.81	7.77
9	1.07	4.09	7.22	9	2.01	1.52	7.30	7.16
10	1.10	4.68	6.72	10	2.20	2.03	7.66	6.46
11	1.35	5.31	6.44	11	2.54	2.72	7.96	6.04
12	1.63	5.78	6.06	12	2.84	3.39	7.98	5.56
13	1.86	6.01	5.39	13	3.03	3.94	7.66	4.81
14	2.32	6.35	4.66	14	3.39	4.80	7.17	4.01
15	2.99	6.56	3.75	15	3.83	5.84	6.27	3.11
16	3.61	6.38	2.88	16	4.11	6.62	4.96	2.33
17	4.41	6.44	2.44	17	4.55	7.68	3.89	2.04
18	5.30	6.70	2.47	18	5.10	8.86	3.15	2.25
19	5.68	6.22	2.00	19	5.25	8.80	2.31	1.87
20	6.48	5.76	0.99	20	5.85	8.63	1.56	0.83
21	6.76	4.61	0.15	21	5.95	7.40	0.74	0.03
22	7.70	3.93	0.00	22	6.63	6.82	0.26	0.00
23	8.15	2.93	0.12	23	6.91	5.54	0.01	0.24
24	8.45	1.87	0.36	24	7.11	3.96	0.00	0.58
25	8.18	0.98	0.54	25	6.87	2.50	0.08	0.82
26	6.49	0.49	0.49	26	5.46	1.46	0.14	0.72
27	3.41	0.39	0.18	27	2.91	0.87	0.19	0.26
28	1.76	0.35	0.00	28	1.53	0.60	0.16	0.00
29	1.50	0.18	0.03	29	1.30	0.35	0.13	0.04
30+	3.70	0.00	0.17	30+	3.15	0.28	0.18	0.27

The fact that both models are about equally good in approximating the observed variation in the data set is partly a consequence of the similarity of their coarsest and finest end members. The minimal improvement in goodness-of-fit is further clarified by expressing the end members of the three-end-member model as mixtures of the end members of the four-end-member model (Fig. 4.4A). The least-squares mixing coefficients are shown in Figure 4.4B. For instance, EM2 of the three-end-member model is closely approximated by a mixture of 58% EM2 and 42% EM3 of the four-end-member model. In the four-end-member model, the EM2:EM3 ratio varies on average only slightly about this mean value. Consequently, the marginal improvement of the goodness-of-fit reflects the addition of end members that explain only a small fraction of the compositional variation in the data. As there are no reasons to prefer the four-end-member model, we will now investigate the applicability of the three-end-member model.

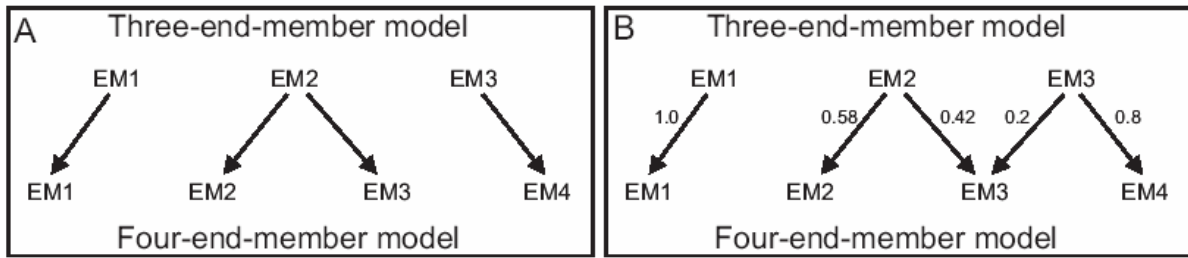


**Fig. 4.4 — A: Most likely combinations of the end members of the three and four-end-member models. B: Least-squares mixture coefficients.**

*Three-End-Member Model*

*Comparison between observed and modelled grain-size distributions.—*

In the ternary mixing model, spatial and temporal changes in grain-size distributions are expressed as changes in the relative abundances of the end members. In spite of the significant size reduction of the data set (compressing 30 size classes into three mixing coefficients), the complete grain-size distribution can still be reconstructed, in contrast with a ‘traditional’ description in terms of three graphic or moment measures. The goodness-of-fit of each modelled grain-size distribution can be visualised by comparing it to the observed grain-size distribution. Figure 4.5 shows the modelling results of two samples from core NIOP492. Sample NIOP492/35 (Fig. 4.5A) is composed of EM2 (66%) and EM3 (34%), while sample NIOP492/110 (Fig. 4.5B) is a mixture of all three end members (23% EM1, 57% EM2, 20% EM3).

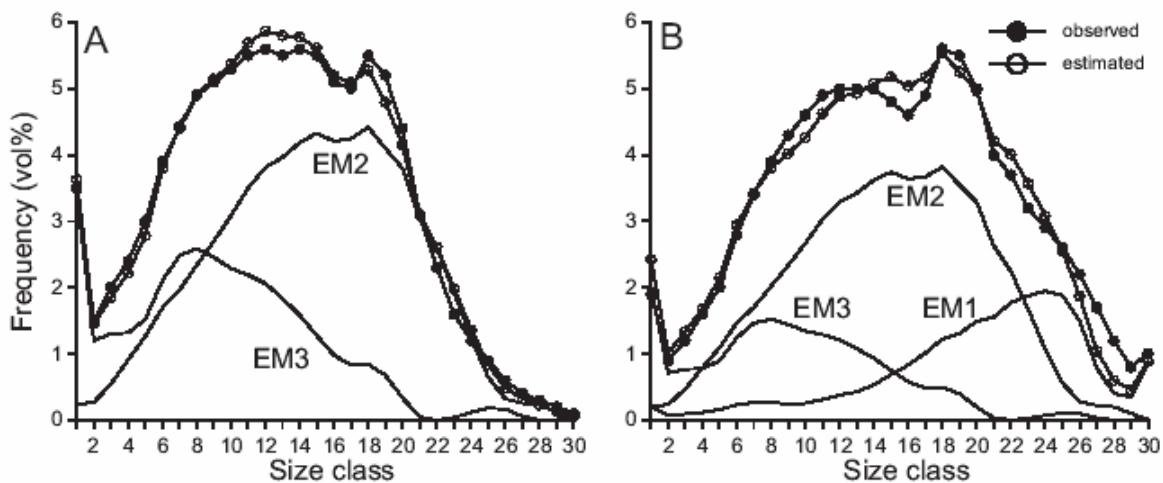


**Fig. 4.5 — Approximation of observed grain-size distributions by the three-end-member model. A: Estimated composition of sample NIOP492/35: 0% EM1, 66% EM2 and 34% EM3. B: Estimated composition of sample NIOP492/110: 23% EM1, 57 % EM2 and 20 % EM3.**

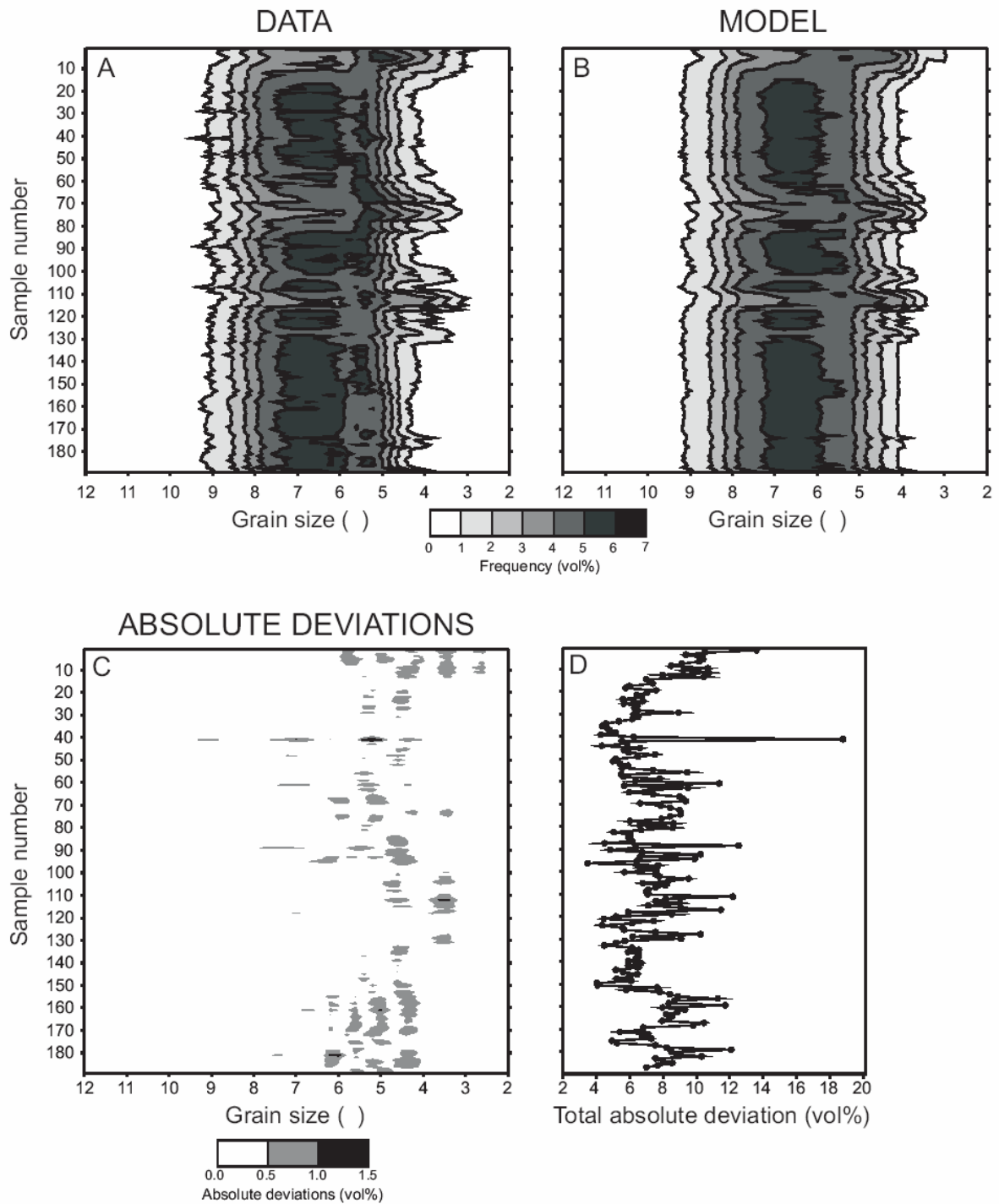


**Fig. 4.6** — Modelling results of core NIOP492. A: Grain-size spectra diagram of observed grain-size distributions (vol% per  $0.2\phi$  interval). B: Estimated grain-size distributions according to the three-end-member model. Note smoothing effect due to reduced variance of the mixing model. C: Contour map of absolute deviations between data and model. D: Summed total absolute deviation per sample.

Grain-size spectra diagrams (c.f. Dowling, 1977) of the observed and modelled records of core NIOP492 are shown in Figures 4.6A and 4.6B. These diagrams are contour maps of the mass proportions per size class in the space-size domain. In this particular example ‘space’ refers to the sample numbers plotted in stratigraphic order (sample 1 is top and sample 189 is base of core NIOP492). The size domain has been subdivided into equal size intervals on a logarithmic scale (widths  $0.2 \phi$ ; units of mass are expressed as volume percentages per size interval).

The modelled grain-size spectra diagram (Fig. 4.6B) is somewhat less irregular than the observed grain-size spectra diagram (Fig. 4.6A). This reflects the reduction of the variance, which has simplified the grain-size distributions and (provided that the basic assumptions are valid and the model parameters have been successfully estimated) suppressed the noise in the observations. The overall pattern observed in the space-size domain can be fairly well reproduced with three end members. Figure 4.6C shows the ‘residuals’ in the space-size domain, i.e., the difference between the observed and modelled grain-size distributions in terms of absolute deviations (vol% per size interval). The summed absolute deviations for each observation (Fig. 4.6D) are of the same order of magnitude as typical sampling and measurement errors for the studied core material, which have been determined from replicate analyses. It is concluded that the three-end-member model successfully reproduces the compositional variation in the data.

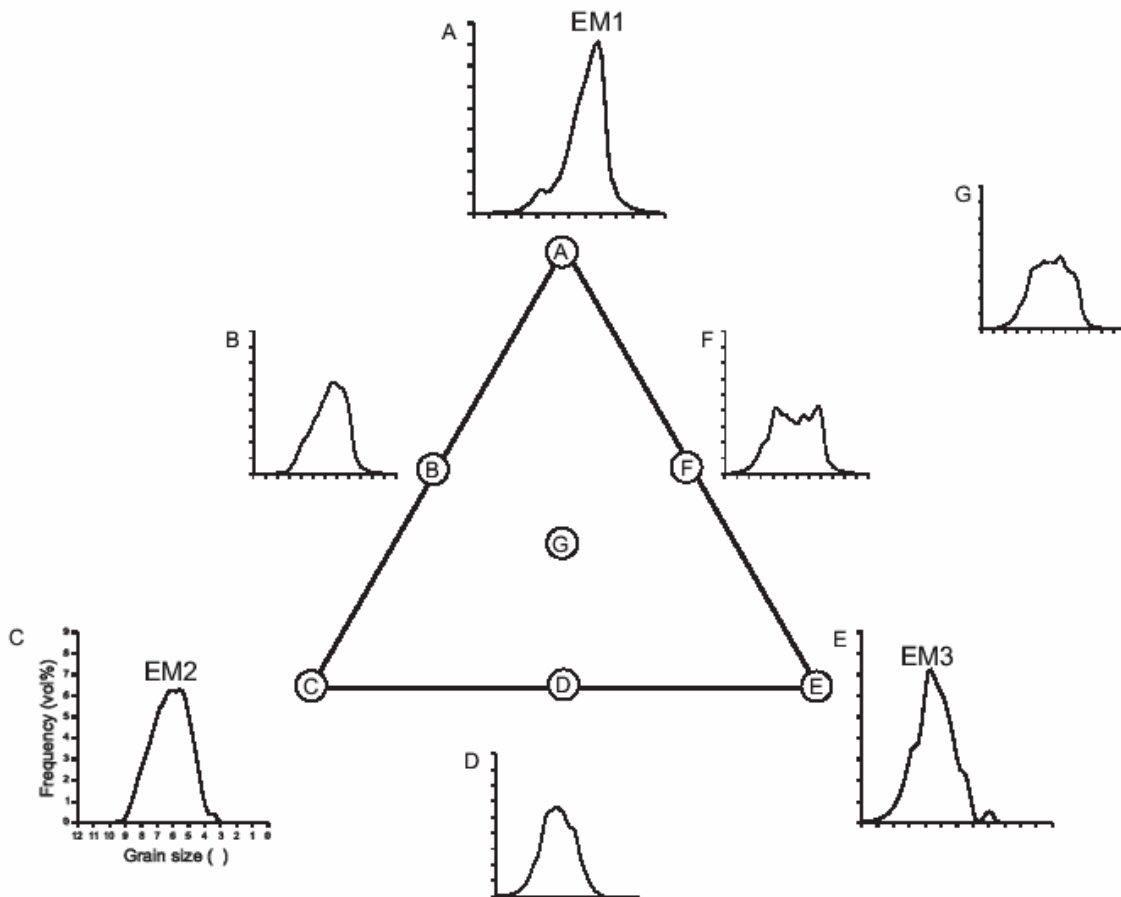


**Fig. 4.7 — Three-end-member model plotted in ternary diagram, showing grain-size distributions of end members (A, C, E) and hypothetical mixtures (B, D, F, G).**

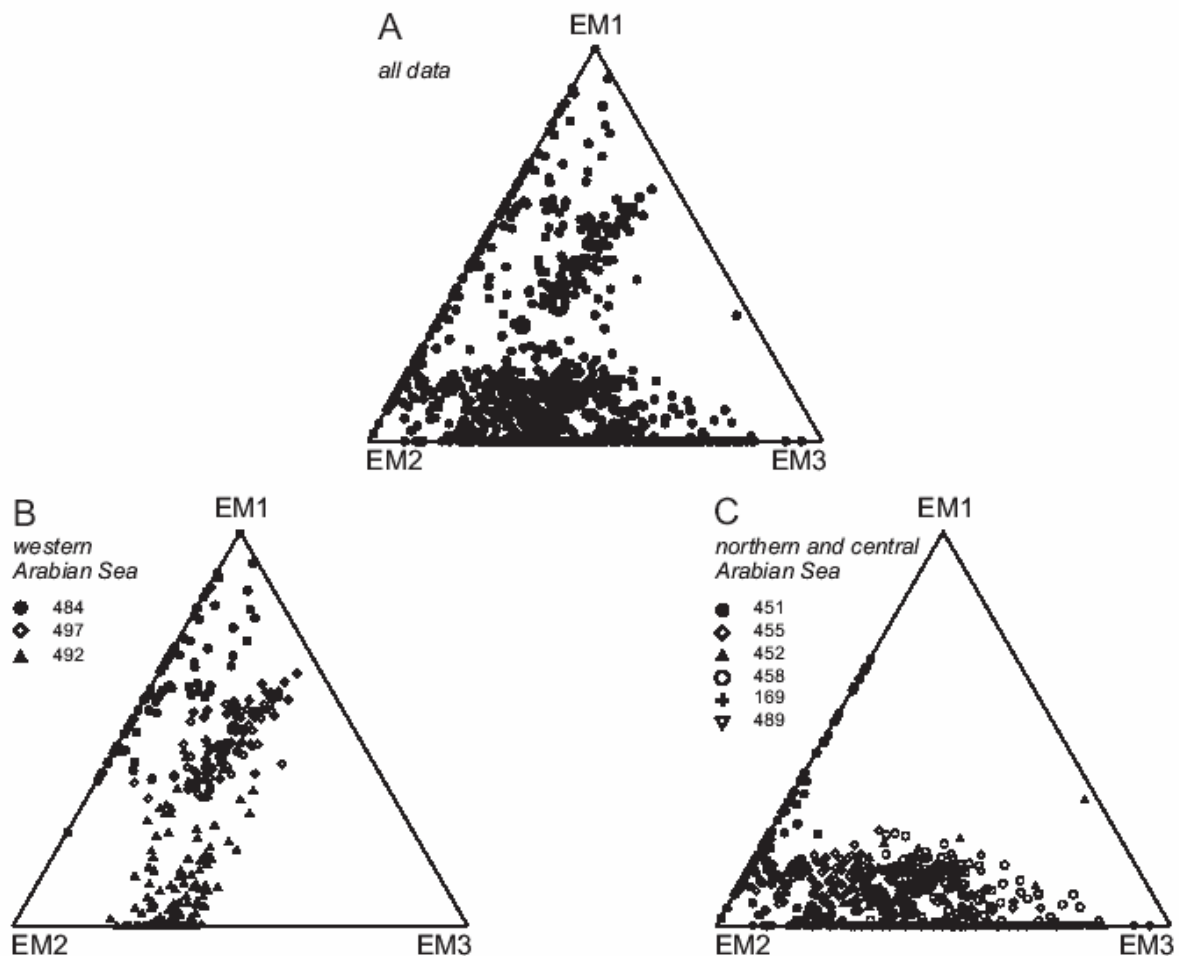


Fig. 4.8 — A: Mixing model of the 1102 Arabian Sea sediment samples. B: Binary mixing of end members EM1 and EM2 prevails in the western Arabian Sea sediments (NIOP484, 492, and 497). C: Binary mixing of end members EM2 and EM3 prevails in the northern and central Arabian Sea sediments (NIOP451, 452, 455, 458, 489, and SO90-169KL).

*Spatial variations in mixing coefficients.—*

The total range of compositional variation has been visualised in a ternary diagram (Fig. 4.7) of which the modelled end members form the three vertices (hypothetical observations A, C, E). Three hypothetical binary mixtures are shown as observations B, D, F, and a ternary mixture as observation G. The individual data points of the estimated compositions of the 1102 samples form a large scatter in the ternary mixing space (Fig. 4.8A). Binary mixtures of EM1 and EM3 (cf. hypothetical observation F in Figure 4.7) are practically absent. When the data of the cores from the two geographical regions, the western and the northern Arabian Sea, are plotted separately in ternary diagrams some clear trends become visible.

Samples from cores NIOP484, NIOP492 and NIOP497 are described as mixtures of predominantly EM1 and EM2 as they plot on the left side of the ternary diagram (Fig. 4.8B). The sediments in the cores from the northern Arabian Sea (NIOP451, NIOP452, NIOP455, NIOP458, and SO90-169KL) are described as mixtures of predominantly EM2 and EM3 (Fig. 4.8C). The same applies to core NIOP489 from the central part of the Arabian Sea.

Spatial changes in average sediment composition have been visualised by plotting the 90-95-99% confidence regions of the population means of the sediments sampled in each core

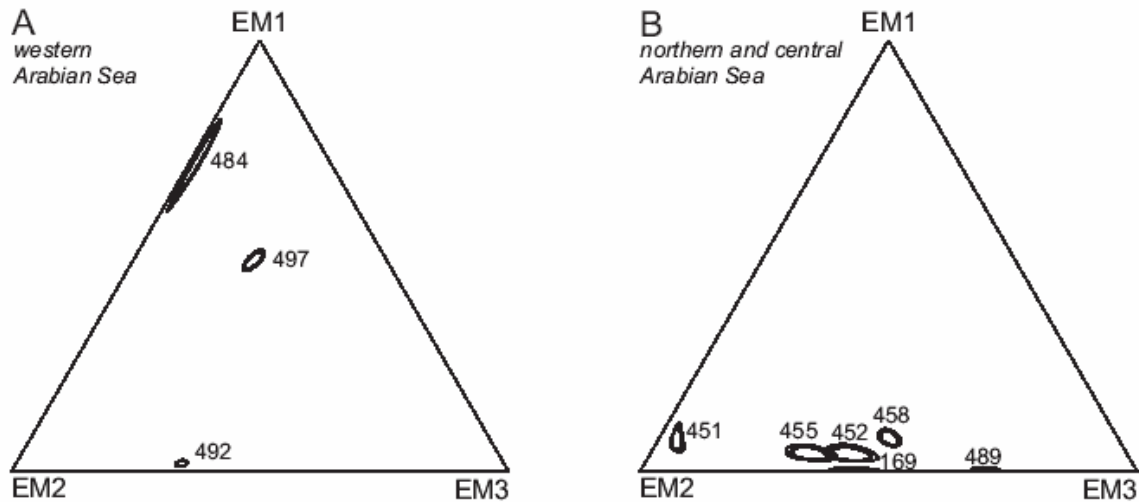


**Fig. 4.9** — Confidence regions (90-95-99%) of the population means of cored sediments in ternary mixing space. A: Population means of sediments from the western Arabian Sea (NIOP484, 492, and 497). B: Population means of sediments from the northern and central Arabian Sea (NIOP451, 452, 455, 458, 489, and SO90-169KL).

(using an algorithm described by Weltje, 1997b). Figure 4.9A shows the confidence regions associated with cores from the western Arabian Sea, and Figure 4.9B those from the northern and central parts of the Arabian Sea. The grain-size population means at the sites of cores NIOP484, NIOP492 and NIOP497 differ significantly from one another at a 99% confidence level as they do not overlap one another (Fig. 4.9A). In the transect NIOP484-497-492 (W-E, shallow-deep, proximal-distal; Fig. 4.1) the average composition changes from EM1-dominated sediments towards EM2-dominated sediments.

The population means of the grain-size distributions at core sites in the northern and central Arabian Sea differ significantly from one another at a 99% confidence level, except those of cores NIOP452 and NIOP455 which differ significantly from one another at a 90% confidence level (Fig. 4.9B). In the transect NIOP451-455-452-458 (N-S, shallow-deep, proximal-distal; Fig. 4.1) the ratio EM2:EM3 gradually decreases, reflecting a spatial trend in the composition of the sediments. Sediments from core SO90-169KL, obtained from the levee south of the Indus Canyon, have relatively low EM2:EM3 ratios and low EM1 content compared with NIOP455 which was obtained from the same water depth. Especially the sediments from core NIOP489 have high proportions of EM3. In this core, samples are mixtures of EM2 and EM3 exclusively.

*Interpretation of end members.—*

End members of a series of grain-size distributions may be related to two kinds of processes (Syvitski, 1991b). When two end-member grain-size distributions are mixed in various proportions they will provide a suite of sediment samples with attributes falling between these end members. Such sediments could represent true mixtures of materials supplied by different sources, which have been transported by independent mechanisms. However, end-member distributions may also represent the beginning and end of a selective process of transport and deposition. For instance, selective mechanisms operating during unidirectional transport and deposition produce sediments whose grain-size distributions change systematically with distance from the source. Unmixing of such data sets results in ‘proximal’ and ‘distal’ end members. Hence, the number of actual sediment sources is per definition equal to or less than the number of end members.

Different spatial trends in sediment composition have been recognised in both the western and northern Arabian Sea. Along the western Arabian Sea transect the average composition changes basinward from EM1-dominated sediments to EM2-dominated sediments. Along the northern Arabian Sea transect the average composition changes basinward from EM2-dominated sediments to EM3-dominated sediments. Both trends represent basinward fining.

The compositional trend along the western transect is illustrated by the grain-size distributions of four representative samples of approximately the same age (early Holocene, ~8-10 ka BP) from cores NIOP484, NIOP497, NIOP492 and NIOP489 (Fig. 4.10). Analysis of the chemical composition and mineralogy of selected size ranges of these four samples (Chapter 6, and unpublished data) reveals a high degree of compositional similarity, which strongly suggests that the sediments were derived from the same source. The presence of the clay mineral palygorskite in each of the samples indicates that the dominant source of the terrigenous fraction is the Arabian peninsula (Kolla *et al.*, 1976; Sirocko and Lange, 1991). The absence of large river systems debouching in the western Arabian Sea, coupled with the location of the cores (NIOP492 on the Owen Ridge and NIOP489 on the middle Indus Fan) allow us to exclude the possibility that the bulk of the sediment of Arabian provenance represents anything else than eolian dust. The NIOP489 sample of eolian origin was taken from a calcareous ooze unit which drapes the Pleistocene river-derived sediments of the Indus Fan (see Chapter 6). The basinward fining trend is expressed as changes in the relative proportions of the end members. The ratio EM1:EM2 decreases while the proportion of EM3 increases when going from the Oman continental margin towards the Indus Fan. The 'proximal-distal' fining trend most likely represents the result of preferential settling of the coarse fraction during eolian transport from the desert source. EM1 may thus be interpreted as 'proximal', relatively coarse-grained eolian dust and EM2 as 'distal', relatively fine-grained eolian dust. These end members thus represent the 'beginning' and 'end' of a depositional process (cf. Syvitski, 1991b).

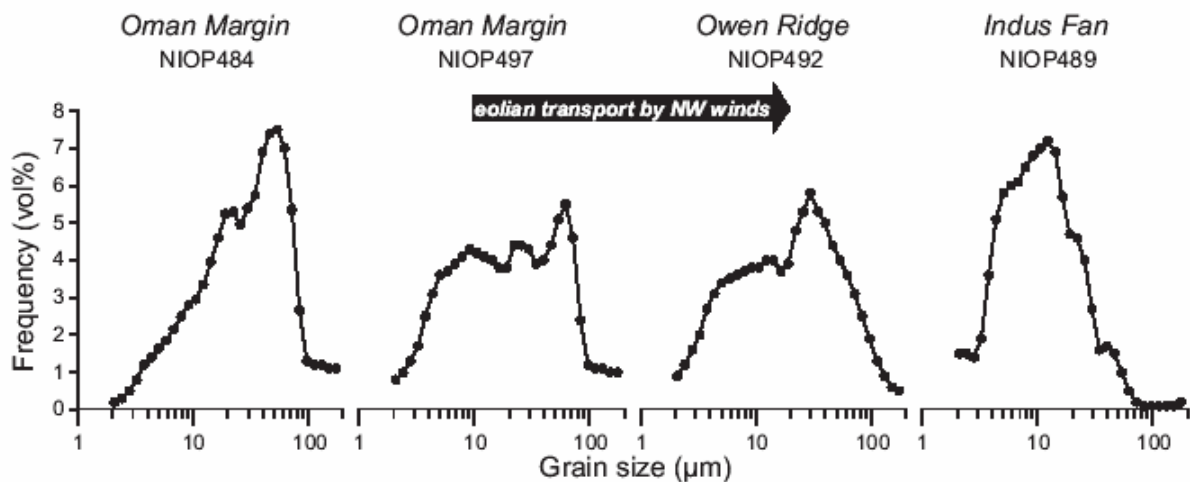


**Fig. 4.10** — Grain-size distributions of four early Holocene eolian-dust-dominated samples obtained along a transect approximately perpendicular to the Arabian coast. Progressive fining of the sediment in a downwind direction is reflected in the relative proportions of the end-members. Compositions of the samples expressed as EM1/EM2/EM3: NIOP484/60 79/21/0; NIOP497/4 53/20/27; NIOP492/4 46/34/20; NIOP489/117 0/59/41.

The Pleistocene channel-levee sediments of the middle Indus Fan (NIOP489) are dominated by contributions of EM3 muds, which were deposited at very high rates ( $\sim 30 \text{ g/cm}^2/\text{ka}$ ). Mineralogy and chemical composition of the turbidite muds are identical to those of sediments obtained from the Indus Canyon, indicating that the dominant source of the terrigenous fraction is the Indus River (see Chapter 6). Turbidity currents supplied huge amounts of river-derived sediments through the Indus Canyon, which were eventually deposited on the middle Indus Fan within the main sediment depocentres (Kolla and Coumes, 1987; Kenyon *et al.*, 1995). The finest fractions are deposited out of the low-density low-velocity ‘tails’ of the turbidity currents within and well outside the main depocentres of the river-derived silts and sands. In view of the location of core NIOP489 it is concluded that EM3 represents ‘fluvial mud’ supplied by the Indus River and deposited out of low-density turbidity currents. The EM3 muds deposited on the continental slope and upper Indus Fan, west of the Indus Canyon, are probably derived from the Pakistan shelf area. These muds may have been supplied across the shelf directly by the Indus River, most likely during flood events, or as wave-induced sediment resuspension clouds. Resuspension of shelf muds is probably also the most likely process of dispersal of the EM3 muds in the western Arabian Sea where river input is insignificant.

In summary, sediments obtained from the western Arabian Sea are essentially mixtures of coarse and fine-grained eolian dust (EM1 and EM2), whereas sediments from the northern Arabian Sea are essentially mixtures of fine-grained eolian dust and fluvial mud (EM2 and EM3). The presence of multiple grain-size trends in the same basin fill clearly indicates that temporal variations in grain size must be interpreted with great care. The ‘mixing structure’ of the Arabian Sea sediments suggests that paleoclimatic information may be extracted from the grain-size records as follows. The ratio EM1:EM2 is an indicator of the grain size of the eolian dust, and may therefore be used as a proxy for variations in paleo-wind speed. The ratio (EM1+EM2):EM3 indicates the relative importance of the mode of sediment transport during time of deposition, i.e., eolian transport versus low-density turbidity transport. The input of eolian dust increases during periods with an arid continental climate, whereas the input of fluvial mud increases during periods with a humid continental climate. Consequently, changes in the ratio (EM1+EM2):EM3 may be used as a proxy for changes in continental aridity.

#### *Comparison of Records from the Upper Indus Fan and the Owen Ridge*

##### *Sediment flux.—*

Temporal changes in the flux and composition of sediments from the western and northern Arabian Sea will be illustrated for two sediment cores: NIOP458 from the upper Indus Fan and NIOP492 from the Owen Ridge. The *Neogloboquadrina dutertrei*  $\delta^{18}\text{O}$  records of cores NIOP458 and NIOP492 were correlated with the  $\delta^{18}\text{O}$  record of core NIOP464 in order to convert depth into age (Fig. 4.11). This correlation shows that the sedimentary records in core NIOP492 and NIOP458 span the last 186 ka (isotopic stages 1 to 6) and 208 ka (isotopic stages 1 to 6, and part of isotopic stage 7).

The carbonate records of cores NIOP458 and NIOP492 show some marked differences. The carbonate content in core NIOP458 varies between 9-50 wt% (Fig. 4.12A), while in core NIOP492 it varies between 45-75 wt% (Fig. 4.12B). The carbonate content on the Owen Ridge (NIOP492) tend to be highest during the interglacial stages (1, 3, 5). A very good anti-correlation between magnetic susceptibility and carbonate content can be observed in core NIOP492, whereas in core NIOP458 this correlation is less clear.

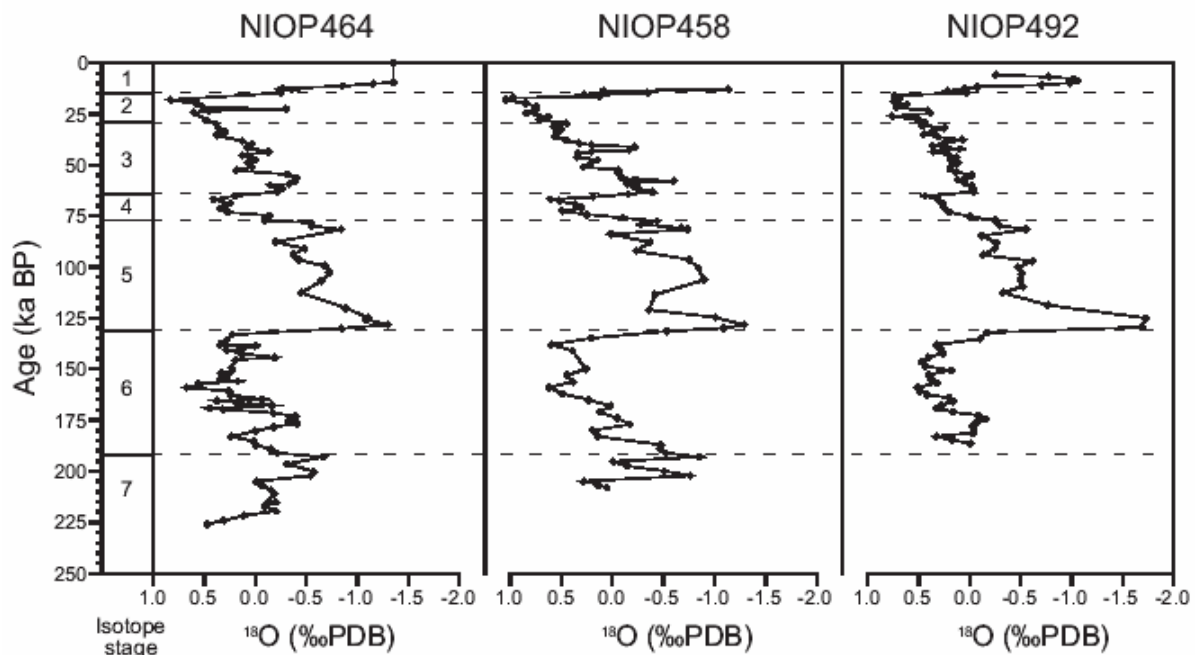


Fig. 4.11 — Age models of cores NIOP458 and NIOP492 based on correlation of the  $\delta^{18}\text{O}$  (*N. dutertrei*) records with core NIOP464.

In this study, the contribution of terrigenous material to the sediment was simply taken as total mass minus carbonate mass. This method underestimates the proportion of terrigenous material in the presence of detrital carbonate, and overestimates the proportion of terrigenous material in the presence of biogenic opal and organic carbon. Sirocko *et al.* (1991) showed that the contribution of detrital carbonates to the sediment very close to the coast of Oman reaches maxima of >10 %, but rapidly decreases basinward. The average contribution of detrital carbonates to the sediment is estimated as less than 5% in the region where cores NIOP458 and NIOP492 were obtained. According to Murray and Prell (1991), opal and organic carbon are only minor components of the Owen Ridge sediments. Organic carbon content varies from 0.4 % to 2.0 %. Opal content varies from 0.5 to 2.5 %, with distinct maxima occurring in interglacials. SEM inspection of selected grain-size fractions of samples from NIOP492 showed that the bulk of the biogenic opal is confined to the sand fraction (> 63  $\mu\text{m}$ ). In core NIOP458 the organic carbon content varies between 0.2 and 2.3 % (Reichart *et al.*, 1997), and SEM inspection shows that the opal content is insignificant. All these observations indicate that our approximation of the terrigenous contribution is reasonably accurate.

Total linear sedimentation rates (LSR;  $\text{cm/ka}$ ) and total mass-accumulation rates (total MAR;  $\text{g/cm}^2/\text{ka}$ ) are highest during glacials at both sites. The same holds for the carbonate MAR and siliciclastic MAR. While the carbonate MAR are about equal at both sites throughout the studied time period, the siliciclastic MAR is about three times higher at site NIOP458 when compared with the values recorded at site NIOP492. Hence, the carbonate content may be interpreted as a dilution signal (c.f. Shimmield *et al.*, 1990), rather than an indicator of dissolution or changes in surface productivity.

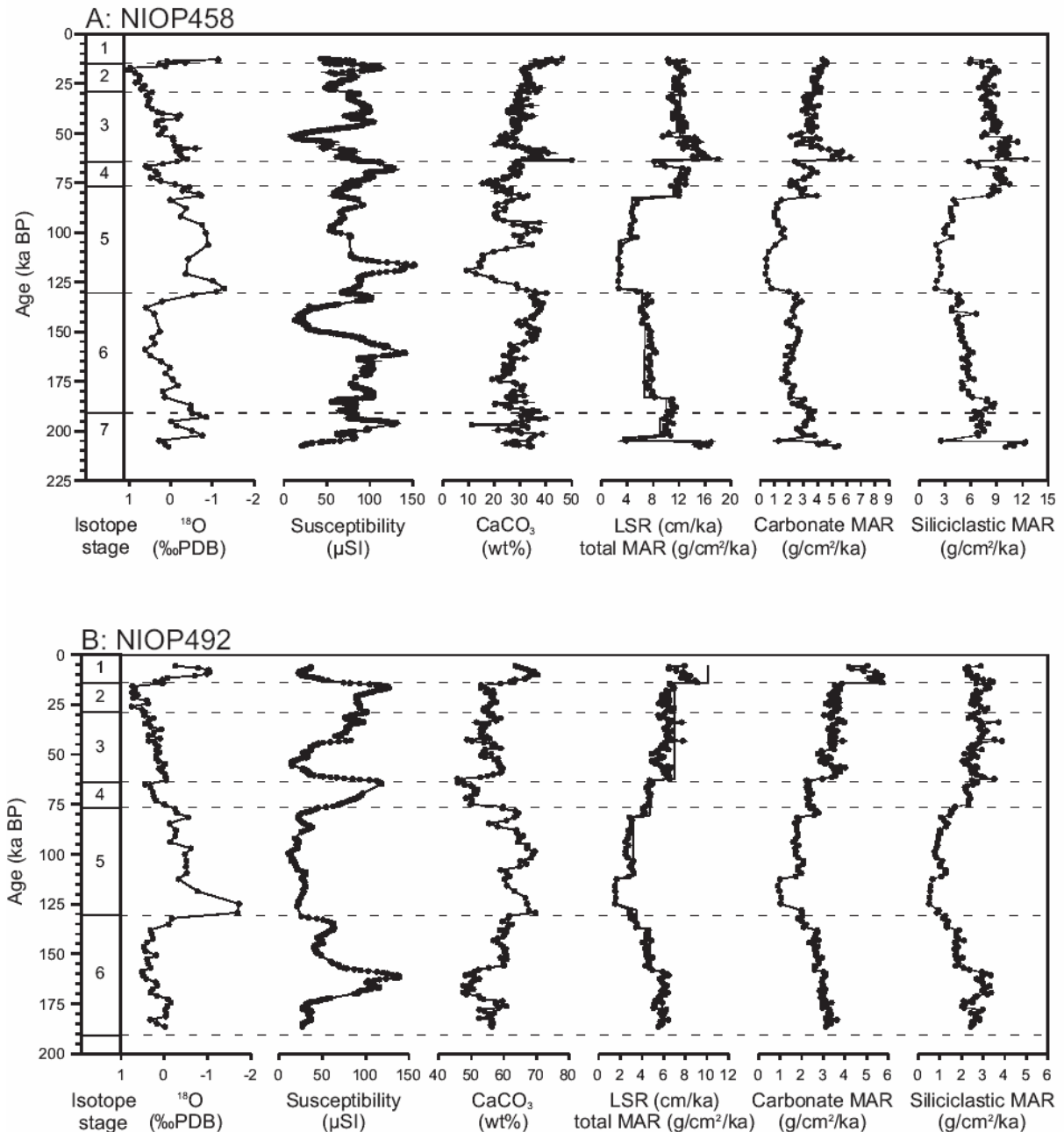
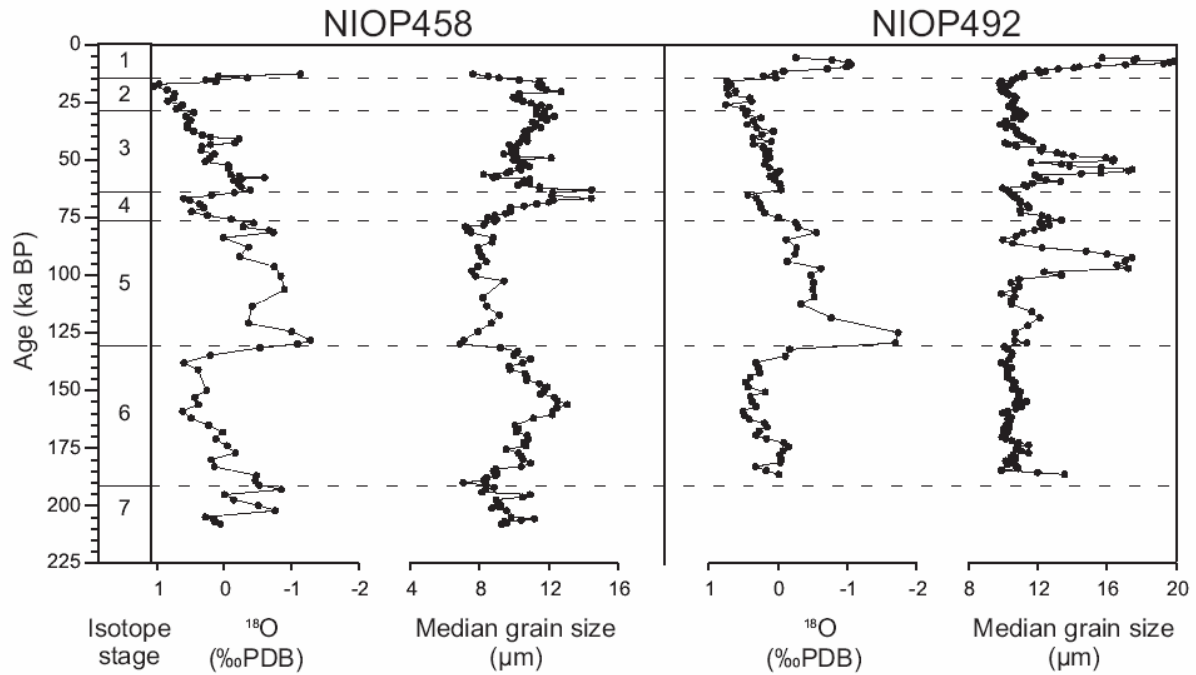


Fig. 4.12 — Time series of  $\delta^{18}\text{O}$  (*N. dutertrei*), magnetic susceptibility, carbonate content, linear sedimentation rates (LSR) and mass-accumulation rates (MAR). A: NIOP458, upper Indus Fan. B: NIOP492, Owen Ridge.

*Median grain size.*—

Time series of the median grain size of cores NIOP458 and NIOP492 are shown in Figure 4.13. In core NIOP458 an almost perfect positive correlation between the median grain size and the  $\delta^{18}\text{O}$  records is observed, indicating relatively fine-grained mud deposition during interglacial stages (1, 3, 5, 7) and relatively coarse-grained mud deposition during glacial stages (2, 4, 6). Within stage 5 even the substages are expressed in the grain-size record (substages 5.1, 5.3, 5.5 are relatively fine-grained). The opposite is observed in the record of core NIOP492, which shows an almost perfect negative correlation between the median grain



**Fig. 4.13** — Variations in median grain size of the siliciclastic fraction in cores NIOP458 and NIOP492 compared with climate change as indicated by the  $\delta^{18}\text{O}$  (*N. dutertrei*) records.

size and the  $\delta^{18}\text{O}$  curves. The glacials are characterised by deposition of relatively fine-grained muds, while during interglacials relatively coarse-grained muds are deposited. The changes in grain size during the substages of isotopic stage 5 are clearly visible.

*Relative end-member contributions.*—

In core NIOP458 (Fig. 4.14A) the relative contributions of EM1 tend to be highest (up to 24%) during glacials and lowest (down to 0%) during interglacials. The relative contributions of EM2 show a similar pattern of relative contributions which vary between 17 and 65%. Consequently, the relative contributions of EM3 (26-78%) are highest during interglacials. The proportional contributions of EM1 to the sediment at site NIOP492 (Fig. 4.14B) reach values up to 46% during interglacial stages 1, 3, 5 (substages 5.1, 5.3 and 5.5). They are smallest during glacials and substages 5.2 and 5.4. The relative abundances of EM2 and EM3 in core NIOP492 are highest during glacials. Between 30-78% of the siliciclastic fraction of the sediment consists of EM2, while EM3 varies between 15-41%.

A comparison of the coarse-grained eolian dust (EM1) records of the western and northern Arabian Sea reveals a negative correlation. The same applies to the fluvial mud (EM3) records of both areas. However, the fine-grained eolian dust (EM2) records show a strong positive correlation. The remarkable difference between the median grain-size records of the two sites can now be fully explained in terms of different sediment supply mechanisms. Grain-size distributions on the upper Indus Fan (NIOP458) mainly reflect mixing of eolian dust and fluvial mud in varying proportions. At this locality, the median grain size may be used as a proxy for changes in continental aridity. Variations in median grain size on the Owen Ridge (NIOP492) are mainly controlled by the relative abundances of the two eolian dust end members. At this locality, the median grain size may be used as a proxy for paleowind strength (although the arithmetic mean is a much more sensitive measure for this particular purpose).

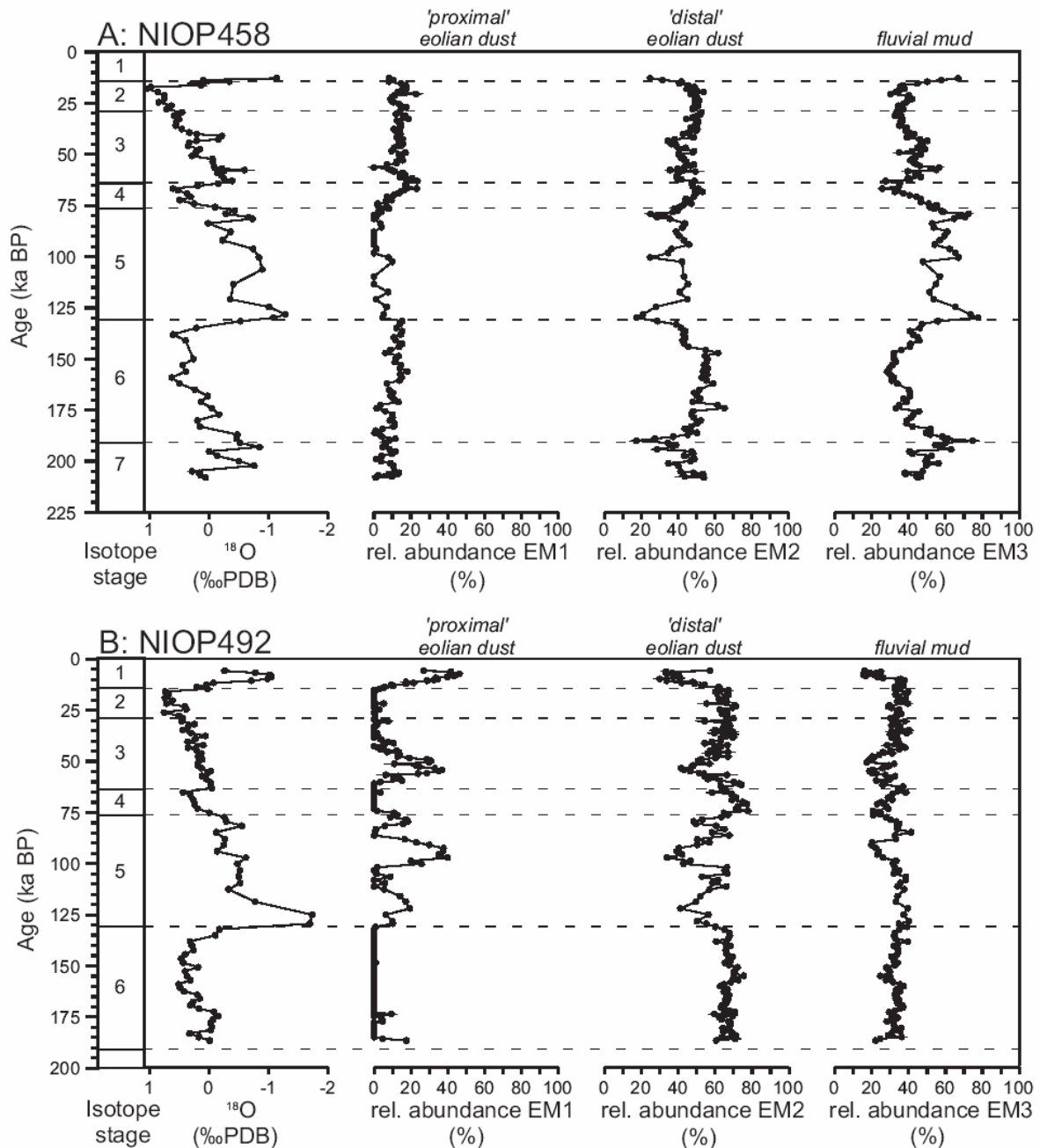


Fig. 4.14 — Variations in relative abundances of end members compared with climate change as indicated by the  $\delta^{18}\text{O}$  (*N. dutertrei*) records. A: core NIOP458. B: core NIOP492.

*End-member ratios: proxies for continental aridity and wind strength.—*

The use of the end-member ratios EM1:EM2 and (EM1+EM2):EM3 as paleoclimate proxies is illustrated in Figure 4.15. Confidence regions of the population means of glacial (stages 2-4,6) and interglacial (stages 1, 5, 7) sediments have been plotted separately for cores NIOP492 and NIOP458 in ternary diagrams. The subdivision into glacial and interglacial stages highlights the most important compositional variation in the terrigenous sediment records. In both cores, the interglacial population differs significantly from the glacial population at a 99% confidence level as these regions do not overlap one another.

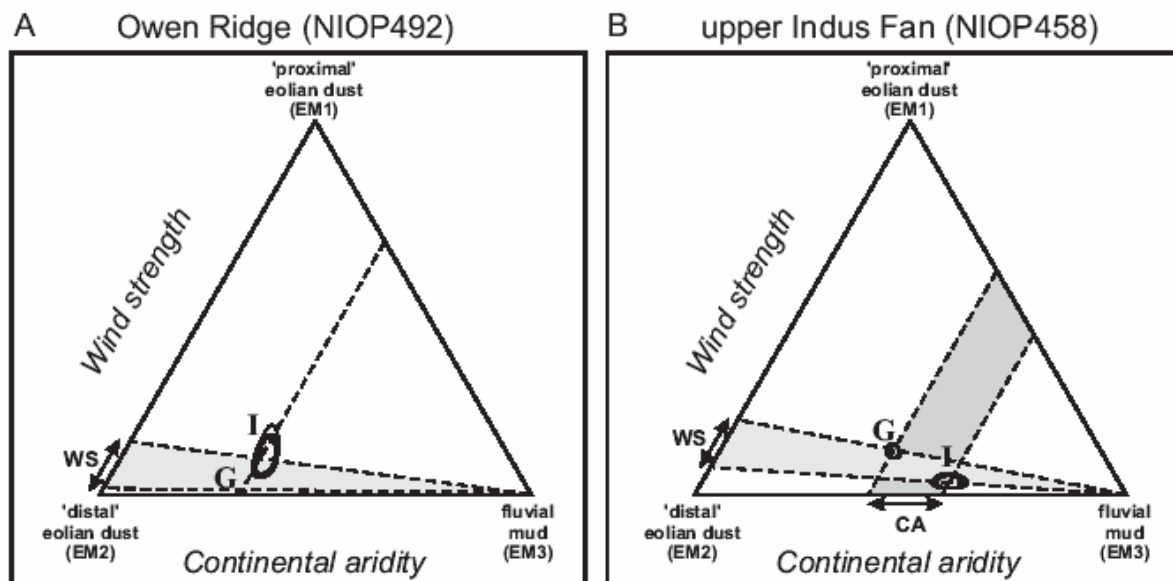


Fig. 4.15 — Ratios of end-member contributions as proxies for variation in wind strength ( $\Delta WS$ ) and continental aridity ( $\Delta CA$ ), illustrated by plotting the confidence regions (90-95-99%) of glacial (G) and interglacial (I) population means. A: EM1:EM2 ratios in NIOP492 indicate stronger summer monsoons during interglacials. B: EM1:EM2 ratios in NIOP458 indicate stronger winter monsoons during glacials. (EM1+EM2):EM3 ratios in NIOP458 indicate increased continental aridity during glacials.

Lines drawn from the EM3 vertex of the ternary diagram towards the opposite side of the diagram represent compositions with equal EM1:EM2 ratios. Likewise, compositions with equal (EM1+EM2):EM3 ratios are located on lines parallel to the upper left edge of the diagram. Such lines have been drawn through the population means of the interglacial and glacial samples to illustrate the temporal differences of the ratios at both coring sites.

Changes in the EM1:EM2 ratio between glacial and interglacials portray differences in paleo-wind speed over time, denoted by  $\Delta WS$  in Figure 4.15. At site NIOP492, the highest EM1:EM2 ratios are recorded during interglacial periods. In contrast, at site NIOP458 the highest EM1:EM2 ratios are recorded during glacial periods. Differences in continental aridity between glacials and interglacials are shown as changes in (EM1+EM2):EM3 ratio, denoted by  $\Delta CA$  in Figure 4.16. High (EM1+EM2):EM3 ratios are recorded during glacial stages at site NIOP458 indicating increased continental aridity during glacial times. At site NIOP492 the differences in the (EM1+EM2):EM3 ratios between the glacial and interglacial periods are not significant.

An alternative indicator for paleo-wind speed may be obtained by calculating the grain-size distribution of eolian dust by subtracting the proportion of fluvial mud (EM3) from the observed grain-size distributions of the total siliciclastic fraction. This approach circumvents possible discrepancies between data and model (Fig. 4.6C) by operating on the raw data directly. The eolian dust grain-size record of core NIOP492 (Fig. 4.16A) shows high frequency variations with sharp peaks, indicating intensified wind speeds, during the interstadials and interglacial stages 1, 3, 5.1, 5.3 and 5.5. In contrast, within core NIOP458, small eolian dust grain sizes (Fig. 4.16B) indicate weak dust-transporting winds during the interstadials and interglacial stages 1, 3, 5.1, 5.3, 5.5 and 7. The NIOP458 record of the logratio (EM1+EM2):EM3 is shown in Figure 4.16C. The observed high-frequency variation in this record, portraying variations in continental aridity on the Pakistan-Indian peninsula, correlates in detail with the variations observed in the  $\delta^{18}O$  record of core NIOP458 (Fig. 4.16D). Variations in continental aridity are associated with glacial-interglacial cycles.

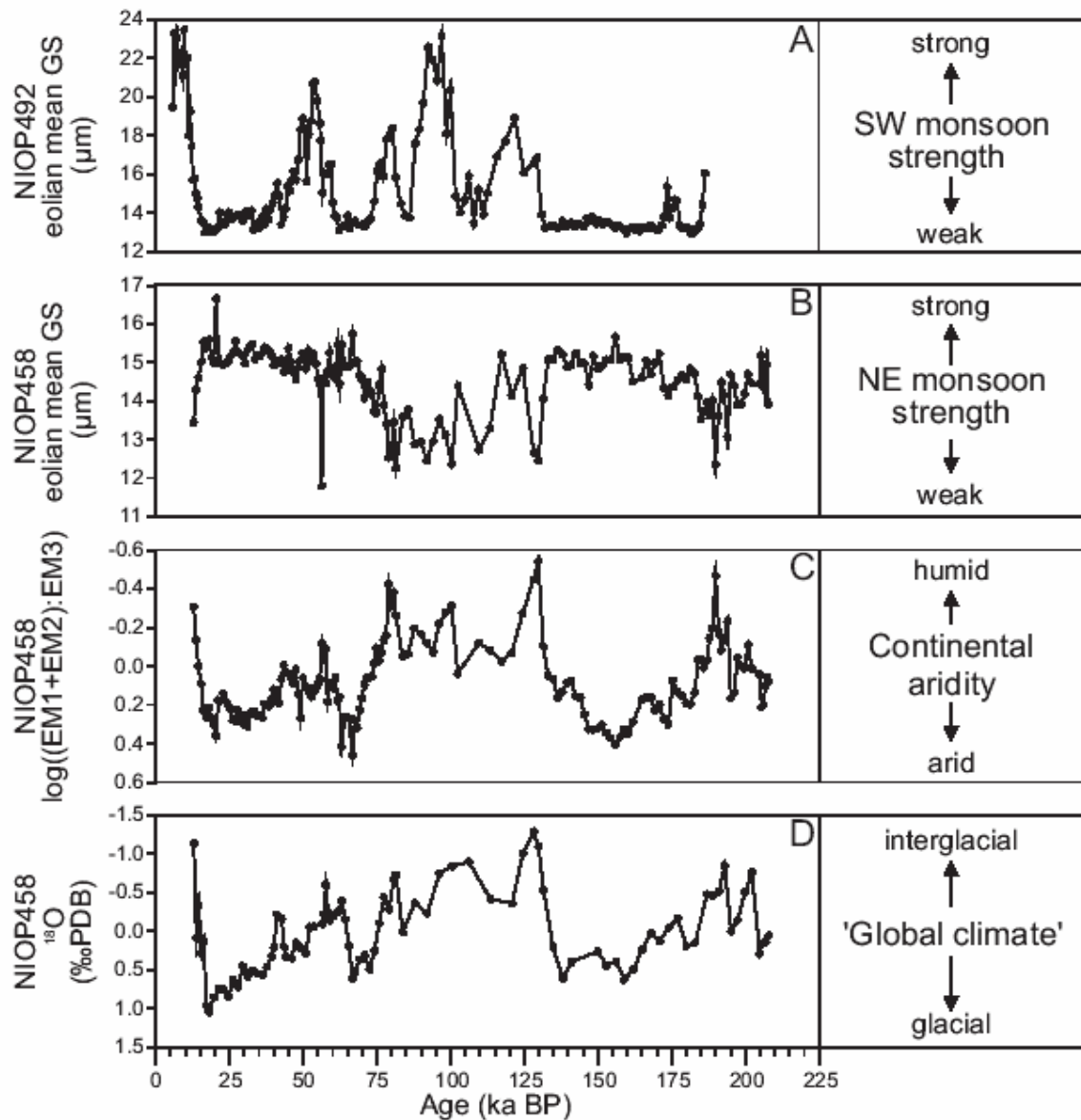


Fig. 4.16 — Late Quaternary reconstruction of variations in Arabian Sea monsoon climate. A: Summer-monsoon strength indicated by the eolian grain-size record of NIOP492. B: Winter-monsoon strength indicated by the eolian grain-size record of NIOP458. C: Continental aridity indicated by  $\log((EM1+EM2):EM3)$  record of NIOP458. D: 'Global climate' indicated by  $\delta^{18}O$  (*N. dutertrei*) record of NIOP458.

The eolian dust grain-size records from the Owen Ridge (NIOP492) and the upper Indus Fan (NIOP458) are inversely correlated. This apparent contradiction may be resolved by taking into account the characteristics of the present-day monsoon climate. The seasonal reversing atmospheric circulation pattern causes differences in the timing of eolian dust supply from the Arabian and Pakistan-Indian peninsulas which are the main source areas for the eolian dust deposited at sites NIOP492 and NIOP458. In the western Arabian Sea, the bulk of the eolian dust is deposited during the summer season (SW monsoon), while in the northern Arabian Sea most of the eolian dust from the Pakistan-Indian deserts is supplied during winter (NE monsoon). Taking this situation as a model for the late Quaternary, our data indicate that the SW monsoon was stronger during interglacials (inferred from eolian dust record site

NIOP492) while the NE monsoon was stronger during glacials (inferred from eolian dust record site NIOP458). The good correlation between the eolian dust grain-size record of core NIOP492 and the (EM1+EM2):EM3 record of core NIOP458 suggests a link between past variations in SW monsoon intensity and continental aridity in the drainage basin of the Indus River.

*Improvements of End-Member Modelling over Descriptive Statistics*

End-member modelling of grain-size distributions allows the distinction of subpopulations present within a basin fill. Such subpopulations may be related to different sediment sources or modes of transport (cf. Syvitski, 1991b). Comparison of the grain-size records (Fig. 4.13) from the Owen Ridge (NIOP492) and upper Indus Fan (NIOP458) illustrates very clearly that the results of grain-size analyses of deep-sea sediments must be interpreted with great care. Variations in grain-size distributions in basin fills thus cannot be summarised with simple descriptive statistics like the median or mean grain size if the objective of the study is to infer paleoclimate changes from the data.

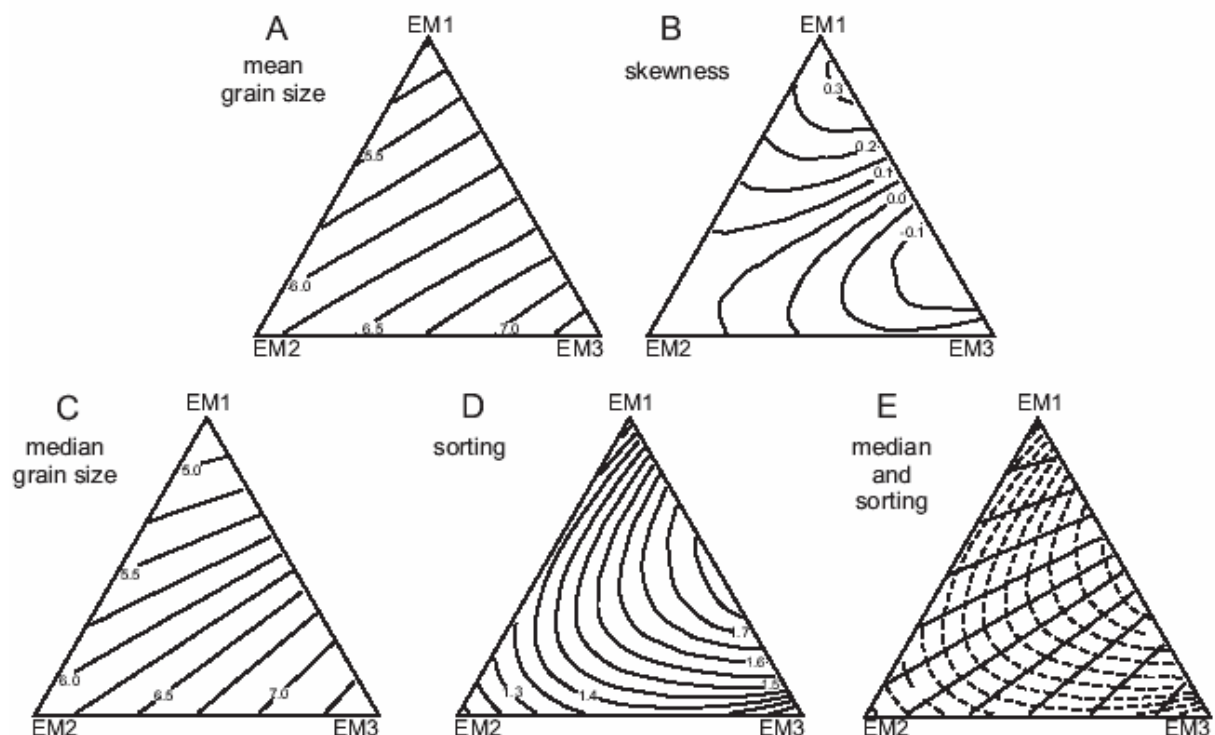


**Fig. 4.17** — Contour plots of descriptive statistics ( $\phi$  units) projected onto mixing space of the three-end-member model. A: Mean grain size. B: Skewness. C: Median grain size. D: sorting. E: Unique fingerprint is obtained by combining median (heavy lines) and sorting (dashed lines).

The disadvantage of using descriptive statistics are illustrated for the three-end-member model developed in this study. Contour lines of mean and median grain size, sorting and skewness (in  $\phi$ ) have been constructed in ternary diagrams for a range of mixtures of EM1, EM2 and EM3 (Figs. 4.17A-D). As shown repeatedly in this study, variations in median size (or in any of the other grain-size statistics) cannot be interpreted unequivocally unless the grain-size distributions of the end members are known. For instance, a sediment with a mean grain size of 6.0  $\phi$  could be a mixture of 15% EM1 and 85% EM2, or a mixture of 57% EM1 and 43 % EM3, or a mixture of varying proportions of all three end members. Additional information about the grain-size distribution is needed besides the mean grain size to fully

characterise the sample. The location of each observation in the ternary mixing space can be uniquely defined by combining the median grain size and the sorting, as shown in Figure 4.17E. However, without the existence of the three-end-member model these conclusions could not have been drawn.

## DISCUSSION

### *Problems Associated with Proxies of Continental Aridity*

The most widely used indicator of continental aridity is the flux of eolian dust. The construction of an eolian dust MAR record requires an age model of the sediment core, extraction of the terrigenous component, and extraction of the eolian dust component from the terrigenous component. The quality of the eolian dust flux record is highly dependent on the accuracy of each of these steps.

Age models of marine sediment records are normally based on the correlation of a limited number of age calibration points recognised in the  $\delta^{18}\text{O}$  record with equivalent identifiable features on an orbitally based chronostratigraphy, in most cases the standard oxygen-isotope records of Imbrie *et al.* (1984) or Martinson *et al.* (1987). Because the age model is based on relatively few calibration points it produces only an 'approximate' flux record. High-frequency variations in sediment flux occurring between two calibration points cannot be documented accurately.

In general, the distinction between the pelagic (eolian dust) and the hemipelagic (fluvial mud) terrigenous components is the most difficult and fundamental part of the problem associated with the construction of eolian dust flux records. As shown in this study, end-member modelling of grain-size distributions allows such a distinction to be made, but the resulting eolian dust flux record still has limited use as a paleoclimatic indicator of continental aridity as it fails to capture high-frequency variations accurately.

The variations in weight percent of the terrigenous fraction observed by Clemens and Prell (1990, 1991), Shimmiel *et al.* (1990) and Shimmiel and Mowbray (1991), and the strong positive correlation between the terrigenous weight percent and magnetic susceptibility of sediments deposited on the Owen Ridge (Clemens and Prell, 1991), agree well with our observations on core NIOP492 (Fig. 4.12B). Clemens and Prell (1991) suggested that the strong positive correlation between the terrigenous weight percent and magnetic susceptibility could be used to establish a terrigenous MAR. Under the assumption that the terrigenous fraction is of exclusive eolian origin, they proposed to use magnetic susceptibility as a high resolution proxy for continental aridity. However, the terrigenous weight percent and magnetic susceptibility are both dependent on the ratio of carbonate and terrigenous MAR's, which implies that they cannot be used as indicators of continental aridity.

Within core NIOP458 a relatively poor fit between terrigenous weight percent and magnetic susceptibility is observed (Fig. 4.12A). The poor fit may be attributed to early diagenetic processes that affected the redox stability of iron-bearing minerals and changed the magnetic properties of the sediment (Karlin and Levi, 1983). The alteration of the magnetic susceptibility records of sediment cores obtained from the oxygen minimum zone off Pakistan and from the Murray Ridge has been related to oxidation of organic matter within these sediments (Reichart *et al.*, 1994; Reichart *et al.*, 1997). Multiple terrigenous sources can further complicate the interpretation of the susceptibility signal. Especially when the input of hemipelagic mud is important, like in core NIOP458, both terrigenous weight percent and magnetic susceptibility lose their usefulness as indicators of continental aridity.

*Linking Arabian Deep-Sea Records with Continental Records of the Chinese Loess Plateau*

Several studies have suggested that the loess-paleosol sequences on the Loess Plateau of central China can be viewed as a proxy record of variations in Asian monsoon climate. The intensity of pedogenesis on the Loess Plateau is linked to summer monsoon precipitation. During pedogenesis ultrafine-grained magnetite is produced which is a highly susceptible mineral. The magnetic susceptibility of the loess-paleosol sequence is therefore regarded as a proxy of summer monsoon strength (An *et al.*, 1991). Several grain-size parameters of the loess have been used to reconstruct variations in strength of winter monsoon winds that were responsible for most of the dust transport (e.g., Ding *et al.*, 1995; Xiao *et al.*, 1995; Porter and An, 1995). Xiao *et al.* (1995) concluded that winter monsoon strength is in general inversely related to the summer monsoon strength. On the Loess Plateau the summer monsoon intensified during stages 1, 3, 5 and 7 (An *et al.*, 1991; Maher and Thompson, 1992) while the winter monsoon was strongest during stages 2, 4 and 6 (Xiao *et al.*, 1995).

Clemens and Prell (1990) argued that the western Arabian Sea (Owen Ridge) lithogenic MAR record from core RC27-61 (dust source aridity indicator) and the magnetic susceptibility record from the Loess Plateau correlate well, from which they concluded the existence of a common aridity forcing mechanism. Maher and Thompson (1992) found only a general correspondence between the loess magnetic susceptibility record and their own lithogenic mass accumulation record at ODP site 722 (Owen Ridge). The discrepancy between the two records was explained by the fact that loess susceptibility records primarily reflect pedogenesis (formation of secondary magnetite), and to a much lesser extent the accumulation rate of the loess. In addition, they discussed the intrinsic problems of estimating accumulation rates of eolian dust in deep-sea cores. We fully support their conclusions: The problems associated with estimation of accumulation rates have been discussed above. The mass accumulation record presented by Clemens and Prell (1990) is difficult to interpret because no distinction was made between eolian and hemipelagic sediments. The possible error associated with the assumption that the sediment is of exclusive eolian origin potentially refutes any correlation, as shown in this study.

The present-day monsoon precipitation on the Indian subcontinent and the associated continental runoff and sediment discharge by the Indus River are largely confined to the summer season (Beg, 1977; Nair *et al.*, 1989), and are therefore coupled with the SW monsoon. Based on this scenario, we propose that the (EM1+EM2):EM3 ratio in core NIOP458, which depicts the relative importance of eolian dust transport with respect to lutite flow transport on the upper Indus Fan, may be used as an indicator of SW monsoon intensity and therefore also of continental runoff. The good correlation between the eolian grain-size record in core NIOP492 (Fig. 4.16A), which can only be related to SW monsoon strength, and the (EM1+EM2):EM3 ratio of core NIOP458 (Fig. 4.16C) supports this idea.

The (EM1+EM2):EM3 ratio in core NIOP458 shows an excellent correlation with the oxygen-isotope curve (compare Fig. 4.16C and D), which allows us to infer that the late Quaternary history of continental runoff and summer monsoon intensity closely mimics the global oxygen-isotope record of Imbrie *et al.* (1984). Maher and Thompson (1992) showed that the record of loess susceptibility closely fits the global oxygen-isotope record of Imbrie *et al.* (1984). The late Quaternary history of pedogenesis and summer monsoon intensity on the Loess Plateau thus mimics the history of summer monsoon intensity in the area around the Arabian Sea. This suggests a physical connection between the regional summer monsoon patterns of the Arabian Sea and the Chinese Loess Plateau: the common aridity forcing mechanism postulated by Clemens and Prell (1990).

A physical connection between the regional winter monsoon patterns can also be established. The variations in NE monsoon intensity, inferred from the eolian dust grain-size

record of core NIOP458 (Fig. 4.16B), indicate intensification of the winter monsoons during the glacial periods. This interpretation matches the conclusions of Xiao *et al.* (1995) with respect to intensity of the winter monsoon on the Loess Plateau.

In conclusion, our reconstruction of the late Quaternary monsoon climate, inferred from the grain-size distribution data of Arabian Sea sediments, corresponds well with paleoclimate reconstructions based on analysis of loess-paleosol sequences on the Loess Plateau of central China. The proposed correlation between terrestrial loess-paleosol sequences of central China and marine eolian-fluvial mud sequences from the Arabian Sea will be presented in Chapter 5.

## CONCLUSIONS

1. Detailed analysis of grain-size distributions in combination with the application of the end-member modelling algorithm allows the distinction of climate-induced changes of sediment supply patterns in deep marine depositional environments.
2. The siliciclastic fractions of the 1102 pelagic and hemipelagic mud samples from the western, northern and central Arabian Sea are adequately described as mixtures of three end members. End-member modelling of grain-size distributions allows the distinction between coarse-grained eolian dust, fine-grained eolian dust and fluvial mud.
3. The median grain-size records from the upper Indus Fan and the Owen Ridge are inversely correlated, reflecting contrasting sedimentation patterns in the two areas. Deposition on the Owen Ridge records selective transport and deposition of materials from a single source, whereas deposition on the upper Indus Fan records physical mixing of materials from two different sources (fluvial mud and eolian dust).
4. The grain-size distribution of eolian dust is calculated by subtracting the modelled contribution of the fluvial-mud end member from the grain-size distribution of the entire siliciclastic fraction.
5. The grain size of eolian dust is a high-resolution paleoclimatic indicator of wind strength.
6. Summer monsoon intensity is inversely correlated with winter monsoon intensity: an intensified SW monsoon is recorded on the Owen Ridge during interglacials, whereas an intensified NE monsoon is recorded on the upper Indus Fan during glacials.
7. The ratio of eolian and fluvial contributions in sediments of the upper Indus Fan is a high-resolution paleoclimatic indicator of continental aridity, which closely matches the marine oxygen-isotope record. Increased continental aridity is recorded throughout the Arabian Sea during glacials.
8. The reconstructed variations in the Arabian Sea monsoon climate, inferred from grain-size distribution data, correlate well with the paleoclimate records of the Loess Plateau in central China. Physical connections between regional summer and winter monsoon patterns are established.

## ACKNOWLEDGEMENTS

We are indebted to all scientists, technicians, and crew members on board R.V. *Tyro* for their commitment during the Netherlands Indian Ocean Programme. We thank U. von Rad (BGR, Hannover, BRD) who kindly allowed us to sample the PAKOMIN core SO90-169KL. C. Laban (NITG-TNO, Haarlem) is thanked for his permission to use the GEOTECH multisensor core logger. We thank P. Anten, A. van Dijk, G. Ittman, M. Reith, G. van 't Veld, and H. de Waard for analytical support. J. Cleveringa, P.P. Lebbink, I.R. de Lugt, E.J.A.H. Noordhuis, G.J. Reichart, J.-B.W. Stuut, and H.J. Visser are thanked for their contributions to this study, which comprise grain-size data, chemical analyses, magnetic susceptibility records and a computer code for spline interpolation (not to mention a few wild ideas). We are especially grateful to G.J. Reichart who kindly provided oxygen-isotope and carbonate data, as well as age models of cores NIOP458 and NIOP464.

## TELECONNECTIONS BETWEEN THE ASIAN MONSOONS AND THE NORTH ATLANTIC CLIMATE DURING THE LATE QUATERNARY

M.A. Prins<sup>1</sup>, G.J. Reichert<sup>1</sup>, J.-B.W. Stuut<sup>1,2</sup>, G.J. Weltje<sup>3</sup> and G. Postma<sup>1</sup>

### ABSTRACT

Grain-size distribution data of pelagic and hemipelagic siliciclastic muds from various parts of the Arabian Sea are used to reconstruct late Quaternary changes in the Arabian Sea monsoonal climate. The grain-size distribution of eolian dust is used as an indicator of the strength of the dust-transporting wind system: eolian-dust grain-size records from the Owen Ridge (western Arabian Sea) reflect changes in the summer-monsoon strength, and the eolian-dust grain-size records from the continental slope off the Indus Delta and on the upper Indus Fan (north-eastern Arabian Sea) reflect changes in the winter-monsoon strength. The ratio of contributions of eolian and fluvial sediment in the north-eastern Arabian Sea is used as an indicator of continental aridity on the Indian Peninsula.

Our reconstruction of the late-Quaternary variability in the Arabian Sea monsoonal climate corresponds well with interpretations of the loess-paleosol sequences on the central Loess Plateau of China. In both areas, the bulk of the annual precipitation is confined to the summer monsoon season. Intensification of the summer monsoon during interstadials and interglacials, which has been identified as the principal control on pedogenesis on the Loess Plateau, explains increased discharge of Indus-River-derived muds to the north-eastern Arabian Sea. Independent evidence for summer-monsoon strength, provided by the eolian-dust grain-size record of the western Arabian Sea, fully supports this conclusion. The strength of the summer monsoon, therefore, provides an aridity/humidity-forcing mechanism for both the Arabian Sea and the Loess Plateau. The grain-size records of eolian dust deposited in the north-eastern Arabian Sea and on the Loess Plateau both indicate intensified winter monsoons during glacials. High-frequency variations in the last glacial eolian-dust grain-size records of the north-eastern Arabian Sea and the Loess Plateau correlate well, which implies that the history of the winter-monsoon strength around the Arabian Sea mimics the history of winter-monsoon strength on the Loess Plateau very closely.

High-frequency variability in our Arabian Sea monsoon-indicator records is correlated with high-frequency changes in the climate-indicator records of the North Atlantic region. Enhancements of summer-monsoon strength (and weakening of winter-monsoon strength) correlate with major warm interstadials (Dansgaard-Oeschger events) and long-term cooling cycles (Bond cycles) in North Atlantic climate-indicator records. Enhancements of winter-monsoon strength (and weakening of summer-monsoon strength) correlate with major cold episodes in the North Atlantic region, including the Heinrich events, occurring at the end of

---

<sup>1</sup> Institute for Paleoenvironments and Paleoclimate Utrecht (IPPU), Faculty of Earth Sciences, Utrecht University, P.O. Box 80021, 3508 TA Utrecht, The Netherlands

<sup>2</sup> Netherlands Institute for Sea Research (NIOZ), Department of Marine Chemistry and Geology, P.O. Box 59, 1790 AB Den Burg, The Netherlands

<sup>3</sup> (a) Department of Geo-Energy, Netherlands Institute of Applied Geoscience TNO, P.O. Box 6012, 2600 JA Delft, The Netherlands; (b) Subfaculty of Applied Earth Sciences, Delft University of Technology, P.O. Box 5028, 2600 GA Delft, The Netherlands

the long-term cooling cycles. Correlation between climate events in the Arabian Sea, China and the North Atlantic during the last glacial period suggests that the monsoons of Asia and the climate of the North Atlantic region were linked by the effect of westerly winds.

## INTRODUCTION

During the last decade, many studies of the marine sedimentary record in the Arabian Sea (NW Indian Ocean; Fig. 5.1) and of the loess-paleosol sequences on the Loess Plateau of central China (Fig. 5.1) have revealed that these records allow reconstructions of late Quaternary changes of the Arabian-Sea and East-Asian monsoonal climates. A correlation between changes in continental aridity on the Arabian Peninsula and on the Loess Plateau has been suggested by Clemens and Prell (1990). They used the mass-accumulation rate of terrigenous material (of presumed eolian origin) at a site on the Owen Ridge (western Arabian Sea) as an indicator of aridity on the Arabian Peninsula. However, Maher and Thompson (1992) and Prins and Weltje (1999; Chapter 4) pointed out that there are several problems associated with the use of this indicator of aridity. Prins and Weltje (1999; Chapter 4) proposed alternative indicators of the late Quaternary Arabian Sea monsoonal climate based on the grain-size distribution of pelagic and hemipelagic siliciclastic sediments in the Arabian Sea. They postulated a correlation between their winter and summer-monsoon indicator records of the Arabian Sea and the monsoon-indicator records of the Loess Plateau. Moreover, recent studies suggest teleconnections between the monsoonal climates of both the Loess Plateau (Porter and An, 1995; An and Porter, 1997; Chen *et al.*, 1997; Fang *et al.*, 1999) and the Arabian Sea (Sirocko *et al.*, 1996; Reichert *et al.*, 1997; Schulz *et al.*, 1998) with the climate of the North Atlantic region.

In this chapter we will expand the work of Prins and Weltje (1999; Chapter 4) by presenting new climate-indicator records based on the grain-size distribution of hemipelagic siliciclastic muds obtained from various parts of the Arabian Sea (Fig. 5.1). Our records provide new evidence for teleconnections between the Arabian-Sea monsoonal climate, the East-Asian monsoonal climate and the North Atlantic climate. The objectives of this study are: (1) to present eolian-dust grain-size records from the western and north-eastern Arabian Sea (indicator records of summer and winter-monsoon strength), and records of the ratio of eolian and fluvial contributions of sediments from the north-eastern Arabian Sea (indicator records of continental aridity) that allow reconstruction of the Arabian Sea monsoonal climate during the last two glacial-interglacial cycles (0-185/210 ka BP); (2) to demonstrate a correlation between marine eolian-fluvial mud sequences of the north-eastern Arabian Sea and terrestrial loess-paleosol sequences of central China indicating an atmospheric teleconnection between the Arabian Sea and East-Asian summer and winter monsoonal climates during the last glacial-interglacial cycle (focus on 0-135 ka BP); (3) to present a correlation between the summer and winter monsoon indicator records of the Arabian Sea and the climate-indicator records of the North Atlantic region, including the oxygen-isotope record of the GISP2 ice core of Greenland (Grootes *et al.*, 1993), indicating an atmospheric teleconnection between the climate systems of the Arabian Sea and the North Atlantic region during the last glacial period (focus on 0-100 ka BP).

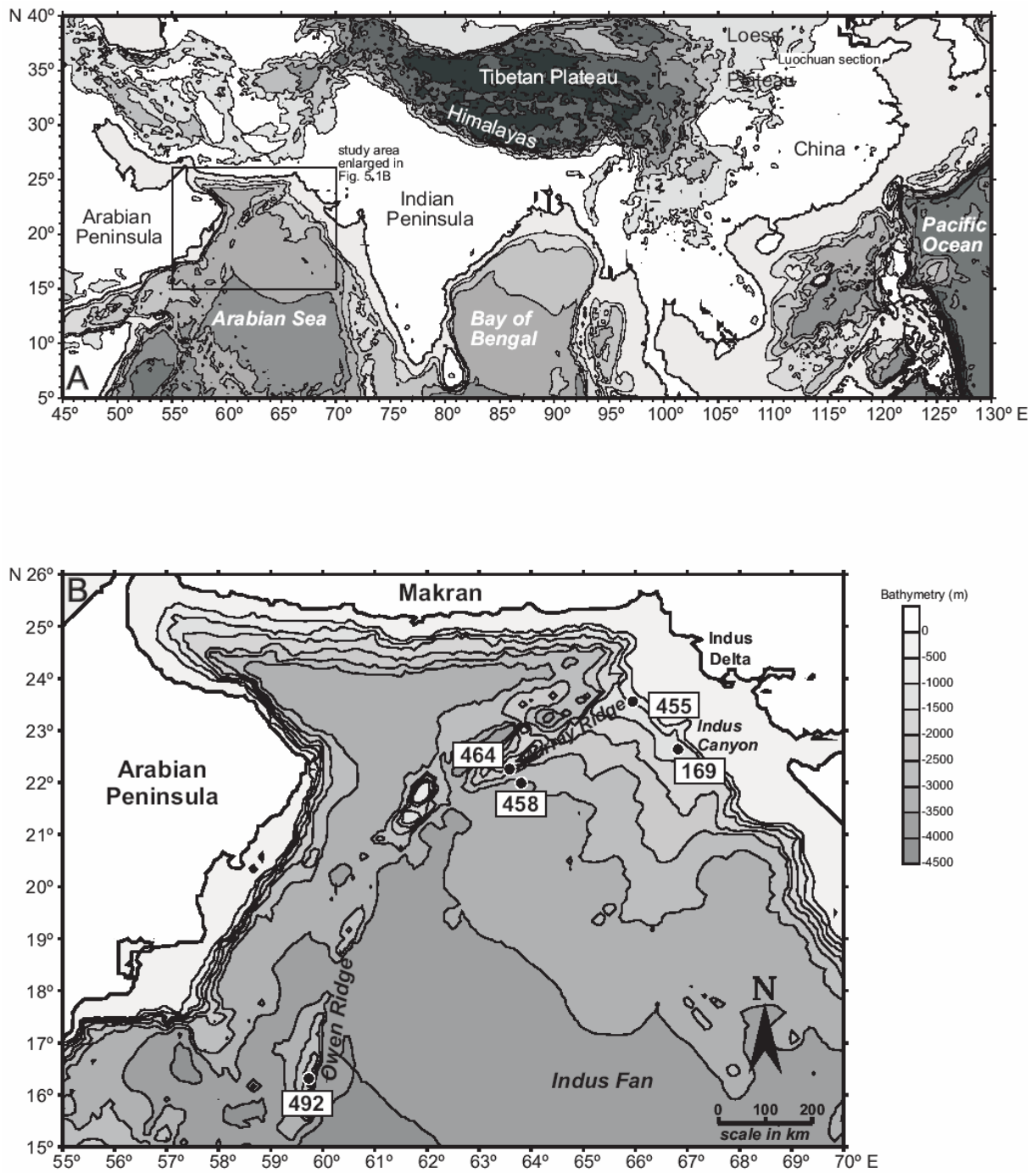


**Fig. 5.1** — The Arabian Sea and adjacent landmasses. **A:** Locations of the study area in the Arabian Sea (enlarged in Fig. 5.1B) and the Luochuan section on the central part of the Chinese Loess Plateau are indicated. Contour interval 1000 m. **B:** Location of sediment cores from the Arabian Sea. Contour interval 500 m. Topographic data from U.S. National Geophysical Data Center/World Data Center A for Marine Geology and Geophysics.

## Asian Monsoons

The monsoonal climate of Asia is a dynamic, interactive system that involves the ocean, land, and atmosphere (e.g. Clemens and Prell, 1990; Clemens *et al.*, 1991; Sirocko, 1991; Xiao *et al.*, 1995). The monsoons are driven by strong differential heating between the Asian continent and the Indian Ocean to the south and the Pacific Ocean to the east, and by the availability of vast amounts of latent heat, collected over the southern hemisphere Indian and Pacific Ocean. Differential heating (cooling) during the northern hemisphere winter causes low surface pressure over the relatively warmer ocean and high surface pressure over the high elevations of north-central Asia (Fig. 5.2A). The cold high-pressure cell is centred at about  $100^{\circ}$  E and  $50^{\circ}$  N and is referred to as the Mongolian High. The pressure gradient between the continent and the ocean results in the flow of cold, dry air out of north-central Asia, i.e., the winter monsoon. The winter monsoon circulation manifests itself as NW winds on the Loess Plateau and NE winds over the Arabian Sea. During northern hemisphere spring, when the Asian continent starts to heat up, W to NW winds prevail over the Arabian Sea. In northern hemisphere summer, the atmospheric pressure gradient is reversed, i.e., differential heating causes the formation of high surface pressure over the cool Indian and Pacific oceans and low surface pressure over the much warmer Asian continent (Fig. 5.2B). This pressure gradient results in a steady flow of moist maritime air onto the continent resulting in the release of latent heat over the Asian landmasses, the area of monsoon precipitation. The summer monsoon circulation manifests itself as strong SW winds (Indian monsoon) over the Arabian Sea and SE winds (East-Asian monsoon) over the Pacific Ocean.

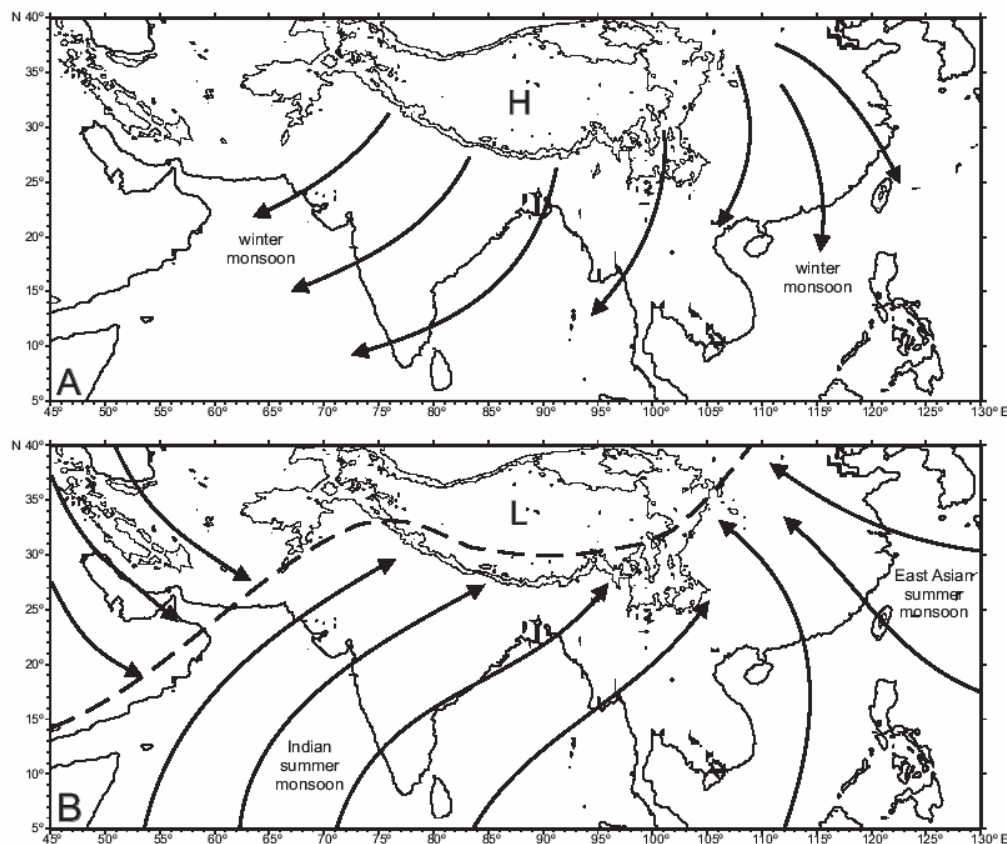


**Fig. 5.2** — Atmospheric circulation patterns during northern hemisphere winter (A) and summer (B). Approximate trajectories of the monsoons are indicated by arrows, and northern limit of summer-monsoon precipitation (intertropical convergence zone ITCZ) is indicated by dashed line.

### *Modern Monsoon-Driven Sediment-Supply Patterns in the Arabian Sea*

At present the monsoons control the supply of eolian dust and fluvial mud to the Arabian Sea. The NW winds associated with the summer monsoon are responsible for the transport of large quantities of eolian dust from the Arabian Peninsula, and minor amounts from Pakistan. The SW summer monsoon supplies minor amounts of eolian dust from Somalia. The NE winter monsoon transports minor amounts of eolian dust from Pakistan and northern India towards the Arabian Sea (Sirocko, 1991).

The summer monsoon carries large amounts of water vapour which is released as precipitation over the Asian continent. This precipitation provides the runoff for river systems draining the Himalayas, including the Indus River which flows into the Arabian Sea. Highest discharges and suspended sediment loads of the Indus River coincide with the peak of the rain season, and up to 80 % of the annual discharge occurs during the summer monsoon season (Beg, 1977; Milliman *et al.*, 1982).

Nair *et al.* (1989) recorded strong seasonality in particle flux at three sediment-trap sites (western, central, eastern Arabian Sea) with peaks during the summer and winter monsoon periods. Highest terrigenous particle fluxes are recorded during the summer monsoon season. At the western sediment trap site 80% of the annual terrigenous particle flux is recorded during this season. As the western trap site is close to the Arabian Peninsula, deposition is dominated by eolian dust blown in from the Arabian deserts. At the eastern site 67% of the annual cumulative terrigenous particle flux is recorded during the summer season and it is dominated by input of Indus River muds.

The above observations indicate that the deep-sea terrigenous sediments of the Arabian Sea are mixtures of eolian and fluvial sediment, the relative contributions of the two types of sediment depending on the location in the basin. At any given location, the relative contributions of materials from both sources are likely to have varied through time as well.

#### *'Sedimentologic' Indicators of Arabian Sea Monsoonal Climate*

Several studies suggested that the analysis of pelagic-hemipelagic sediment records from the western and northern Arabian Sea (Oman continental slope, Owen Ridge, Murray Ridge) allows estimation of past aridity on the Arabian Peninsula (most important eolian source region) via determinations of terrigenous sediment flux (Clemens and Prell, 1990; Shimmield *et al.*, 1990; Clemens and Prell, 1991; Clemens *et al.*, 1991; Shimmield and Mowbray, 1991; Clemens *et al.*, 1996; Reichart *et al.*, 1998). Clemens and Prell (1990, 1991) and Clemens *et al.* (1991, 1996) used the median grain size of terrigenous sediments deposited on the Owen Ridge as an indicator of summer-monsoon strength. Above proposed indicators of continental aridity and wind strength, i.e., the flux and the grain size of the terrigenous fraction within deep-sea sediments, are only valid, however, if the terrigenous fraction is exclusively of eolian origin. The presence of major eolian and fluvial sources around the Arabian Sea makes it highly unlikely that this prerequisite is fulfilled in many (if any) parts of the basin.

Sirocko (1991) and Sirocko *et al.* (1991) recognised this 'mixing problem' and used a somewhat arbitrary size cut-off to partition eolian (terrigenous fraction  $>6 \mu\text{m}$ ) and fluvial (terrigenous fraction  $<6 \mu\text{m}$ ) sediments, in order to map the distribution pattern of eolian dust in the marine sediment record of the Arabian Sea. They observed a NW to SE gradient in eolian dust content from which they inferred that eolian dust is supplied mainly from the Arabian Peninsula by the northwesterlies. The extent of the eolian dust distribution pattern over the ocean was used to approximate the position of the front (intertropical convergence zone ITCZ) between the northwesterlies and the SW summer monsoon. Shifts of the position of this front are inferred from changes in grain-size parameters and mineralogy of western

Arabian Sea sediments (Sirocko *et al.*, 1991; Sirocko and Lange, 1991; Sirocko *et al.*, 1993). So clearly, successful reconstructions of paleoclimate from Arabian Sea terrigenous deep-sea records depend primarily on the capability of distinguishing between sediments of eolian and fluvial origin. Prins and Weltje (1999; Chapter 4) presented an approach which allows the distinction of eolian and fluvial sediments based on their grain-size distribution: a summary of their results is given below.

### *End-Member Modelling of Grain-Size Distributions*

#### *Indicators of wind strength and continental aridity.—*

In certain cases, use can be made of *a priori* knowledge of provenance and dispersal patterns to distinguish eolian and fluvial sediment input based on their grain-size distribution (e.g. Koopmann, 1981; Sarnthein *et al.*, 1981, 1982; Sirocko *et al.*, 1991; Rea and Hovan, 1995). However, in most geological applications of grain-size analysis, no *a priori* knowledge is available to distinguish subpopulations of sediments with different provenances. The best way to proceed in such cases would be to use an inverse method which does not require detailed assumptions about the geological system being studied. Weltje (1994, 1997a) developed an inversion algorithm for end-member modelling of compositional data aiming at ‘unmixing’ of multi-sourced basin fills in the absence of prior knowledge. Experiments with sediment mixtures indicate that the algorithm produces good estimates of mixing proportions and end-member grain-size distributions in the absence of prior knowledge (see Chapter 3).

Prins and Weltje (1999; Chapter 4) applied the end-member modelling algorithm to a large data set of 1102 grain-size distributions of pelagic and hemipelagic siliciclastic sediments from the Arabian Sea. Their modelling results indicate that the grain-size distributions of the siliciclastic sediments from the Oman continental slope, the Owen Ridge, the Pakistan continental slope and the Indus Fan are adequately described as mixtures of three end members (Fig. 5.3). The spatial variation in relative contribution of the end members allowed

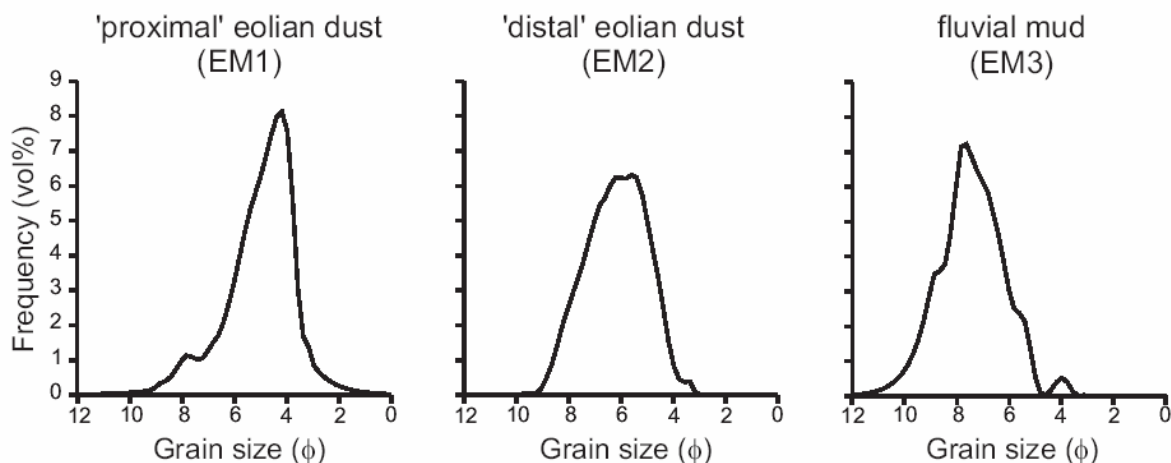


**Fig. 5.3** — Modelled end member grain-size distributions of Arabian Sea pelagic and hemipelagic siliciclastic sediments. The grain-size distributions are represented by splined curves whereby the size domain has been subdivided into equal size intervals on a logarithmic scale (widths 0.2  $\phi$ ) with a computer code for spline interpolation.

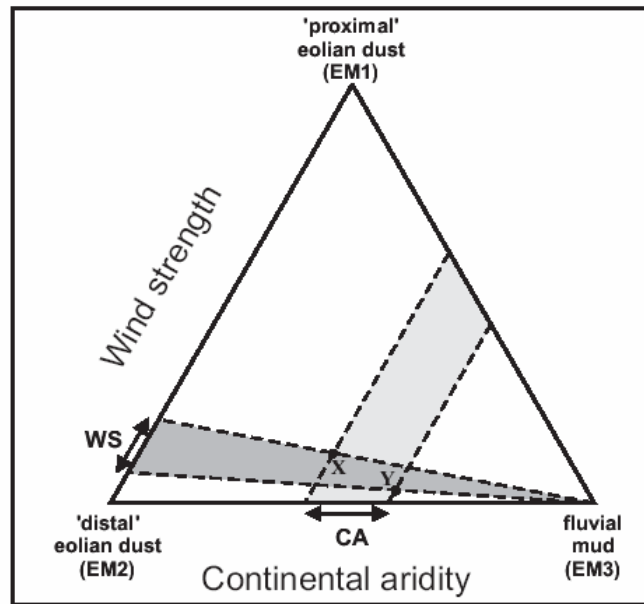


**Fig. 5.4** — Ratios of end-member contributions as indicators of variation in wind strength ( $\Delta WS$ ) and continental aridity ( $\Delta CA$ ), illustrated by plotting the composition of two hypothetical samples X and Y. Sample X recorded stronger winds and more arid climate conditions in comparison with sample Y.

interpretation of the end members in terms of transport processes and provenance. The end members represent ‘proximal’ eolian dust (EM1), ‘distal’ eolian dust (EM2), and fluvial mud (EM3). The granulometric composition of the Arabian Sea pelagic and hemipelagic siliciclastic sediments, expressed as a function of the relative contributions of the three end members, can be visualised in a ternary mixing space (Fig. 5.4). At any given location, temporal changes in the relative contribution of the end members can be interpreted in terms of climate change: the ratio of contributions of eolian and fluvial sediment reflects continental aridity, the ratio of contributions of the two eolian end members reflects the strength of the dust-transporting winds. An alternative indicator of paleo-wind speed may be obtained by calculating the grain-size distribution of eolian dust by subtracting the proportion of fluvial mud (EM3) from the observed grain-size distributions of the total siliciclastic fraction. This approach circumvents possible discrepancies between data and model by operating on the raw data directly.

*Records from the Owen Ridge and the upper Indus Fan.—*

Prins and Weltje (1999; Chapter 4) presented timeseries of siliciclastic grain size and its paleoclimatic interpretation of two sediment cores from the Arabian Sea: core NIOP492 from the Owen Ridge and core NIOP458 from the upper Indus Fan (Fig. 5.1). Mean grain-size records of eolian dust from the Owen Ridge (NIOP492; Fig. 5.5A) and from the upper Indus Fan (NIOP458; Fig. 5.5B) were used as indicators of the strength of the summer monsoon and winter monsoon, respectively. The ratio of eolian and fluvial contributions in sediments of the upper Indus Fan (NIOP458) was used as an indicator of continental aridity (Fig. 5.5C). Summer-monsoon intensity appeared to be generally inversely correlated with winter-monsoon intensity: an intensified SW monsoon is recorded on the Owen Ridge during interglacials, whereas an intensified NE monsoon is recorded on the upper Indus Fan during glacials. The proposed indicator of continental aridity, which closely matches the marine oxygen-isotope record (Fig. 5.5D), indicates increased continental aridity during glacial periods. According to Prins and Weltje (1999; Chapter 4), the correlation between the eolian-

dust grain-size record of core NIOP492 (Fig. 5.5A) and the continental-aridity-indicator record of core NIOP458 (Fig. 5.5C) suggests a link between past variations in summer-monsoon intensity and aridity in the drainage basin of the Indus River.

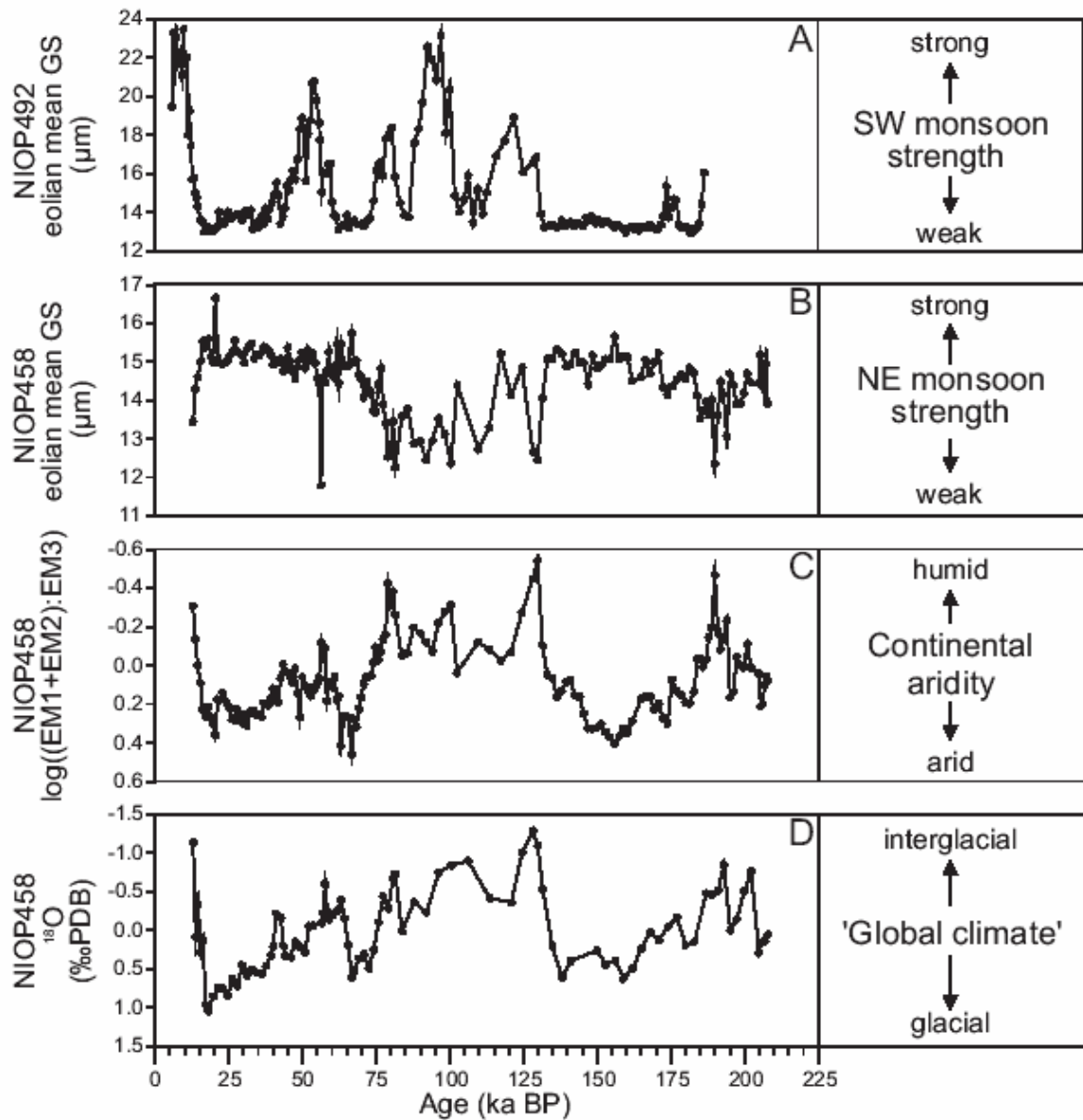


Fig. 5.5 — Reconstruction of variations in late Quaternary Arabian Sea monsoonal climate. A: Summer-monsoon strength indicated by the eolian-dust grain-size record of NIOP492. B: Winter-monsoon strength indicated by the eolian-dust grain-size record of NIOP458. C: Continental aridity indicated by  $\log((EM1+EM2):EM3)$  record of NIOP458. D: 'Global climate' indicated by  $\delta^{18}O$  (*N. dutertrei*) record of NIOP458.

## MATERIAL AND METHODS

Sediment cores used in this study were collected during the Netherlands Indian Ocean Programme (NIOP) on RV *Tyro* (Van der Linden and Van der Weijden, 1994) and during the SO90 PAKOMIN Expedition on RV *Sonne* (Von Rad *et al.*, 1995). The cores, containing predominantly pelagic and hemipelagic sediments, were obtained from the Owen Ridge (NIOP492), the Pakistan continental slope (NIOP455, NIOP458) and the eastern levee of the major channel radiating from the Indus Canyon (SO90-169KL). Figure 5.1 and Table 5.1 provide detailed information on the core locations. Information about sampling and laboratory procedures, analytical methods and the end-member modelling technique applied in this study are given in Prins and Weltje (1999; Chapter 4). For detailed information about the end-member modelling technique see Weltje (1994, 1997a).

Construction of the age models of the cores are based on the correlation of the *Neogloboquadrina dutertrei* (150-595  $\mu\text{m}$  sieve fraction)  $\delta^{18}\text{O}$  records of the cores with the  $\delta^{18}\text{O}$  record of 'reference core' NIOP464. The chronology of core NIOP464 was constructed by correlation of its  $\delta^{18}\text{O}$  record with the astronomically calibrated  $\delta^{18}\text{O}$  time series of Mediterranean core MD84641: for details see Reichart *et al.* (1997). The age models of cores NIOP455, NIOP458, NIOP464 and NIOP492 are taken from Reichart *et al.* (1997) and Prins and Weltje (1999; Chapter 4). The age model of core SO90-169KL is presented in this chapter.

**TABLE 5.1 — SEDIMENT CORES USED IN THIS STUDY**

Core number	Position (Lat. N, Long.E)	Area	Water depth (m)
NIOP455	23°33'.4, 65°57'.0	middle Pakistan continental slope	1002
NIOP458	21°59'.4, 63°48'.7	upper Indus Fan	3001
NIOP492	16°19'.0, 59°43'.6	Owen Ridge	2400
SO90-169KL	22°38'.5, 66°49'.3	channel levee, Indus Canyon	1283

## RESULTS AND INTERPRETATION

The *Neogloboquadrina dutertrei*  $\delta^{18}\text{O}$  records of cores NIOP455 and SO90-169KL are shown next to the  $\delta^{18}\text{O}$  records of cores NIOP458, NIOP492 and NIOP464 in Figure 5.6. The two additional cores SO90-169KL and NIOP455 from the north-eastern Arabian Sea contain hemipelagic mud records which span the last 105-115 ka.

Within cores NIOP455 and SO90-169KL a positive correlation between the median siliciclastic grain size and the  $\delta^{18}\text{O}$  records is observed (Fig. 5.7B, C). Temporal variability in siliciclastic median grain size in cores NIOP455 and SO90-169KL appears to be comparable to the variability observed in core NIOP458 (Fig. 5.7A). According to the end-member model presented by Prins and Weltje (1999; Chapter 4), variations in the median siliciclastic grain size in the cores from the north-eastern Arabian Sea are mainly due to variations in the relative abundance of fluvial mud (EM3) with respect to eolian dust (EM1, EM2): the

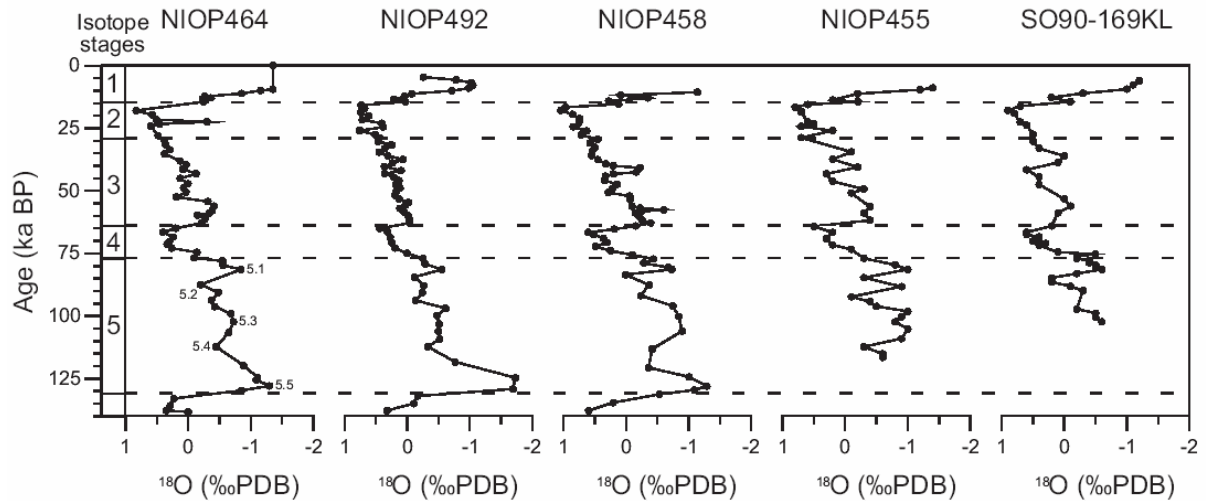


**Fig. 5.6** — Age models of cores NIOP492, NIOP458, NIOP455 and SO90-169KL are based on correlation of the  $\delta^{18}\text{O}$  (*N. dutertrei*) records with core NIOP464.

variability of the eolian-dust grain size (i.e., the ratio of EM1 to EM2) is of secondary importance.

Following Prins and Weltje (1999; Chapter 4), the ratio of eolian and fluvial contributions (end-member ratio (EM1+EM2):EM3) in sediments of the continental slope off the Indus Delta and the upper Indus Fan is used as a paleoclimate indicator of continental aridity. In case of the north-eastern Arabian Sea, the eolian-dust grain size is applied as a paleoclimate indicator of winter-monsoon strength, i.e., the strength of the dominant wind system supplying eolian dust from the Pakistan-Indian landmasses towards the Pakistan continental slope and upper Indus Fan. Time series of the end-member ratio (EM1+EM2):EM3 and the mean eolian-dust grain size of cores NIOP455 and SO90-169KL are shown next to the records of core NIOP458 in Figure 5.8 and 5.9.

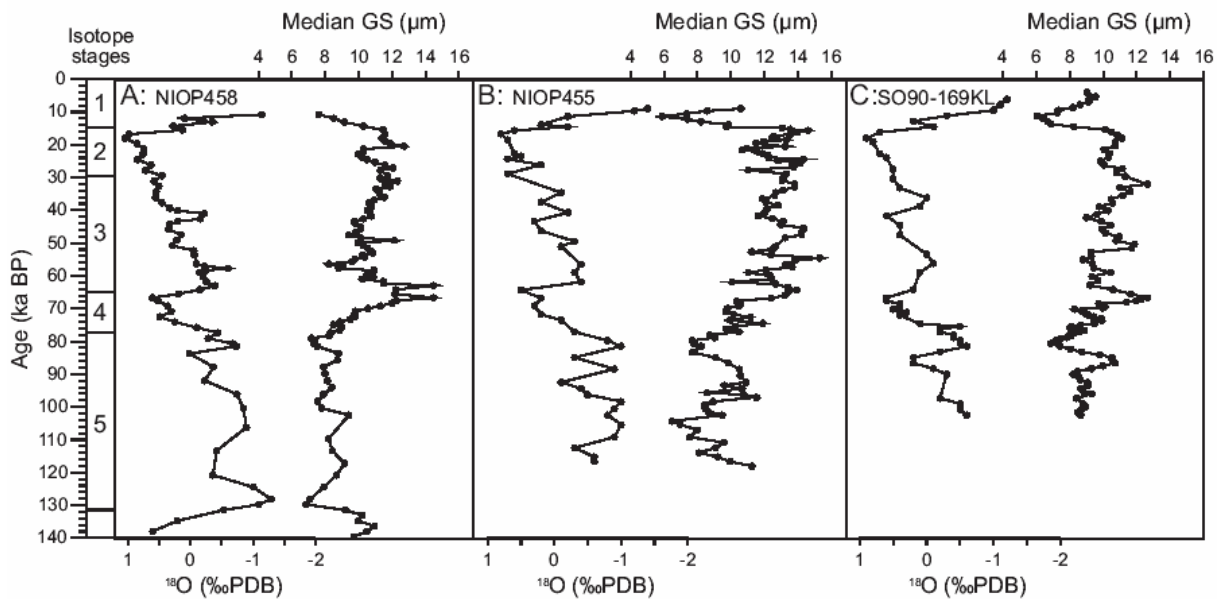


**Fig. 5.7** — Time series of median siliciclastic grain size in sediment cores from the north-eastern Arabian Sea compared with climate change as indicated by the  $\delta^{18}\text{O}$  (*N. dutertrei*) records. A: NIOP458. B: NIOP455. C: SO90-169KL.

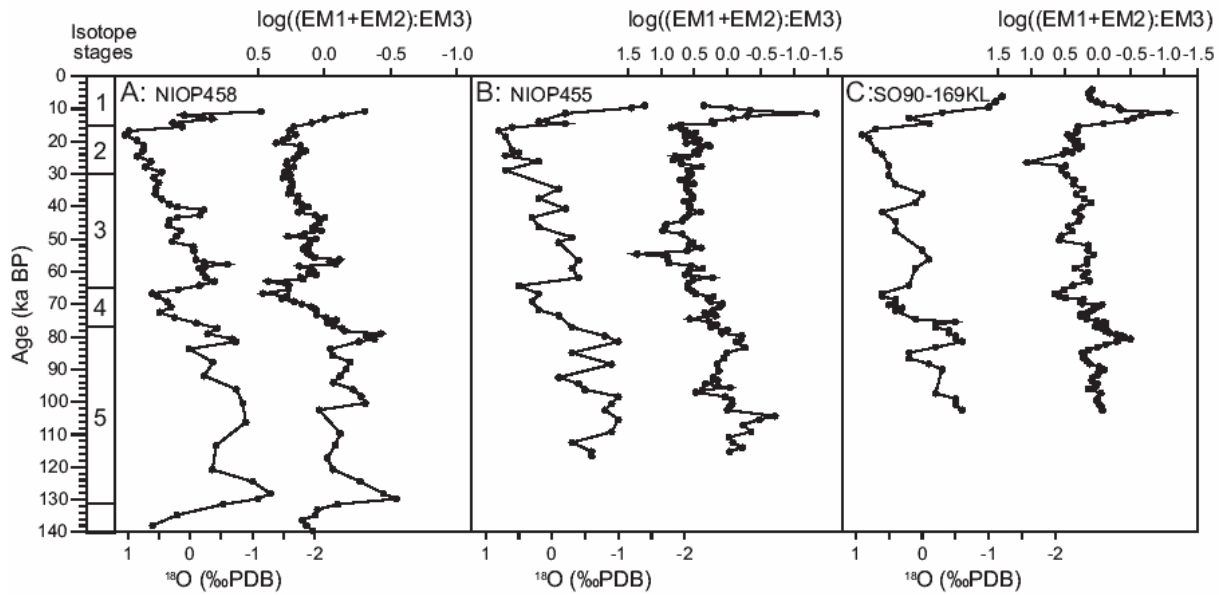


Fig. 5.8 — Time series of the indicator of continental aridity (end-member ratio (EM1+EM2):EM3) in sediment cores from the north-eastern Arabian Sea compared with climate change as indicated by the  $\delta^{18}\text{O}$  (*N. dutertrei*) records. A: NIOP458. B: NIOP455. C: SO90-169KL.

The indicator records for continental aridity of cores NIOP455 and SO90-169KL (Fig. 5B, C) are strongly correlated with their *Neogloboquadrina dutertrei*  $\delta^{18}\text{O}$  records. The end-member-ratio records indicate periods of increased humidity during isotope stage (early) 1, and substages 5.1 and 5.3. The increased continental humidity during stage 3 inferred from the end-member-ratio record of core NIOP458 (Fig. 5.8A), is not recorded clearly in cores NIOP455 and SO90-169KL. However, overall trends in the continental-aridity-indicator records of the three cores are very similar.

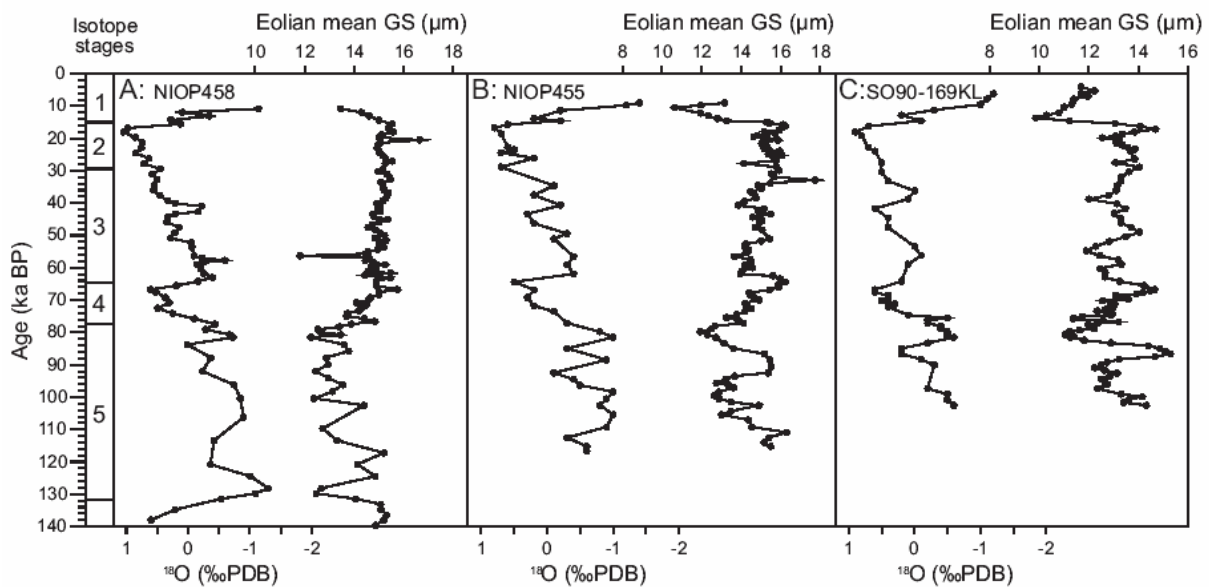


Fig. 5.9 — Time series of the indicator of winter-monsoon intensity (eolian-dust mean grain size) in sediment cores from the north-eastern Arabian Sea compared with climate change as indicated by the  $\delta^{18}\text{O}$  (*N. dutertrei*) records. A: NIOP458. B: NIOP455. C: SO90-169KL.

The eolian-dust mean grain-size records of cores NIOP455 and SO90-169KL (Fig. 5.9B, C) show fairly positive correlations with their *Neoglobobadrina dutertrei*  $\delta^{18}\text{O}$  records. Small eolian-dust grain sizes, indicating relatively weak dust-transporting winter monsoons, are observed at both continental slope sites during the interstadials and interglacial stages (early) 1, 5.1, 5.3. An intensified winter monsoon occurred during isotope stages and substages (late) 1, 2-4, 5.2 and 5.4. Overall trends in both grain-size records are very similar to those in core NIOP458 (Fig. 5.9A). In addition to the glacial-interglacial variability of the eolian-dust grain size, the records of cores NIOP455 and SO90-169KL, and to a lesser extent also that of core NIOP458, display several correlatable high-frequency, partly high-amplitude variations in eolian-dust grain size that imply rapid and significant changes in winter-monsoon strength.

## LATE QUATERNARY VARIABILITY OF THE ASIAN MONSOONS

### *'Sedimentologic' Indicators of the Arabian Sea Monsoons*

The present-day monsoonal precipitation on the Indian subcontinent and the associated continental runoff and suspended-sediment discharge by the Indus River are largely confined to the summer season (Beg, 1977; Nair *et al.*, 1989), and are, therefore, coupled with the summer monsoon. Based on this scenario, Prins and Weltje (1999; Chapter 4) proposed that the end-member ratio (EM1+EM2):EM3 in core NIOP458, which depicts the relative importance of eolian dust supply with respect to fluvial mud supply to the upper Indus Fan, may be used as an indicator of continental runoff and, therefore, of summer-monsoon intensity. The good correlation between the eolian-dust grain-size record of core NIOP492 (Fig. 5.5A), which can only be related to summer-monsoon strength, and the continental aridity indicator of the cores from the north-eastern Arabian Sea (e.g. NIOP458, Fig. 5.5C) support this idea. The aridity-indicator records of cores NIOP455 and SO90-169KL presented in this study correlate reasonably well with the record of core NIOP458 (Fig. 5.8), indicating the 'regional validity' of the aridity signals. Likewise, from our results it appears that the overall trends in the eolian-dust grain-size records from the north-eastern Arabian Sea are very similar (Fig. 5.9) indicating the 'regional validity' of the winter-monsoon signals as well.

The next step is to compare our reconstruction of the late Quaternary variability in Arabian Sea monsoonal climate with available climate reconstructions of the Loess Plateau of central China. This comparison allows the recognition of a possible teleconnection between the Arabian Sea and East-Asian monsoon 'subsystems' during the late Quaternary. Firstly, a brief overview of paleoclimate reconstructions of the East-Asian monsoons on basis of loess-paleosol sequences of the Loess Plateau will be given.

### *'Sedimentologic' Indicators of the East-Asian Monsoons*

Loess, with interstratified paleosols, is widespread in north-central China and began to accumulate about 2.5 Ma ago (Liu *et al.*, 1985; Kukla and An, 1989). The loess-paleosol sequence on the Loess Plateau of central China has long been regarded a well-preserved record of global glacial-interglacial climate cycles during the Quaternary (Sasajima and Wang, 1984; Liu *et al.*, 1985; Kukla and An, 1989; Kukla *et al.*, 1990). Recent studies, however, suggest that the sequence can be viewed as an indicator record of variations in the East-Asian monsoonal climate (An *et al.*, 1991; Ding *et al.*, 1995; Porter and An, 1995; Xiao *et al.*, 1995; An and Porter, 1997), which -of course- forms part of the global glacial-interglacial climate cycles.

*Summer monsoon.*—

The parameter most widely used to make a quantitative distinction between loess units and paleosol units is magnetic susceptibility (e.g. Kukla and An, 1989). Loess units are characterised by a relatively low magnetic susceptibility and paleosols by a relatively high magnetic susceptibility. There is wide agreement that the enhancement of the magnetic susceptibility in the Chinese paleosols is mainly caused by high contents of ultrafinegrained magnetic minerals in the paleosols, but there is no general consensus about the sources and the causes of the magnetic susceptibility signal. Five explanations of enhancements of the magnetic susceptibility signal are currently in circulation (see Meng *et al.*, 1997, and references listed in it). The enhancement of magnetic susceptibility values are related to: (1) production of magnetic minerals due to post-depositional weathering and/or pedogenic processes, (2) concentration of magnetic minerals by decalcification and soil compaction, (3) concentration of magnetic eolian particles from distant sources during times when loess (silt with low magnetic susceptibility values) accumulation is slow, (4) heating of the loess by natural fires, (5) decomposition of vegetation. The first hypothesis is currently the most favoured one. The intensity of present-day pedogenesis on the Loess Plateau, inferred from the concentration of the ferrimagnetic iron oxides in modern soils, is strongly correlated with the amount of annual rainfall (Maher *et al.*, 1994). The magnetic susceptibility of the loess-paleosol sequence is therefore regarded as an indicator of paleorainfall, i.e., summer-monsoon strength (An *et al.*, 1991; Maher *et al.*, 1994).

Several studies (e.g. Liu *et al.*, 1985; Kukla and An, 1989; An *et al.*, 1991; Bloemendaal *et al.*, 1995; Porter and An, 1995; Xiao *et al.*, 1995) showed that the magnetic-susceptibility records from the Loess Plateau correlate closely with the marine oxygen-isotope record of Imbrie *et al.* (1984) and Martinson *et al.* (1987). High magnetic-susceptibility values, corresponding with the paleosols, are recorded during interglacial periods, whereas low magnetic susceptibility values, corresponding with loess units, are recorded during glacial periods. Interpretation of the magnetic-susceptibility record in terms of summer-monsoon strength thus indicates that the East-Asian summer monsoon was most intense during the interglacial periods.

*Winter monsoon.*—

The inland deserts of northern and north-western China are the source of the eolian dust deposited on the Loess Plateau. The regional decrease in the grain size and thickness of the loess (last glaciation) from north-west to south-east implies supply by a north-westerly wind system, a direction matching that of the present average winter monsoon. Several grain-size parameters of the loess have therefore been regarded as indicators of the winter-monsoon strength (e.g. Ding *et al.*, 1995; Porter and An, 1995; Xiao *et al.*, 1995; An and Porter, 1997). Ding *et al.* (1995), Xiao *et al.* (1995) and Vandenberghe *et al.* (1997) showed that the grain-size records correlate closely with the standard marine oxygen-isotope record (Imbrie *et al.* 1984; Martinson *et al.*, 1987). Periods with weakened winter monsoons, i.e., low grain-size values, coincide with interglacial periods. Periods with strengthened winter monsoons, i.e., high grain-size values, coincide with glacial periods.

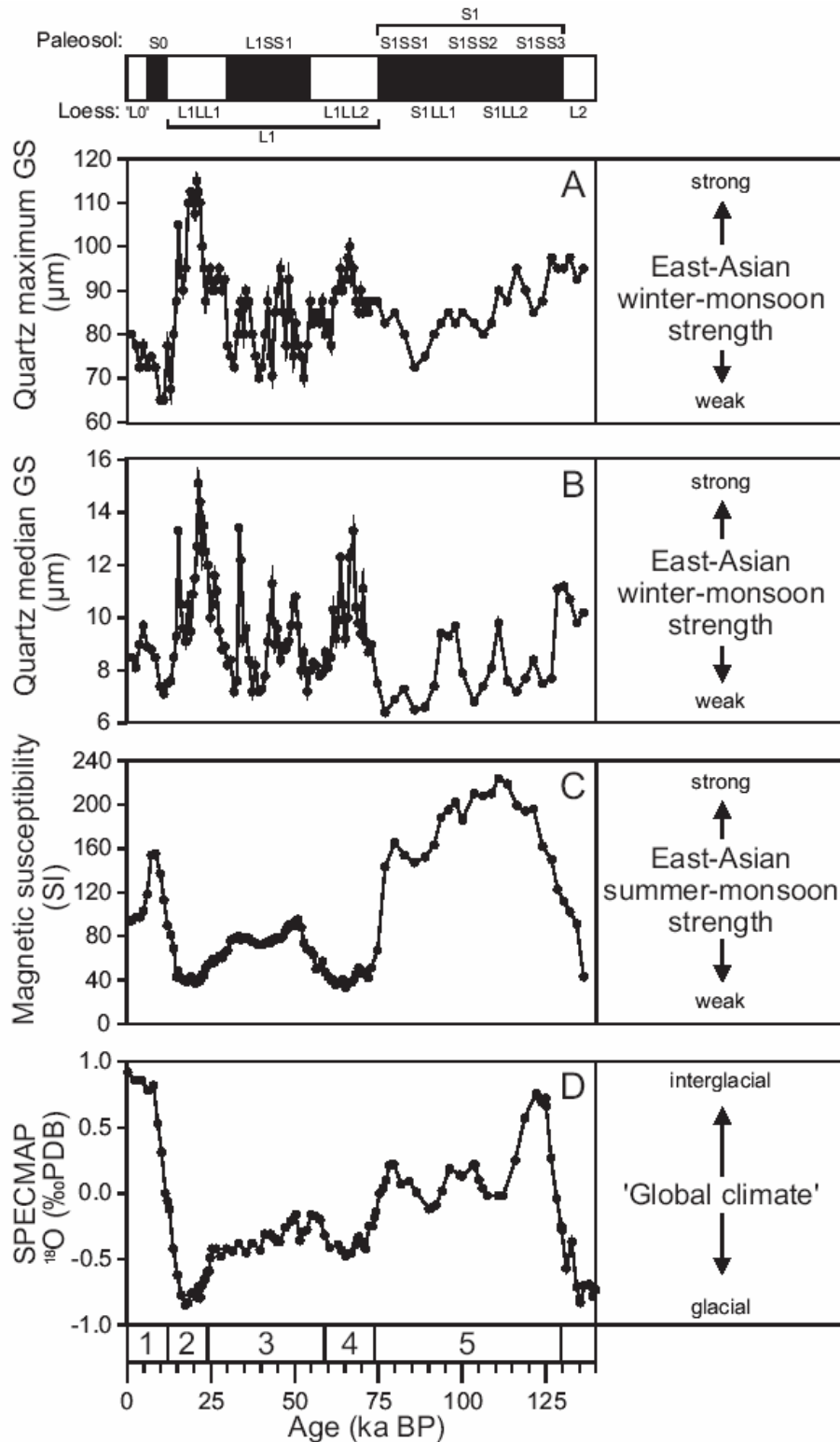


**Fig. 5.10** — Reconstruction of late-Quaternary variations in East-Asian monsoonal climate inferred from the Luochuan loess-paleosol sequence of the central Chinese Loess Plateau. Designation of lithogenic units follows Kukla and An (1989). Chronology of the Luochuan section follows Porter and An (1995). A, B: Maximum (A) and average (B) winter-monsoon strength is indicated by the maximum and median grain size of the quartz components in the loess (Xiao *et al.*, 1995). C: Summer-monsoon strength (continental aridity) is indicated by the magnetic susceptibility (An *et al.*, 1991). D: ‘Global climate’ indicated by SPECMAP oxygen-isotope record (Martinson *et al.*, 1987).

*Luochuan loess-paleosol sequence.—*

We will use the well-studied loess-paleosol sequence at two exposed sections (Potou, Xiaheimu) near Luochuan in the central part of the Chinese Loess Plateau (35°45' N, 109°25' E; see Fig. 5.1A) as the 'reference site' for the Loess Plateau. Magnetic susceptibility of bulk sediment samples and grain size of monomineralic quartz were analysed through the upper ~12 meter of the Luochuan section by An *et al.* (1991) and Xiao *et al.* (1995). Xiao *et al.* (1995) pointed out that the grain size of loess is only an approximate index of winter-monsoon strength because both paleosols and loess have been modified, to various degrees, by weathering processes that have produced pedogenic clays. As the quartz component of loess and paleosols is largely unaffected by weathering processes, Xiao *et al.* (1995) proposed to use the quartz median and maximum grain size as a more reliable indicator of average and maximum winter-monsoon strength. The chronostratigraphy ('grain-size model' after Porter and An, 1995) and the records of magnetic susceptibility (An *et al.*, 1991), quartz median and maximum grain size (Xiao *et al.*, 1995) of the last ~140 ka BP of the Luochuan loess-paleosol sequence are shown in Figure 5.10. Designation of lithogenic units in the Luochuan loess-paleosol sequence (e.g. S0, S1SS1 for paleosols and L1LL1, L2 for loess units) follows Kukla and An (1989).

## CORRELATION OF CLIMATE-INDICATOR RECORDS

### *Arabian Sea - Chinese Loess Plateau*

Xiao *et al.* (1995) concluded from the data presented in Figure 5.10 that on the Chinese Loess Plateau winter-monsoon strength is in general inversely related to the summer-monsoon strength. The climate-indicator records presented by Prins and Weltje (1999; Chapter 4) and this study indicate a very similar general relation between winter-monsoon and summer-monsoon strength for the Arabian Sea. Below we present correlations between our indicator records for the Arabian Sea monsoons and the indicator records for the East-Asian monsoons from the Chinese Loess Plateau.

#### *Summer monsoon.—*

The continental-aridity-indicator records of cores NIOP458, NIOP455 and SO90-169KL from the north-eastern Arabian Sea show a fairly strong correlation with the magnetic-susceptibility record of the Luochuan loess-paleosol sequence (Fig. 5.11). This correlation indicates that periods of most intense pedogenesis (formation of 'mature' paleosols S0 and S1 with high magnetic susceptibility values) on the Loess Plateau coincide with periods of highest continental runoff (negative extremes in  $\log((EM1+EM2):EM3)$  records) in the drainage area of the Indus River. Likewise, periods of enhanced eolian dust deposition (loess units 'L0', L1, L2 with low magnetic susceptibility values) on the Loess Plateau coincide with periods of increased aridity (positive extremes in  $\log((EM1+EM2):EM3)$  records) on the Indian Peninsula, i.e., the source area of the sediment deposited in the north-eastern Arabian Sea. Paleosol S1 is subdivided into three paleosols (S1SS1, S1SS2, S1SS3) and two loess units (S1LL1, S1LL2). Similar 'subdivisions' are present in the continental-aridity-indicator records from the north-eastern Arabian Sea: humid climate conditions around the Arabian Sea prevailed during isotope-substages 5.1, 5.3 and 5.5 and coincided with the formation of the

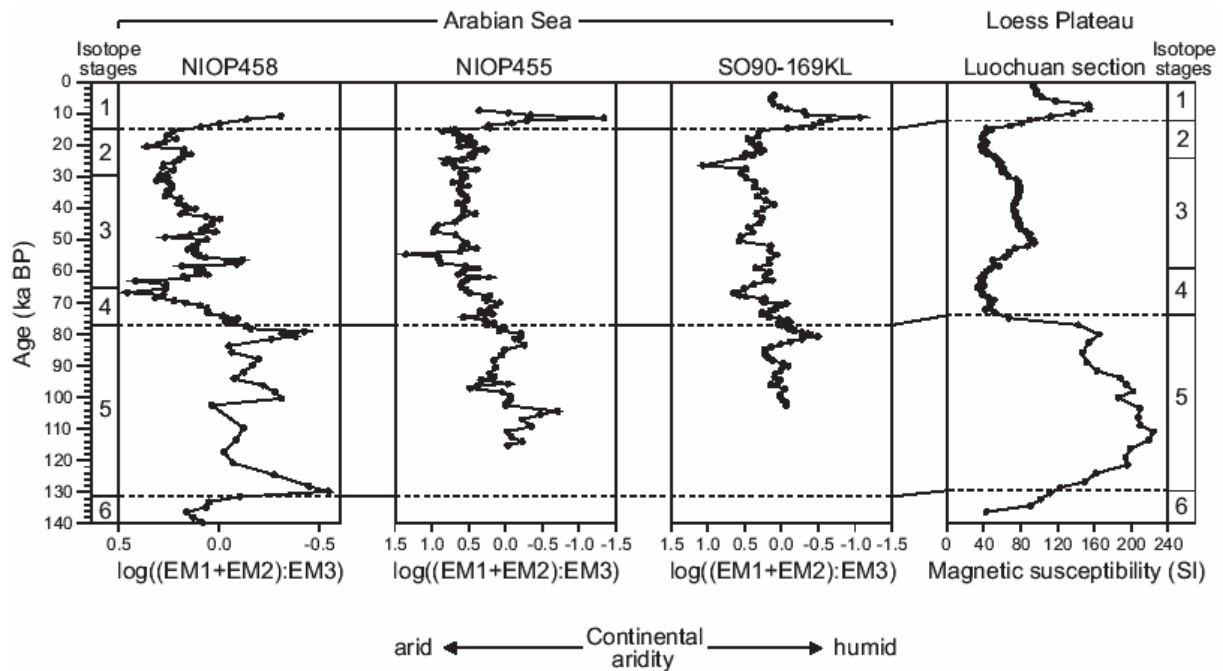


**Fig. 5.11** — Correlation between continental-aridity-indicator records from the north-eastern Arabian Sea and the Loess Plateau of central China. The  $\log((EM1+EM2):EM3)$  records of cores NIOP458, NIOP455 and SO90-169KL indicate the relative contribution of eolian dust (EM1+EM2) and fluvial mud (EM3) in sediments from the north-eastern Arabian Sea. The magnetic-susceptibility record of the Luochuan section from the central Loess Plateau is used as an indicator of the degree of pedogenesis (An *et al.*, 1991; Porter and An, 1995).

three paleosols S1SS1-3 on the Loess Plateau, and arid climate conditions prevailed during isotope-substages 5.2 and 5.4 and coincided with deposition of the two loess units S1LL1-2. A less clear correlation is observed between the period of formation of the ‘incipient’ paleosol L1SS1 on the Loess Plateau and increased continental humidity in the Arabian Sea as inferred from the end-member-ratio records of the cores from the north-eastern Arabian Sea.

Clemens and Prell (1990) noticed that the terrigenous mass-accumulation-rate record of a core from the Owen Ridge (applied as dust-source-aridity indicator) and the magnetic-susceptibility record from the Loess Plateau correlate well, from which they concluded the existence of a common aridity-forcing mechanism. Our results also indicate that the late Quaternary history of precipitation on the Loess Plateau mimics the history of precipitation in the Arabian Sea region. This suggests a physical connection between the regional summer monsoon patterns of the Arabian Sea and the Chinese Loess Plateau: the common aridity-forcing mechanism postulated by Clemens and Prell (1990). The Arabian Sea and East-Asian summer monsoon ‘subsystems’ thus experienced similar changes in intensity during the late Quaternary.

#### *Winter monsoon.*—

A physical connection between the Arabian Sea and the East-Asian winter monsoon patterns can also be demonstrated. Prins and Weltje (1999; Chapter 4) mentioned that the history of the winter monsoon in the north-eastern Arabian Sea, inferred from the eolian-dust grain-size record of core NIOP458 (Fig. 5.5B), matches the reconstruction of the intensity of the winter monsoon on the Loess Plateau by Xiao *et al.* (1995), inferred from their (long-term average) quartz median grain-size record of the Luochuan section. In both areas the winter monsoon

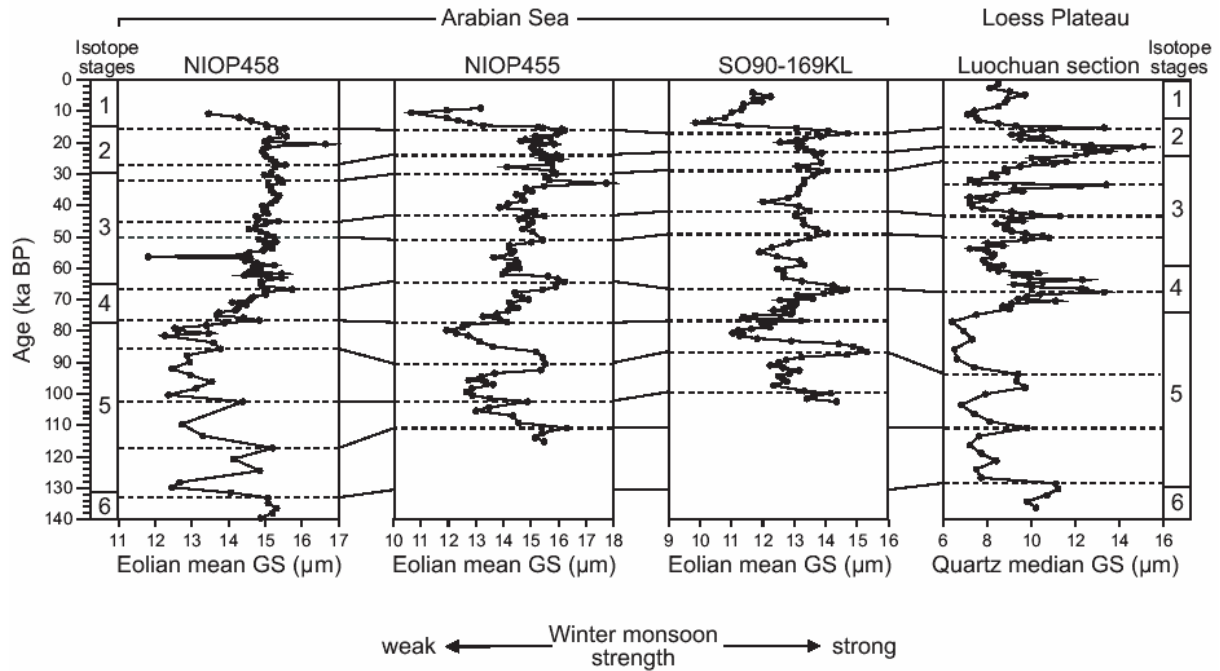


**Fig. 5.12** — Correlation between winter-monsoon-indicator records from the north-eastern Arabian Sea and the Loess Plateau of central China. The eolian dust mean grain-size records of cores NIOP458, NIOP455 and SO90-169KL and the quartz median grain-size record of the Luochuan section (Porter and An, 1995; Xiao *et al.*, 1995) show correlatable high-frequency variability in winter-monsoon intensity.

intensified during glacial periods and weakened during interglacial periods.

Next to the low-frequency (glacial-interglacial) variation in winter-monsoon strength, the eolian-dust grain-size records from both the Loess Plateau and the north-eastern Arabian Sea indicate high-frequency changes in winter-monsoon strength during the last glacial-interglacial cycle. A fairly strong correlation exists between a series of eolian-dust grain-size maxima in the last glacial records (last ~80 ka) from the Arabian Sea and the Luochuan section (Fig. 5.12). This implies that the last glacial history of winter-monsoon strength around the Arabian Sea mimics the history of winter-monsoon strength on the Loess Plateau closely. This suggests a physical connection between the regional winter monsoon patterns of the Arabian Sea and the Chinese Loess Plateau.

In conclusion, our high-resolution reconstruction of the late Quaternary Arabian Sea monsoonal climate, inferred from grain-size distribution data of Arabian Sea pelagic and hemipelagic siliciclastic sediments, corresponds well with reconstructions of the East-Asian monsoonal paleoclimate based on analysis of loess-paleosol sequences on the Loess Plateau of central China.

#### *Arabian Sea - North Atlantic*

Several recent studies presented evidence for teleconnections between the monsoonal climate system of the Chinese Loess Plateau (Porter and An, 1995; Chen *et al.*, 1997; Fang *et al.*, 1999), the Bay of Bengal (Colin *et al.*, 1998) and the Arabian Sea (Sirocko *et al.*, 1996; Reichert *et al.*, 1997; Schulz *et al.*, 1998) with the climate of the North Atlantic Ocean during the last glacial period. In general these studies suggest a correlation of either winter-monsoon strengthening or summer-monsoon weakening 'cycles' with 'cold events' in the North Atlantic region. These North Atlantic 'cold events' are characterised by massive iceberg release (Heinrich events: Heinrich, 1988; Bond *et al.*, 1992; Grousset *et al.*, 1993) into the

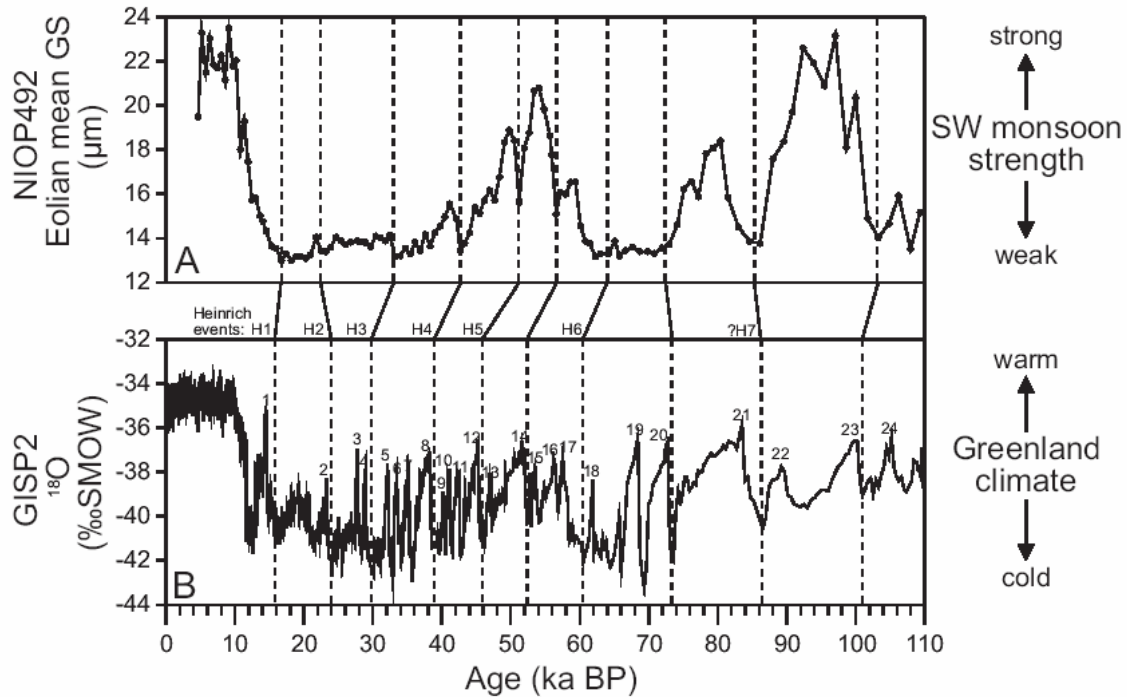


Fig. 5.13 — Comparison between (A) the eolian-dust grain-size record of core NIOP492 from the western Arabian Sea (summer-monsoon-indicator record) and (B) the  $\delta^{18}\text{O}$  record of the GISP2 ice core on Greenland (Grootes *et al.*, 1993). Position of interstadial numbers 1-24 and Heinrich events H1-H6 are indicated.

North Atlantic Ocean, unusually cold North Atlantic surface water (Bond cycles: Bond *et al.*, 1993) and cold air temperatures over Greenland (Dansgaard-Oeschger events: Dansgaard *et al.*, 1993; Grootes *et al.*, 1993).

Below we will investigate the potential correlations of the monsoon-indicator records for the Arabian Sea with the climate-indicator records for the North Atlantic region. Grootes *et al.* (1993) showed that the oxygen-isotope record of the GISP2 Greenland ice core matches closely the record of the GRIP ice core for the last glacial but that there are significant differences between the two records below interstadial 22. They suggested that the difference between the two ice cores is likely due to ice flow which may have altered the chronological sequences of the stratigraphy for the bottom part of one or both of the cores. Therefore, a closer look at the correlation between the Arabian Sea paleoclimate records and the  $\delta^{18}\text{O}$  record of the GISP2 ice core is only useful for the last ~110 ka BP.

#### *Summer monsoon.—*

The eolian-dust mean-grain-size record of core NIOP492 (0-110 ka BP) is plotted next to the  $\delta^{18}\text{O}$  record of the GISP2 ice core of central Greenland (Grootes *et al.*, 1993) in Figure 5.13. Comparison of the two climate-indicator records suggests that maxima in the NIOP492 eolian-dust grain-size record are correlated to individual warm interstadials (e.g. interstadial number 21, 24) and asymmetrical longer-term cooling cycles recognised in the GISP2 ice core and North Atlantic sediments (Bond cycles). The timing of the cooling cycles composed of interstadials 15-17, 13-14, 9-12 and 5-8 correlates with changes in the eolian-dust grain size in core NIOP492. Distinct eolian-dust grain-size minima in core NIOP492 have ages which correspond closely with the ages of major cold events over Greenland and the episodes of massive discharge of icebergs into the North Atlantic (Heinrich events: H1-H6). However, it

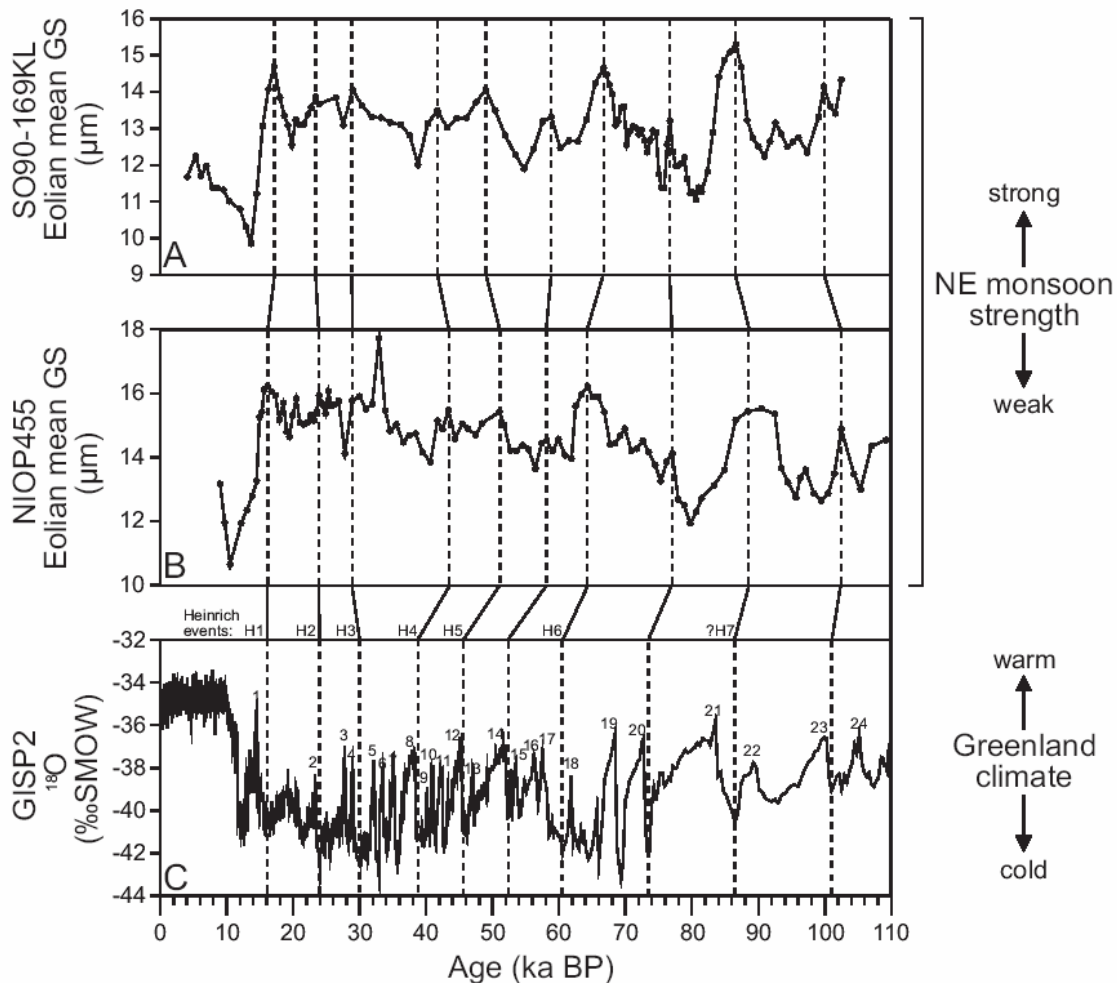


Fig. 5.14 — Comparison between the eolian-dust grain-size record of (A) core SO90-169KL and (B) core NIOP455 from the north-eastern Arabian Sea (winter-monsoon-indicator records), and (C) the  $\delta^{18}\text{O}$  record of the GISP2 ice core on Greenland (Grootes *et al.*, 1993). Position of interstadial numbers 1-24 and Heinrich events H1-H6 are indicated.

must be noted that some well-defined interstadials in the GISP2 ice core (e.g. interstadials 1, 19, 20, 22, 23) do not have ‘counterparts’ in the eolian-dust grain-size record of core NIOP492.

#### *Winter monsoon.—*

The eolian-dust grain-size records (0-110 ka BP) of cores SO90-169KL and NIOP455 are plotted next to the  $\delta^{18}\text{O}$  record of the GISP2 ice core in Figure 5.14. Both the pattern and timing of changes in winter-monsoon intensity in the north-eastern Arabian Sea are correlated with major warming-cooling trends over Greenland. The ages of the eolian dust grain-size maxima recorded in the Arabian Sea sediment cores agree fairly well with those of major cold episodes in the North Atlantic region. Heinrich events H1 to H6 correlate with pronounced grain-size maxima. The cold episodes recognised in the GISP2 ice core between interstadials 14-15, 20-21, 21-22 and 23-24 are correlated to grain-size maxima in the records from the north-eastern Arabian Sea as well.

In summary, our high-resolution reconstruction of the late Quaternary Arabian Sea monsoonal climate indicates that high-frequency changes in the Arabian Sea monsoonal climate can be correlated with high-frequency changes in the climate of the North Atlantic

region. Enhancements of summer-monsoon strength (and weakening of winter-monsoon strength) correlate with warm interstadials (Dansgaard-Oeschger events) and long-term cooling cycles (Bond cycles) in North Atlantic climate-indicator records. Enhancements of winter-monsoon strength (and weakening of summer-monsoon strength) correlate with major cold episodes in the North Atlantic region, including the Heinrich events, occurring at the end of the long-term cooling cycles.

## DISCUSSION

### *Summer-Monsoon Intensity and Continental Aridity*

Visual inspection of the eolian-dust grain-size record of core NIOP492 (Owen Ridge, western Arabian Sea) (Fig. 5.5A) indicates that low-frequency variations in this summer-monsoon-indicator record are dominated by the precession component of the Earth's orbital variations. This supports the conclusions of previous work on terrigenous grain-size records from the Owen Ridge (Clemens and Prell, 1990, 1991; Clemens *et al.*, 1996) indicating the importance of precessional insolation changes as a major driving force for the Indian summer monsoon. Moreover, the strength of the Indian summer monsoon appears to be sensitive to the extent of Northern Hemisphere glaciation as two 'expected' precession-punctuated grain-size 'maxima' during isotope stages 2 and 6 (around ~25-30 ka BP and ~145-150 ka BP) are reduced significantly.

The correlation between the low-frequency changes in the summer-monsoon indicator record from the western Arabian Sea (NIOP492) and the continental-aridity-indicator records from the north-eastern Arabian Sea (e.g. NIOP458) suggests a link between past variations in the Indian summer-monsoon intensity and continental aridity in the drainage basin of the Indus River. The general good correlation between the continental-aridity-indicator records from the north-eastern Arabian Sea and the magnetic-susceptibility record of the Luochuan section from the central Loess Plateau further indicates that changes in the precipitation patterns in both areas occurred simultaneously. From the latter observation we infer that low-frequency changes in the Indian and East-Asian summer monsoons occurred simultaneously, both forced by precessional insolation changes and the extent of Northern Hemisphere glaciation.

Our interpretations of the grain-size distribution data from the western and north-eastern Arabian Sea in terms of summer-monsoon strength and continental aridity indicate that a very pronounced change in climate is recorded at the transition from the last glacial period to the Holocene (~boundary between oxygen-isotope stage 2 and 1). Full glacial conditions are characterised by a relatively weak summer monsoon and arid climate conditions, whereas the early Holocene is characterised by a strong summer monsoon and humid climate conditions. Numerous studies reporting on continental records from hyperalkaline spring, lacustrine, fluvial and eolian sediment records (e.g. McClure, 1976; Sarnthein, 1978; Williams and Royce, 1982; Williams and Clarke, 1984; Clark and Fontes, 1990; Gasse *et al.*, 1991; Sukumar *et al.*, 1993; Gasse and Van Campo, 1994) provide support for wide-spread humid climate conditions during the early Holocene (~9 ka BP) in North Africa, the Middle East and west Asia. A possible link between variations in continental humidity and summer-monsoon strength around the Arabian Sea was also suggested by Sirocko *et al.* (1993). They studied a sediment core from the western Arabian Sea (East Sheba Ridge) in order to reconstruct changes in summer-monsoon intensity and aridity on the Arabian Peninsula, and presented evidence of a northward shift of the track of the summer monsoon during the early Holocene. The northward shift of the convergence between the SW summer monsoon and the

northwesterlies and its associated pattern of precipitation is held responsible for the observed increase in humidity on the continents bordering the Arabian Sea (see also Chapter 7).

*Teleconnection between the Asian Monsoons and the North Atlantic Climate*

*Arabian Sea monsoons.—*

High-frequency (sub-Milankovitch) changes in the Indian summer monsoon during the last glacial period, inferred from the eolian-dust grain-size record of core NIOP492, appear to correlate with high-frequency changes in the climate of the North Atlantic region. Sirocko *et al.* (1996) noticed that the late glacial minimum in intensity of summer-monsoon-driven upwelling productivity (inferred from low Ba content in core 74KL) and the maximum aridity in Arabia (inferred from high terrigenous content in core 74KL) coincided with the time of deposition of Heinrich Layer 1 in the North Atlantic Ocean. Although their records indicated that changes in the Indian summer monsoon correlate well with changes in the climate of the North Atlantic, Sirocko *et al.* (1996) stated that it is unclear whether this correlation is indicative of a true teleconnection during the summer season or that the strength of summer monsoon is moderated by the intensity of the winter monsoon. Our results from core NIOP492 support the conclusion drawn by Sirocko *et al.* (1996) that the Indian summer monsoon weakened during the time of deposition of Heinrich Layer 1. Moreover, our data indicate that the Indian summer monsoon weakened significantly during other episodes of extreme cold climate in the North Atlantic as well.

Reichart *et al.* (1997) presented evidence for high-frequency occurrence of episodes of deep convective turnover of the water column in the north-eastern Arabian Sea during the last glacial period. These episodes coincide with major cold events including the last six Heinrich events in the North Atlantic region. They inferred deep convective turnover from peak occurrences of planktonic foraminifera *G. truncatulinoides* and *G. crassaformis* and enhanced preservation of pteropods in sediment cores (including NIOP455) obtained from the Pakistan continental slope. The abundance of pteropods is positively correlated with the Sr/Ca ratio of the bulk sediment as their shells are made up of aragonite which has a higher Sr content than calcite (Sutherland *et al.*, 1984). Reichart *et al.* (1997) suggested that variations in deep convective turnover are due to variations in winter-monsoon intensity. Additional paleo-oceanographic evidence for an intensified winter monsoon during the last glacial period was presented by Duplessy (1982), Fontugne and Duplessy (1986) and Sarkar *et al.* (1990). The independent indicator records of winter-monsoon intensity (eolian-dust grain size) presented in this study supports the interpretations by Reichart *et al.* (1997) as roughly all the Sr/Ca peaks coincide with eolian-dust grain size maxima in cores from the Pakistan continental slope (in core NIOP455 as well as in core SO90-169KL; see also Chapter 8).

A detailed correlation between the north-eastern Arabian Sea sediment record (Murray Ridge, Pakistan continental slope) and the GISP2 Greenland ice core was presented by Schulz *et al.* (1998). They indicated the existence of a striking correlation between the GISP2  $\delta^{18}\text{O}$  record and various records from the Arabian Sea, including records of planktonic foraminifera *Globigerinoides ruber*  $\delta^{18}\text{O}$ , organic-carbon content and sonic velocity. The latter parameter was used as a 'proxy' of bulk compositional changes in the sediment. They found that fluctuations in these records clearly reflect Dansgaard-Oeschger events 1-24 and also Heinrich events 1-7. Schulz *et al.* (1998) stated that the variability in their organic-carbon records ('productivity') are due to changes in summer-monsoon strength. Laminated, organic-carbon-rich bands, correlating with the mild interstadial climate events in the North Atlantic region, are inferred to reflect strong summer-monsoon-induced productivity. In contrast,

bioturbated, organic-carbon-poor, and pteropod-rich bands, correlating with the cold stadial climate events in the North Atlantic region (including Heinrich events), are inferred to reflect periods of lowered summer-monsoon intensity. Our data fully supports their conclusion that the Greenland climate oscillations are correlated with monsoonal climate variability. However, our data indicate that the compositional changes in the records from the north-eastern Arabian Sea are not solely due to variations in summer-monsoon strength, but are due to variations in both summer- and winter-monsoon strength.

*East-Asian monsoons.*—

Independent evidence for high-frequency variations in the Indian and East-Asian summer monsoons during the last glacial period has been inferred from the sedimentary record of the Bay of Bengal and the Andaman Sea (Colin *et al.*, 1998) and the Chinese Loess Plateau (Chen *et al.*, 1997; Fang *et al.*, 1999).

Colin *et al.* (1998) studied the magnetic properties of two sediment records from the Bay of Bengal and the Andaman Sea from which they inferred the degree of chemical weathering of the hemipelagic (fluvial) sediments supplied by the Ganges-Bramaputra and Irrawaddy river systems. The degree of weathering was supposed to be indicative of the amount of precipitation in the sediment source area (eastern Himalayan and Burman ranges) and thus of the intensity of the Indian summer monsoon. High-frequency variations in their weathering record from the Bay of Bengal during the last 70 ka BP could be correlated with variations in the GISP2 ice core  $\delta^{18}\text{O}$  record. A low degree of weathering related to dry conditions on the continent is recorded during Heinrich events and cold stadial events, whereas during warm interstadial events the degree of weathering is high, pointing to humid conditions on the continent.

Chen *et al.* (1997) and Fang *et al.* (1999) reported high-frequency variations (0-60/75 ka BP) in various sediment characteristics (magnetic susceptibility, carbonate content, soil colour, grain size) in loess-paleosol sequences on the western Chinese Loess Plateau. Their data show that the East-Asian summer monsoon experienced rapid episodic pulse enhancements which are bundled into high-frequency weakening cycles. The pattern and timing of the summer monsoon enhancements show that these can be well correlated to most major warm (Dansgaard-Oeschger) episodes and long-term cooling (Bond) cycles of North Atlantic paleoclimate records.

The reconstructions of the last glacial Asian summer monsoon variability presented by Colin *et al.* (1998), Chen *et al.* (1997) and Fang *et al.* (1999) agree well with our observations on core NIOP492. Both Colin *et al.* (1998) and Fang *et al.* (1999) suggested that the summer monsoon and the North Atlantic climate are connected via the effects of the westerly winds. Fang *et al.* (1999) explained the link between summer monsoon enhancements and warm episodes in the North Atlantic by temporary weakening and northward shift of the westerlies causing a weak expansion of the summer monsoon over the western Loess Plateau. We suggest that a true atmospheric teleconnection between the North Atlantic and the Arabian Sea during the summer season, according to the mechanism postulated by Fang *et al.* (1999), explains well the observed variability of the Arabian Sea summer monsoon.

The high-frequency eolian-dust grain-size maxima in the north-eastern Arabian Sea records presented in this study correlate with both eolian dust grain-size maxima in the Luochuan loess-paleosol sequence on the central Loess Plateau and with major cold episodes in the North Atlantic region. Porter and An (1995) showed that the ages of the high-frequency grain-size maxima in the loess (0-80 ka BP) of the Luochuan section match closely the ages of major cold episodes in the North Atlantic region including the ages of the last six Heinrich events. The grain-size record of a section on the western Loess Plateau presented by Chen *et*

*al.* (1997) supports fully the findings of Porter and An (1995). From the correlation between their grain-size record and the North Atlantic paleoclimate records, Porter and An (1995) inferred that the intensity of the East-Asian winter monsoon is linked to the climate system of the North Atlantic region by the effect of westerly winds. Their 'model' is also valid for the Arabian Sea winter monsoon as our results indicate that the winter monsoon systems of the Arabian Sea and the Loess Plateau were linked with each other and with the climate of the North Atlantic region.

## CONCLUSIONS

1. The grain-size distribution of eolian dust, which is calculated by subtracting the modelled contribution of fluvial mud from the grain-size distribution of the entire siliciclastic fraction, is a high-resolution paleoclimate indicator of wind strength. Intensity of the summer monsoon is in general inversely correlated with the intensity of the winter monsoon. An intensified summer monsoon is recorded in the western Arabian Sea (Owen Ridge) during interglacials, whereas an intensified winter monsoon is recorded in the north-eastern Arabian Sea (upper Indus Fan, Pakistan continental slope) during glacials.
2. The ratio of eolian and fluvial contributions to sediments in the north-eastern Arabian Sea is a high-resolution paleoclimate indicator of continental aridity, which closely matches the marine oxygen-isotope record. Increased continental aridity is recorded during glacials, and increased continental humidity during interglacials. Aridity in the drainage area of the Indus River is closely correlated with the intensity of the Arabian Sea summer monsoon.
3. Intensification of the Arabian Sea and East Asian summer monsoon 'subsystems' resulted in synchronous changes in regional precipitation patterns: periods of increased Indus River runoff coincide with periods of pedogenesis on the Chinese Loess Plateau. Weakening of both summer monsoon 'subsystems' resulted in increased eolian dust deposition on the Loess Plateau and in the Arabian Sea. Simultaneous changes in the Arabian Sea and East-Asian winter-monsoon intensity are evidenced by simultaneous changes in the grain size of eolian dust deposited in the north-eastern Arabian Sea and on the Chinese Loess Plateau.
4. High-frequency variability in our Arabian Sea monsoon-indicator records are correlated with high-frequency changes in the climate-indicator records of the North Atlantic region. Enhancements of summer-monsoon strength (and weakening of winter-monsoon strength) correlate with warm interstadials (Dansgaard-Oeschger events) and long-term cooling cycles (Bond cycles) in North Atlantic climate-indicator records. Enhancements of winter-monsoon strength (and weakening of summer-monsoon strength) correlate with major cold episodes in the North Atlantic region, including the Heinrich events, occurring at the end of the long-term cooling cycles. Correlation between climate events in the Arabian Sea, China and the North Atlantic during the last glacial period are obvious. We suggest that the monsoons of Asia and the climate of the North Atlantic region were linked by the effect of westerly winds.

## ACKNOWLEDGEMENTS

We are indebted to all scientists, technicians, and crew members on board R.V. *Tyro* for their commitment during the Netherlands Indian Ocean Programme. We thank U. von Rad (BGR, Hannover, BRD) who kindly allowed us to sample PAKOMIN core SO90-169KL. We thank P. Anten, A. van Dijk, G. Ittman, M. Reith and G. van 't Veld for analytical support. S.C. Porter (University of Washington, USA) and Jule Xiao (Institute of Geology, Chinese Academy of Sciences, Beijing, China) are thanked for their support as they kindly provided the data of the Luochuan section from the Loess Plateau.



## CONTROLS ON LATE PLEISTOCENE-HOLOCENE SEDIMENTATION ON THE INDUS FAN

M.A. Prins<sup>1</sup>, G. Postma<sup>1</sup>, J. Cleveringa<sup>1</sup>, U. von Rad<sup>2</sup>, A. Cramp<sup>3</sup> and N.H. Kenyon<sup>4</sup>

### ABSTRACT

Long-range side-scan sonar (GLORIA) data have revealed a distributary complex of large channel-levee systems radiating from the mouth of the Indus Canyon. Lower-order distributary complexes, each consisting of 7 or more smaller channel-levee systems, have been developed on the middle Indus Fan. Sediment cores from the Indus Canyon and the middle Indus Fan are studied in order to reconstruct the timing of turbidite sedimentation on the fan.

Sediment cores from the middle fan show that turbidite sedimentation on the second-youngest large channel-levee system ceased and switched to the youngest channel-levee system at the transition from oxygen-isotope stage 3 to 2 (~24.8 <sup>14</sup>C ka BP). Turbidite sedimentation on the youngest channel-levee system ceased during the last deglaciation (~11.5 <sup>14</sup>C ka BP). The Indus Fan is draped by a pelagic calcareous ooze of approximately Holocene age. Within the main feeder channel and Indus Canyon, turbidite sedimentation continued up to (sub)recent times. The geochemical, mineralogical and grain-size characteristics of the (hemi-) pelagic sediments on the middle Indus Fan are analysed to determine temporal variations in the flux and the provenance of the terrigenous sediment fraction. Terrigenous sediments deposited on the middle fan during the last glacial period were mainly supplied by the Indus River (fluvial sediments) while during the Holocene they were derived predominantly from the Arabian Peninsula (eolian dust).

The timing and pattern of channel-levee system evolution will be discussed in relation to controlling autocyclic and allocyclic (e.g. sea-level fluctuations) mechanisms. Moreover, a comparison between the timing of active growth of the Indus Fan, and erosion and deposition in the Indus Canyon and on the adjacent outer shelf and continental slope is made. It appears that erosional and depositional cycles on the Indus Fan are strongly controlled by changes in sea level.

### INTRODUCTION

Sediment transport by turbidity currents is the dominant process on deep-sea fan systems whereby terrigenous sediment is transported from the continents and continental margins to the deep sea. The rate of terrigenous sediment input to the deep sea is controlled by mechanisms including sea-level changes, climate changes and tectonic activity. Next to these allocyclic mechanisms, internal (autocyclic) mechanisms may cause avulsions of canyons and

---

<sup>1</sup> Institute for Paleoenvironments and Paleoclimate Utrecht (IPPU), Faculty of Earth Sciences, Utrecht University, P.O. Box 80021, 3508 TA Utrecht, The Netherlands

<sup>2</sup> Bundesanstalt für Geowissenschaften und Rohstoffe (BGR), PF510153 Hannover, Germany

<sup>3</sup> Department of Geology, University of Wales, Cardiff CF1 3YE, United Kingdom

<sup>4</sup> Institute of Oceanographic Sciences, Deacon Laboratory, Surrey GU8 5UB, United Kingdom

channels. The autocyclic mechanisms include slumping resulting in channel plugging and sediment build-ups within channels, and, as a consequence of these sedimentary processes, the tendency of channels to occupy the adjacent topographically low inter-channel areas.

Despite the variety of controlling factors, changes in sea level are widely accepted as the dominant factor controlling turbidite deposition on large deep-sea fan systems like the Amazon Fan, the Mississippi Fan and the Bengal Fan (Manley and Flood, 1988; Bouma *et al.*, 1989; Feeley *et al.*, 1990; Weimer, 1990; Kolla and Perlmutter, 1993; Weber *et al.*, 1997). For the Indus Fan a similar process-response model is proposed (McHargue and Webb, 1986; Kolla and Coumes, 1987; Kolla and Macurda, 1988; McHargue, 1991; Kenyon *et al.*, 1995; Von Rad and Tahir, 1997). From these studies it appeared that, in general, sea-level fall and lowstand enhances turbidite deposition on deep-sea fan systems, whereas sea-level rise reduces sediment supply to deep-sea fan systems.

In this chapter we focus on the evolutionary pattern of the youngest large channel-levee system of the Indus Fan against the background of late Pleistocene and Holocene changes in sea level and climate. The geochemical, mineralogical and grain-size characteristics of the (hemi-) pelagic sediments on the middle Indus Fan were analysed to determine temporal variations in the flux and the provenance of the terrigenous sediment fraction. By studying the cores from the middle fan, we were able to date a major fan-lobe switch and the duration of turbidite deposition on the youngest large channel-levee system. We will show that the fluctuations in sea level of the last ~25 <sup>14</sup>C ka triggered large-scale reorganisations in channel-levee pattern and that avulsion for smaller channel-levee systems is unrelated to sea-level changes.

### *Geological Setting of the Indus Fan*

With a length of 1600 km and a maximum width of 1000 km, covering an area of approximately 1.1-1.25 million km<sup>2</sup> (McHargue and Webb, 1986; Kolla and Coumes, 1987), the Indus Fan is the second largest deep-sea fan in the world. The Indus Fan is developed off the passive continental margin of Pakistan-India and is bounded by the Chagos-Laccadive Ridge in the east, by the Owen-Murray Ridges in the west, and in the south by the Carlsberg Ridge, which is a portion of the Central Indian Ridge (Fig. 6.1). Another topographic feature is the Lakshmi Ridge that divides the Arabian Basin into two sub-basins, referred to as the Western and Eastern Basin by Naini and Kolla (1982).

The initiation of Indus Fan sedimentation (middle Oligocene - late Miocene) is in time related to the uplift of the Himalayan mountain range, possibly combined with sea-level lowering (Kolla and Coumes, 1987). In the shelf and slope area near the Indus Delta, three canyon complexes, recognised on seismics, merge landward into one extensive erosional zone referred to as the Indus Trough (McHargue and Webb, 1986; Kolla and Coumes, 1987). The canyon complexes served as conduits for *en mass* sediment transport to the deep sea. Several large channel-levee systems radiate from each canyon complex, and form a channel-levee complex. The youngest complex comprises the recently active Indus Canyon. The long-term lateral eastward shift of the channel-levee complexes, corresponding with the eastward shifts of the canyons, has been associated with uplift of the Murray Ridge. The orientation of the channels within the large channel-levee complexes is related to basin-floor relief inherited from tectonic evolution and depositional history (Droz and Bellaiche, 1991). Kolla and Coumes (1987) and Kolla and Schwab (1995) showed that both the canyons and the channels in the upper fan migrated both gradually and in discrete 'jumps' by channel avulsion.

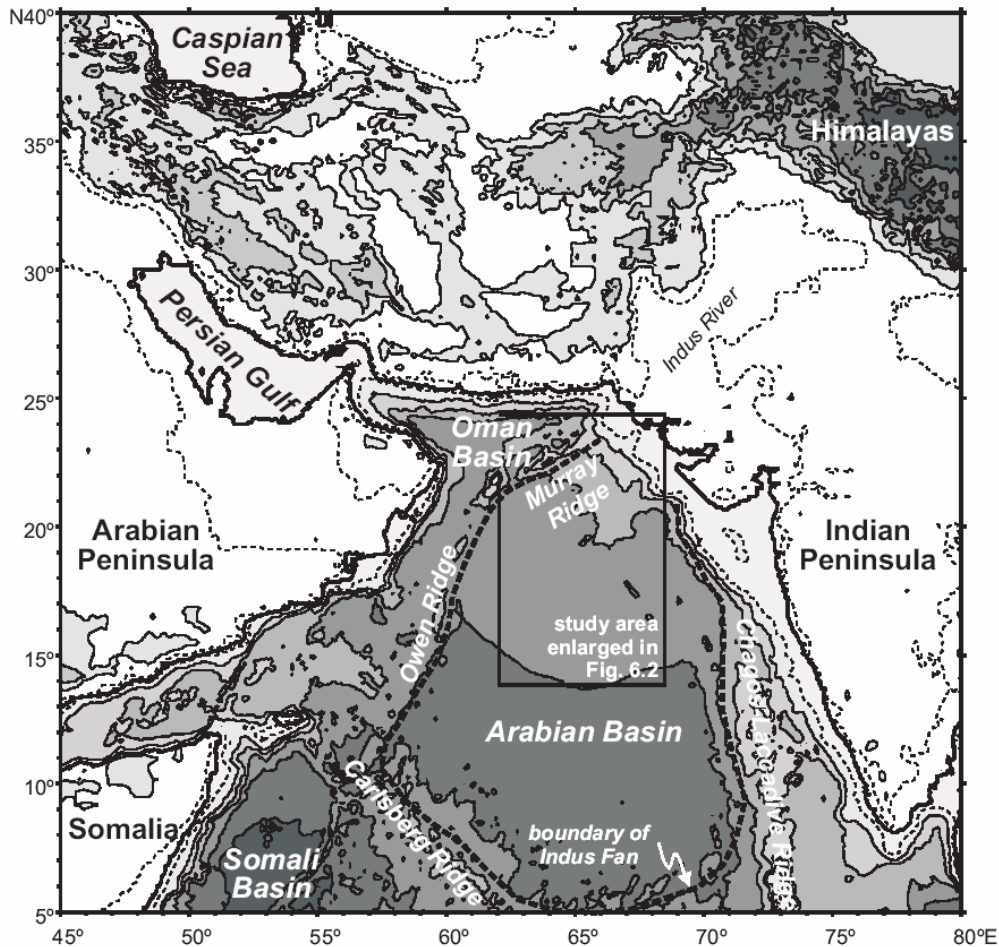


**Fig. 6.1** — Topography and bathymetry of the Arabian Sea and its surrounding land masses at a 1000 m contour interval (dashed contour lines are -125 and +200 m). The Indus Fan exhibits clearly the smooth fan morphology within the deep Arabian Basin. The GLORIA long-range side-scan sonar (Kenyon *et al.*, 1995) covered large parts of the area in the box of which a blow-up is shown in Figure 6.2. Topographic data from U.S. National Geophysical Data Center/World Data Center A for Marine Geology and Geophysics.

The youngest channel-levee complex, in particular its two youngest large channel-levee systems, has been mapped in detail using long-range side-scan sonar (GLORIA) (Kenyon *et al.*, 1995). The study of Kenyon *et al.* (1995) resulted in a new scheme for labelling the Indus Fan channels on the basis of their relative age (Fig. 6.2). The main channel of the youngest system A has levees up to 80 km wide and up to 1100 m thick. On the middle fan, about 500 km basinward from the mouth of the Indus Canyon, system A branches into a distributary pattern of at least 7 smaller, laterally shingling, channel-levee systems, of which only one was active at a time. These smaller systems are up to 50 km wide and up to 60 m thick. East of the depositional lobe of system A, older small channel-levee systems of system B are found. It has been suggested that channel-levee system B may have been fed by the same source, but through another, less prominent canyon: the Saraswati Valley (Kolla and Coumes, 1987; Kenyon *et al.*, 1995). The channels belonging to systems A and B can be traced throughout the area mapped by GLORIA. On the lower fan, south of the area mapped by GLORIA, the channels terminate into sandy depositional lobes. This is indicated by decreasing channel dimensions (depth, width) and the high percentage and large maximum thickness of silty/sandy turbidites within the upper 5 meters of the sediment column (Kolla and Coumes, 1987). Only the channel of the youngest small channel-levee system (A1) terminates in the

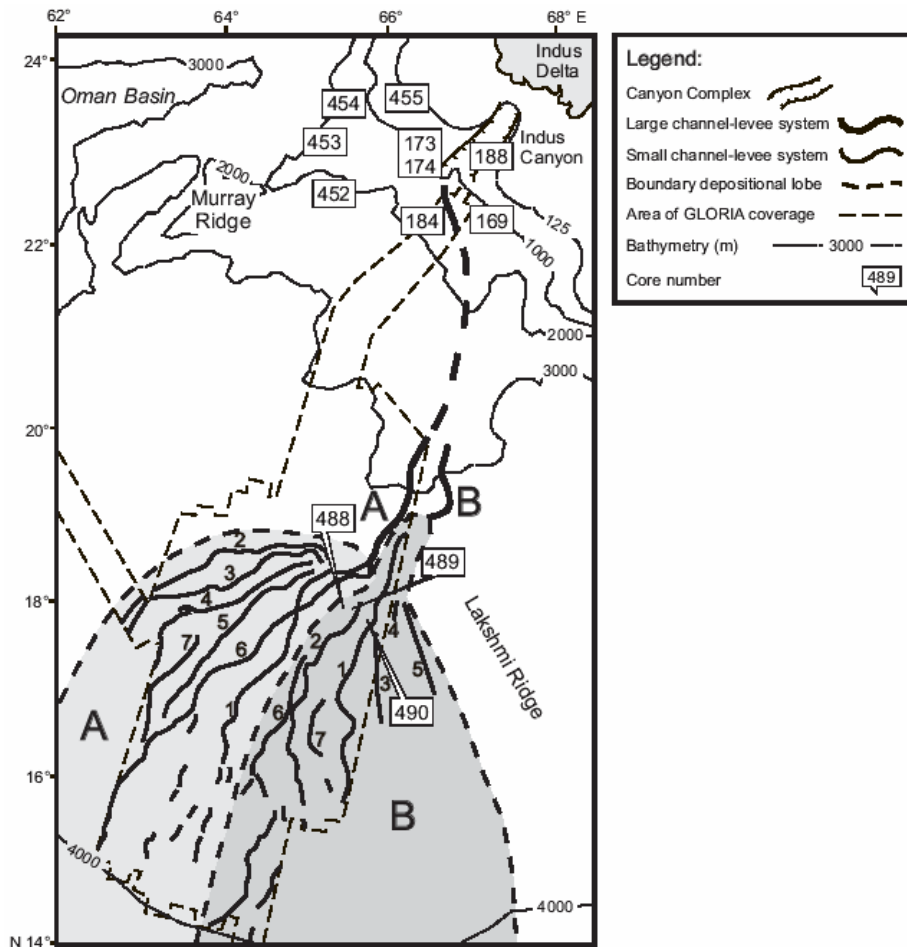


**Fig. 6.2** — Interpretation of the GLORIA mosaic after Kenyon *et al.* (1995). Shown are the Indus Canyon and part of the complex of associated large channel-levee systems (A is younger than B), and of the small channel-levee systems (A1 is younger than A2, etc.). Location of sediment cores is indicated (see also Table 6.1).

area mapped by GLORIA at a distance of over 1100 km from the mouth of the Indus Canyon. The main focus of our study is to determine the timing of the avulsion of channel B and the associated initiation of channel A, and to determine the timing of the avulsions of the smaller channels on the depositional lobe of system A.

## MATERIAL AND METHODS

Sediment cores used in this study were collected during the Netherlands Indian Ocean Programme (NIOP) on RV *Tyro* (Van der Linden and Van der Weijden, 1994) and during the SO90 PAKOMIN Expedition on RV *Sonne* (Von Rad *et al.*, 1995). Cores were collected from (1) the axial valley of the Indus Canyon (SO90-173KG, SO90-174SL, SO90-184KL and SO90-188KL), (2) the eastern levee of the major channel just south of the canyon (SO90-169KL) and (3) the levees of two channels of the large channel-levee system B on the middle Indus Fan (NIOP488, NIOP489 from channel B2 and NIOP490 from channel B1): see Figures 6.2, 6.3 and 6.4. Detailed information on core locations is listed in Table 6.1.

Unsplit 1-m-sections of cores NIOP452, NIOP454, NIOP455, NIOP488, NIOP489 and NIOP490 were logged at 2 cm intervals with a GEOTEC automated multisensor corelogger to

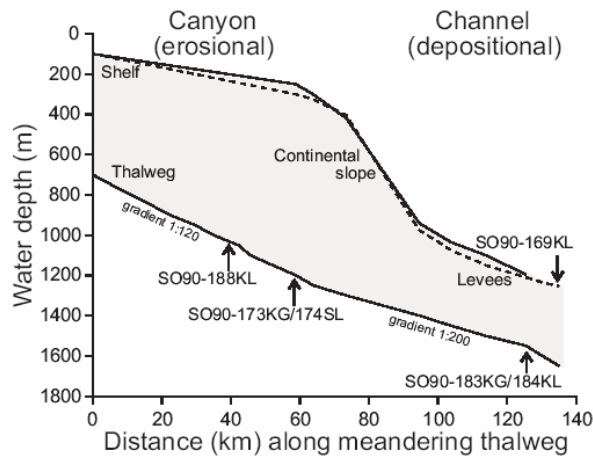


Fig. 6.3 — Longitudinal profile along the meandering thalweg and both flanks (eastern: dashed line) of the Indus Canyon, extending from the outermost shelf to the upper Indus Fan. An abrupt decrease in channel gradient is observed around 1250 m water depth. Within this zone the Indus Canyon reaches its maximum depth of 900 m and changes from an exclusively erosional feature into a depositional leveed channel. Approximate location of sediment cores is indicated. Profiles are based on the bathymetry map presented by Von Rad and Tahir (1997).

measure the whole-core magnetic susceptibility and gamma-ray transmissivity (Reichert *et al.*, 1994). The magnetic susceptibility was measured with a Bartington Instruments' MS2 pass-through loop sensor. Gamma-ray transmissivity was measured by placing the core between a  $^{137}\text{Cs}$  gamma-ray source and a shielded scintillation counter using a gamma-ray count period of 10 seconds. The gamma-ray transmissivity is expressed as the ratio between the gamma ray count of a sample relative to the gamma ray count of a blank, i.e., the gamma ray count of a measurement with no material between source and detector.

From the splitted 1-m-sections of core NIOP489 samples were taken from the hemipelagic mud and calcareous ooze units (upper ~8 m) at 5-10 cm intervals. Muddy sediment in core SO90-188KL was sampled at irregular intervals (4-38 cm) as a consequence of the presence of sand beds. Fixed volume samples were taken with a syringe, and were dried and weighted for measurement of dry-bulk density ( $\text{g}/\text{cm}^3$ ). One set of subsamples was washed and sieved (150-595  $\mu\text{m}$  fraction) to collect the fauna; another set of dried bulk subsamples was used for analysis of the elemental chemical composition of the sediment (ICP). Wet subsamples were used for analysis of grain size and mineralogical composition (XRD).

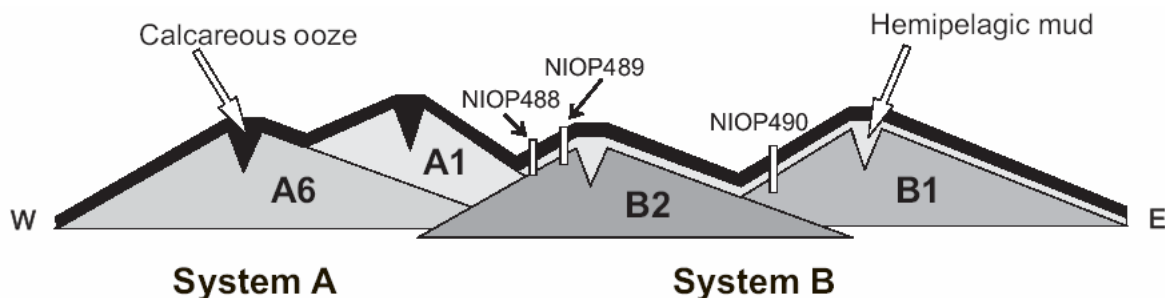


Fig. 6.4 — Schematic cross section of the channel-levee systems of the middle Indus Fan. After turbidite sedimentation switched from system B to system A, system B was draped by a hemipelagic mud unit time-equivalent with system A. At present the Indus Fan as a whole is draped by calcareous ooze. Location of cores is schematically indicated.

**TABLE 6.1 — SEDIMENT CORES USED IN THIS STUDY**

Core number	Position (Lat. N, Long. E)	Area	Water depth (m)
SO90-169KL	22°38'.5, 66°49'.3	channel levee, Indus Canyon	1283
SO90-173KG	23°02'.4, 66°53'.1	axial valley, Indus Canyon	1192
SO90-174SL	23°02'.4, 66°53'.0	axial valley, Indus Canyon	1186
SO90-184KL	22°39'.6, 66°42'.4	axial valley, Indus Canyon	1535
SO90-188KL	23°07'.9, 67°02'.8	axial valley, Indus Canyon	1012
NIOP452	22°56'.9, 65°28'.4	lower Pakistan continental slope	1992
NIOP454	23°27'.6, 65°52'.0	middle Pakistan continental slope	1221
NIOP455	23°33'.4, 65°57'.0	middle Pakistan continental slope	1002
NIOP488	17°53'.6, 65°28'.2	channel levee B2, middle Indus Fan	3437
NIOP489	17°56'.0, 65°52'.5	channel levee B2, middle Indus Fan	3375
NIOP490	17°29'.3, 65°57'.3	channel levee B1, middle Indus Fan	3450

Carbonate was removed from the sediment samples by treatment with excess of 3% HCl solution, in order to measure the grain-size distribution of the siliciclastic fraction. The grain-size distributions of the bulk samples and non-carbonate (siliciclastic) fractions were measured on a Malvern 2600 laser diffraction size analyser using a lens with 100 mm focal length. This configuration provided measurements in 32 discrete size classes between 0.5 and 188  $\mu\text{m}$  (equivalent volume diameter; see Table 2.1 in Chapter 2).

Prior to the XRD analysis, carbonate was removed from the sediment samples by treatment with excess of 5% HAc solution. Separation of the clay fraction was done by centrifuging. The supernatant suspension (containing the clay fraction) was concentrated and added on a glass slide. Ethylene glycol-solvated samples were used for qualitative and 'semi-quantitative' analysis of the minerals present in the clay fraction. Analyses were performed on a Philips PW 1700 diffractometer (Cu- $\alpha$  radiation). The results are expressed as reflection peak height ratios, the latter being a 'semi-quantitative' measure of the relative abundances of the different clay minerals.

Samples for ICP analysis were thoroughly ground in an agate mortar prior to an  $\text{HClO}_4$ ,  $\text{HNO}_3$ , HF acid digestion. The final residue was taken up in 1 M HCl. The elemental chemical composition was measured using an ICP-ES (ARL 34000). The carbonate content was calculated from the total Ca concentration, using a correction for clay-derived Ca;  $\text{CaCO}_3 = 2.5(\text{Ca}_{\text{tot}} - (\text{Ca}/\text{Al}_{\text{clay}} \times \text{Al}_{\text{tot}}))$ , where  $\text{Ca}/\text{Al}_{\text{clay}}$  is 0.345 (Turekian and Wedepohl, 1961). This method works well with  $\text{CaCO}_3$ -rich sediments, but is in error with sediments poor in  $\text{CaCO}_3$  (Shimmield and Mowbray, 1991). To assess the influence of sediment source versus grain size on the chemical composition of the siliciclastic sediment fraction, we analysed the composition of selected size ranges (silt fractions B, C, D with modal grain sizes of  $\sim 5$ ,  $\sim 15$ ,  $\sim 40$   $\mu\text{m}$ ) of sediment samples. The silt fractions were extracted from the bulk siliciclastic fractions by selective settling in settling tubes.

The oxygen-isotope composition ( $\delta^{18}\text{O}$ ) of 100 hand-picked specimens of planktonic foraminifera *Neoglobobadrina dutertrei* (150-595  $\mu\text{m}$  sieve fraction) per sample was

TABLE 6.2 — AMS <sup>14</sup>C DETERMINATIONS

Core number	Sample number	Core depth (m)	Analysed fraction	<sup>14</sup> C age* (yrs BP)	Error (yr)
NIOP489	489/56	5.37	foraminifera‡	24820	-180/+190
NIOP489	489/102	1.19	foraminifera‡	12210	70
NIOP489	489/107	0.85	foraminifera‡	12700†	80
NIOP489	489/113	0.53	foraminifera‡	9970	70
SO90-188KL	188/33	3.24	shell	10590	70
SO90-188KL	188/31	3.09	organic carbon	1801	38

\* A -400 yr correction has been made to allow for the estimated age of sea water (Bard, 1988).

† Age is stratigraphically not consistent; data not incorporated in age model.

‡ Planktonic foraminifera *Globorotalia menardii*.

measured on a VG SIRA 24 mass spectrometer. Replicate analyses and repetitive analyses of the laboratory standard showed a standard deviation of 0.1 ‰ for  $\delta^{18}\text{O}$ .

Four samples from core NIOP489 and two samples from core SO90-188KL were dated using the accelerator mass spectrometry (AMS) <sup>14</sup>C method (Table 6.2). In case of the NIOP489 samples the datings were executed on 10 mg of hand-picked specimens of planktonic foraminifera *Globorotalia menardii*. Because of the scarcity of foraminifera in core SO90-188KL, the datings were performed on organic carbon or shell material. A -400-yr correction was applied for the age of the sea water (Bard, 1988).

Linear sedimentation rates (LSR, in cm/ka) were assumed between the (partly AMS-<sup>14</sup>C dated) age calibration points. Total mass accumulation rates (total MAR = LSR × DBD; MAR in g/cm<sup>2</sup>ka) were calculated using the dry-bulk density (DBD, in g/cm<sup>3</sup>) of the sediment. Fractionated MAR's, i.e., carbonate MAR and non-carbonate (siliciclastic) MAR, were determined by multiplying the total MAR with the carbonate fraction and with the siliciclastic fraction (1 - carbonate fraction).

## RESULTS

### *Middle Indus Fan*

#### *Correlation of sediment records.—*

All three piston cores (NIOP488, NIOP489, NIOP490) from the middle fan (Fig. 6.2) revealed a similar sedimentary succession which consists of a sequence of silty-sandy turbidites draped by a very homogenous hemipelagic mud unit, which in turn is overlain by a calcareous ooze unit (Fig. 6.4). Within the hemipelagic mud unit a few silty-sandy turbidites occur.

A lithostratigraphic correlation was established using the whole-core magnetic susceptibility and gamma-ray transmissivity records of the cores (Fig. 6.5). Magnetic susceptibility is a measure of the concentration of magnetic material in the sediment. Within pelagic and hemipelagic sediments, the down-core variations in magnetic susceptibility mainly reflect variations in the relative concentration of terrigenous material (Kent, 1982). Magnetic susceptibility records of (hemi-) pelagic sediments are commonly inversely correlated to carbonate content, and have been proven useful as a tool for inter-core correlation (e.g. Reichart *et al.*, 1994; Robinson, 1993). The gamma-ray transmissivity is a function of sediment grain density and porosity and is thus a measure for wet bulk density ('high' gamma-ray transmissivity values indicate 'low' wet bulk density values). The magnetic-

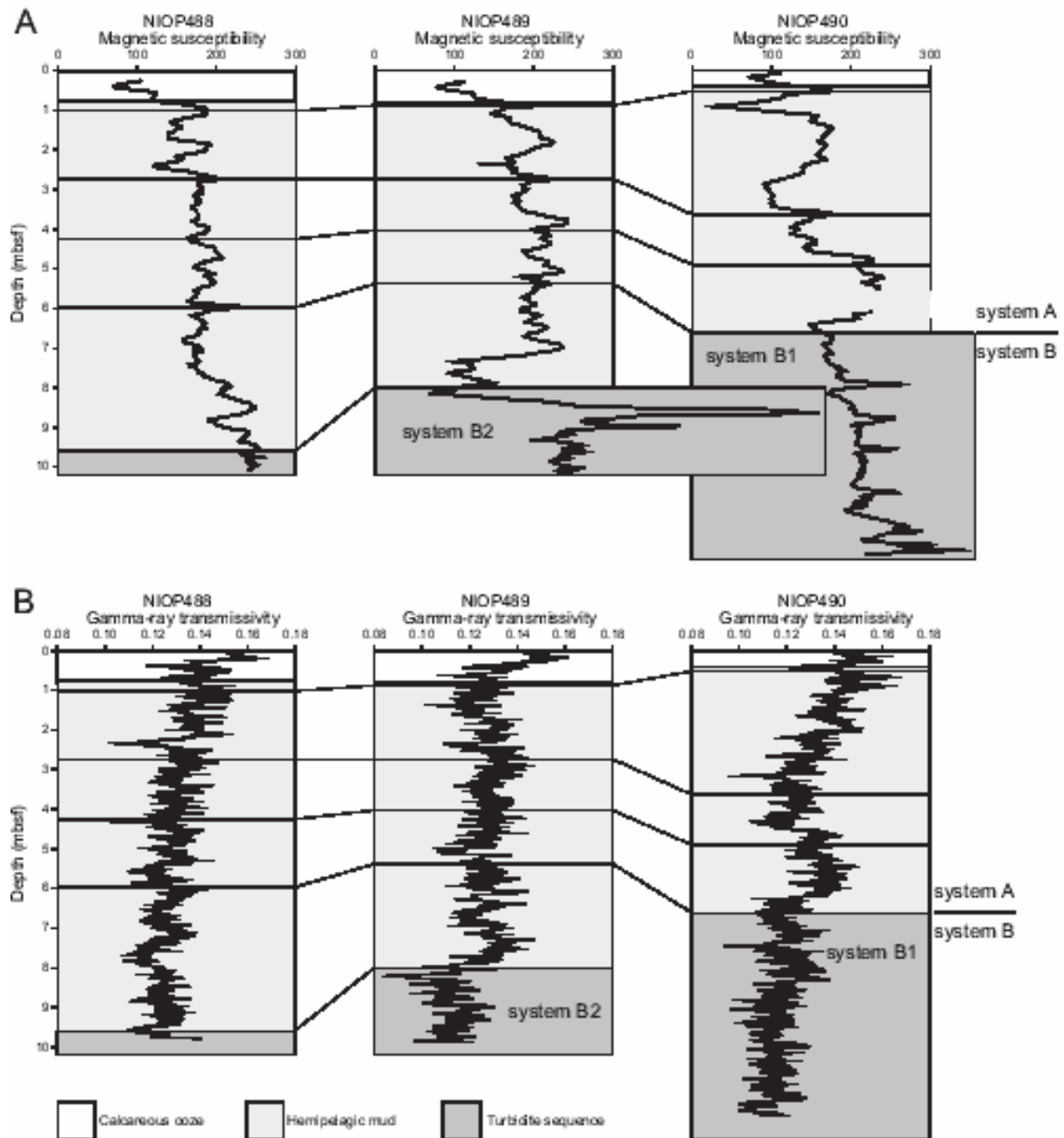


**Fig. 6.5** — Lithostratigraphic correlation between cores NIOP488, NIOP489 and NIOP490 based on the whole-core (A) magnetic susceptibility and (B) gamma-ray transmissivity records. Correlation lines between the hemipelagic mud units correspond with the occurrence of turbidites within at least two cores. The wide-spread occurrence of turbidite deposition coincides with changes in channel configuration, as is indicated by the abandonment of channel B1 (visible in core NIOP490). The magnetic susceptibility ‘spikes’ recorded within the turbidite sequences (NIOP489, NIOP490) indicate the presence of relatively (several cm) thick sandy turbidites. Extreme high magnetic susceptibility values (shown as a data gap) in core NIOP490 (5.5-6 mbsf) is contributed to contamination by pipe-rust.

susceptibility-based correlation between cores NIOP488, NIOP489 and NIOP490 (Fig. 6.5A) is in agreement with the correlation based on the gamma-ray transmissivity (Fig. 6.5B).

It appears that the drape unit (hemipelagic mud and calcareous ooze units) in cores NIOP488 and NIOP489 is thicker and older than the drape unit in core NIOP490. Core NIOP490 was obtained from the youngest channel (B1) of the large channel-levee system B

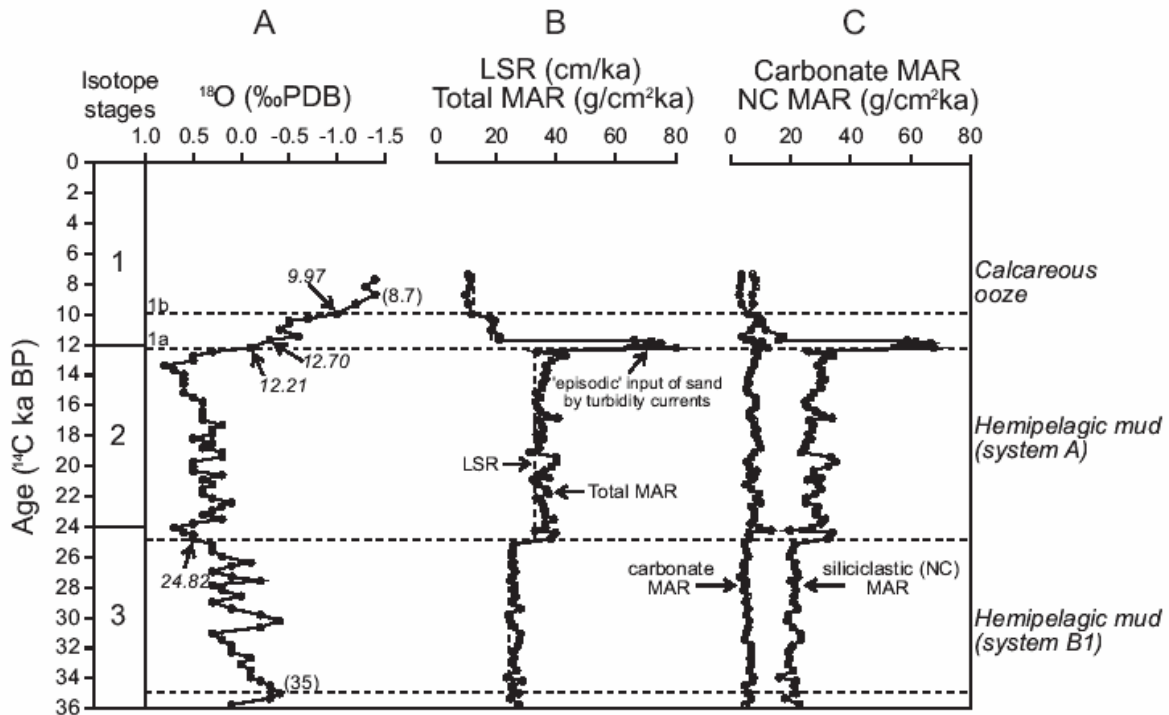


Fig. 6.6 — Sediment flux records of core NIOP489. A: The distinct decrease in  $\delta^{18}\text{O}$  of the planktonic foraminifer *Neogloboquadrina dutertrei* towards the top of the core represents the transition from the last glacial period to the Holocene interglacial period. AMS- $^{14}\text{C}$  dated samples and two additional age calibration points are indicated; B: High linear sedimentation rates (LSR: dashed line) and total mass accumulation rates (total MAR) are recorded during oxygen-isotope stages 2 and 3: low LSR and total MAR are recorded during oxygen-isotope stage 1; C: Fractionated MAR show that the variations in LSR and total MAR are mainly due to variations in the input of siliciclastics (NC MAR: closed circles): the carbonate MAR (open circles) can be regarded as nearly constant. The temporal high sedimentation rate around 12  $^{14}\text{C}$  ka BP is caused by overbank spilling of turbidity currents from channel A1.

(accidentally labelled B2 in the original scheme of Kenyon *et al.*, 1995); cores NIOP488 and NIOP489 were obtained from the somewhat older B2 channel (accidentally labelled B1 in the original scheme of Kenyon *et al.*, 1995). To date the drape unit, core NIOP489 was selected for detailed analysis.

#### *Age model of core NIOP489.—*

The distinct decrease in  $\delta^{18}\text{O}$  (Fig. 6.6A) towards the top of core NIOP489 represents the transition from the last glacial period to the Holocene interglacial period (transition from oxygen-isotope stage 2 to 1: termination 1). The two radiocarbon ages of 12.21 and 9.97  $^{14}\text{C}$  ka BP (at 1.19 and 0.53 mbsf) agree reasonable well with the ages of terminations 1b and 1a. The upper part of the  $\delta^{18}\text{O}$  curve (after ~14  $^{14}\text{C}$  ka BP) correlates closely with the two-step deglaciation known from many marine records (e.g. Sirocko *et al.*, 1993; Weber *et al.*, 1997) and the glacio-eustatic sea-level curve (Fairbanks, 1989, 1992). The dating of 12.7  $^{14}\text{C}$  ka BP (at 0.845 mbsf) is not incorporated in the age model because it is stratigraphically not consistent ('too old'). This dating is inferred to have been done on (partly) redeposited foraminifera, as the sample was taken from the top of a thin turbidite sequence. The sediment sample taken from core NIOP489 at 5.37 m depth was dated at 24.82  $^{14}\text{C}$  ka BP. This sample was selected based on the inter-core correlation shown above: the horizon from which it was taken correlates with the transition from the hemipelagic mud unit of system B1 to the hemipelagic mud unit of system A observed in core NIOP490. The lowest  $\delta^{18}\text{O}$  value near the

top of core NIOP489 (at 0.37 mbsf) was set at 8.7  $^{14}\text{C}$  ka BP as a result of correlation with the well-dated core 74KL from the western Arabian Sea (Sirocko *et al.*, 1993). The temporal low  $\delta^{18}\text{O}$ -‘event’ near the base of the drape unit (at 7.86 mbsf) was set at 35 ka BP considering correlation with the  $\delta^{18}\text{O}$ -records of cores SO90-169KL (core from the channel levee south of the Indus Canyon; see Chapter 5). The latter age should be considered as an approximate.

*Sedimentation rates.—*

Linear sedimentation rates (LSR: cm/ka) at site NIOP489 were calculated between the five age calibration points. Mass accumulation rates (MAR:  $\text{g}/\text{cm}^2\text{ka}$ ) were calculated using the downcore variation in linear sedimentation rate and dry-bulk density (Fig. 6.6B). The separate flux records of the carbonate and non-carbonate (siliciclastic) fractions are shown in Figure 6.6C. It was impossible to calculate sedimentation rates for the turbidite unit of system B2 because of the lack of age control.

Linear sedimentation rates appeared to be high (33 cm/ka) during the last glacial period (oxygen-isotope stage 2). During this period the hemipelagic mud unit of channel-levee system A was deposited. Slightly lower sedimentation rates (24 cm/ka) are recorded during the time interval when small channel-levee system B1 developed (end of oxygen-isotope stage 3). However, the latter value should be considered as an approximate value because of the uncertainty in the age of the oldest age calibration point (35 ka BP). For the thin turbidite sequence just below the calcareous ooze, consisting of ~50% hemipelagic mud and ~50% turbidite silts and sands, a sedimentation rate of 66 cm/ka is estimated, that is twice the calculated sedimentation rate for the underlying hemipelagic mud.

A gradual decrease in sedimentation rates (LSR and total MAR) appeared during the last deglaciation, directly after deposition of the thin series of turbidites (~12  $^{14}\text{C}$  ka BP). The striking decrease in mass accumulation rate between ~11.5 and ~9  $^{14}\text{C}$  ka BP is entirely caused by a decrease in siliciclastic (non-carbonate) sediment supply (Fig. 6.6C). After about 10  $^{14}\text{C}$  ka BP the accumulation rate of pelagic carbonate, which shows only small variations around ~7  $\text{g}/\text{cm}^2\text{ka}$  throughout the studied time interval, started to exceed the accumulation rate of siliciclastic material. According to the age model, the flux of the siliciclastic fraction has been reduced to ~3  $\text{g}/\text{cm}^2\text{ka}$  during the Holocene. These values should be regarded as approximate (probably maximum) values as the top of the sediment record is not dated. The oxidised (brownish-coloured) top of core NIOP489 indicates that the sediment column has been recovered completely.

*Carbonate content and grain size.—*

The carbonate content within the ~7.2 m thick hemipelagic mud unit in core NIOP489 varies around 20 wt% (10-30 wt%), with one exceptional sample (5.17 mbsf; ~24  $^{14}\text{C}$  ka BP) containing up to 40 wt% carbonate (Fig. 6.7B). The transition from the hemipelagic mud to the calcareous ooze unit is clearly visible in the carbonate record: carbonate content increases sharply after ~11.5  $^{14}\text{C}$  ka BP and reaches stable values of ~70 wt% during the Holocene.

Grain-size analyses of both the bulk and non-carbonate fractions in the drape unit confirm the very homogenous nature of the hemipelagic mud unit. Throughout the unit, the mean grain sizes of the bulk (Fig. 6.7C) and the siliciclastic fraction (Fig. 6.7D) remain nearly constant around 10  $\mu\text{m}$ . The lowermost two samples contain slightly coarser-grained siliciclastic material as a result of admixture of some turbidite silt, likely as a result of burrowing activity.

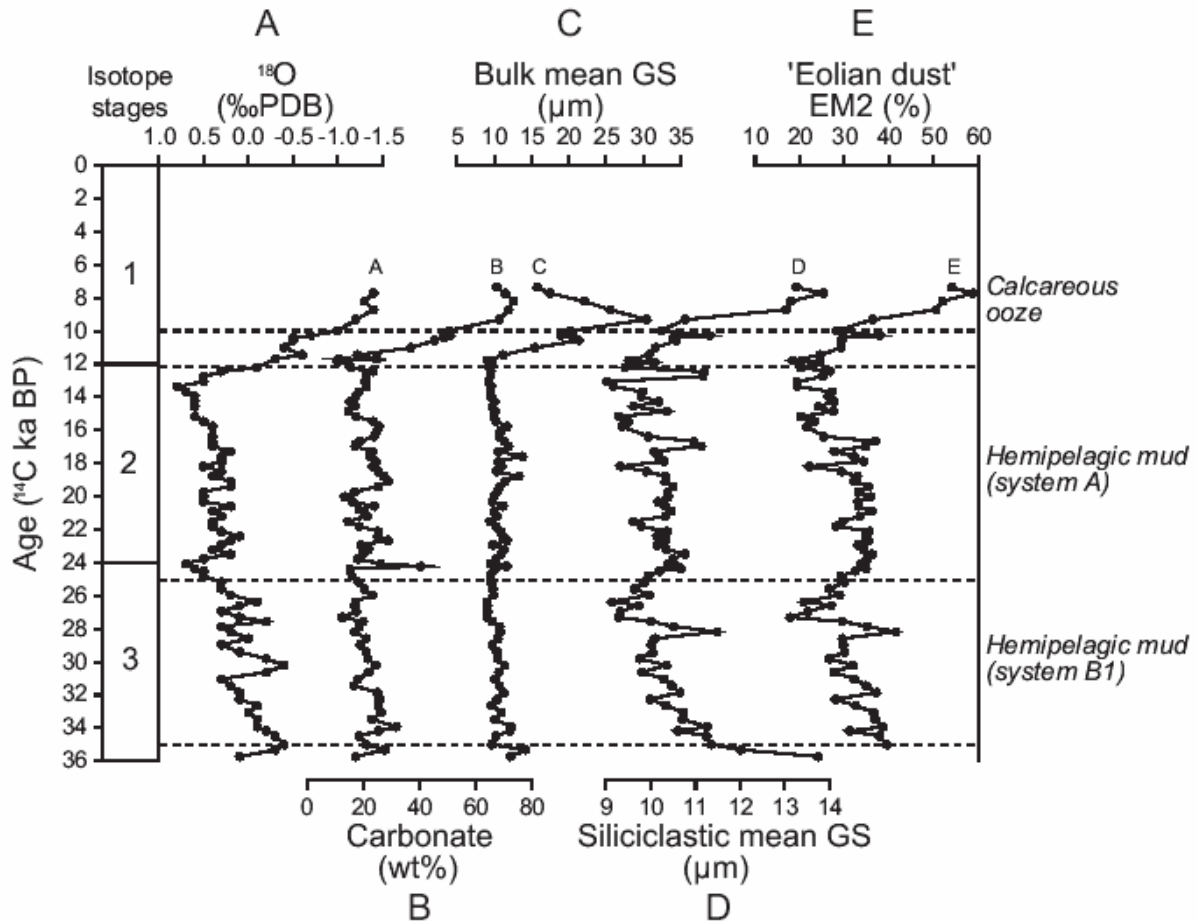
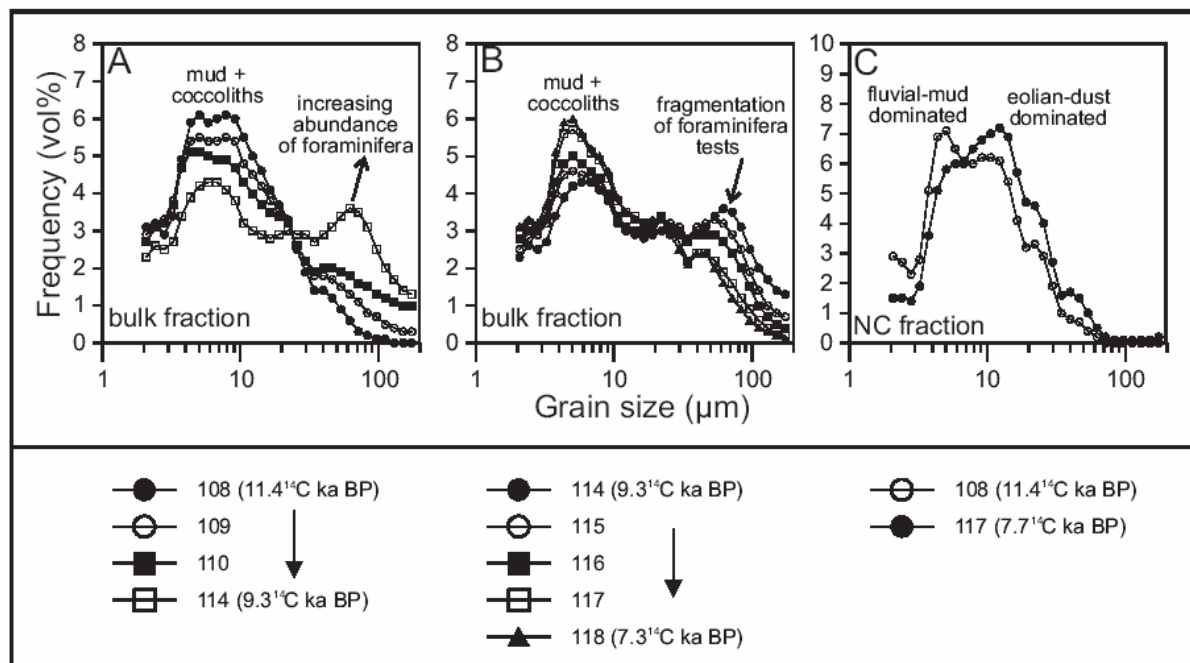


Fig. 6.7 — Composition of sediment in core NIOP489. A:  $\delta^{18}\text{O}$  of the planktonic foraminifer *Neogloboquadrina dutertrei*; B: Carbonate content (wt%); C: Mean grain size of bulk sediment; D: Mean grain size of siliciclastic (non-carbonate) sediment; E: Relative contribution of 'fine' eolian dust (end-member EM2, see Chapter 4).

The mean grain size of the bulk sediment increases sharply at the transition from the hemipelagic mud to the calcareous ooze and reaches a maximum at  $\sim 9$   $^{14}\text{C}$  ka BP. The coarsening of the bulk sediment coincides with the increase of the carbonate content.

Microscopic examination of the coarse fraction (150–595  $\mu\text{m}$ ) and inspection of the grain-size distributions of individual samples (Fig. 6.8A) indicates that the gradual coarsening of the bulk sediment deposited 11.5–9  $^{14}\text{C}$  ka BP reflects an increasing abundance of well preserved foraminiferal tests, i.e., an increasing proportion and increasing modal size of particles  $>10$   $\mu\text{m}$ . Within the upper part ( $<0.45$  mbsf; after  $\sim 9$   $^{14}\text{C}$  ka BP) of the calcareous ooze the mean grain size of the bulk sediment decreases while the carbonate content stays at a constant high level. Microscopic examination of the coarse fraction (150–595  $\mu\text{m}$ ) and inspection of the individual grain-size distributions (Fig. 6.8B) indicate that the fining is due to increased fragmentation of the foraminiferal tests, i.e., an decreasing proportion and decreasing modal size of particles  $>10$   $\mu\text{m}$ . The fragmentation of the foraminiferal tests is likely caused by dissolution of carbonate, as core NIOP489 lies well below the present-day lysocline ( $\sim 3000$  m). The carbonate fraction  $<10$   $\mu\text{m}$  probably consists of predominantly coccoliths and coccoliths fragments (e.g. McCave *et al.*, 1995).

The grain size of the siliciclastic fraction (Fig. 6.7D) shows an abrupt shift towards coarser sizes in the upper part of the calcareous ooze (after  $\sim 9$   $^{14}\text{C}$  ka BP). The mean grain size increases from  $\sim 10$   $\mu\text{m}$  during the glacial period and deglaciation to about 13–14  $\mu\text{m}$  during



**Fig. 6.8** — Grain-size distribution of sediment samples from core NIOP489. **A:** Grain-size distribution of the bulk fraction of four samples with ages between 11.5  $^{14}\text{C}$  ka BP (sample 489/108) and 9  $^{14}\text{C}$  ka BP (sample 489/114). The increase in carbonate content (Fig. 7B) and bulk mean grain size (Fig. 7C) between 11.5 and 9  $^{14}\text{C}$  ka BP is due to the increasing abundance of well-preserved foraminiferal tests ('sand'); **B:** Grain-size distribution of the bulk fraction of five samples with ages between 9  $^{14}\text{C}$  ka BP (sample 489/114) and 7.5  $^{14}\text{C}$  ka BP (sample 489/118). The decrease in bulk mean grain size (Fig. 7C) between 9–7.5  $^{14}\text{C}$  ka BP is due to the increasing fragmentation of the foraminiferal tests as a result of carbonate dissolution; **C:** Grain-size distribution of the siliciclastic (non-carbonate NC) fraction of samples 489/108 (11.5  $^{14}\text{C}$  ka BP) and 489/117 (8  $^{14}\text{C}$  ka BP). End-member modelling (Prins and Weltje, 1999; Chapter 4) indicates that sample 489/108 is composed of 25% eolian dust (EM2) and 75% fluvial mud (EM3) and sample 489/117 is composed of 60% eolian dust and 40% fluvial mud.

the Holocene: the grain-size distributions of two representative samples are shown in Figure 6.8C to illustrate the subtle changes in grain size. End-member modelling of the siliciclastic grain-size distributions (Prins and Weltje, 1999; Chapter 4) indicates that the change in grain size at site NIOP489 reflects the extent to which fluvial mud (EM3) and 'fine' eolian dust (EM2) are mixed (contribution of 'coarse' eolian dust EM3 is zero). The eolian dust (EM2) record of core NIOP489 is shown in Figure 6.7E. The relative contribution of eolian dust varies around 20–30% during the last glacial period, and increases abruptly to values of 50–60% after  $\sim 9$   $^{14}\text{C}$  ka BP. These results suggest an abrupt change in the provenance of sediment deposited on the middle Indus Fan which coincided with the notable drop in siliciclastic sediment flux during the last deglaciation (Fig. 6.6C). Similar changes in the bulk and the siliciclastic grain size are observed in the uppermost meter of the sediment record at site NIOP490. As in core NIOP489, the grain-size shift coincides with the transition from the hemipelagic mud to the calcareous ooze unit (Fig. 6.5).

#### *Sediment provenance.*—

In Figure 6.9 the timeseries of the Mg/Al and Ti/Al ratios, and the smectite/illite and palygorskite/illite ratios of core NIOP489 are plotted to highlight the changes in terrigenous sediment composition on the middle fan during the late Pleistocene and Holocene. The homogeneity of the hemipelagic muds deposited during the last glacial period (oxygen-

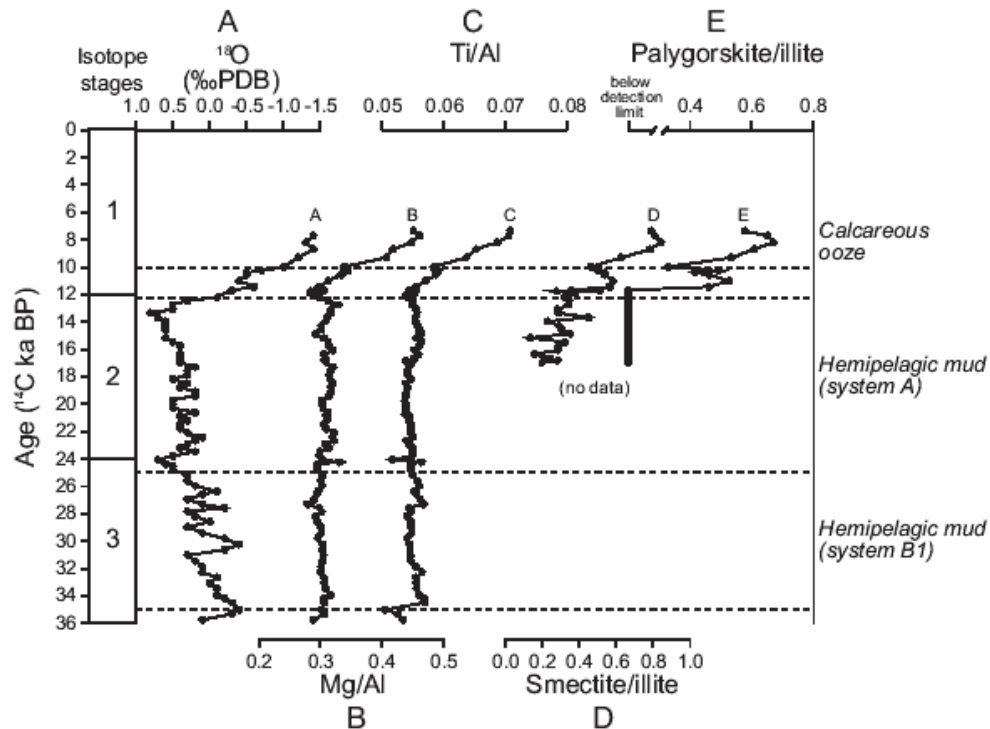


**Fig. 6.9** — Composition of sediment in core NIOP489. A:  $\delta^{18}\text{O}$  of the planktonic foraminifer *Neoglobobulimina dutertrei*; B: Mg/Al ratio; C: Ti/Al ratio; D: smectite/illite ratio; E: palygorskite/illite ratio. The mineral/illite ratios refer to hkl (001) peak-height ratios as determined on the XRD diagrams of the clay fraction.

isotope stages 2 and 3) is evidenced by the constant chemical composition and mineralogy of the siliciclastic sediment fraction. Coinciding with the waning terrigenous-sediment supply during the deglaciation (oxygen-isotope stage 1), distinct changes in the composition of the siliciclastic muds can be observed.

The mineralogy of the muds deposited during oxygen-isotope stage 2 (Fig. 6.10A) differs from that of the muds deposited during oxygen-isotope stage 1 (Fig. 6.10B). The composition of the oxygen-isotope-stage-2 muds is characteristic of an Indus River origin (Steward *et al.*, 1965), as these muds are relatively rich in illite and chlorite, contain some smectite (low smectite/illite ratios: Fig. 6.9D), and contain no detectable amounts of palygorskite (low palygorskite/illite ratios: Fig. 6.9E). Palygorskite is a very characteristic mineral of Arabian provenance (Kolla *et al.*, 1976; Kolla *et al.*, 1981; Sirocko and Lange, 1991; Sirocko *et al.*, 1991). According to these authors the basin-wide dispersal of palygorskite is caused by the north-westerly winds which prevail over the Arabian peninsula and raise large amounts of dust from this arid region. The increase in relative abundance of palygorskite and smectite (Fig. 6.9D, E) in the middle-fan sediments during the deglaciation indicates that the relative contribution of eolian dust of Arabian provenance increased during this time interval.

The gradual increase of the Mg/Al (Fig. 6.9B) and Ti/Al (Fig. 6.9C) ratios during the deglaciation need some more consideration. A change in these ratios reflect either a change in grain size or a change in the provenance of the sediment, or a combination of the two. To assess the influence of sediment source versus grain size on the chemical composition of the siliciclastic sediment fraction, we analysed the composition of selected size ranges (silt fractions B, C and D with modal grain sizes of  $\sim 5$ ,  $\sim 15$  and  $\sim 40$   $\mu\text{m}$ ) of sediment samples of which the provenance is known a priori. The silt fractions were extracted from the bulk siliciclastic fractions by selective settling in settling tubes. The 'end-member' samples were

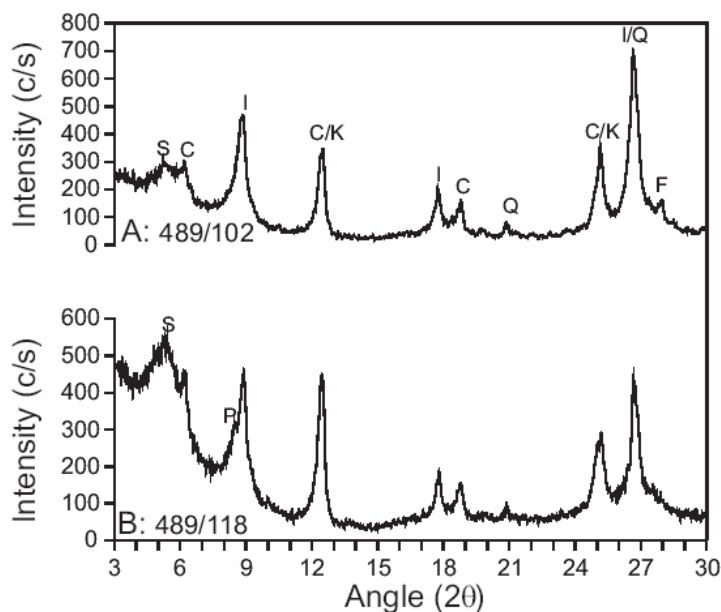


**Fig. 6.10** — X-ray diffraction diagrams of glycolated samples from core NIOP489. **A:** Fluvial-mud-dominated sample 489/102 (12.21  $^{14}\text{C}$  ka BP); **B:** Eolian-dust-dominated sample 489/118 (7.5  $^{14}\text{C}$  ka BP). Minerals detected include smectite (S), chlorite (C), palygorskite (P), illite (I), quartz (Q), ?kaolinite (K) and feldspar (F).

taken from cores obtained from the Oman continental slope (core NIOP484, samples 484/72 and 484/76; Arabian source) and from the Indus Canyon (core SO90-173KG, samples 173KG/1 and 173KG/2; Indus River source). Analysis of the chemical composition of the size fractions from these samples allows characterisation of the Arabian and Indus sources. Comparison of the composition of selected NIOP489 samples with the composition of the ‘end member’ samples permits to classify the source areas of the Indus Fan sediments. The NIOP489 samples are taken from the basal turbidite sequence (NIOP489/14 and 489/18), the hemipelagic mud unit (NIOP489/98:  $\sim 13.5$   $^{14}\text{C}$  ka BP), and the calcareous ooze unit (NIOP489/117:  $\sim 8$   $^{14}\text{C}$  ka BP). A cross-plot of the Mg/Al and Ti/Al ratios of the sediment fractions is shown in Figure 6.11.

The chemical composition of the Oman continental slope sediments (NIOP484) is distinctively different from that of the sediments from the Indus Canyon (SO90-173KG). In general, the sediment fractions of ‘Arabian source’ have higher Mg/Al ratios and, to a lesser extent, higher Ti/Al ratios in comparison with the sediments which were supplied by the Indus River. Besides this source effect, a clear compositional trend is observed between the three size fractions extracted from sediments supplied from both source areas (size effect). In both sources the Mg/Al ratio decreases systematically with increasing grain size (fraction B has ‘high’ Mg/Al ratios, fraction D has ‘low’ Mg/Al ratios). The Ti/Al ratio shows a clear size effect in the sediments of Arabian provenance: the Ti/Al ratio increases systematically with increasing grain size (fraction B has ‘low’ Ti/Al ratios, fraction D has ‘high’ Ti/Al ratios). In contrast, this size effect is not observed in the Indus sediments as the three silt fractions are characterised by approximately the same Ti/Al ratio.

The silt fractions extracted from the turbidite and hemipelagic mud samples of core NIOP489 are chemically identical to the Indus Canyon samples, and are therefore grouped as ‘Indus source’ samples in Figure 6.11. This compositional similarity is not surprising as the turbiditic and hemipelagic sediments of the middle Indus Fan are ultimately derived from the Indus River. However, the results indicate that the provenance of sediments can be determined

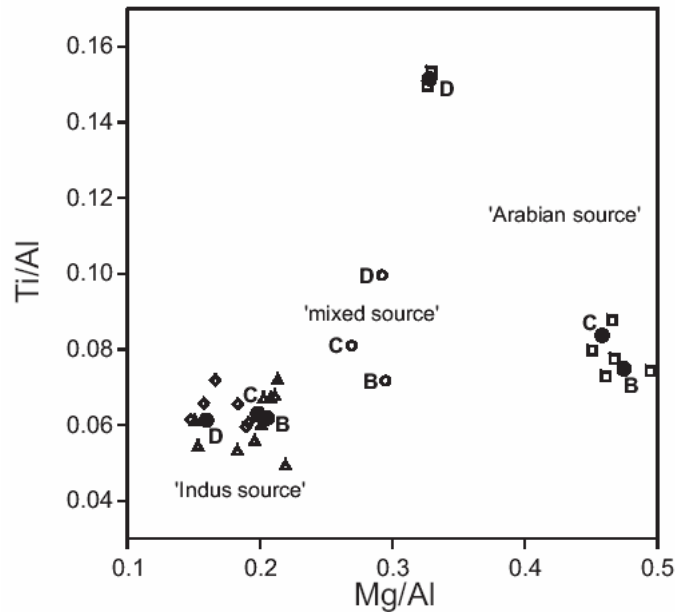


**Fig. 6.11** — Cross-plot of Mg/Al and Ti/Al to illustrate the ‘source effect’ and ‘size effect’ on the composition of terrigenous sediments. Silt fractions B, C and D have modal grain sizes of ~5, ~15 and ~40  $\mu\text{m}$ . Samples from the Oman continental slope (NIOP484/72+76: open squares) are used as reference for the ‘Arabian source’ and samples from the Indus Canyon (SO90-173KG/1+2: open diamonds) are used as reference for the ‘Indus source’. Hemipelagic mud (NIOP489/98) and turbidite samples (NIOP489/14+18) from the Indus Fan (open triangles) are identical to the reference samples of the ‘Indus source’. The composition of the sample (NIOP489/117: open circles) taken from the calcareous ooze unit draping the middle Indus Fan suggests that it is a mixture of fluvial mud and eolian dust (‘mixed source’). Closed circles denote the average compositions of the three silt fractions (B, C, D) for the ‘Arabian source’ and ‘Indus source’ samples.

successfully by analysis of the composition of size fractions (eliminating the size effect). The silt fractions extracted from sample NIOP489/117 have intermediate compositions with respect to the Arabian-sourced and the Indus-sourced sediments, suggesting that the siliciclastic sediment fraction within the calcareous ooze unit is supplied from both source areas (‘mixed’ source).

The above results indicate that the higher Mg/Al (Fig. 6.9B) and Ti/Al ratios (Fig. 6.9C) during the Holocene in core NIOP489 are not caused by the observed increase of siliciclastic grain size (Fig. 6.7D). Rather, the compositional changes are due to a change in provenance of the terrigenous sediment: the fan sediments from the glacial period were supplied predominantly from the Indus-River source, whereas the Holocene sediments were mainly supplied from the Arabian source.

### *Indus Canyon*

All sediment cores (SO90-173KG, 174SL, 184KL, 188KL) obtained from the axial valley of the Indus Canyon revealed a fine-grained, turbidite-dominated sedimentary succession. Turbidites are generally up to a few centimetres thick: one exception is a 1.07 m thick graded and parallel-laminated sand-silt bed at the top of core SO90-174SL. Within this core also a 10-15 cm thick slumpfold is present. The sedimentary facies in the cores indicate that the Indus Canyon acted ‘recently’ as a conduit for downslope sediment transport.

Core SO90-188KL consists of two distinct lithological units (Fig. 6.12A). The lower unit (3.20-7.94 mbsf) consists of homogeneously-coloured greyish mud with two greenish-coloured mud turbidites near the top of the unit. The upper unit (0-3.20 mbsf) consists of

heterogeneously-coloured greyish-blackish mud with a thinning-upward sequence of sixteen turbidites in the lower part of this unit. The boundary (3.20 mbsf) between the units coincides with a layer of coarse-grained shell debris. The shift in lithology at this shell layer is accompanied by shifts in the median grain size and dry-bulk density records of the hemipelagic muds (Fig. 6.12B, C). The abrupt shift in dry-bulk density shows that the lower unit is relatively well consolidated, whereas the upper unit is poorly consolidated. Both the abrupt shift in dry-bulk density and the occurrence of the shell layer (lag deposit), suggest the presence of an erosional unconformity. This erosional unconformity may have been formed during a period of episodic input of sediment into the Indus Canyon. Shell material within the shell lag was dated at 10.59  $^{14}\text{C}$  ka BP. Organic matter within the hemipelagic mud just above the shell lag revealed an age of 1.8  $^{14}\text{C}$  ka BP. When the unconformity was formed exactly remains unclear as the shells represent redeposited ('old') material. The two datings, however, give us the maximum and minimum age of the erosional unconformity.

South of the Indus Canyon mouth, both levees of the main channel display the characteristic elevated ridge topography, caused by frequent overbank spilling of turbidity currents from the channel (McHargue and Webb, 1986; Von Rad and Tahir, 1997). Core SO90-169KL obtained from the eastern levee contains predominantly alternating dark-greenish to light-greenish/grey hemipelagic muds. Analyses of down-core variations in  $\delta^{18}\text{O}$  of the planktonic foraminifer *Neogloboquadrina dutertrei* shows that the base of this core is about 100 ka old (see Chapter 5). During the last 100 ka only two very thin (~0.5 cm) turbidites have been deposited at site SO90-169KL. These turbidites are rich in foraminifera from which it is inferred that they probably originated on the continental slope ('local source') and were not deposited by turbidity currents overflowing the channel levee ('Indus source'). The great depth of the main channel (300-400 m; Fig. 6.3) in the upper part of the Indus Fan clearly hindered coarse silty-sandy material to escape from the channel and to be deposited on the channel levee during the last 100 ka.

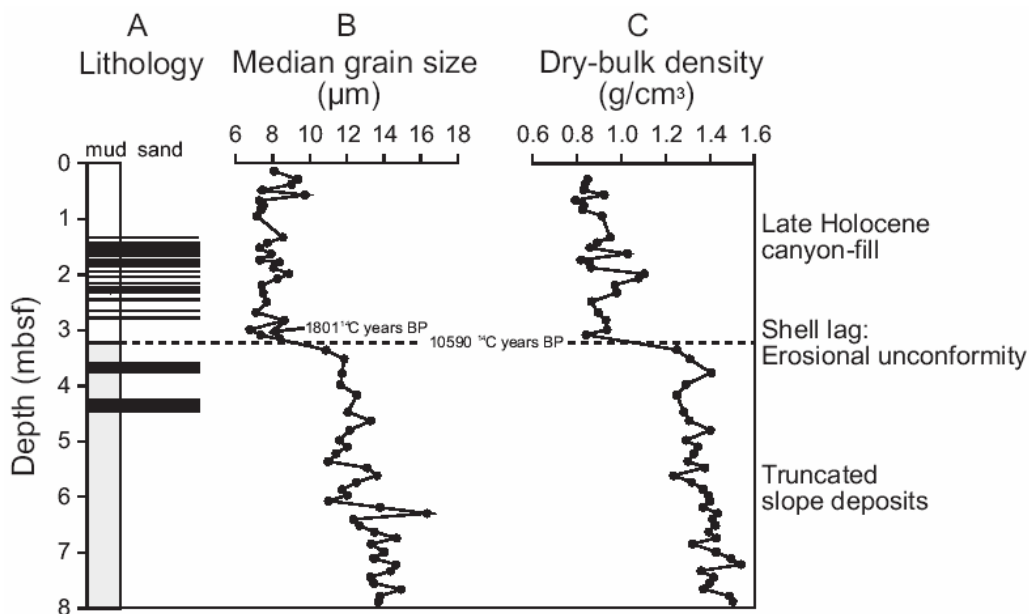
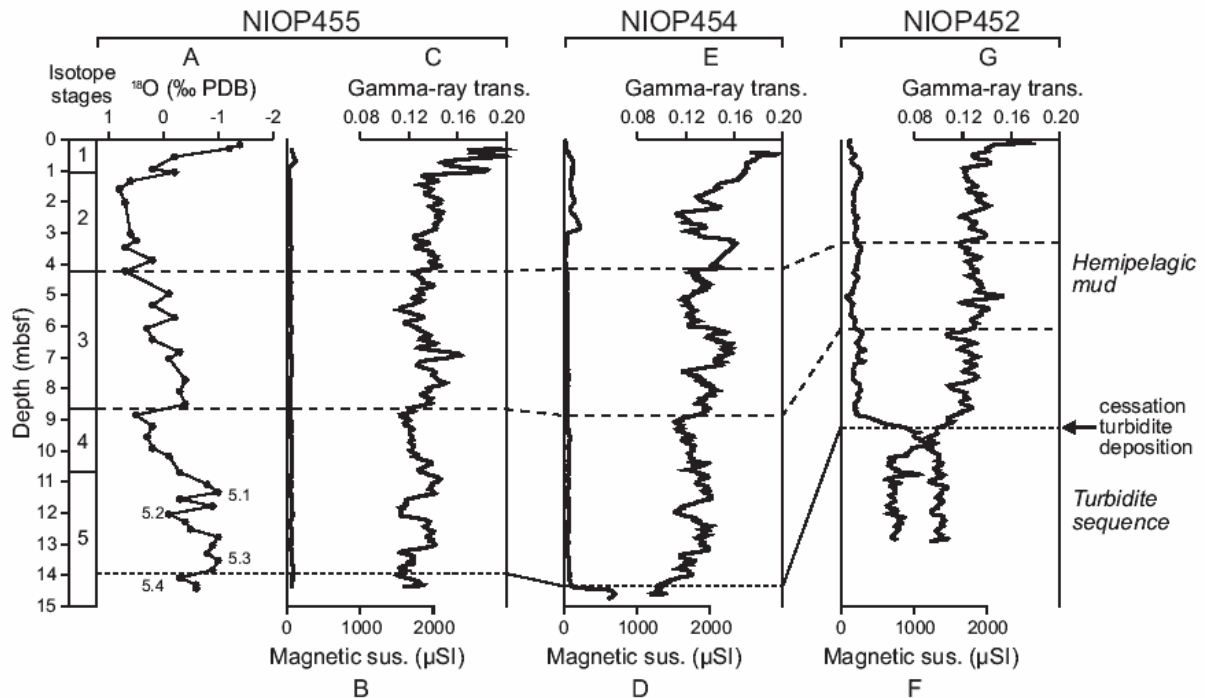


Fig. 6.12 — Core SO90-188KL, Indus Canyon. A: Lithology, showing the position of silty-sandy turbidites; B: Median grain size of bulk sediment; C: Dry-bulk density of bulk sediment. Dashed horizontal line represents position of shell lag. AMS- $^{14}\text{C}$  dated samples are indicated.

## Continental Slope

Sediment cores NIOP452, NIOP454 and NIOP455 were obtained from the continental slope west of the Indus Canyon from water depths ranging between 1000-2000 m. All cores revealed the top of a turbidite sequence at the base of the core which is draped by a ~9 to ~14.5 meter thick hemipelagic mud unit. The cores were correlated on basis of their magnetic susceptibility and gamma-ray transmissivity records (Fig. 6.13). The turbidite sequences in cores NIOP452 and NIOP454 are characterised by relatively high magnetic susceptibility and low gamma-ray transmissivity values. The hemipelagic mud units are characterised by low magnetic susceptibility values. Correlation of the base of the hemipelagic mud units on the basis of the gamma-ray transmissivity records suggests that turbidite deposition stopped simultaneously at the three coring sites. Correlation of the top of the turbidite sequence with the  $\delta^{18}\text{O}$  record (*Neogloboquadrina dutertrei*) of core NIOP455 indicate that the series of turbidites has been deposited prior to ~115 ka BP, i.e., prior to the end of oxygen isotope substage 5.4.



**Fig. 6.13** — Lithostratigraphic correlation between cores NIOP452, NIOP454 and NIOP455 based on the whole-core (B, D, F) magnetic susceptibility and (C, E, G) gamma-ray transmissivity records. The boundary between the hemipelagic mud unit and the turbidite sequence, indicated by the lowermost correlation line, is dated at ~115 ka BP on basis of the oxygen-isotope  $\delta^{18}\text{O}$  record of the planktonic foraminifer *Neogloboquadrina dutertrei* in core NIOP455.

## EVOLUTION OF THE YOUNGER CHANNEL-LEVEE SYSTEMS

## Channel Avulsions

A comprehensive physical theory of channel avulsion in deep-sea fan systems is lacking. Observations of avulsions in modern rivers indicate that avulsion is driven by local superelevation of some part of the channel or channel complex above its surroundings. This superelevation is produced by sedimentation, which tends to occur at higher rates near the

channel than further out in the flood plain. Experimental studies of avulsion on laboratory-scale fluvial fans indicated that avulsion frequency increases strongly with increasing sedimentation rate (Bryant *et al.*, 1995). Possible mechanisms controlling channel avulsion on the upper fan (system B to A) and on the middle Indus Fan (within depositional lobe of system A) will be discussed below.

During deposition of the youngest channel-levee complex (including systems A-F of Kenyon *et al.*, 1995), the avulsions tended to be clustered in two areas, i.e., on the upper and the middle fan. The cluster of avulsions on the upper fan is immediately south of the canyon mouth, where the (erosional) canyon evolves into a (depositional) channel. This zone is referred to as the 'transitional zone' by McHargue and Webb (1986). Commencing from the shelf and slope areas, the depths and cross-sectional areas of the canyon and the channels decrease seaward. The channel dimensions reach a 'regional/local' minimum at a distance of about 100 km from the foot of the continental slope, i.e., on the upper portion of the upper fan. On the middle portion of the upper fan, at a distance of 150-300 km, the channel dimensions increase. Farther downfan, on the lower portions of the upper fan, the dimensions decrease again. The minimum channel dimensions on the upper portion of the upper fan makes this zone a suitable place for avulsion to occur (Kolla and Coumes, 1987).

The other cluster of avulsions is situated on the middle fan, approximately 500 km from the canyon mouth. These avulsions lie above the buried extension of the Lakshmi Ridge (Droz and Bellaiche, 1991). Initially, the avulsions have probably been controlled by a change in sea-floor gradient due to reactivation of buried normal faults. Following the initial avulsion on the middle fan, the levees upstream continued to build up. So also at this point the channels became markedly smaller down-fan. Further avulsions are thus likely to occur at or beyond the initial avulsion point.

#### *Development of Channel-Levee System A*

Of all the mechanisms possibly controlling the timing of turbidite sedimentation on the Indus Fan during the last ~35 ka BP, changes of glacio-eustatic sea level and the position of the shoreline on the shelf can be regarded as the most important. The NIOP489 timeseries of  $\delta^{18}\text{O}$ , carbonate content and Mg/Al are plotted next to the Barbados sea-level curve (Fairbanks, 1989, 1992) in Figure 6.14 to illustrate this point.

Near the boundary between oxygen-isotope stages 3 and 2 (24.8  $^{14}\text{C}$  ka BP), turbidite deposition abruptly ceased on channel-levee system B and the locus of turbidite deposition switched to the west, i.e., the development of large channel-levee system A started. The fall in glacio-eustatic sea level during the transition from oxygen-isotope stage 3 to 2 most likely enhanced the rate of sediment supply to the deep sea. A sudden increase in sediment supply may have been caused by mass slumping or increased headward erosion in the canyon. The catastrophic increase in sediment supply and subsequent *en mass* transport then resulted in the breaching of the levees or plugging of the main channel on the upper fan, eventually leading to avulsion of channel B and, subsequently, the abandonment of channel-levee system B. At this point we have to address that the above causal relationship between a rapid falling sea level and channel avulsion is not definite as the available data are too limited: (1) correlation between the magnetic susceptibility records of cores NIOP489 and NIOP490 may have introduced some 'error' in the exact age of cessation of turbidite deposition in system B; (2) the fall in sea level at the boundary between oxygen-isotope stages 3 and 2 is not well documented in the Barbados sea-level data set of Fairbanks (1992). Therefore, the apparent

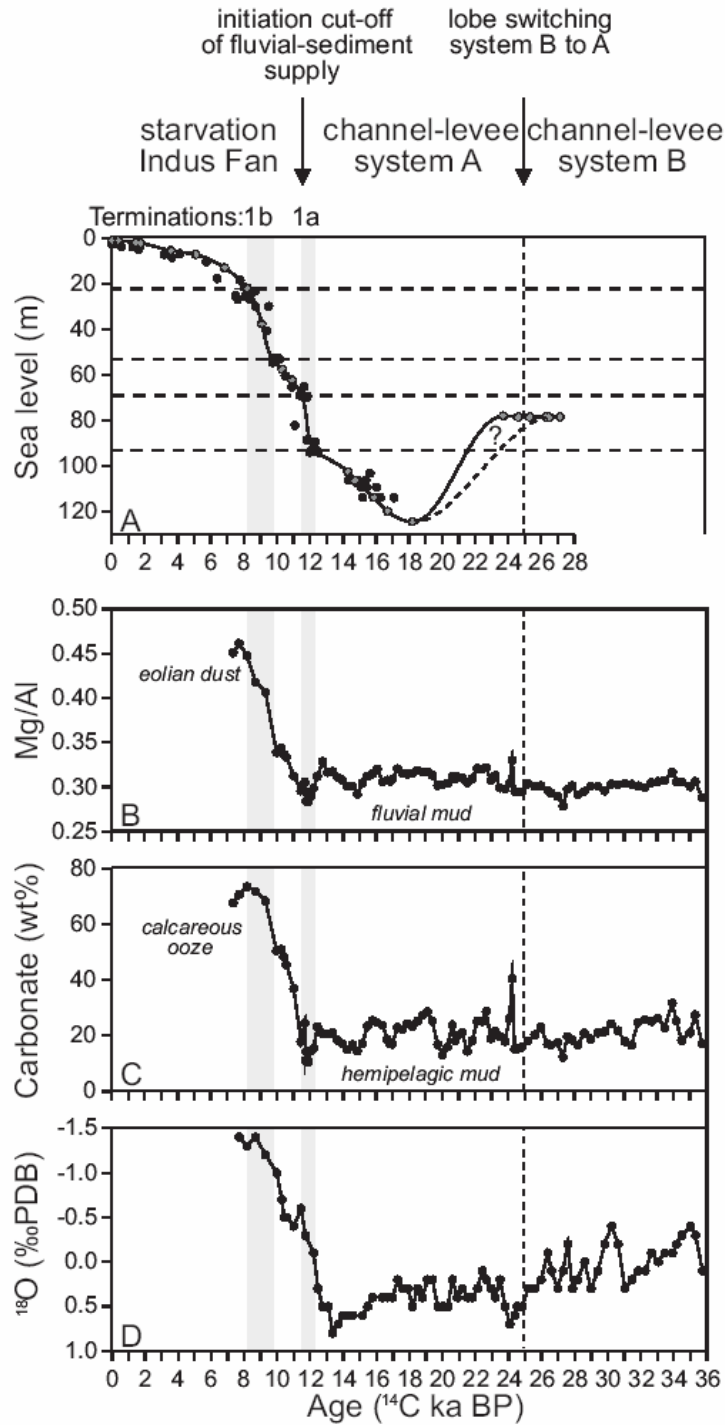


Fig. 6.14 — Diagram showing the relationship between glacio-eustatic sea-level fluctuations and sediment composition on the middle Indus Fan. A: Barbados sea-level curve (Fairbanks, 1992); B: Changes in the Mg/Al ratio in core NIOP489 are indicative of the provenance of the sediment being either derived from the ‘Arabian source’ (high values; eolian dust) or the ‘Indus source’ (low values; fluvial mud); C: Changes in the carbonate content in core NIOP489 mainly reflect changes in terrigenous sediment supply; D: Oxygen-isotope  $\delta^{18}\text{O}$  record of the planktonic foraminifer *Neogloboquadrina dutertrei* in core NIOP489.

'misfit' between the age of the lobe switch from system B to A (dates at 24.8  $^{14}\text{C}$  ka BP in core NIOP489) and the rapid falling sea level (after 23.7  $^{14}\text{C}$  ka BP, see Fig. 6.14A) may be caused by the above uncertainties.

Channel-levee system A developed during oxygen-isotope stage 2 which is a period characterised by a very low sea-level stand (between -80 and -124 m). Turbidity currents, funnelled through the Indus Canyon and upper-fan channel, supplied river-derived sediments to channel-levee system A. The high rates of sediment supply during the period of sea-level lowstand suggest that either the Indus Canyon experienced maximum erosion during this period and/or that the Indus River supplied its material directly into the Indus Canyon.

Deposition of the last series of turbidites at site NIOP489 around  $\sim 12$   $^{14}\text{C}$  ka BP (during termination 1a) coincided with the first interval of rapid sea-level rise (-90 to -70 m; Fig. 6.14A) observed in the Barbados sea-level curve. Between  $\sim 11.5$  and  $\sim 10$   $^{14}\text{C}$  ka BP, i.e., during the Younger Dryas, the supply of terrigenous sediment decreases sharply at site NIOP489 indicating cessation of turbidite deposition on channel-levee system A and starvation of the Indus Fan. The carbonate content and eolian-dust content both show an increase during this period and reflect the decrease in fluvial-sediment supply. Apparently sea level rose above a certain 'threshold' ( $> -70$  m; Fig. 6.14A) which initiated a change in the depositional system eventually resulting in a decreased fluvial-sediment supply to the Indus Canyon and the Indus Fan. During the second interval of rapid sea-level rise (-70 to -20 m; Fig. 6.14A), between  $\sim 8$  and  $\sim 10$   $^{14}\text{C}$  ka BP (during termination 1b), the supply of eolian dust from the Arabian Peninsula started to dominate terrigenous sedimentation processes. During the latter period the supply of Indus-River sediment to the middle Indus Fan was effectively cutoff indicating that the Indus River stopped to be a direct feeder system of the middle fan. However, the cores obtained from the Indus Canyon indicate that Indus-River sediments have continued to be deposited in the upper portion of the main channel and canyon up to recent times.

#### *Channel Avulsions on Channel-Levee System A*

In the period of major channel switch (B to A), turbidites were deposited at the three core sites (NIOP488-490) on the middle Indus Fan (Fig. 6.5). Apparently wide-spread unconfined, non-channellised turbidity flows were active. After a short period of non-channellised turbidity flow, a new channel started to develop (channel A7) west of the core sites. At three other horizons within the hemipelagic mud drape, i.e., the distal equivalent of system A, we find turbidites intercalated. In these cases, the presence of turbidites is inferred to indicate the switching of turbidite sedimentation within channel-levee system A (e.g. A2 to A1). The youngest series of turbidites, belonging to system A1, is related with the MAR-'spike' in core NIOP489 (Fig. 6.6). Although seven smaller channels belonging to channel-levee system A were recognised on the GLORIA mosaic, only four 'turbidite-events' are recognised from the lithology in cores NIOP488-490.

The volumes of the individual small channel-levee systems (A1-A7) are roughly similar as inferred from their geometry seen on the GLORIA mosaic and on high-resolution seismic profiles; it seems if channels built up to a certain threshold dimension and then avulsed (autocyclicity). Apparently, such process can be envisaged by channel plugging as a result of progressive decrease of down-fan channel gradients. After a rapid period of backfilling (retrogradational infilling of channel), turbidity currents shifted towards the adjacent topographically low inter-channel areas and started to develop a new channel-levee system in the best reachable valley.

The youngest channel-levee system A1 is exceptional as this channel terminates into a sandy channel-mouth lobe at a relatively proximal position (Kenyon *et al.*, 1995). This

unusual pattern can be explained by the timing of deposition. The small channels A7 to A2 developed during the last glacial period, each within a time span of approximately 2000 years (between ~25 and ~12 <sup>14</sup>C ka BP). Channel A1 started to develop at ~12 <sup>14</sup>C ka BP but the supply of sediment clearly started to diminish between ~11.5 and ~9.5 <sup>14</sup>C ka BP (Fig. 6.6). The rapidly rising sea level resulted in a decrease in sediment supply causing the up-dip contraction of the channel-mouth lobe and eventually the abandonment of channel-levee system A. At present we observe the 'fossilised' channel configuration of ~9.5 <sup>14</sup>C ka BP.

The avulsions of the smaller channel-levee systems of system A (channels A7-A1) cannot be related to sea-level-induced changes in sediment supply: during oxygen-isotope stages 2 sea level was constantly very low. However, millennium-scale periodicities (~2 ka) have been reported in various upwelling indices in cores from the western Arabian Sea suggesting similar periodicities in the strength of the summer monsoon (Naidu and Malmgren, 1995; Sirocko *et al.*, 1996). It is therefore very tempting to infer that avulsion frequency may have been determined by high-frequency variations in climate-induced sediment supply. However, our data is not sufficient to support this hypothesis.

## DISCUSSION

### *Correlation between Shelf-Slope-Canyon and Fan*

Von Rad and Tahir (1997) used high-resolution seismics and sediment cores to map the morphology and echo-facies distribution and to describe the late Quaternary sedimentation on the outer shelf and continental slope off the Indus Delta. They distinguished four distinct episodes during which sea-level change was the most important mechanism controlling the late Quaternary history of erosion and deposition in the Indus Canyon and on the adjacent outer shelf and continental slope: (1) Deposition of fluvial sediment on the inner shelf, aggradation of the shelf and failure of prodelta muds by slumping, forming a gullied upper slope (500-1700 m) morphology during late Pleistocene (?Eemian; prior to the last glacial maximum) times of relatively high sea level; (2) Progradation of the Indus Delta across the outer shelf and maximum erosion of the Indus Canyon during the last glacial sea-level lowstand (from ~20 to 7-10 ka BP); (3) Drowning of the former delta and the formation of biogenic sediments and build-up of shallow-water algal bioherms on the outer shelf between terminations 1a and 1b (9-12 ka BP); (4) Flooding of the shelf and deposition of Indus delta-front sediments on the alluvial plain and the innermost part of the broadened shelf during the early Holocene sea-level rise (~9 ka BP and hereafter).

The deposition of the series of turbidites at sites NIOP452-455 may very well be related to the formation of gullies in the upper slope similar to what Von Rad and Tahir (1997) observed west of the Indus Canyon. These turbidites were deposited prior to ~115 ka BP, i.e., during the beginning of oxygen-isotope substage 5.4 and maybe during oxygen-isotope substage 5.5 (the Eemian interglacial period), when sea level was at a highstand. Our data indicate that during the last 115 ka the continental slope off the Indus Delta was draped by continuous, hemipelagic sedimentation and that the slope is avoid of coarse-grained fluvial sediments.

The development of channel-levee system A on the middle fan (between 25-11.5 ka BP) coincides largely with the period of maximum erosion of the canyon (Von Rad and Tahir, 1997). According to these authors, the maximum sea-level lowstand during the last glacial maximum (~18-15 ka BP) caused the Indus Delta to form a braided stream valley on the alluvial plain, to advance across the present shelfbreak (135 m), and to shed fluvial silty clays directly onto the upper slope (135-500 m) and into slope canyons. A deep-water delta formed.

From ~20 to 7-10 ka BP the Indus Canyon experienced maximum erosion and overbank spilling produced constructional terraces and major (50-200 m high) levee-overbank complexes along the lower canyon and the upper-fan valley coinciding with major slumping along the canyon and continental slope. The turbidites of channel-levee system A on the middle fan can be related to the slumping of delta sediments in the canyon and erosion of the canyon.

The cessation of turbidite deposition on channel-levee system A, inferred from the rapidly decreasing input of fluvial muds at site NIOP489, occurred between terminations 1a and 1b (11.5-10 <sup>14</sup>C ka BP). The timing of Indus Fan starvation correlates with the timing of drowning of the Indus Delta (Von Rad and Tahir, 1997). They suggested that the rising sea level during the deglaciation caused the former delta to be drowned. Several sea-level stillstands are indicated by the presence of relict biogenic sediments and buildup of algal bioherms forming shoals on the outer Indus shelf at a water depth of a few tens of metres, dated between 8.5 and 13 ka BP. Most of these sea-level stillstands occurred during the period between terminations 1a and 1b, coinciding with the Younger Dryas period.

Our data indicate that during the early Holocene sea-level rise the supply of fluvial sediment to the middle fan was reduced to a minimum. During this period the shelf was flooded and the delta-front sediments of the Indus River were deposited on the alluvial plain and the innermost part of the broadened shelf. River-derived sediments did not reach the outer shelf during the Holocene as indicated by the presence of the carbonate-rich relict sediments (Stewart *et al.*, 1965; Kolla *et al.*, 1981; Von Rad and Tahir, 1997). During the late Holocene, the Indus Delta experienced rapid seaward progradation: Wells and Coleman (1982) reported progradation rates of 30 m/yr during the last 5 ka, Milleman *et al.* (1982) reported rates of 40 m/yr during the last 2 ka, and McHargue and Webb (1986) reported rates of nearly 35 m/yr since 300 BC. A westward migration of the river course in the lower part of the Indus coastal plain was accompanied by a corresponding migration of the delta towards the west during the late Holocene. Since 5-6 ka BP the Indus river and delta has experienced four major shifts (Kazmi, 1982).

Presently, the development of the subaqueous part of the delta is restricted by the close proximity of the head of the Indus Canyon with respect to the Indus Delta (Hayter, 1960) resulting in downslope (down-canyon) transport of fluvial sediment (Coleman and Wells, 1982). Sediment loading and failure of delta-front sediments, induced by high sediment supply rates, near the head of the Indus Canyon is the prime way to form turbidity currents which transport sediment seaward through the canyon: the formation of hyperpycnal flows at the mouth of the Indus River is thought to be unimportant at present (Mulder and Syvitski, 1995). Von Rad and Tahir (1997) observed a >70-m-thick layered sediment sequence on their high-resolution seismic profiles in the flatter central parts of the Indus Canyon and the upper fan channel. Most likely these sediments were deposited as a transgressive sequence during the deglaciation after channel-levee system A was abandoned (since ~11.5 ka BP). If this is true, sedimentation rates in the canyon and upper fan channel were >6 m/ka. The Indus Canyon experienced an ongoing activity of turbidity currents during very recent times. Based on the hemipelagic drape (8-25 cm) at the surface of our canyon floor cores and a sedimentation rate of 150 cm/ka (core SO90-188KL) we calculate that during the last 50-165 years only hemipelagic muds draped the Indus Canyon floor, even within the axial channel. Besides the offshore transport of sediment through the canyon, sediments are presently predominantly accumulating on the inner shelf east of the Indus Delta and are transported along-shore in a SE direction during the SW monsoon period (Nair *et al.*, 1982). Modern sediment trap data of Nair *et al.* (1989) indicate that still a very small proportion of the Indus-derived muds is supplied to the deep sea.

### Comparison with other Deep-Sea Fan Systems

The cessation of turbidite deposition on the continental slope off the Indus Delta at ~115 ka BP indicates that the main locus of deposition shifted from the continental slope to another location, most likely to the channel-levee systems (?B, ?C) of the Indus Fan. This scenario is very similar to the configuration found for the Amazon Fan. During the last interglacial Eemian sea-level highstand, the Amazon Fan was sediment-starved as indicated by the calcareous ooze draping the fan (Damuth, 1977; Damuth *et al.*, 1988). The initiation of turbidite deposition on the continental slope off the Amazon Delta occurred at ~120 ka BP (transition oxygen-isotope substage 5.5 to 5.4) and on the Amazon Fan at ~110 ka BP (oxygen-isotope substage 5.4). These observations indicate that turbidite deposition on deep-sea fans may initiate without having a significant drop in sea level.

Rapid falling sea level can, however, result in episodic input of siliciclastics and trigger large-scale reorganisations of channel pattern. The abandonment of channel-levee system B and initiation of channel-levee system A on the Indus Fan has been the result of such a rapid fall in sea level ~25 ka BP. Significant erosion of the continental slope off major deltas and subsequent development of turbidite systems on the associated deep-sea fans due to the fall in sea level at ~24 ka BP (transition oxygen-isotope stage 3 to 2) as well as at ~75 ka BP (transition oxygen-isotope stage 5 to 4) has been observed on the Amazon Fan (Manley and Flood, 1988) and the Mississippi Fan (Feeley *et al.*, 1990).

Kolla and Perlmutter (1993) showed that turbidite deposition on the Mississippi Fan continued until about 12-11 ka BP on backstepping channel-attached lobes, a situation very similar to what we found on the Indus Fan. Many deep-sea fan systems like the Amazon Fan (Damuth, 1977; Damuth *et al.*, 1988), the Mississippi Fan (Nelson *et al.*, 1992) and the Indus Fan (Kolla and Coumes, 1987; Kenyon *et al.*, 1995; this study) are draped by a pelagic calcareous ooze of approximately Holocene age. So, clearly, the rapid rise in sea level during the last deglaciation resulted world-wide in the cessation of river-derived sediment supply towards large deep-sea fan systems. Subsequently, the deceleration in sea-level rise between 8.5 and 6.5 <sup>14</sup>C ka BP resulted in a world-wide initiation of deltas as the rate of fluvial sediment input overtook the declining rate of sea-level rise along coasts (Stanley and Warne, 1994).

Although the distal Bengal Fan is draped by a pelagic calcareous ooze of Holocene age (Stow *et al.*, 1989), the middle Bengal Fan experienced active growth during the most recent sea-level rise and the Holocene highstand (Weber *et al.*, 1997). Weber *et al.* (1997) demonstrated that between terminations 1b and 1a, and especially at the end of the Younger Dryas, a 13-km-wide channel built up levees 50 m high. The continued sea-level rise during the early Holocene resulted in a general decrease of sediment supply to the Bengal Fan and turbidity currents were confined to the channel and gradually filled it. The Indus Fan and the Bengal Fan thus responded in a very similar way to the rising sea level of the last deglaciation, although the degree of sediment starvation is different.

## CONCLUSIONS

1. Major lobe switching on the upper Indus Fan (abandonment of channel-levee system B, initiation of channel-levee system A) concurred with the fall in sea level at the transition from oxygen-isotope stage 3 to 2 (25 <sup>14</sup>C ka BP);
2. Channel-levee system A developed during the last glacial sea-level lowstand coinciding with oxygen-isotope stage 2 (25-11.5 <sup>14</sup>C ka BP);
3. The rise in sea-level during the last two-step deglaciation gradually cut off the Indus River as the main source of sediment for the channel-levee system A: turbidite sedimentation ceased at termination 1b (11.5 <sup>14</sup>C ka BP); fluvial-mud supply decreased sharply between termination 1b and 1a (11.5-9 <sup>14</sup>C ka BP); terrigenous sedimentation has been dominated by eolian dust of Arabian provenance after terminations 1a (after 9 <sup>14</sup>C ka BP);
4. The dominant control on channel shifting, occurring every ~2 ka, within channel-levee system A remains unclear and may involve either high-frequency climate-induced changes in sediment supply or autocyclicality. The updip contraction of the channel-mouth lobe of channel-levee system A1 is caused by a decreasing fluvial-sediment input as a result of sea-level rise;
5. Sea-level-induced changes in the growth pattern of the Indus Fan correspond with distinct episodes of erosion and deposition in the Indus Canyon and on the adjacent outer shelf and continental slope: development of channel-levee system A coincided largely with the period of maximum erosion of the Indus Canyon; cessation of turbidite deposition on channel-levee system A coincided with the initial drowning of the Indus Delta; the gradual cutoff of fluvial-mud supply to the Indus Fan coincided with the flooding of the shelf and the deposition of delta-front sediments of the Indus River on the alluvial plain, the inner shelf and partly in the Indus Canyon.

## ACKNOWLEDGEMENTS

Although hindered by technical problems during Leg D1 of the Netherlands Indian Ocean Programme, the scientists, technicians, and crew members on board R.V. *Tyro* during Leg D3 were able to recover a series of sediment cores from the middle Indus Fan. We are very thankful to them, because without the rearrangement of their cruise programme this material could not have been collected. We are indebted to all SO-90 scientists, technicians and crew members of the RV *Sonne* for their commitment during the PAKOMIN project. We thank A. Inam and M. Tahir (NIO, Karachi, Pakistan) for their cooperation during Leg D1. We are grateful to H. Schulz (BGR, Hannover), G.J. Reichert, H.J. Visser and J.-B.W. Stuut for their assistance during sampling of the SO-90 cores. We thank P. Anten, T. Broer, A. van Dijk, G. Ittman, M. Reith, G. van 't Veld, T. Zalm for assistance in the laboratory and analytical work. G. Klaver and B. van Os (NITG-TNO, Haarlem) are thanked for their co-operative support of J.C. during his research carried out in Haarlem. K. van der Borg (R.J. van de Graaff Laboratory, Utrecht University) is thanked for the AMS-<sup>14</sup>C datings. C. Laban (NITG-TNO, Haarlem) is thanked for his permission to use the GEOTECH multisensor core logger.

## CONTROLS ON LATE PLEISTOCENE-HOLOCENE SEDIMENTATION ON THE MAKRAN CONTINENTAL SLOPE

M.A. Prins<sup>1</sup>, G. Postma<sup>1</sup> and G.J. Weltje<sup>2</sup>

### ABSTRACT

The input of terrigenous sediment along the tectonically active Makran continental margin off south-western Pakistan (Gulf of Oman, northern Arabian Sea) is studied on the basis of sediment cores distributed along a transect from the upper slope to the abyssal plain. Spatial and temporal variations in sediment composition, sedimentation rate and turbidite frequency in late Pleistocene-Holocene time (~20-0 <sup>14</sup>C ka BP) will be discussed and related to changes in sea level and climate, and tectonic activity.

Numerical-statistical algorithms have been used to model end-member grain-size distributions of the hemipelagic and turbiditic sediments on the Makran continental slope. The grain-size distributions can be adequately described as mixtures of three end members. The end members represent turbidite sand, turbidite silt or eolian dust, and fluvial mud. The geochemical and mineralogical composition of the hemipelagic sediments indicate that the eolian dust was dominantly supplied from the northern Arabian Peninsula and the Persian Gulf region, and that the fluvial input is from the Makran. The ratio of contributions of eolian and fluvial sediment in the hemipelagic intervals is used as an indicator of continental aridity, i.e., summer-monsoon intensity.

The highest Holocene turbidite frequencies and sedimentation rates are recorded at the deepest coring sites. They are related to the local tectonic setting of these sites, i.e., the proximity of the deformation front of the accretionary prism. Turbidite sedimentation on the upper continental slope was most frequent during the last glacial period of sea-level lowstand, and continued during the entire deglaciation period with sea-level rise. Infrequent turbidite sedimentation occurred during the Holocene highstand of sea level. Turbidite sedimentation during the period of late sea-level rise and the Holocene sea-level highstand is inferred to be due to the strong impact of episodic events (i.e., flash floods and earthquakes) and because of the narrow shelf of the active Makran continental margin.

### INTRODUCTION

Changes in sea level and climate on river-delta-fan systems can result in distinctly different fan deposits depending on whether the river system discharges onto a passive or an active continental margin. The largest Quaternary deep-sea fan systems have developed along passive continental margins and are fed by large, lowland river systems. Turbidite

---

<sup>1</sup> Institute for Paleoenvironments and Paleoclimate Utrecht (IPPU), Faculty of Earth Sciences, Utrecht University, P.O. Box 80021, 3508 TA Utrecht, The Netherlands

<sup>2</sup> (a) Department of Geo-Energy, Netherlands Institute of Applied Geoscience TNO, P.O. Box 6012, 2600 JA Delft, The Netherlands; (b) Subfaculty of Applied Earth Sciences, Delft University of Technology, P.O. Box 5028, 2600 GA Delft, The Netherlands

sedimentation on such deep-sea fan systems is primarily controlled by glacio-eustatic sea-level fluctuations. During the last ~25 ka, turbidite sedimentation on the Amazon Fan, the Mississippi Fan, the Bengal Fan and the Indus Fan was largely confined to the last glacial period of sea-level lowstand. The rapid rise in sea level during the last deglaciation resulted in a sharp decrease of sediment supply towards these deep-sea fan systems. Consequently, large parts of these ‘passive-margin systems’ are draped by a pelagic calcareous ooze of approximately Holocene age (e.g. Damuth, 1977; Kolla and Coumes, 1987; Damuth *et al.*, 1988, Stow *et al.*, 1989; Nelson *et al.*, 1992; Kenyon *et al.*, 1995; Weber *et al.*, 1997; Chapter 6). In contrast, sediments discharged by small mountainous rivers on active continental margins are more likely to escape to the deep sea during sea-level highstands due to the greater impact of episodic events (i.e. flash floods and earthquakes) on small drainage basins and because of the narrow shelves associated with active margins (Milliman and Syvitski, 1992). Turbidite systems associated with active margins often have a fluvio/deltaic source. In such case, sediment supply can be controlled strongly by variations in river discharge due to climate change (Postma *et al.*, 1993, Weltje and De Boer, 1993).

The aim of this study is to investigate the controls on the input of terrigenous sediment along the tectonically active Makran continental margin off south-western Pakistan (Gulf of Oman, northern Arabian Sea). For this study we analyzed hemipelagic mud and turbidite sedimentation in late Pleistocene-Holocene time (~20-0 <sup>14</sup>C ka BP) at five localities on the Makran continental slope. The geochemical, mineralogical and grain-size characteristics of the hemipelagic sediments were analyzed to determine temporal variations in the flux and the provenance of the terrigenous sediment fraction. The end-member modelling algorithms of Weltje (1994, 1997a) were applied to the data set of grain-size distributions in order to model end-member grain-size distributions of turbiditic and hemipelagic sediments.

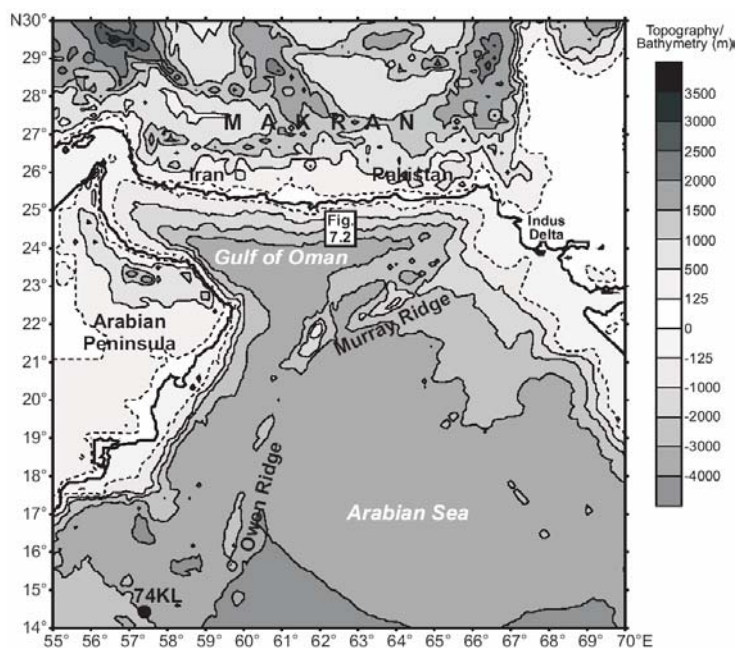


**Fig. 7.1** — Topography of the northern Arabian Sea, the Gulf of Oman and the surrounding landmasses. Elevation is contoured at 500 m intervals whereas bathymetry is contoured at 1000 m intervals (note: dashed contour lines are -125 and +125 m). Location of study area (enlarged in Figure 7.2) on the Makran continental slope of south-western Pakistan and ‘reference core’ 74KL (see text for discussion) are indicated. Topographic data from U.S. National Geophysical Data Center/World Data Center A for Marine Geology and Geophysics.

#### *Geological Setting of the Makran*

The continental margin of Iran and south-western Pakistan is the offshore extension of the Makran subduction complex, where oceanic crust of the Gulf of Oman (northern Arabian Sea) has been subsiding under the Asian continent since the Late Cretaceous or early Tertiary (White, 1982; Arthurton *et al.*, 1982; McCall and Kidd, 1982). The subduction process has caused a topography of uplifted ridges and intervening basins lined parallel to the coast (White, 1982) comparable to other 'imbricated terraced forearc systems' as described by Dickinson and Seely (1979). A major episode of uplift started in the course of the mid Pleistocene, and as a result 'sub-Recent' shoreline sediments were raised up to 500 m. These uplifted terranes have been cannibalised and their sediment is transferred to the youngest shelf-slope lobes (Harms *et al.*, 1984).

A small area (~70x90 km) on the Makran continental slope (Fig. 7.1) was surveyed in detail through seismic profiling (White, 1982). The survey showed that sediments are initially folded in a frontal fold, being the toe of the accretionary prism (Fig. 7.2), and that further folding and faulting occurs landward of the toe. Fowler *et al.* (1985) mapped the porosity-depth gradient across the prism on the basis of seismic velocities in the sediments and showed a marked change in porosity at the seaward side of the frontal fold. This change marks the boundary between the tectonically compacted sediments within the Makran accretionary prism to the north and the undeformed abyssal plain sediments to the south. Basins between the uplifted folds have been filled with sediment, the amount of infill increasing towards the coast (White, 1982). This study reports on the type and origin of the sediments deposited in these basins during the late Pleistocene and Holocene.

## **MATERIAL AND METHODS**

During the Netherlands Indian Ocean Programme on RV Tyro (Van der Linden and Van der Weijden, 1994), five piston cores were taken along a transect perpendicular to the Makran continental slope (Fig. 7.2; Table 7.1). Cores were taken from the upper slope (core NIOP468; 1325 m), from three slope basins (cores NIOP469-NIOP471; 1768, 1840, 2482 m respectively) and from the abyssal plain (core NIOP472; 3274 m).

Splitted 1-m-sections of cores NIOP468-NIOP472 were logged at 5 cm intervals with the CorTex XRF corescanner aboard ship (Reichart *et al.*, 1994). The CorTex corescanner, designed and built at the Netherlands Institute for Sea Research (NIOZ), offers the opportunity to obtain a qualitative impression of the chemical composition of the sediment (Jansen *et al.*, 1998). Specific radiation intensities (in counts per second) were calculated for eight elements. In this study only the Ca-profiles will be presented.

In total, 319 hemipelagic mud samples were taken from cores NIOP468-NIOP472 and 65 turbidite samples from cores NIOP469 and NIOP472 (Table 7.1). The hemipelagic mud layers, which occur intercalated between turbidite sands and muds, were identified on the basis of the occurrence of 'scattered' foraminifera and burrows (clearly identifiable on X-ray images). One series of hemipelagic mud samples (n=53) from core NIOP469 was decarbonated with excess of 3% HCl solution in order to measure the grain-size distribution of the siliciclastic sediment fraction; measurement of the other samples provided the grain-size distribution of the bulk fraction. The grain-size distribution of the samples was measured with a Malvern 2600 laser-diffraction size analyser using a lens with 100 mm focal length. This configuration provided measurements in 32 discrete size classes between 0.5 and 188

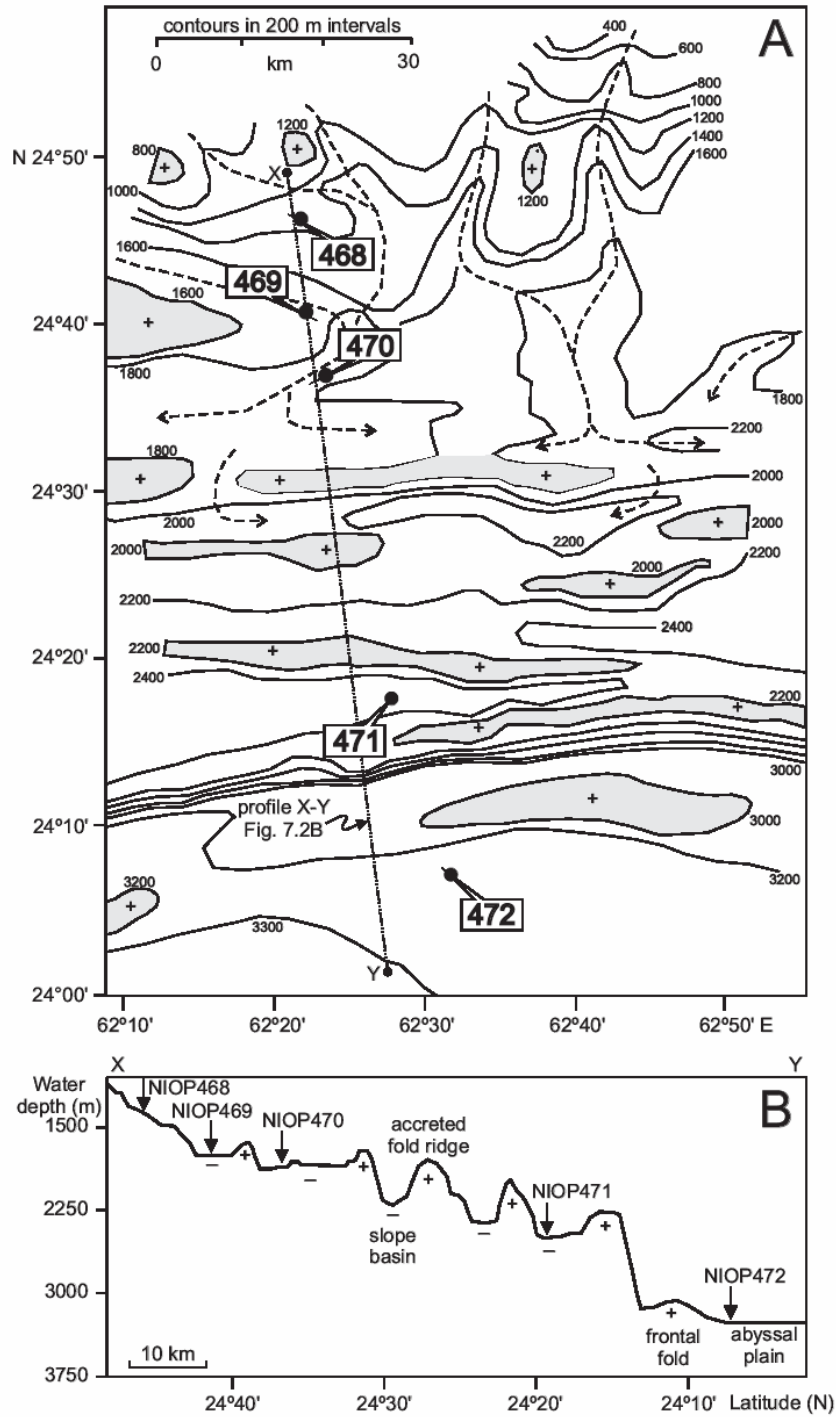


**Fig. 7.2** — A: Bathymetric map of the study area (see Figure 1 for location) over the offshore Makran accretionary belt, drawn after White (1982). Note the well-lined sequence of topographic highs (shaded) and intervening basins. Canyons are visible on the upper portion of the slope. Core sites NIOP468-NIOP472 are indicated. Bathymetry is contoured at 200 m intervals. B: Profile X-Y correspond with seismic reflection profile C of White (1982). The ‘projected’ position of cores NIOP468-NIOP472 is indicated.

$\mu\text{m}$  (equivalent volume diameter; see Table 2.1 in Chapter 2). The three coarsest size classes contain, on average, a very small proportion of the total mass. They were amalgamated into a single class to reduce the number of input variables for the end-member modelling algorithms to 30. A brief summary of the end-member modelling technique of Weltje (1994, 1997a) is given in Chapter 3.

The mineralogical and chemical composition of samples from core NIOP469 was investigated by means of XRD and ICP. Prior to the XRD analysis, carbonate was removed from the sediment samples by treatment with excess of 5% HAc solution. The clay fraction was separated by centrifuging. The supernatant suspension (containing the clay fraction) was concentrated and put on a glass slide. Ethylene glycol-solvated samples were used for qualitative analysis of the minerals present in the clay fraction. Analyses were performed on a Philips PW 1700 diffractometer (Cu- $k\alpha$  radiation).

Samples for ICP analysis were thoroughly grounded in an agate mortar prior to  $\text{HClO}_4$ ,  $\text{HNO}_3$ , HF acid digestion. The final residue was taken up in 1 M HCl. The elemental chemical composition was measured using an ICP-ES (ARL 34000). The carbonate content was calculated from the total Ca concentration in the bulk sediment samples, using a correction for clay-derived Ca;  $\text{CaCO}_3 = 2.5(\text{Ca}_{\text{tot}} - (\text{Ca}/\text{Al}_{\text{clay}} \times \text{Al}_{\text{tot}}))$ , where  $\text{Ca}/\text{Al}_{\text{clay}}$  is 0.345 (Turekian and Wedepohl, 1961). To assess the influence of sediment source versus grain size on the chemical composition of the siliciclastic sediment fraction, we analysed the composition of selected size ranges (silt fractions AB, C, D with modal grain sizes of  $\sim 5$ ,  $\sim 15$ ,  $\sim 40 \mu\text{m}$  and the sand fraction E  $> 63 \mu\text{m}$ ) of sediment samples. The silt fractions were separated from the bulk siliciclastic fractions by means of a settling tube, and the sand fraction was extracted by sieving.

An oxygen-isotope stratigraphy, based on  $\delta^{18}\text{O}$  analyses of the carbonate tests of the planktonic foraminifera species *Neogloboquadrina dutertrei* (150-595  $\mu\text{m}$ ) was constructed for cores NIOP469 and NIOP472. The chronology of core NIOP469 is based on several AMS- $^{14}\text{C}$  datings of total organic carbon or planktonic foraminifera. Because of the scarcity of foraminifera in core NIOP469, the datings were performed on a mixture of planktonic foraminifera ( $\sim 10 \text{mg}$ ). A -400-yr correction was applied for the age of the sea water (Bard, 1988).

**TABLE 7.1 — SEDIMENT CORES USED IN THIS STUDY**

Core number	Position (lat. N, long. E)	Area	Water depth (m)	Core length (m)	Number of samples	
					'mud'	'turbidite'
NIOP468	24°46'.4, 62°20'.8	upper slope	1325	5.51	48	
NIOP469	24°40'.9, 62°22'.0	slope basin	1768	13.96	104†	11
NIOP470	24°36'.9, 62°22'.9	slope basin	1840	5.50	51	
NIOP471	24°18'.4, 62°27'.1	slope basin	2482	9.49	54	
NIOP472	24°07'.0, 62°29'.2	abyssal plain	3274	10.46	62	54

† The grain-size distribution of the bulk fraction was measured on 51 samples and the grain-size distribution of the siliciclastic fraction was measured on 53 samples.

## RESULTS

*Turbidite Sand Bed Thickness and Distribution*

All five sediment cores showed a fine-grained turbidite-dominated succession (Fig. 7.3). Core NIOP468 contains 9, core NIOP469 contains 145, core NIOP470 contains 53, core NIOP471 contains 49, and core NIOP472 contains 114 sand beds. The average frequency of occurrence is 8.24 sand beds per metre of sediment. The sand beds form the base of turbidite beds and vary in thickness between 0.1 and 16 cm. The sand beds grade into silty sand and silt. In core NIOP469, turbidite sand-bed thickness shows an overall upward thinning between 14 and 3 metres below the sea floor (mbsf). Above 3 mbsf only a few thicker turbidites are present. The change from a succession of closely spaced thin turbidites to a succession of less abundant, overall thicker turbidites, is visible in core NIOP472 as well. The uppermost metres of especially cores NIOP468 and NIOP469 are devoid of turbidite beds. In order to investigate if the changes in turbidite facies at the different coring sites were synchronous, we established an inter-core correlation based on various compositional parameters of particularly the intercalated hemipelagic mud intervals.

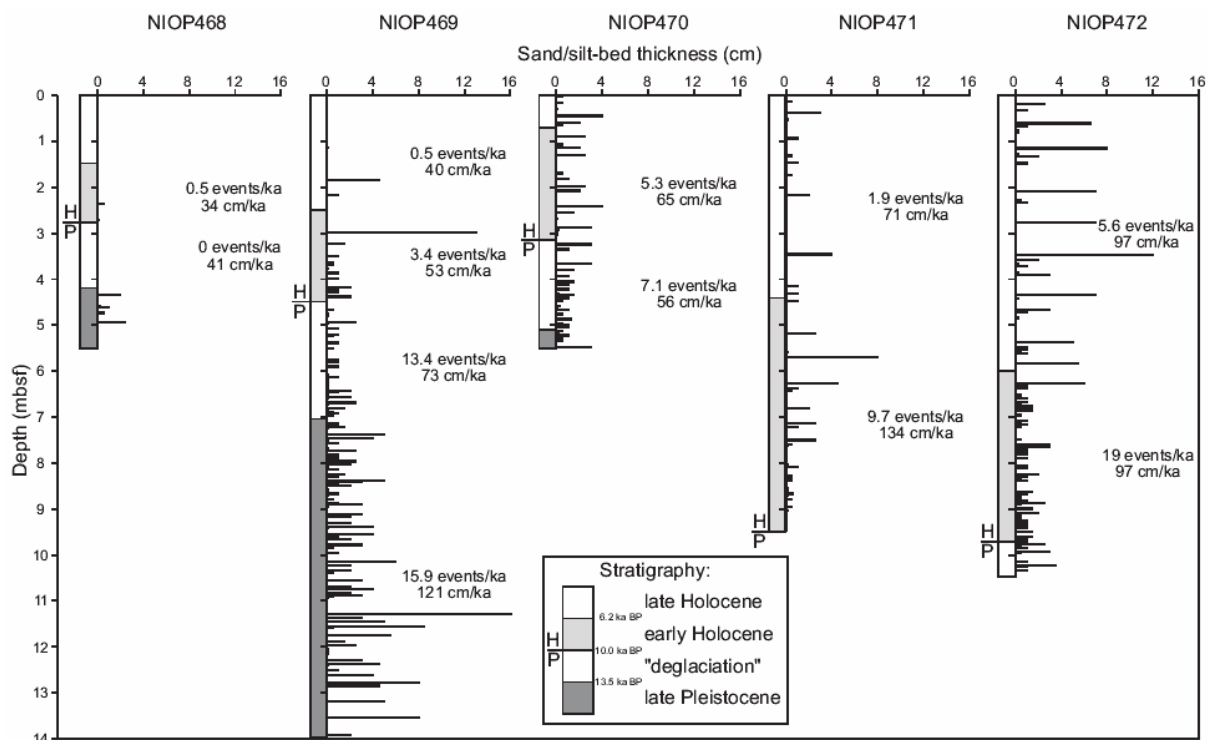


Figure 7.3 — Turbidite distribution and turbidite sand bed thickness in cores NIOP468-NIOP472. The division of core NIOP469 into chronostratigraphic units is based on  $^{14}\text{C}$  datings; subdivision of the other cores is based on correlation of various compositional parameters ( $\delta^{18}\text{O}$ , Ca content, grain-size distribution; see Figures 7.4, 7.5, 7.14), determined on intercalated hemipelagic muds (see text for discussion), with the records of core NIOP469. For each unit the turbidite frequency and sedimentation rate are indicated.

## Age Models

The *Neogloboquadrina dutertrei*  $\delta^{18}\text{O}$  records of cores NIOP469 and NIOP472 are shown in Figure 7.4. The distinct decrease in  $\delta^{18}\text{O}$  towards the top of core NIOP469 represents the transition from the last glacial period to the Holocene interglacial period and the transition from isotope stage 2 to 1 (termination I). In core NIOP469 this transition is a two-step change, which correspond to terminations Ia (~6.5 mbsf) and Ib (~4.5 mbsf). The Bølling/Allerød (low  $\delta^{18}\text{O}$  values around 6 mbsf) and the Younger Dryas (high  $\delta^{18}\text{O}$  values at 5 mbsf) are recognisable in the  $\delta^{18}\text{O}$  record of core NIOP469. The base of core NIOP472 has  $\delta^{18}\text{O}$  values of the same magnitude as the Younger Dryas in core NIOP469. The sediment in the uppermost ~10 metres in core NIOP472 is therefore inferred to be of Holocene age, i.e., the record spans the last ~10  $^{14}\text{C}$  ka.

The radiocarbon ages of the organic-carbon fractions at ~3, 5 and 7 mbsf appear to be systematically older than the planktonic foraminiferal fractions extracted from the same depth intervals in core NIOP469 (Table 7.2). For construction of the chronology of core NIOP469 we therefore neglected the radiocarbon ages of the organic fractions. The planktonic foraminiferal ages of 8090 and 12190  $^{14}\text{C}$  yrs BP (at ~7 and 9 mbsf) are not incorporated in the age model because they are stratigraphically not consistent and, according to the ages expected on the basis of the  $\delta^{18}\text{O}$  record, the ages are 'too young'. These misfits are inferred to be the result of laboratory errors (mixing up of samples or bad administration of results). The chronology of core NIOP469 is therefore based on only three datings of planktonic foraminifera taken from ~3, 5 and 13 mbsf. These datings indicate that the sedimentary record in core NIOP469 spans the last <20  $^{14}\text{C}$  ka.

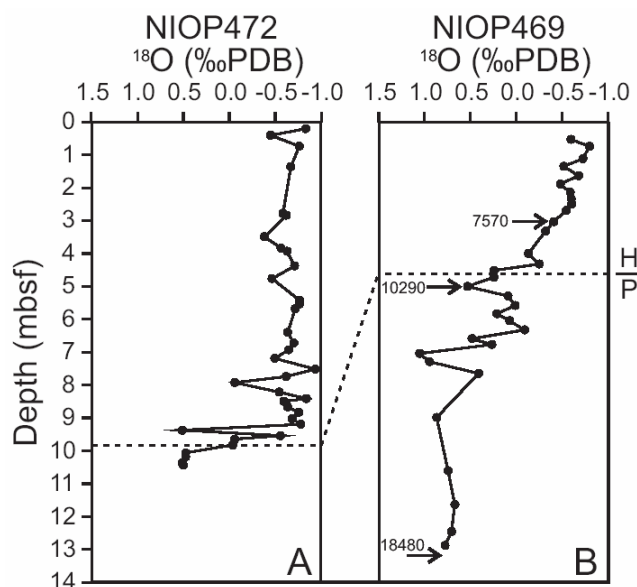


Fig. 7.4 — Planktonic foraminifer *Neogloboquadrina dutertrei*  $\delta^{18}\text{O}$  records of cores NIOP472 (A) and NIOP469 (B). Position of AMS- $^{14}\text{C}$  dated NIOP469 samples and radiocarbon ages ( $^{14}\text{C}$  yrs BP) are indicated (see also Table 7.2). The dashed line corresponds with the Holocene-Pleistocene boundary.

TABLE 7.2 — AMS  $^{14}\text{C}$  DETERMINATIONS IN CORE NIOP469

Sample number	Core depth (m)	Analysed fraction	$^{14}\text{C}$ age* (yrs BP)	Error (yr)
c80	3.00	planktonic forams	7570	70
61	5.00	planktonic forams	10290	150
50	7.04	planktonic forams	8090†	80
33	8.98	planktonic forams	12190†	70
7	13.07	planktonic forams	18480	150
c80	3.00	organic carbon	11520†	90
61-c66	4.98	organic carbon	13320†	90
‘above 50’	7.03	organic carbon	15540†	100

\* A -400 yr correction was applied for the estimated age of sea water (Bard, 1988).

† Age is stratigraphically not consistent; data not incorporated in age model.

### *CorTex Ca Records*

The down-core distribution patterns of Ca in cores NIOP468-NIOP472 were determined with the CorTex scanner and are shown in Figure 7.5. The Ca content was determined on samples taken from core NIOP469 by ICP analysis; results are shown next to the CorTex Ca profile. The overall resemblance of both Ca profiles of core NIOP469 testifies to the general usefulness of the CorTex results as a tool for inter-core correlation (indeed one of the intentions for building the CorTex scanner; see Jansen *et al.*, 1998). Variations in Ca concentration are inferred to record mainly variations in carbonate content (see also ‘sediment composition’ section below). Background Ca values of 100-200 counts per second are recorded in all five cores corresponding in core NIOP469 to a carbonate content of approximately 10 wt% (see Fig. 7.17). Enhanced Ca values are recorded in discrete intervals in cores NIOP468, NIOP469 and NIOP470. The sedimentary records could be correlated on the basis of these Ca peaks. Cores NIOP471 and NIOP472 could not be correlated with the other cores on the basis of the Ca records.

### *Median Grain-Size Records*

The median grain-size records of the hemipelagic muds in cores NIOP468-NIOP472 are shown in Figure 7.6. Comparison of the median grain-size record (Fig. 7.6) and the  $\delta^{18}\text{O}$  record (Fig. 7.4B) of core NIOP469 indicates that relatively coarse-grained muds have been deposited during the last glacial period (~7-14 mbsf) and during the late Holocene (upper ~2.5 mbsf). Within core NIOP469, the median grain size decreased gradually during the transition from the last glacial period to the Holocene interglacial period, and reached a distinct minimum during the early Holocene (~3 mbsf). Comparison of the median grain-size record (Fig. 7.6) and the  $\delta^{18}\text{O}$  record (Fig. 7.4A) of core NIOP472 supports the observations made in core NIOP469 that relatively fine-grained muds have been deposited during the early Holocene (below ~6 mbsf) and relatively coarse-grained muds during the late Holocene (above ~6 mbsf).

Correlation of cores NIOP468, NIOP470 and NIOP471 with cores NIOP469 and NIOP472 on the basis of their median grain-size records will not be done as variations in median grain size cannot be interpreted unambiguously (see also Prins and Weltje, 1999; Chapter 4). Therefore, the end-member modelling results of the grain-size distributions and their interpretation will be considered first. The inter-core correlation will be based on the end-member modelling results (see Figure 7.14).

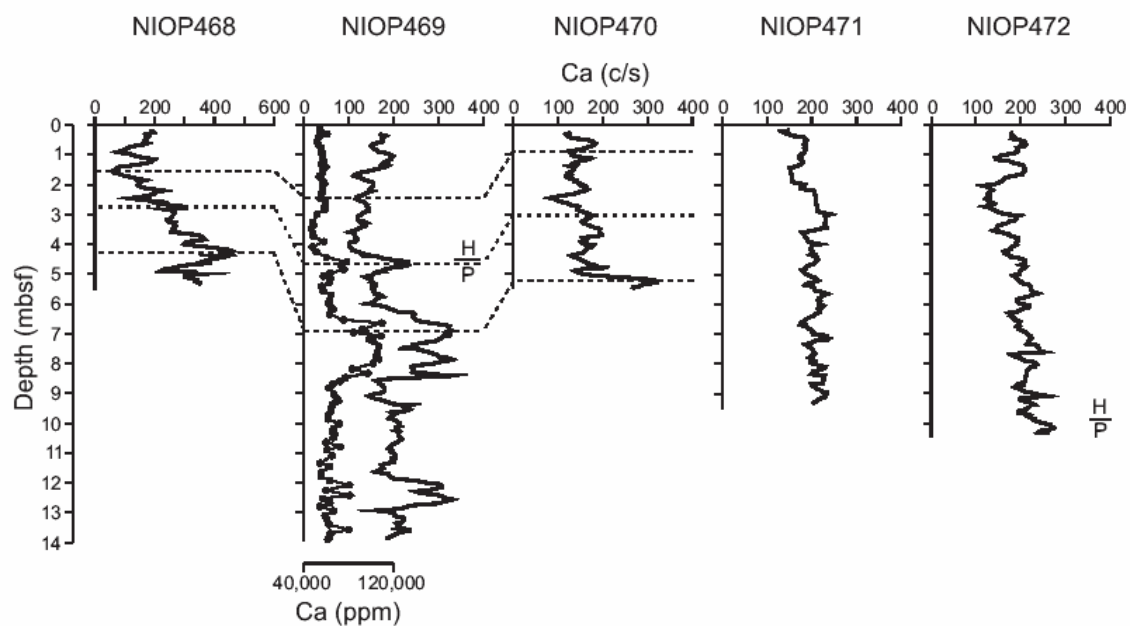


Fig. 7.5 — Lithostratigraphic correlation (dashed lines) between cores NIOP468, NIOP469 and NIOP470 is based on the visual correlation of the Ca records (in counts/second; 5-points moving average) determined with the CorTex XRF corescanner. The Ca record (in ppm) of core NIOP469 determined with ICP analysis is shown for comparison with the XRF results. The Pleistocene-Holocene boundary (H/P) is indicated in cores NIOP469 and NIOP472 (see Fig. 7.4).

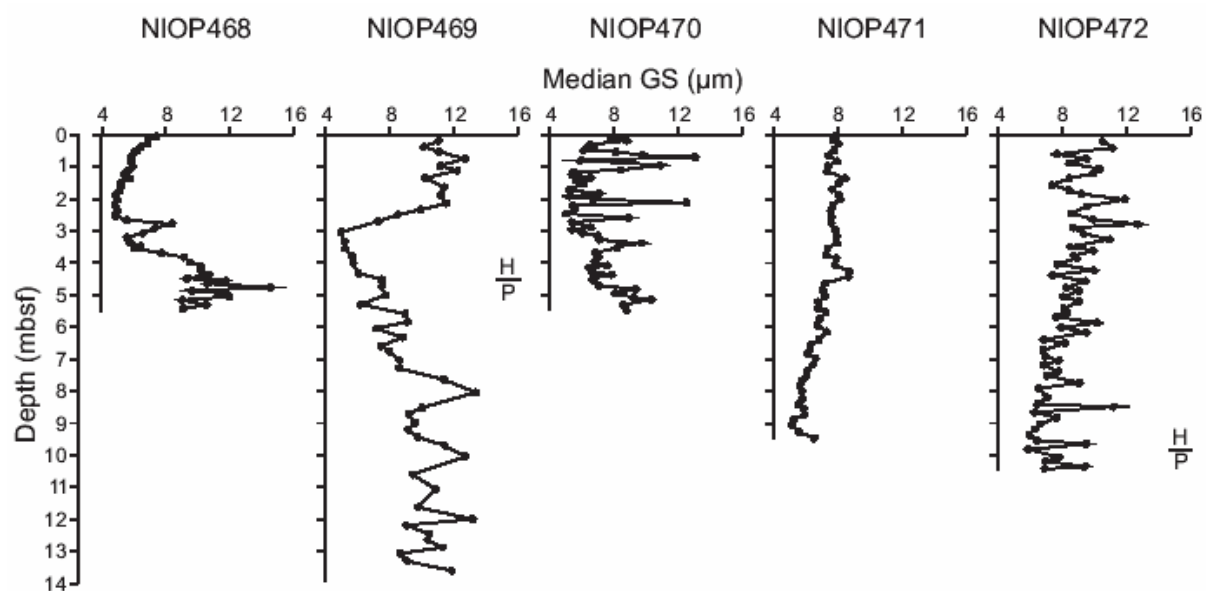


Fig. 7.6 — Median grain-size records of cores NIOP468-NIOP472. The Pleistocene-Holocene boundary (H/P) is indicated in cores NIOP469 and NIOP472 (see Fig. 7.4).

## End-Member Modelling of Grain-Size Distributions

*Estimating the number of end members.—*

The grain-size distributions of the hemipelagic mud and turbidite samples ( $n=384$ ) from cores NIOP468-NIOP472 were used as input data for the end-member modelling algorithms. The minimum number of dimensions (end members  $q$ ) required for a satisfactory approximation of the data is estimated by calculating the coefficients of determination. The coefficients of determination represent the proportions of the variance of each variable (i.e., grain-size class) that can be reproduced by the approximated data. This proportion is equal to the squared correlation coefficient ( $r^2$ ) of the input variables and their approximated values (see Chapter 3).

Figure 7.7A illustrates the distribution of the coefficients of determination across the grain-size classes for different numbers of end members. Several size ranges (classes 1, 4-5, 14-20 and 27-30) are poorly reproduced by a two-end-member model. The coefficients of determination for classes 27-30 are not weighted heavily in choosing the preferred end-member model, because the mass in the coarse tails of the grain-size distributions comprises only a small fraction of the total mass in the data set. Reproducibility of the other grain-size

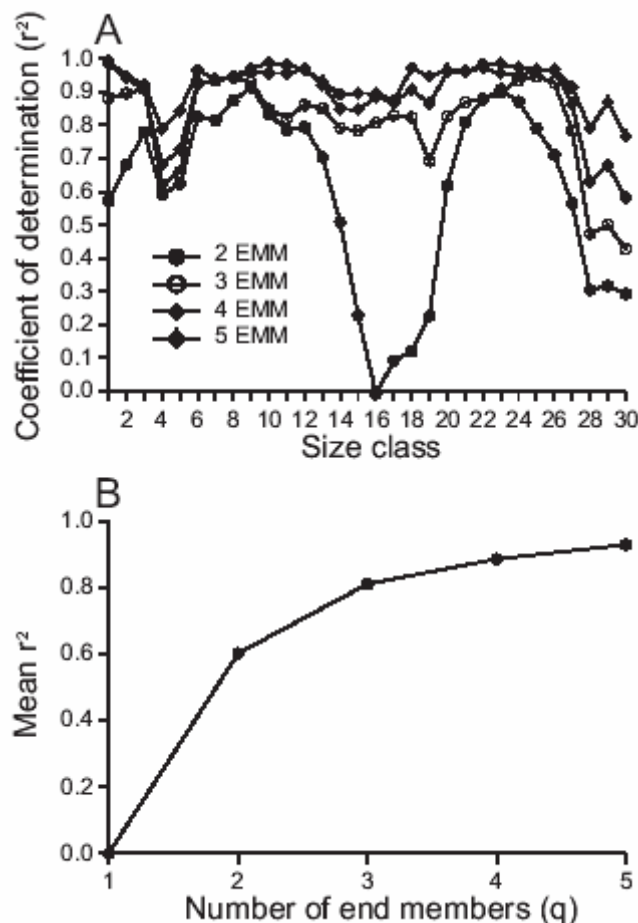


Fig. 7.7 — Goodness-of-fit statistics used to estimate the number of end members. A: Coefficients of determination for each size class. B: Mean coefficient of determination across size classes. At least three end members are needed to reproduce all variables adequately; a two-end-member model shows distinct lack of fit in several size ranges. Use of four or more end members hardly improves the goodness-of-fit relative to a three-end-member model.

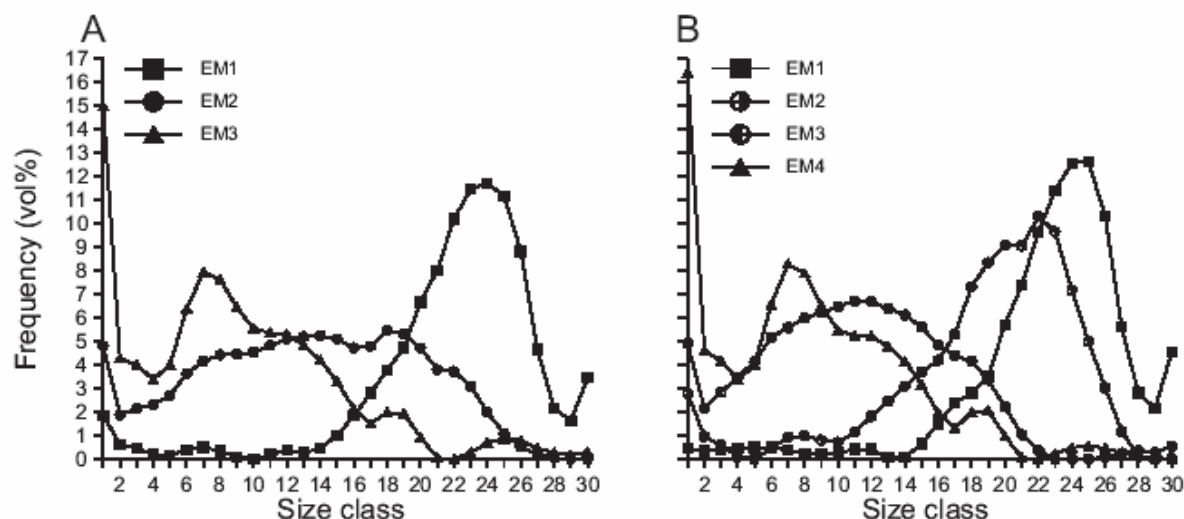


Fig. 7.8 — Modelled end members of turbiditic and hemipelagic sediments obtained from the Makran continental slope (see also Table 7.3). A: three-end-member model. B: four-end-member model.

ranges by the mixing model is considered to be of much greater importance, because this size range contains a considerable proportion of the total sediment mass. All of the 30 variables except size classes 28-30 are adequately reproduced by a three-end-member model, as indicated by their coefficients of determination which exceed 0.6 (equivalent to a correlation coefficient of 0.77).

The mean coefficient of determination across the grain-size classes (Fig. 7.7B) increases when the number of end members is increased. The mean coefficient of determination for a three-end-member model is 0.81, i.e., on average 81% of the variance in each grain-size class can be reproduced. A four-end-member models reproduces on average 88% of the input variances. The mean coefficient of determination increases only slightly for the five-end-member model. In conclusion, the goodness-of-fit statistics suggest that a three or four-end-member model provides a reasonable choice in view of the contradictory requirements of parsimony on the one hand (i.e., a minimal number of end members) and reproducibility on the other hand.

#### *Grain-size distributions of end members.—*

Three and four-end-member solutions were constructed to provide more insight into the nature of grain-size variation. The modelled end-member grain-size distributions for both models are shown in Figure 7.8 and the data are given in Table 7.3.

The first end members (EM1) of both models are almost identical and have a modal grain size of  $\sim 50 \mu\text{m}$  (class 24). End member 3 (EM3) of the three-end-member model is almost identical to end member 4 (EM4) of the four-end-member model. Both have a modal grain size of  $\sim 4.5 \mu\text{m}$  (class 7). End member 2 (EM2) of the three-end-member model has a poorly-sorted, polymodal grain-size distribution with modes around 5, 12, 22 and  $40 \mu\text{m}$  (classes 8, 14, 18 and 22). End members 2 and 3 (EM2 and EM3) of the four-end-member model have their modes at 40 and  $8 \mu\text{m}$  (classes 22 and 11), respectively.

The fact that both models are about equally good in approximating the observed variation in the data set is partly a consequence of the close similarity of their coarsest and finest end members. The small improvement in goodness-of-fit is further clarified by expressing the end members of the three-end-member model as mixtures of the end members of the four-end-member model: the least-squares mixing coefficients are shown in Figure 7.9. For instance,

EM2 of the three-end-member model is closely approximated by a mixture of 32% EM2 and 68% EM3 of the four-end-member model. Consequently, the marginal improvement of the goodness-of-fit reflects the addition of end members that explain only a small fraction of the compositional variation in the data. Comparisons between observed and modelled grain-size distributions (data and model) for both end-member models indicate that the mentioned improvement of the goodness-of-fit is mainly related to the ‘turbidite sand’ samples from core NIOP472. However, as there are no compelling reasons to prefer the four-end-member model above the three-end-member model from a statistical point-of-view, we will now investigate the applicability of the three-end-member model.

**TABLE 7.3 — MODELLED END MEMBERS OF MAKRAN CONTINENTAL SLOPE SILICICLASTIC SEDIMENTS**

Three-end-member model				Four-end-member model				
Size class	EM1 (%)	EM2 (%)	EM3 (%)	Size class	EM1 (%)	EM2 (%)	EM3 (%)	EM4 (%)
1	1.85	4.79	14.97	1	0.43	2.78	4.89	16.39
2	0.63	1.88	4.29	2	0.35	0.94	2.16	4.59
3	0.46	2.15	4.00	3	0.41	0.60	2.83	4.16
4	0.20	2.30	3.39	4	0.44	0.10	3.45	3.36
5	0.17	2.71	4.01	5	0.48	0.00	4.13	3.97
6	0.38	3.63	6.39	6	0.49	0.44	5.15	6.54
7	0.51	4.16	7.94	7	0.37	0.92	5.57	8.27
8	0.34	4.43	7.62	8	0.23	0.98	5.97	7.87
9	0.10	4.45	6.44	9	0.18	0.79	6.20	6.50
10	0.01	4.54	5.54	10	0.26	0.70	6.47	5.44
11	0.19	4.83	5.36	11	0.40	1.13	6.68	5.23
12	0.37	5.10	5.30	12	0.40	1.81	6.66	5.21
13	0.28	5.19	4.83	13	0.06	2.44	6.38	4.77
14	0.45	5.24	4.20	14	0.08	3.08	6.09	4.14
15	1.02	5.10	3.29	15	0.63	3.69	5.59	3.17
16	1.83	4.72	2.14	16	1.50	4.17	4.84	1.96
17	2.81	4.79	1.50	17	2.38	5.28	4.38	1.30
18	3.76	5.47	1.98	18	2.79	7.31	4.15	1.97
19	4.73	5.32	1.94	19	3.53	8.33	3.34	2.05
20	6.66	4.71	0.92	20	5.69	9.06	2.21	0.96
21	8.02	3.80	0.06	21	7.36	9.04	1.03	0.05
22	10.20	3.72	0.00	22	9.63	10.28	0.37	0.00
23	11.46	3.09	0.28	23	11.40	9.64	0.00	0.22
24	11.70	2.00	0.70	24	12.55	7.15	0.00	0.47
25	11.18	1.10	0.88	25	12.63	4.98	0.00	0.55
26	8.83	0.52	0.80	26	10.29	3.03	0.07	0.46
27	4.64	0.22	0.47	27	5.59	1.18	0.24	0.24
28	2.16	0.06	0.28	28	2.79	0.10	0.36	0.11
29	1.63	0.01	0.19	29	2.14	0.00	0.27	0.06
30+	3.45	0.00	0.30	30+	4.53	0.03	0.53	0.00

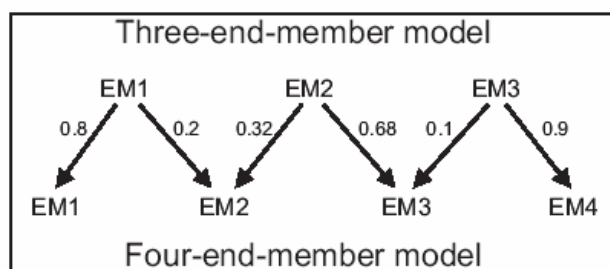


**Fig. 7.9** — Most likely combinations of the end members of the three and four-end-member models; least-squares mixture coefficients are shown.

*Variations in mixing coefficients according to three-end-member model.—*

Continuing with a three-end-member model, we visualised the total range of compositional variation in a ternary diagram (Fig. 7.10) of which the modelled end members form the three vertices. The individual data points of the estimated compositions of the 384 samples form a large scatter in the ternary mixing space (Fig. 7.10A). When the data of the two main sedimentary facies (turbidite, hemipelagic mud) are plotted separately in ternary diagrams some clear trends are visible. Samples from graded sand-mud turbidite beds in cores NIOP469 and NIOP472 can be described as mixtures of predominantly EM1 and EM2, as they plot on the left side of the ternary diagram (Fig. 7.10B). The hemipelagic mud samples from cores NIOP468-NIOP472 can be described as mixtures of predominantly EM2 and EM3 (Fig. 7.10C). However, the relative contribution of the third end member in both sedimentary facies (EM3 and EM1, respectively) is in many samples significant: the relative contribution of EM3 in the turbiditic samples reaches values up to 61% (Fig. 7.10B), and the relative contribution of EM1 in the hemipelagic muds reaches values up to 39% (Fig. 7.10C).

*Interpretation of end members of three-end-member model.—*

End members of a series of grain-size distributions may be related to two kinds of processes: (1) mixing of sediment which is transported by independent mechanisms and/or supplied from different sources and (2) selective mechanisms operating during unidirectional transport and deposition producing sediments whose grain-size distributions change systematically with distance from the source (Syvitski, 1991b). Mixing of fluvial mud and eolian dust as well as selective transport and deposition of eolian dust are held responsible for the observed variability in the grain-size distributions of pelagic and hemipelagic siliciclastic muds of the Arabian Sea (Prins and Weltje, 1999; Chapter 4). The sediments obtained from the Makran continental slope are clearly more complex as they comprise both turbiditic and hemipelagic sediments. Both sediment types are described as mixtures of the same end members (Fig. 7.10A). Consequently, interpretation of the end members in an unambiguous way is not possible. For instance, EM2 is important in the turbiditic as well as in the hemipelagic sediments (Fig. 7.10B, C) and may thus be related to turbidity-current transport or to eolian transport. However, examination of the compositional variation within two turbidite beds in core NIOP472 (Fig. 7.11 and 7.12) and within the hemipelagic muds in core NIOP469 (Fig. 7.13) suggests that EM1 and EM3 can be interpreted more readily.

Detailed grain-size analysis of two 30-40 cm thick turbidite beds in core NIOP472 indicates that the median grain size in both sediment beds decreases systematically from base to top (Fig. 7.11A and 7.12A). The exact nature of the grain-size grading is illustrated by the

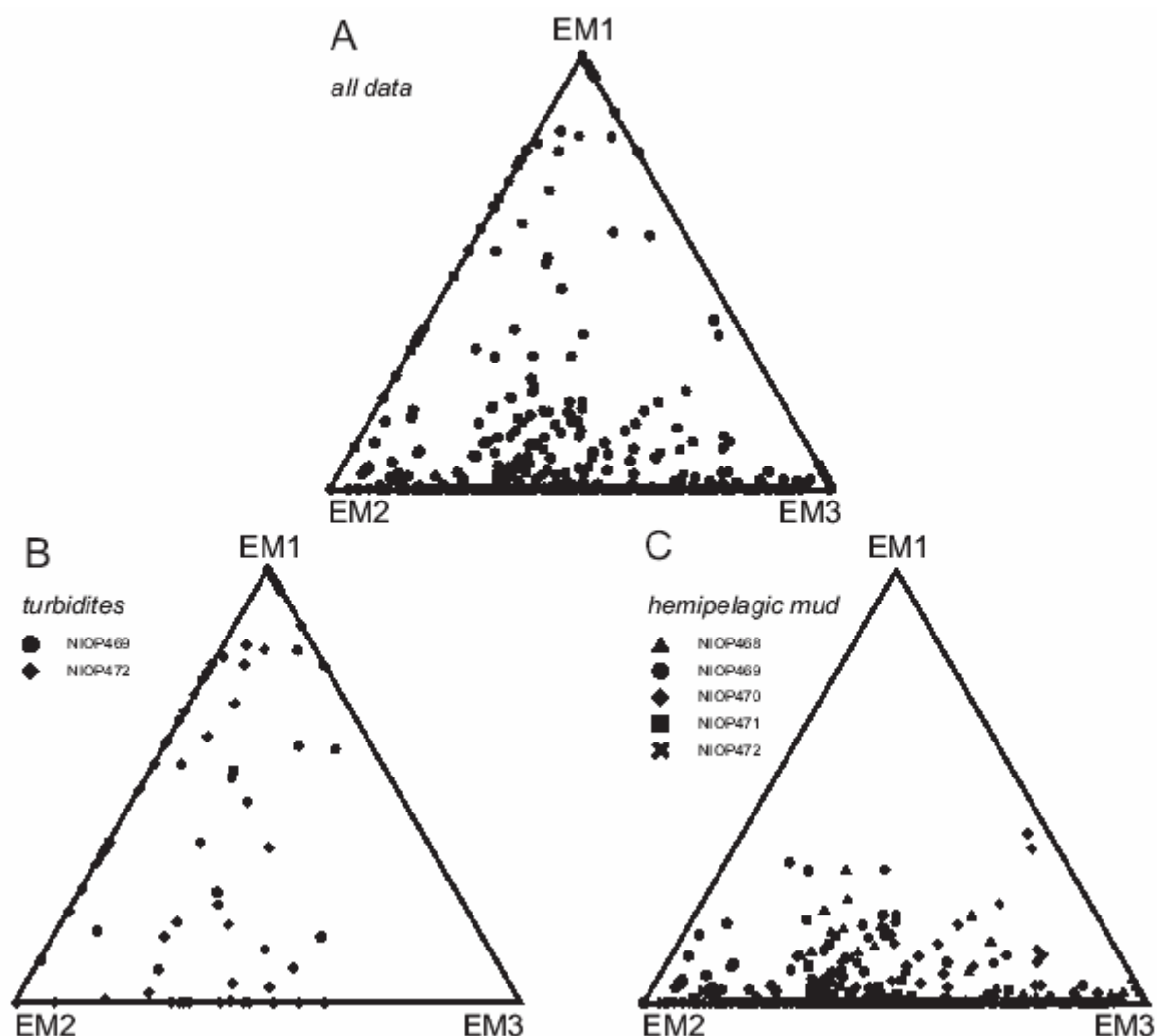


Fig. 7.10 — Mixing model of the Makran continental slope sediment samples. A: All 384 sediment samples. B: Binary mixing of EM1 and EM2 prevails in the turbiditic sediments ( $n=65$ ) in cores NIOP469 and NIOP472. C: Binary mixing of EM2 and EM3 prevails in the hemipelagic sediments ( $n=319$ ) in cores NIOP468-NIOP472.

variations in the grain-size distributions (Fig. 7.11B and 7.12B). The fining-upward trend is evidently related to selective suspension fallout and to deposition from a decelerating turbidity current. The systematic variations in the grain-size distributions are described by systematic variations in the relative contributions of the end members of the three-end-member model (Fig. 7.11C and 7.12C). The difference between the observed and modelled grain-size distributions in terms of absolute deviations (vol% per size interval) are shown for each observation (Fig. 7.11D and 7.12D). The summed absolute deviations are of the same order of magnitude as typical sampling and measurement errors for the studied core material, indicating that the three-end-member model successfully reproduces the compositional variation in the data.

Relative proportions of EM1 are high in the basal units of the turbidites ('sand beds' plotted in Fig. 7.3) and are nearly absent in the upper part of the turbidite bed. EM1 thus represents turbidite 'sand'. EM2 is dominant in the upper part of the turbidite beds and represents turbidite 'silt'. Relative contributions of EM3 increase gradually in the turbidite beds from base to top, however, not reaching values over 60%. Within the hemipelagic mud

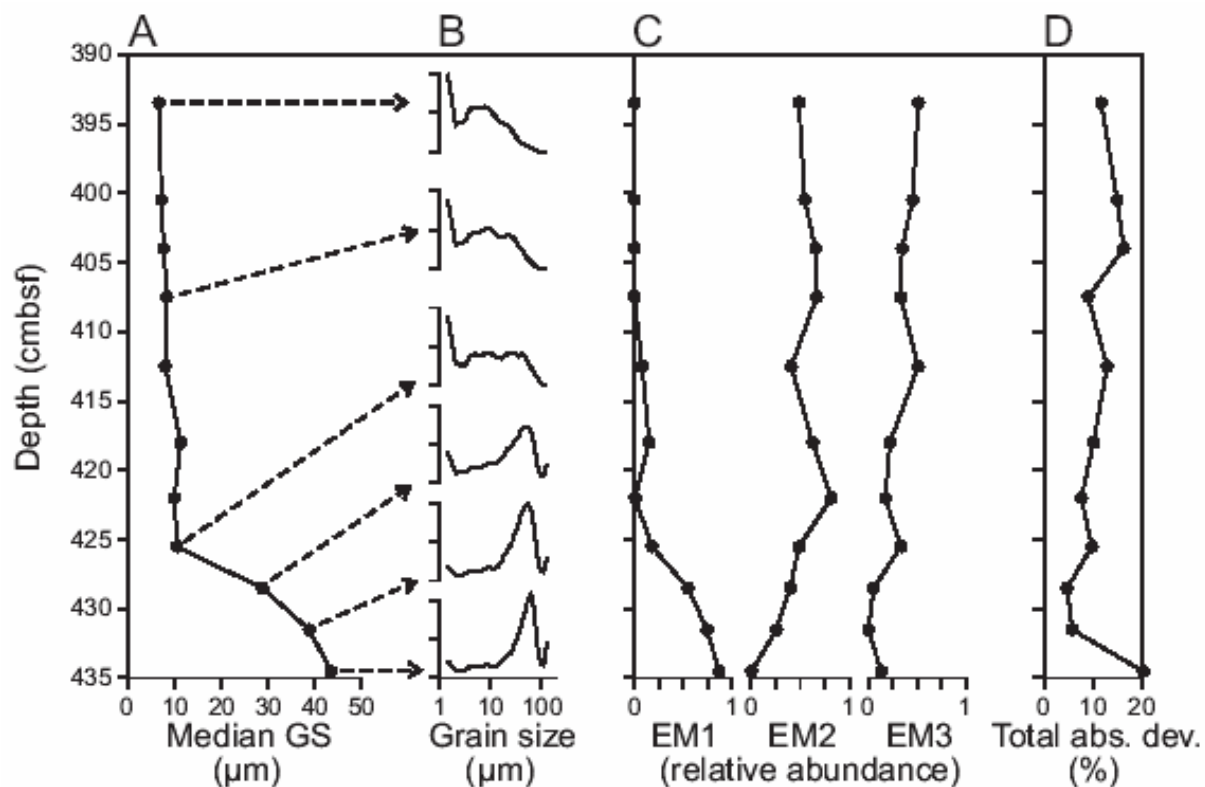


Fig. 7.11 — Detailed record of grain-size variations in a turbidite interval in core NIOP472. A: Decreasing median grain size indicates an upward-fining trend. B: Changes in the grain-size distributions of selected samples indicate the exact nature of the fining trend. C: Major grain-size trend is reflected by changes in the proportional contributions of the end members. D: Summed total absolute deviation between observation and model per sample.

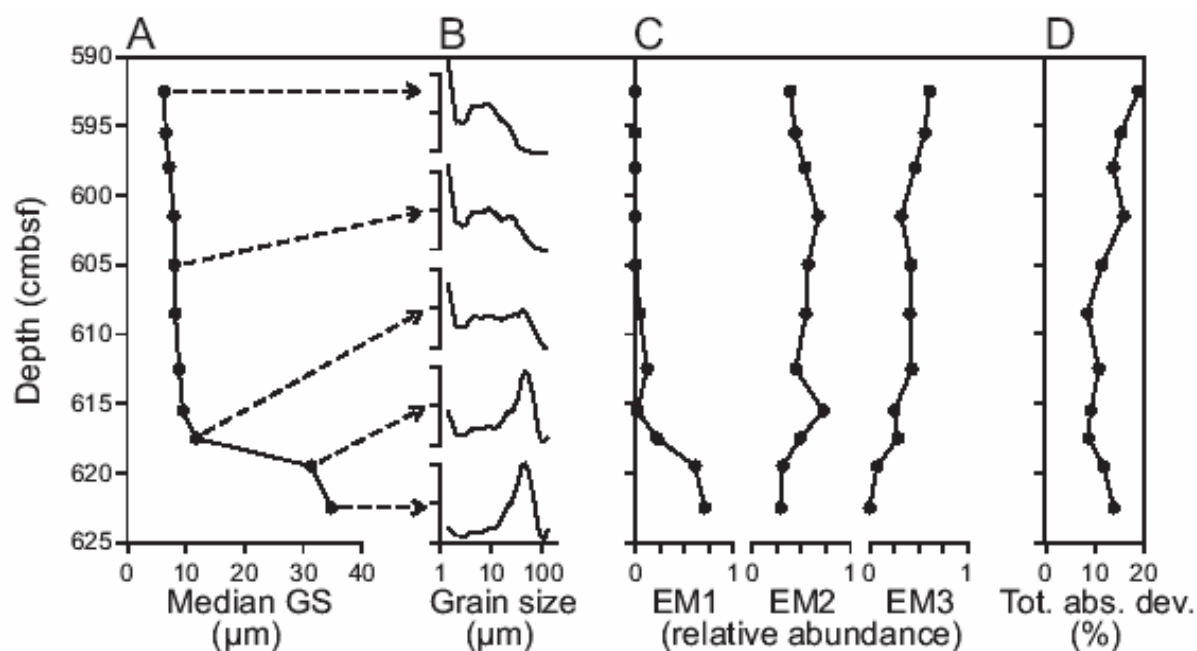


Fig. 7.12 — Detailed record of grain-size variations in a turbidite interval in core NIOP472; compare with Figure 7.11.

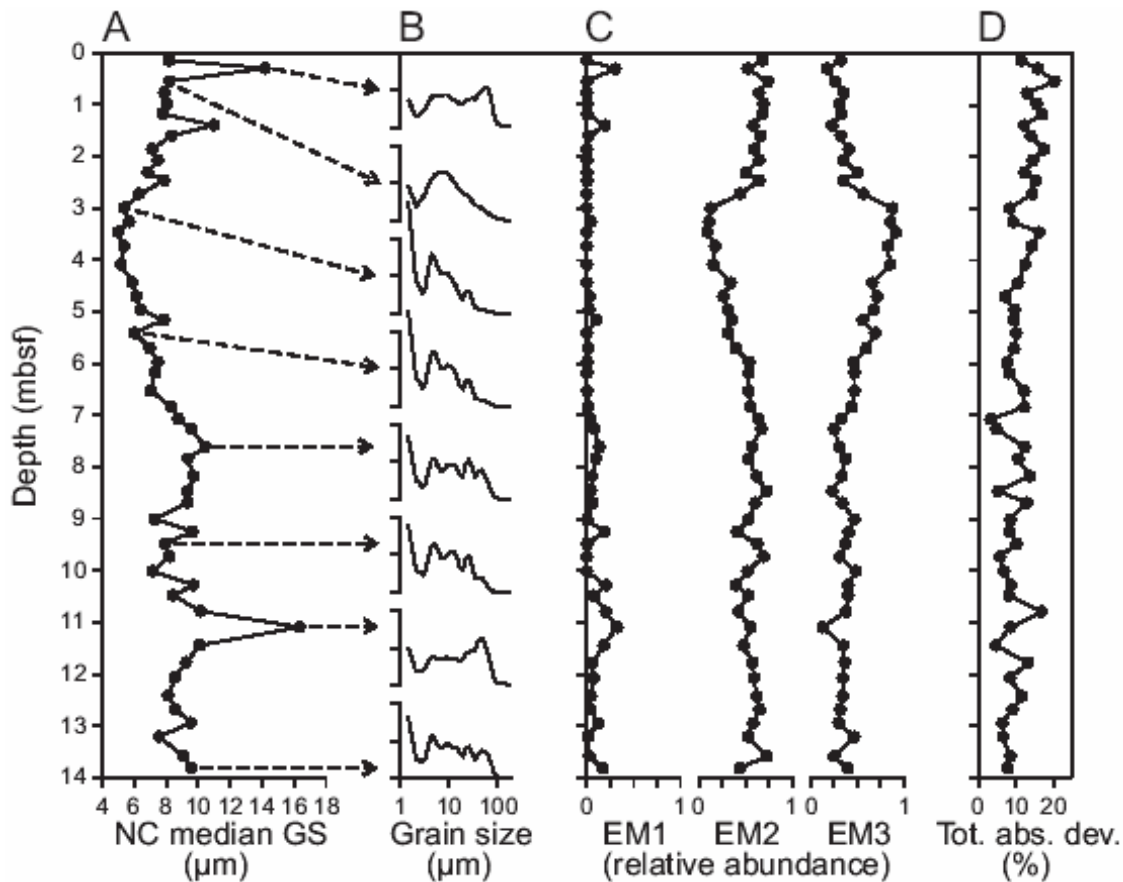


Fig. 7.13 — Grain-size variations in hemipelagites in core NIOP469; compare with Figures 7.11.

intervals the relative contributions of EM3 do reach values of 100% (Fig. 7.10C). Various supply mechanisms for the EM3 ‘clays’ are equally possible. The EM3 ‘clays’ may have been supplied by ‘high-density’ turbidity currents, associated with the supply of turbidite ‘silt’ and ‘sand’ (EM2 and EM3). Another possibility is that the EM3 ‘clays’ have been supplied across the shelf by ‘low-density’ turbidity currents originating from the rivers draining the Makran coastal range, most likely during flood events, or as wave-induced sediment resuspension clouds. EM3 thus represents either turbidite ‘clay’ or fluvial mud (analogous to the fluvial mud end member of Prins and Weltje, 1999; Chapter 4).

Within the hemipelagic mud intervals in core NIOP469, the relative proportion of EM1 is significant only in a few samples characterised by ‘extraordinary’ high median grain sizes (Fig. 7.13). Their grain-size distributions are polymodal and poorly sorted; some examples are shown in Figure 7.13B. The association of the turbidite ‘sands’ (EM1) with the hemipelagic muds is due to either contamination during sampling or mixing as a result of in situ burrowing activity.

The end-member modelling results allow the extraction of the ‘background sedimentation signal’ from the mud record by subtracting the contribution of EM1, e.g. by plotting the results as relative proportions of EM2 relative to EM3. The records of  $\log(\text{EM2}:\text{EM3})$  of cores NIOP469-NIOP472 are shown in Figure 7.14. Correlation of the  $\log(\text{EM2}:\text{EM3})$  records of cores NIOP468-NIOP472 provides extra data for the proposed inter-core correlation in Figure 7.3. The correlation between cores NIOP468, NIOP469 and NIOP470 on the basis of the  $\log(\text{EM2}:\text{EM3})$  records corresponds with the correlation on the basis of the Ca records (Fig. 7.5). The correlation of the  $\log(\text{EM2}:\text{EM3})$  records of cores NIOP471, NIOP472 and the other three cores is supported by the  $\delta^{18}\text{O}$  records of cores NIOP469 and

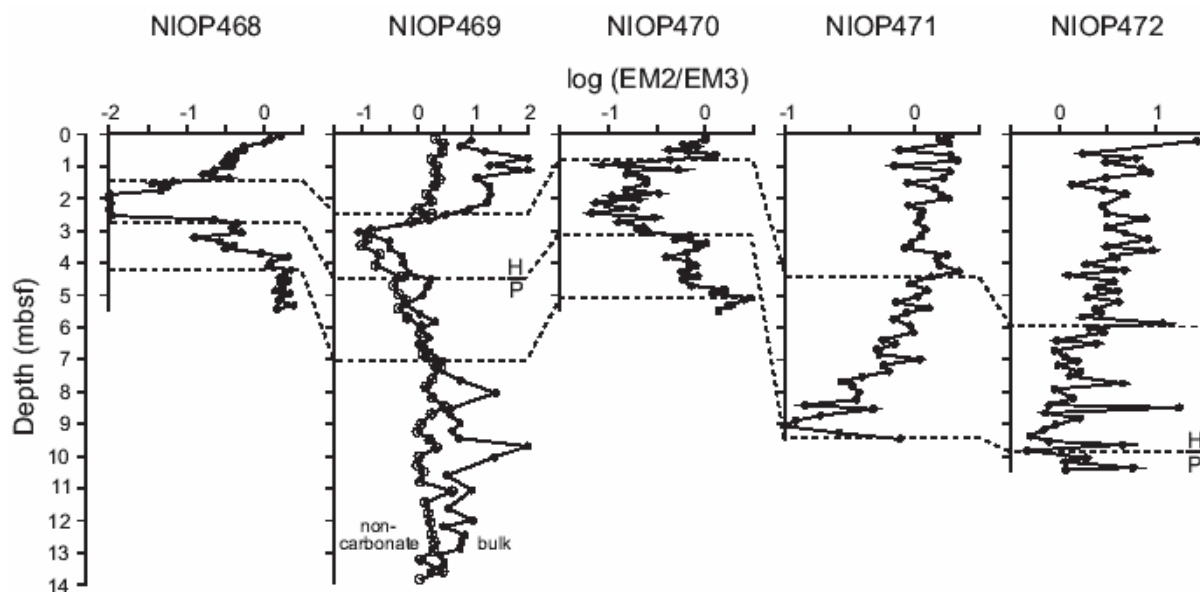


Fig. 7.14 — Variation in relative contributions of EM2 and EM3 in cores NIOP468-NIOP472 expressed as logratios. Dashed lines refer to lithostratigraphically correlatable levels. The Pleistocene-Holocene boundary (H/P) is indicated in cores NIOP469 and NIOP472 (see Fig. 7.4).

NIOP472 (Fig. 7.4). The relatively good correlation between the  $\log(\text{EM2}:\text{EM3})$  records strongly suggests that a regional signal ('background sedimentation') has been extracted from the sedimentary record. A distinct  $\log(\text{EM2}:\text{EM3})$  minimum is recorded in all five cores. The timing of this 'grain-size minimum' is contemporaneous with the early Holocene one recorded on the upper Indus Fan and Pakistan continental slope off the Indus Delta (see Chapter 4 and 5). Grain-size variations in the latter region are inferred to be related to mixing of eolian dust and fluvial mud in varying proportions. Consequently, it is plausible to interpret EM2 and EM3 within the hemipelagic muds on the Makran continental slope as eolian dust and fluvial mud, thus analogous to EM2 and EM3 of Prins and Weltje (1999; Chapter 4).

The less pronounced trends in the  $\log(\text{EM2}:\text{EM3})$  record of core NIOP472 (Fig. 7.14) are likely due to mixing of turbidite 'silt' with the hemipelagic mud, the latter being a mixture of eolian dust and fluvial mud. The fact that the grain-size distributions of the bulk sediment (including the carbonate fraction) is analysed, adds extra 'noise' to the end-member modelling solution; this can be seen for core NIOP469 where the grain-size distribution has been analysed for both the bulk and the carbonate-free sediment fraction (Fig. 7.14). However, as the carbonate content in these sediments is relatively low (<25 wt%; Fig. 7.17B), the overall trends in the two records are very similar. The  $\log(\text{EM2}:\text{EM3})$  record (carbonate-free base) of core NIOP469 has been selected as a record of continental aridity: high relative abundances of eolian dust EM2 (high  $\log(\text{EM2}:\text{EM3})$  values) point to arid climate conditions and low relative abundances of eolian dust EM2 (low  $\log(\text{EM2}:\text{EM3})$  values) point to humid climate conditions in the source area of the sediments, i.e., the northern Arabian Peninsula and Persian Gulf area, and the Makran coastal range (see 'sediment composition' section below).

#### *Sediment Composition*

The grain-size distributions of the hemipelagic muds in core NIOP469 are inferred to indicate significant changes in the dominant mode of fine-grained sediment transport (i.e., eolian versus fluvial sediment input) during the last ~20  $^{14}\text{C}$  ka. The geochemical and mineralogical

compositions of the hemipelagic muds were analysed in order to infer the provenance of the sediments.

*Mineralogy of clay fraction.—*

The mineralogical composition of the carbonate-free clay fraction of a series of hemipelagic mud samples (n=32) from core NIOP469 were analysed by X-ray diffraction. The analyses revealed the presence of both clay and non-clay minerals, i.e., illite, chlorite, kaolinite, quartz and plagioclase. The clay fractions do not contain any detectable amounts of smectite or palygorskite, two mineral species which are abundant in large areas of the Arabian Sea. The relative abundance of the minerals in the clay fraction show only subtle downcore variations: two ‘extreme’ diffractograms are shown in Figure 7.15. Throughout the core, the clay fraction is dominated by illite, chlorite and kaolinite. Quartz and plagioclase are present in only small quantities. The lack of significant variation in mineralogy (data is not shown) suggests that the provenance of the clay fraction remained constant through time. The composition of the clays, i.e., rich in illite, chlorite, kaolinite and lack of smectite and palygorskite, is characteristic for sediments deposited in the entire Gulf of Oman (Steward *et al.*, 1965; Sirocko and Lange, 1991). According to these authors the basin-wide dispersal of these minerals is caused by both the north-westerly winds, raising large amounts of dust from the northern Arabian Peninsula and Persian Gulf area, and by fluvial input from the Makran. The lack of palygorskite and smectite indicates that no significant amounts of sediment were supplied from the central Arabian Peninsula and the Indian Peninsula (Kolla *et al.*, 1976; Kolla *et al.*, 1981; Sirocko and Lange, 1991; Sirocko *et al.*, 1991).

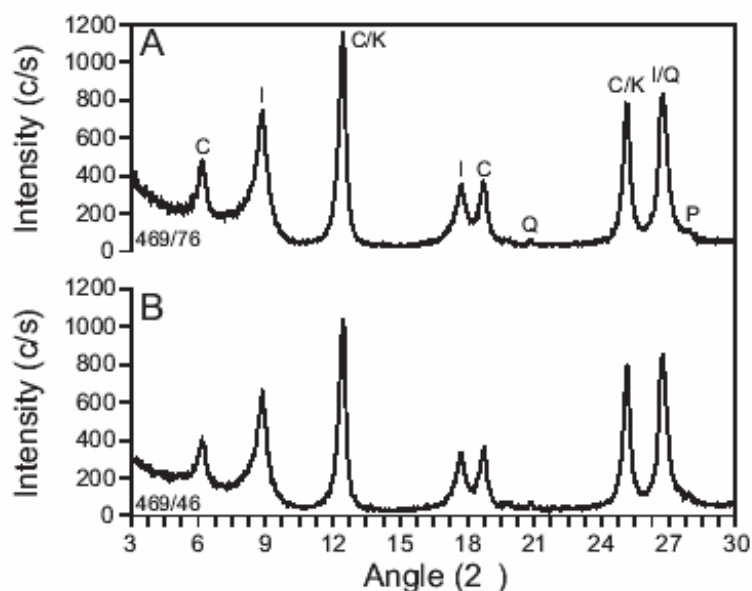


Fig. 7.15 — X-ray diffraction diagrams of glycolated samples from core NIOP469. A: Fluvial-mud-dominated sample 469/76 (2.69 mbsf; ‘maximum humidity’); B: Eolian-dust-dominated sample 469/46 (7.64 mbsf; ‘maximum aridity’). Minerals detected are chlorite (C), illite (I), kaolinite (K), quartz (Q) and plagioclase (P).

*Geochemistry of size fractions.—*

Variation in the geochemical composition of detrital sediments may reflect variation in grain size or variation in the provenance of the sediment, or a combination of the two. To assess the influence of sediment source versus grain size on the geochemical composition of the sediment in core NIOP469, the composition of selected size ranges (silt fractions AB, C and D with modal grain sizes of  $\sim 5$ ,  $\sim 15$  and  $\sim 40$   $\mu\text{m}$ , and sand fraction E  $> 63$   $\mu\text{m}$ ) extracted from the bulk siliciclastic sediment fraction were analysed.

Scatter diagrams of Mg/Al and Ti/Al ratios (Fig. 7.16A), and Fe/Al and Na/Al ratios (Fig. 7.16B) of the size fractions illustrate that the geochemical composition of the siliciclastic sediment fraction is strongly dependent on the grain size. The Mg/Al and Fe/Al ratios decrease systematically with increasing grain size (fraction AB has 'high' ratios, fraction E has 'low' ratios). In contrast, the Na/Al ratio increases systematically with increasing grain size (fraction AB has 'low' ratios, fraction E has 'high' ratios). The Ti/Al ratio shows a more complex relation with grain size: Ti/Al shows a positive correlation with grain size in the 'fine silt' range (fractions AB and C), whereas it shows a negative correlation with grain size in the 'coarse silt-sand' range (fractions D and E). The four element-to-Al ratios show only minor variation within each silt fraction (fractions AB, C, D). However, compositional variation within the sand fraction (fraction E) is considerable, most likely still due to a 'grain-size effect' as this fraction has no defined upper boundary ( $> 63$   $\mu\text{m}$ ). The homogenous geochemical compositions of the silt fractions suggest that the provenance of each of these size fractions remained constant through time.

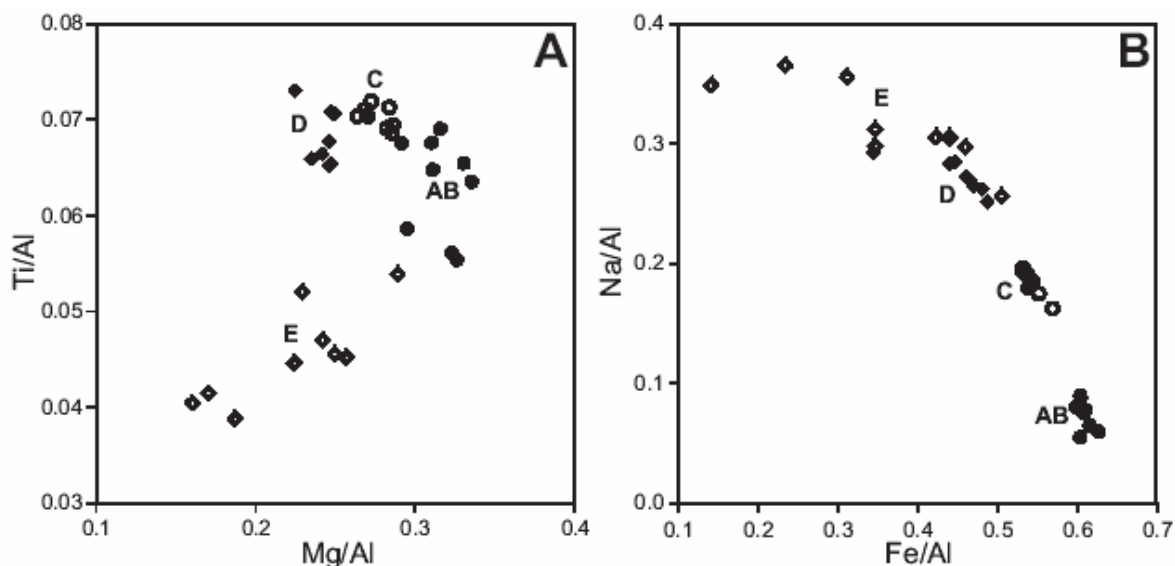


Fig. 7.16 — Composition of siliciclastic size fractions in core NIOP469: the 'source-effect' and 'size-effect' on the composition of terrigenous sediments (see text for discussion). Cross plots are shown of (A) Mg/Al - Ti/Al, and (B) Fe/Al - Na/Al. Silt fractions AB (closed circles), C (open circles) and D (closed diamonds) have modal grain sizes of  $\sim 5$ ,  $\sim 15$  and  $\sim 40$   $\mu\text{m}$ ; sand fraction E (open diamonds) contains particles  $> 63$   $\mu\text{m}$ .

*Bulk sediment composition.—*

Variation in the geochemical composition of bulk marine sediments reflect variation in the relative contributions of marine (e.g. biogenic carbonate, opal) and terrigenous (e.g. siliciclastics, detrital carbonates) material, the composition of the latter being predominantly dependent on the grain size and provenance characteristics. The carbonate content in core NIOP469 varies between 5- <25 wt% (Fig. 7.17B). It must be noted, however, that the method used to calculate the carbonate content (see ‘material and methods’ section) cannot distinguish primary biogenic carbonate (calcite, aragonite) derived from in situ biomass, and detrital carbonate (including dolomite) supplied from the continent. The Sr/Ca and the Mg/Al ratios may provide additional information on possible contributions of aragonite and dolomite in the sediment.

The Sr/Ca ratio of bulk sediments from the upper to middle continental slope off the Indus Delta is positively correlated with the abundance of pteropods (Reichart *et al.*, 1997), as their shells are made up of aragonite which has a higher Sr content than calcite (Sutherland *et al.*, 1984). The Sr/Ca ratio record of core NIOP469 contains two distinct peaks, suggesting enhanced pteropod preservation at the end of the last glacial period and during the Younger Dryas period (Fig. 7.17C). The coincidence of the two carbonate peaks and the Sr/Ca peaks suggests that an important part of the carbonate is made up of pteropods. Reichart *et al.* (1997) relate enhanced preservation of pteropods in the north-eastern Arabian Sea to periods of enhanced deep convective turnover of the water column due to enhanced winter monsoon winds (see also ‘discussion’ in Chapter 5). Accordingly, the Sr/Ca ratio record of core NIOP469 implies enhanced winter-monsoon intensity during two distinct periods during the last ~20 <sup>14</sup>C ka.

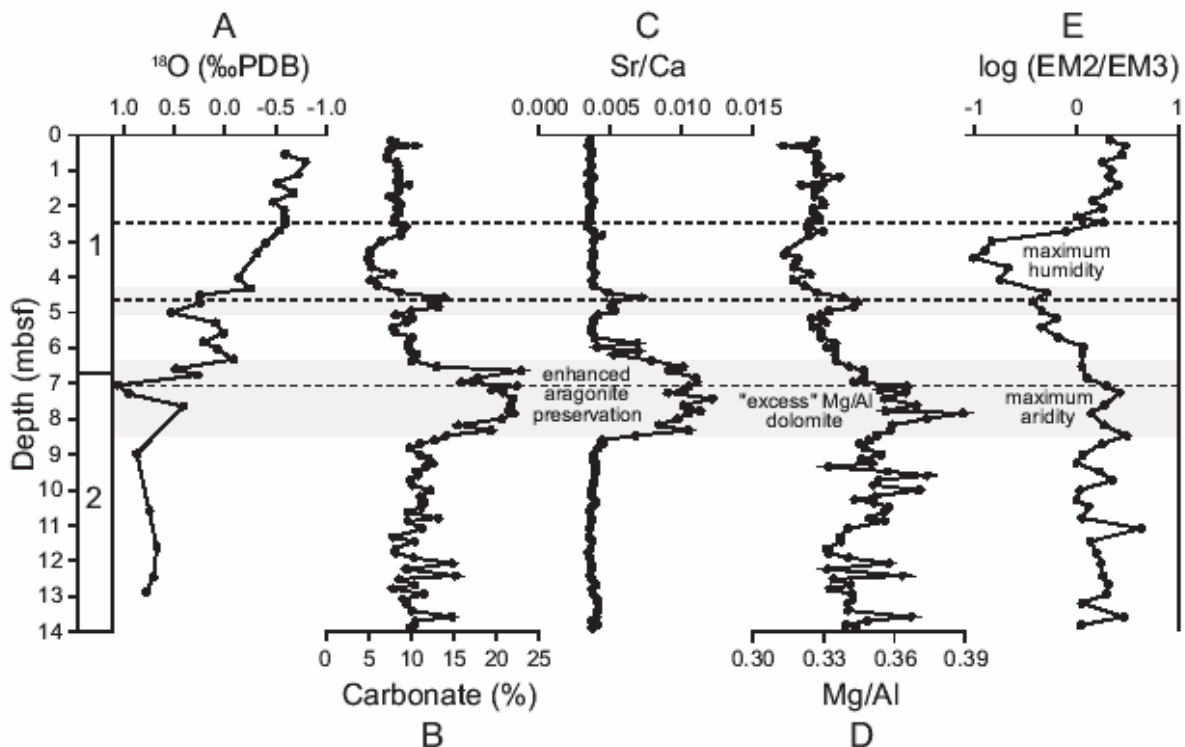


Fig. 7.17 — Sediment composition in core NIOP469. A: *Neogloboquadrina dutertrei*  $\delta^{18}\text{O}$ ; B: carbonate content; C: Sr/Ca ratio in bulk sediment fraction; D: Mg/Al ratio in bulk sediment fraction; E: Logarithm of end-member ratio EM2:EM3 in siliciclastic fraction, NIOP469.

The Mg/Al ratio of the bulk sediment in core NIOP469 varies between 0.31-0.39 (Fig. 7.17D), which is considerable higher than the Mg/Al ratio of the siliciclastic size fractions which varies between 0.16-0.34 (Fig. 7.16A). The size-fraction results indicate that variations in the Mg/Al ratio of the siliciclastic fraction are negatively correlated with variations in the siliciclastic grain size. However, a positive correlation exists between the Mg/Al record of the bulk sediment and the siliciclastic log(EM2:EM3) record (Fig. 7.17D, E). These 'paradoxical' results imply that the 'excess' Mg in the bulk sediment is present in the carbonate fraction of the sediment, most likely incorporated into dolomite. Dolomite is indeed a rather common component in the sediments of the Gulf of Oman and is supplied from the northern Arabian desert and Persian Gulf area by the north-westerly winds (Sirocko *et al.*, 1991). The 'excess' Mg and the clay-mineral data suggest that the dominant source for the eolian dust deposited at site NIOP469 is the northern Arabian Peninsula and the Persian Gulf area. The overall positive correlation between the Mg/Al record and the log(EM2:EM3) record strengthens the idea that they are both records of relative contributions of eolian versus fluvial sediment (and makes it highly unlikely that the 'excess' Mg is incorporated in authigenic carbonates derived from oxidized methane vented from the Makran accretionary prism as found further to the east by Von Rad *et al.*, 1996). Moreover, this correlation is not surprising as dolomite is present predominantly in the silt fraction of the Arabian Sea sediments (Stewart *et al.*, 1965), i.e., approximately the EM2 size range.

#### *Sedimentation Rates and Turbidite Frequency*

##### *Time intervals.—*

On the basis of the AMS-<sup>14</sup>C datings in core NIOP469 and the inter-core correlation discussed above (based on correlation of  $\delta^{18}\text{O}$ , Ca, and grain-size records), the sedimentary record in cores NIOP468-NIOP472 have been subdivided into four time intervals. These time intervals have been labelled the 'late Holocene' (0-6.2 <sup>14</sup>C ka BP), the 'early Holocene' (6.2-10 <sup>14</sup>C ka BP), the last 'deglaciation' period (10-13.5 <sup>14</sup>C ka BP) and the 'late Pleistocene' (prior to 13.5 <sup>14</sup>C ka BP) in Figure 7.3.

For these calculations, the age of the top of cores NIOP469, NIOP471 and NIOP472 were arbitrarily fixed at 0 ka BP. From the correlation of the Ca and log(EM2:EM3) records (Fig. 7.5 and 7.14) it is inferred that the records of late Holocene sediments in cores NIOP468 and NIOP470 are incomplete (erosion?). Hence, it is impossible to calculate reasonable sedimentation rates for the late Holocene (0-6.2 <sup>14</sup>C ka BP) at these coring sites. The age of 6.2 <sup>14</sup>C ka BP is derived for the end of the period characterised by 'maximum humidity' (inferred from the log(EM2:EM3) record; e.g. Fig. 7.17) on the basis of linear interpolation between the 7.57 <sup>14</sup>C ka BP dated depth level and the top in core NIOP469. The age of 10 <sup>14</sup>C ka BP is derived for the Pleistocene-Holocene boundary (recognisable in the  $\delta^{18}\text{O}$  records of NIOP469 and NIOP472, Fig. 7.4; correlatable on the basis of Ca and log(EM2:EM3) records, Fig. 7.5, 7.14) on the basis of linear interpolation between the 7.57 and 10.29 <sup>14</sup>C ka BP dated depth levels in core NIOP469. The age of 13.5 <sup>14</sup>C ka BP is derived for the start of the deglaciation period on the basis of correlation of the  $\delta^{18}\text{O}$  record of core NIOP469 (late glacial maximum at ~7 mbsf) to the well-dated  $\delta^{18}\text{O}$  record of core 74KL in the western Arabian Sea (Sirocko *et al.*, 1993). This level is correlatable between cores NIOP468-NIOP470 on the basis of the Ca and log(EM2:EM3) records (Fig. 7.5, 7.14).

Linear sedimentation rates (cm/ka) and frequencies of turbidite events (events/ka) in cores NIOP468-NIOP472 have been calculated for the above-mentioned time intervals (Fig. 7.3). Sedimentation rates in cores NIOP468-NIOP472 have varied between 34 and 189 cm/ka and

the occurrence of turbidite deposition have varied between 0 and 27 events/ka during the last  $\sim 20$   $^{14}\text{C}$  ka. Some distinct spatial and temporal trends can be observed in both sediment input variables.

*Spatial trends.—*

During the early Holocene, average sedimentation rates at the ‘proximal’ sites NIOP468-NIOP470 were relative low (34-65 cm/ka) compared with average sedimentation rates at the ‘distal’ sites NIOP471 and NIOP472 (97-134 cm/ka). The same trend holds for the late Holocene as the highest sedimentation rates are recorded in the deepest slope basin and in the abyssal plain, i.e., at sites NIOP471 and NIOP472. During the late Holocene, the sedimentation rate was 71-97 cm/ka at the deep sites NIOP471-NIOP472 compared to 40 cm/ka at site NIOP469. A likely explanation for this spatial difference in sedimentation rate rests in the proximity of the coring site with respect to the deformation front of the accretionary prism, i.e., the frontal fold sensu White (1982). This explanation implies that earthquakes associated with tectonic movements in the frontal fold triggered an important part of the turbidity currents which relocated sediments (eventually deposited as turbidites) in the deep basin. During the early Holocene, the frequency of turbidite deposition increased systematically in a basin-ward direction, namely from 0.5, to 3.4, 5.3, 9.7 and 19 events/ka at sites NIOP468-NIOP472, respectively. During the late Holocene, the highest frequency of turbidites is also recorded at site NIOP472 which is located closest to the deformation front. It thus appears that spatial trends in sedimentation rate and turbidite frequency are controlled by differences in local tectonic activity.

*Temporal trends.—*

The sedimentation rate and turbidite-frequency records of core NIOP469 are shown in Figure 7.18 next to the  $\delta^{18}\text{O}$  and  $\log(\text{EM2}:\text{EM3})$  records, i.e., records of ‘global climate’ and regional continental aridity. It must be noted that the linear sedimentation rate and turbidite frequency values of core NIOP469 in Figure 7.18 are slightly different from the values in Figure 7.3, as the first are based on linear interpolation between the age-calibration points. Terrigenous sediment input at site NIOP469 was at a maximum during the last glacial period, decreased during the deglaciation period and was at a minimum during the Holocene interglacial period. Correlation of turbidite frequency and the  $\delta^{18}\text{O}$  record suggests that sea-level changes are important as the main triggering mechanism of turbidity currents on the upper continental slope. There is no evidence of enhanced turbidite deposition at site NIOP469 during the period of increased continental humidity (early Holocene). However, there seems to be a possible correlation between enhanced sedimentation rates at site NIOP469 and increased continental humidity, although this observation depends highly on which flux record is used (Fig. 7.3, 7.18). Enhanced sedimentation rates during the ‘maximum humidity’ interval are also noticed from record NIOP470 (Fig. 7.3). Sedimentation rates at sites NIOP471 were relatively low during the late Holocene (71 cm/ka) when compared with those during the early Holocene (134 cm/ka). The latter trend at site NIOP471 may be the combined result of changes in climate and sea level. Sedimentation rates at site NIOP472 remained constant throughout the Holocene. In summary, tectonics, sea level and climate seem to have controlled depositional processes on the Makran continental slope in a complex way.

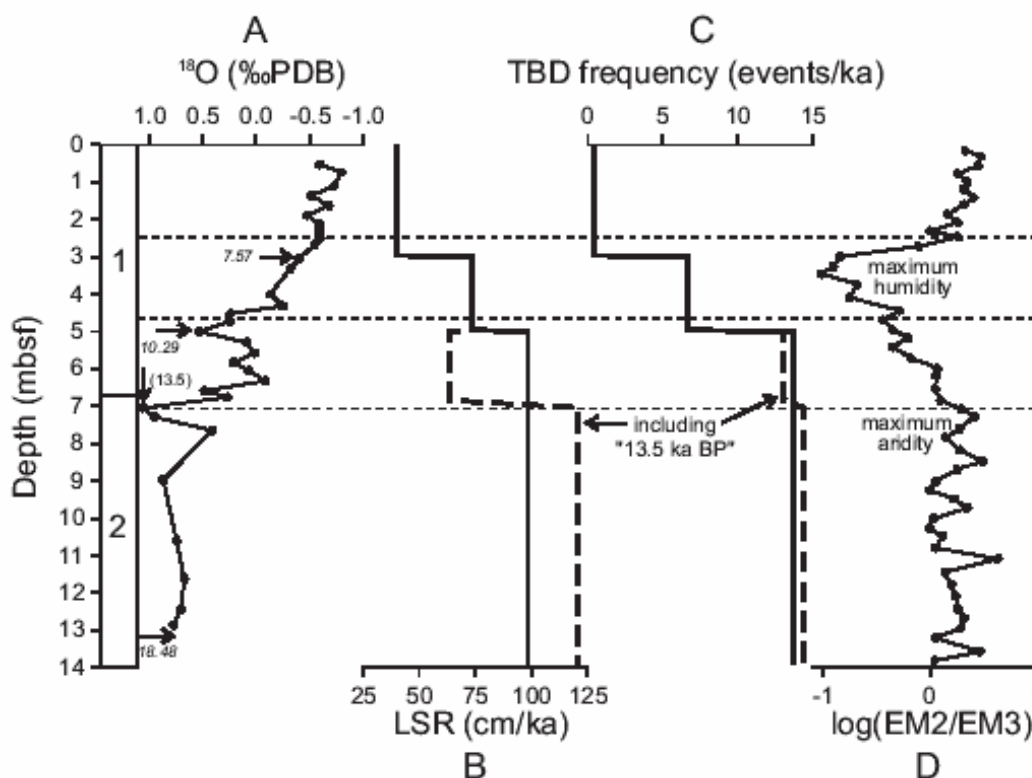


Fig. 7.18 — Core NIOP469. A: *Neogloboquadrina dutertrei*  $\delta^{18}\text{O}$ ; B: linear sedimentation rates (LSR); C: turbidite silt/sand bed frequency; D: Logarithm of end-member ratio EM2:EM3 in siliciclastic fraction. Position of AMS- $^{14}\text{C}$  dated planktonic foraminiferal fractions and radiocarbon ages are indicated in (A). Solid lines in (B) and (C) are calculated using the three radiocarbon datings indicated in (A); for calculation of the dashed lines in (B) and (C) the 'extra' age-calibration point of 13.5 ka BP was included (see text for discussion).

## DISCUSSION

### *Correlation of Climate-Proxy Records*

From the compositional data of the hemipelagic muds we infer that the dominant source of the eolian dust deposited on the Makran continental slope is the northern Arabian Peninsula and Persian Gulf area. The southward-eastward expansion of the dolomite-rich dust plumes entrained in the Persian Gulf area depends on the position of the front (intertropical convergence zone, ITCZ; see Figure 5.2) between the northwesterlies against the south-west monsoon winds during the summer season (Sirocko *et al.*, 1991; 1993). Accordingly, Sirocko *et al.* (1993) applied the abundance of dolomite in core 74KL (last  $\sim 20$   $^{14}\text{C}$  ka) from the western Arabian Sea (Fig. 7.1) as a proxy of the southward-eastward extent of the northwesterlies, i.e., a proxy of summer-monsoon intensity. It appears that the dolomite record of core 74KL and the Mg/Al record of core NIOP469 show very similar variations through time (Fig. 7.19B). Both records indicate an overall high dolomite abundance during the last glacial period (20-13  $^{14}\text{C}$  ka BP in 74KL) and an overall low dolomite abundance during the Holocene (10-0  $^{14}\text{C}$  ka BP). A very likely explanation of the decrease of dolomite abundance on a glacial-interglacial scale, already suggested by Sirocko *et al.* (1993), is the rise of sea level during the last deglaciation rather than an intensification of the summer monsoon. This explanation implies that the dolomite flux is correlated with the extension of

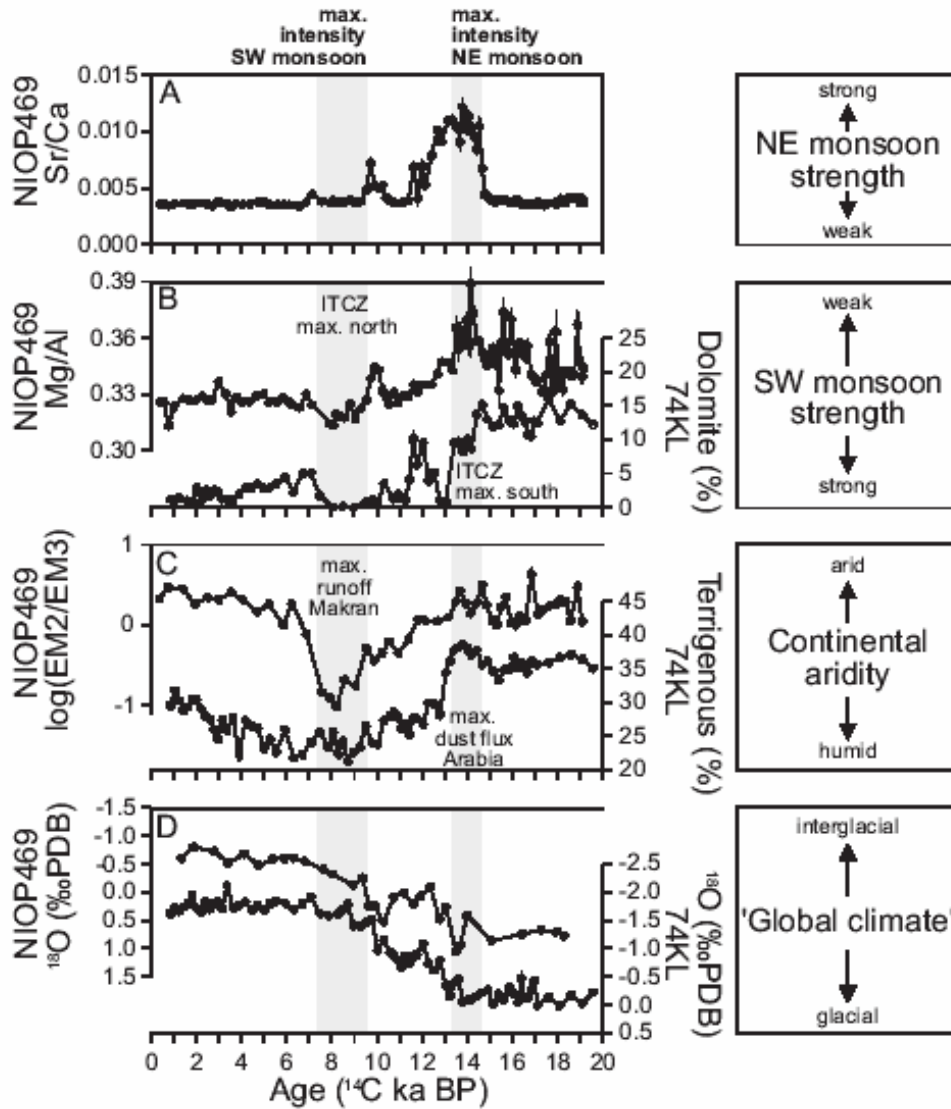


Fig. 7.19 — Correlation of climate-proxy records of core NIOP469 (Makran) and core 74KL (western Arabian Sea). Data of core 74KL is taken from Sirocko *et al.* (1993, 1996). A: Sr/Ca ratio in bulk sediment fraction, NIOP469. B: Mg/Al ratio in bulk sediment fraction, NIOP469; Dolomite content in terrigenous fraction >2  $\mu\text{m}$ , 74KL. C: Logarithm of end-member ratio EM2:EM3 in siliciclastic fraction, NIOP469; Terrigenous sediment content, 74KL. D: *Neogloboquadrina dutertrei*  $\delta^{18}\text{O}$ , NIOP469; *Globigerinoides ruber*  $\delta^{18}\text{O}$ , 74KL.

the dust-entrainment area, including the present-day Persian Gulf during the last glacial period, which varied as a function of sea-level stand.

Correlatable high-frequency changes in the NIOP469 and 74KL dolomite and other climate-proxy records reflect some distinct changes in the atmospheric circulation and associated precipitation patterns during the last  $\sim 20$   $^{14}\text{C}$  ka BP. At the end of isotope stage 2, a brief period is recorded in core NIOP469 (around  $\sim 14$   $^{14}\text{C}$  ka BP) characterised by an intensified winter monsoon (maximum Sr/Ca, Fig. 7.19A), a weakened summer monsoon (maximum Mg/Al, Fig. 7.19B) and maximum continental aridity (maximum  $\log(\text{EM2}:\text{EM3})$ , Fig. 7.19C). Sirocko *et al.* (1996) noticed that this period was characterised by a minimum in intensity of summer-monsoon-driven upwelling productivity in the western Arabian Sea (inferred from low Ba content in core 74KL) and a maximum aridity in Arabia (inferred from high terrigenous content in core 74KL; Figure 7.19C). Moreover, they concluded that this brief climate extreme coincided with the time of deposition of Heinrich Layer 1 in the North

Atlantic Ocean. In Chapter 5, it was inferred from the grain-size distribution data of cores from the western and north-eastern Arabian Sea that high-frequency enhancements of winter-monsoon strength and weakening of summer-monsoon strength correlate with major cold episodes in the North Atlantic region, including the Heinrich Events. The results of core NIOP469 fully support these conclusions for Heinrich Event 1. Moreover, the results of core NIOP469 suggest that around  $\sim 10$   $^{14}\text{C}$  ka BP (Younger Dryas; Heinrich Event '0') the winter monsoon strengthened (high Sr/Ca) and summer monsoon weakened (low Mg/Al) as well (Fig. 7.19A, B).

A brief climate extreme is recorded in core 74KL by the total absence of dolomite dust input from 8.85-7.85  $^{14}\text{C}$  ka BP. This dolomite minimum correlates perfectly with a minimum in the Mg/Al record of core NIOP469 (Fig. 7.19B). These data suggest that during this time interval the dust plumes from the Persian Gulf region did not reach as far south as the position of core 74KL (Sirocko *et al.*, 1993) and did hardly reach as far east as the position of core NIOP469. Sirocko *et al.* (1993) concluded that the track of the southwest monsoon and its associated pattern of precipitation have shifted to their northernmost position during this interval of the early Holocene. The correlation of the minima in the dolomite record of 74KL, the Mg/Al record of NIOP469 and the log(EM2:EM3) record of core NIOP469 (Fig. 7.19B, C) provide additional evidence for a link between maximum summer-monsoon strength and maximum continental humidity around the Arabian Sea (as proposed in Chapters 4 and 5).

#### *Sea-Level Change*

Before comparing the timing of turbidite sedimentation on the Makran continental slope with any eustatic sea-level curve, we must consider the contribution of local tectonics on the local ('relative') sea-level curve. Along the Makran margin, maximum Holocene coastal uplift rates of 1-2 m/ka have been observed along the eastern part of the margin. Uplift rates along the western sector have been remarkable lower, 0.1-0.6 m/ka (Page *et al.*, 1979). If the Holocene uplift rates are extrapolated over the last 18  $^{14}\text{C}$  ka, the total coastal uplift along the central Makran margin will total to about 20 metres during this time interval. Eustatic sea level rose approximately 125 metres during the last 18  $^{14}\text{C}$  ka (Fairbanks, 1989; Fairbanks, 1992). These figures suggest that the rates of coastal uplift have had only a relatively small effect on the 'relative' sea-level curve of the central Makran compared to the glacio-eustatic changes in sea level. This makes it plausible to use the eustatic sea-level curve of Fairbanks (1989, 1992) as a reference curve (Fig. 7.20A).

#### *Controls on Turbidite Sedimentation on the Makran Continental Slope.—*

Terrigenous sediment input (inferred from sedimentation rate, turbidite frequency) on the Makran continental slope was at a maximum during the last glacial period, decreased during the deglaciation period and was at a minimum during the Holocene interglacial period (Fig. 7.3). From the correlation of turbidite frequency and the  $\delta^{18}\text{O}$  record at site NIOP469 (Fig. 7.18), it was inferred that sea-level changes seem important as the mechanism controlling turbidite-facies changes on the upper continental slope. It seems that the first rapid rise in sea level at  $\sim 12$   $^{14}\text{C}$  ka BP (Fig. 7.20A) did not influence the frequency of turbidite deposition at site NIOP469, although the sedimentation rate did decrease during that period (Fig. 7.20C). A possible effect of the second rapid rise in sea level starting at  $\sim 10$   $^{14}\text{C}$  ka BP (Fig. 7.20A) is also not well constrained: while a clear decrease of turbidite frequency is observed at site

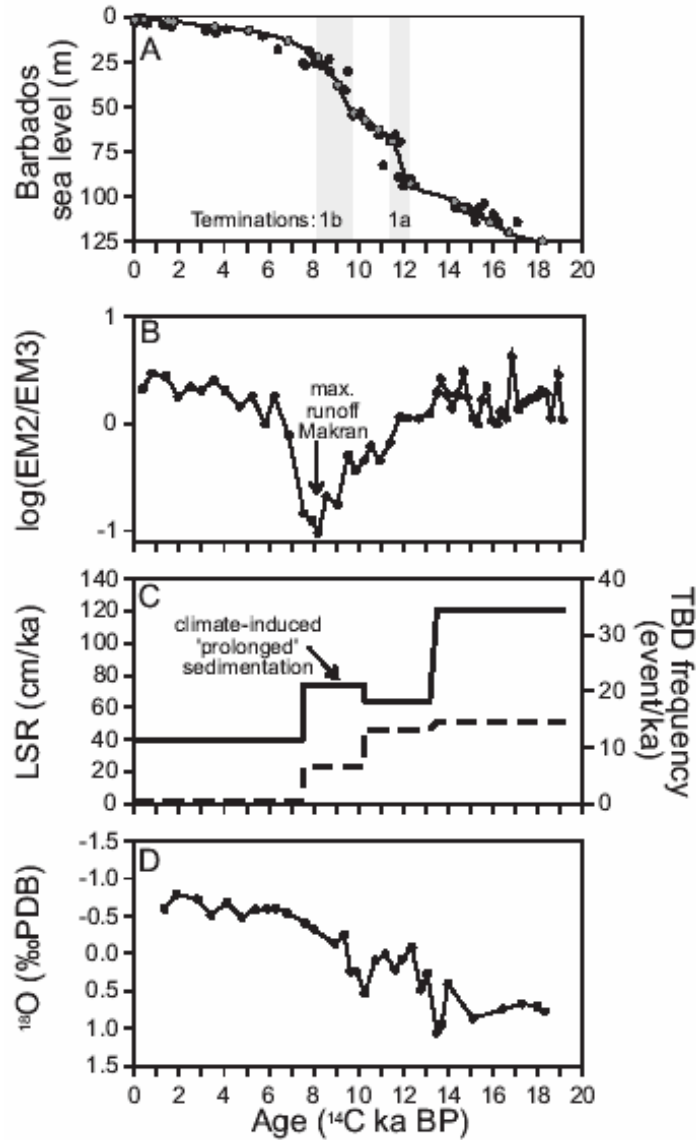


**Fig. 7.20** — Diagram showing the relationship between glacio-eustatic sea-level fluctuations and changes in sedimentation on the Makran continental slope (NIOP469). **A:** Barbados sea-level curve (Fairbanks, 1989, 1992); **B:** Logarithm of end-member ratio EM2:EM3 in siliciclastic fraction; **C:** Linear sedimentation rate (solid line) and turbidite silt/sand bed frequency (dashed line); **D:** *Neogloboquadrina dutertrei*  $\delta^{18}\text{O}$ .

NIOP469, turbidite frequency at site NIOP470 did not change much. A direct fluvial origin of turbidites is favoured during the period of low and rising sea level, because material can be funnelled effectively to the deep via the possibly river-mouth-connected canyons. The fact that turbidite sedimentation did not cease during the period of late sea-level rise may be due to increased river discharges related to the increased continental humidity, i.e., increased summer-monsoon precipitation (Fig. 7.20B). Coincidence of relatively high sedimentation rates (Fig. 7.20C) of muddy sediments with the period of enhanced precipitation suggest that hyperpycnal flows off the river mouths during river floods were frequent.

A sharp decrease in turbidite frequency during the late Holocene is observed on the upper continental slope (NIOP469; Fig. 7.20C), the deepest slope basin (NIOP471; Fig. 7.3) and on the abyssal plain (NIOP472; Fig. 7.3). The change in turbidite frequency appears to have taken place synchronously despite the fact that the cores were obtained from different

physiographic settings. This observation favours indeed an allocyclic control on turbidite deposition. The latter change coincides with low rates of sea-level rise (highstand) on Fairbanks' sea-level curve (Fig. 7.20A). Furthermore, the observed synchronous changes in turbidite deposition points to a configuration of highly-connected slope basins with the same terrigenous source ('mature' slope basins sensu Underwood and Bachman, 1982). Although the rise in sea-level during the Holocene caused a significant decrease of sediment input, turbidite sedimentation did not cease completely in the Holocene. However, the highest sedimentation rates and turbidite frequencies are recorded in the deep basin (NIOP471, NIOP472), suggesting that turbidity currents during the late Holocene were mostly triggered by earthquakes associated with deformation of the accretionary prism.

A comparison between the timing of turbidite sedimentation on the Makran continental slope and on the Indus Fan is made in Chapter 8. The importance of the comparison is that the studied turbidite systems are located in the same sedimentary basin which means that they were subject to similar changes in climate and sea level, but different tectonics. The comparison therefore allows the assessment of the individual contribution of sea-level change, climate change and tectonic activity to the controls on sediment supply to the Arabian Sea.

## CONCLUSIONS

1. The turbiditic (n=65) and hemipelagic (n=319) mud samples from the Makran continental slope are adequately described as mixtures of three end members. End-member modelling of the grain-size distributions allows the distinction between turbidite sand, turbidite silt or eolian dust, and fluvial mud.
2. The geochemical and mineralogical compositions of the hemipelagic sediments indicate that the eolian dust is dominantly supplied from the northern Arabian Peninsula and the Persian Gulf region, and that the fluvial input is from the Makran.
3. The ratio of eolian and fluvial contributions to the hemipelagic sediments on the Makran continental slope is a high-resolution paleoclimatic indicator of continental aridity, which matches similar results obtained for cores from the upper Indus Fan and the Pakistan continental slope off the Indus Delta. Continental aridity on the Makran is closely related to the intensity of the summer monsoon.
4. A brief climate extreme, coinciding with Heinrich Event 1 in the North Atlantic Ocean, is documented around  $\sim 14$   $^{14}\text{C}$  ka BP and is characterised by an intensified winter monsoon, a weakened summer monsoon and maximum continental aridity. Another brief climate extreme, recorded around  $\sim 8.5$   $^{14}\text{C}$  ka BP, is characterised by a weakened winter monsoon, an intensified summer monsoon and maximum continental humidity.
5. Turbidite sedimentation was most frequent during the last glacial sea-level lowstand. Due to the sea-level lowstand, rivers draining the Makran area were directly connected with the slope canyons, causing material to be funnelled downslope effectively. Turbidite sedimentation continued during the period of sea-level rise and may be partly related to the overall high river discharge (humid climate) causing the regular occurrence of hyperpycnal flows of river sediment load during river floods. Infrequent turbidite sedimentation occurred during the period of sea-level highstand. Overall higher turbidite frequencies are observed in the proximity of the deformation front of the accretionary prism.

## ACKNOWLEDGEMENTS

We are indebted to all scientists, technicians and crew members of the RV Tyro for their commitment during the Netherlands Indian Ocean Programme. We are grateful to G.J. Reichart, H.J. Visser and A.R. Tabrez for their assistance during sampling of the sediment cores. A.R. Tabrez is thanked for the oxygen-isotope data as well. We thank P. Anten, T. Broer, G. Ittman, M. Reith, G. van 't Veld, H. de Waard and T. Zalm for analytical support. K. van der Borg (R.J. van de Graaff Laboratory, Utrecht University) is thanked for the AMS-<sup>14</sup>C datings.

## SEA-LEVEL AND CLIMATE SIGNATURES IN TURBIDITE SUCCESSIONS ALONG THE TECTONICALLY ACTIVE AND PASSIVE NORTHERN MARGIN OF THE ARABIAN SEA

M.A. Prins<sup>1</sup> and G. Postma<sup>1</sup>

### ABSTRACT

A comparison between the timing of turbidite sedimentation along an active continental margin (Makran) and a passive continental margin (Sindh; Indus Fan) in the Arabian Sea is made. Turbidite sedimentation in both, tectonically different areas was most frequent during the last glacial sea-level lowstand and decreased during the early sea-level rise (~12-10 <sup>14</sup>C ka BP). Since that time the Indus Fan is being draped by a pelagic calcareous ooze, while turbidite sedimentation on the Makran continental slope continued with a reduced sedimentation rate. Both continental slope sedimentary systems recorded the humid period of the early Holocene (~9-7 <sup>14</sup>C ka), by a minimum grain size in the hemipelagic intervals. Rare turbidite beds in the late Holocene of the Makran succession are inferred to have been seismically triggered.

### INTRODUCTION

A major control on the growth of submarine fans is the fluctuation in sea level. In terrigenous terranes, a relative sea-level fall 'activates' the fan due to an increase of sediment transport from the river and shelf towards the deeper parts of the basin by an increase of the river gradient, through entrenchment of the continental shelf and by an increase of slope instability. During a relative sea-level rise, sediment is trapped in the transgressed nearshore zone prohibiting important sediment transport to the deep (e.g. Shanmugam and Miola, 1982; Klein, 1984; Stow, 1985; Mutti and Normark, 1987; Posamentier and Vail, 1988).

Other factors influencing sediment supply to submarine fans include their tectonic and climatic setting. Broad shelves have a regulating effect on sediment supply to the deep, by intermittent storage during periods of sea-level rise and highstand, and release in times of sea-level fall, in contrast with narrow shelves, where the submarine fans often have a deltaic source and where sediment transport is controlled more directly by river discharge (cf. Mutti and Normark, 1987). The river-fed fans show often a high frequency 'cyclicality' related to allocyclic mechanisms, such as tectonics, relative sea-level change, and climate change in addition to autocyclic processes. In many cases, the individual contribution of each of these variables is difficult or impossible to assess from the geological record.

The aim of this study is to compare turbidite sedimentation along an active continental margin (Makran margin) and a passive continental margin (Sindh margin, Indus Fan). The

---

<sup>1</sup> Institute for Paleoenvironments and Paleoclimate Utrecht (IPPU), Faculty of Earth Sciences, Utrecht University, P.O. Box 80021, 3508 TA Utrecht, The Netherlands

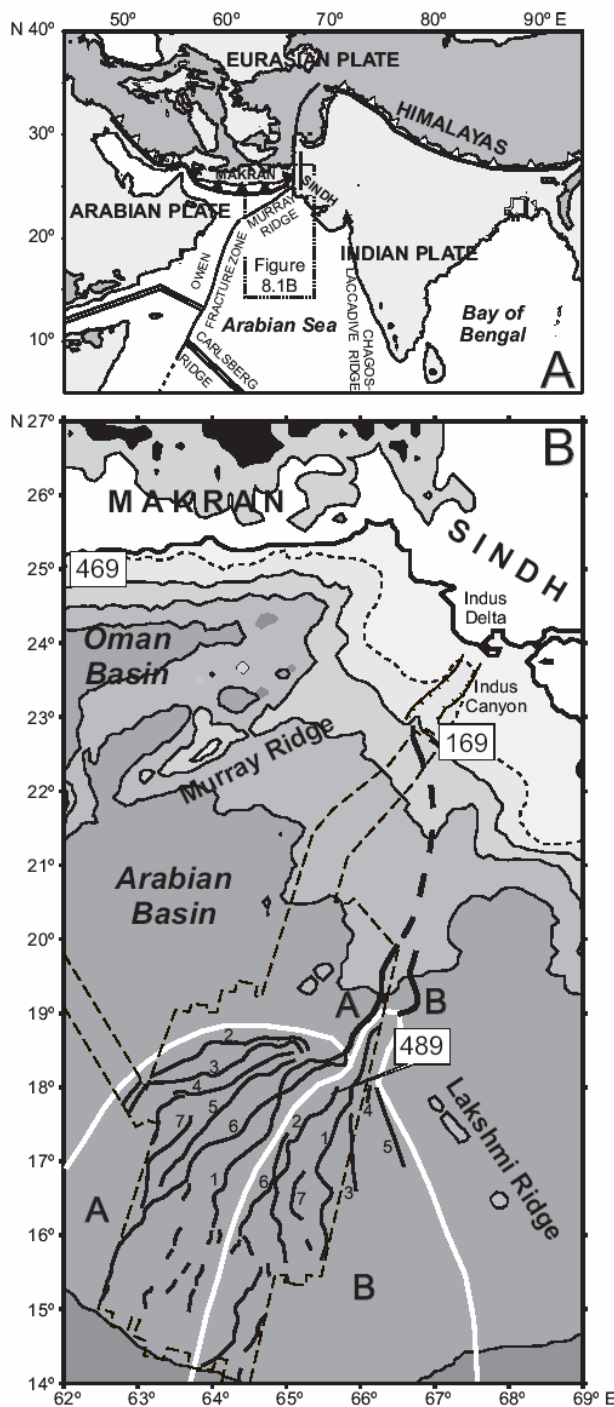


Fig. 8.1 — A. Tectonic setting of the Makran and Sindh continental margins of Pakistan. Plate boundaries between major plates are: open tooth marks = thrusting associated with continental collision; solid tooth marks = thrusting associated with an oceanic subduction; double line = spreading on oceanic ridge; single solid line = transform fault (after Kolla and Coumes, 1987; their Fig. 1). Elevations over 1000 m are shaded with dark grey. B. Locality of cores used in this study is indicated. Shown are the Indus Canyon and part of the complex of associated large channel-levee systems (A is younger than B), and of the small channel-levee systems (A1 is younger than A2, etc.). The relative ages of the channel-levee systems (A, B) on the Indus Fan are from Kenyon *et al.* (1995); bold black lines = channels; bold white line = boundary individual fanlobes on middle fan. Topography at a 500 m and bathymetry at a 1000 m contour interval (dashed contour line is -125 m). Topographic data from U.S. National Geophysical Data Center/World Data Center A for Marine Geology and Geophysics.

importance of the comparison is that the studied turbidite systems are located in the same sedimentary basin (Arabian Sea) which means that they were subject to similar changes in climate and sea level, but different tectonics. The turbidite systems have been studied by means of seismic profiles and piston cores obtained during the Netherlands Indian Ocean Programme on RV Tyro (Van der Linden and Van der Weijden, 1994; Chapter 6 and 7). In this paper we focus on the last glacial and present interglacial intervals (last ~20 <sup>14</sup>C ka) recorded in core NIOP469 from the Makran continental slope, core NIOP489 from the middle Indus Fan, and core SO90-169KL from the Sindh continental slope. The turbidite-free core SO90-169KL is used as reference for the regional climate signal which has been reconstructed on the basis of the composition of the hemipelagic sediments (Chapter 4, 5).

## **GEOLOGICAL SETTING OF MAKRAN AND INDUS FAN TURBIDITE SYSTEMS**

The continental margin of south-western Pakistan is the offshore extension of the Makran subduction complex (Fig. 8.1A). The subduction process has produced a topography of uplifted ridges and intervening basins delineated parallel to the coast (White, 1982). A major episode of uplift started in the course of the mid-Pleistocene, evidenced by raised beaches up to 500 m above present sea level (Harms *et al.*, 1984). Maximum Holocene coastal uplift rates are of the order of 1-2 m/ka, as observed along the eastern part of the margin. Along the western sector these are remarkable lower being 0.1-0.6 m/ka (Page *et al.*, 1979). Extrapolating the Holocene uplift rates over the last ~20 ka means a total coastal uplift of ~20 m for the central Makran margin, south of which core NIOP469 was taken. Core NIOP469 comes from a slope basin at a water depth of 1768 m (Fig. 8.1B). High-resolution seismics show sheet-like deposits and no channelling in this slope basin (NIOP unpublished data).

The Indus Fan has developed off the tectonically passive Sindh continental margin of south-eastern Pakistan (Fig. 8.1A) and is bounded by the Chagos-Laccadive Ridge in the east, the Owen-Murray Ridges in the west, and the Carlsberg Ridge in the south. The Indus Canyon and possibly another, less prominent and now inactive canyon (Saraswati Valley, see Kolla and Coumes, 1987 and Kenyon *et al.*, 1995) served as conduit for en masse sediment transport to the deep sea at least since the development of the youngest channel-levee complexes (Kolla and Coumes, 1987; Droz and Bellaiche, 1991). The two youngest channel-levee complexes (marked A and B in Fig. 8.1B) have been mapped in detail using high-resolution seismics and long-range side-scan sonar (GLORIA) (Kenyon *et al.*, 1995). The feeder channel of complex A has levees up to 80 km wide and up to 1100 m thick and branches on the middle fan into a distributary pattern of at least 7 smaller, laterally shingling channel-levee systems about 500 km basinward. The midfan channel-levee systems, which were active successively, are up to 50 km wide and 60 m thick. The channels terminate into sandy lobes inferred from high percentage and large maximum thickness of silty/sandy turbidites within the upper 5 meters of the sediment column on the lower fan (Kolla and Coumes, 1987). The youngest channel A1 terminates in a lobe on the middle fan at a distance of over 1100 km from the mouth of the Indus Canyon. This channel-lobe transition is marked by decreasing channel dimensions (Prins *et al.* 1994). Cores have been taken from the levees of systems B1 and B2 (e.g. NIOP489, Fig. 8.1B) to date the switch from complex B to A (youngest). In Chapter 6, we dated the switch at ~25 <sup>14</sup>C ka BP, i.e., at the beginning of the last glacial sea-level lowstand.

## METHODS

Sediment cores NIOP469 and NIOP489 were collected during the Netherlands Indian Ocean Programme (NIOP) on RV Tyro (Van der Linden and Van der Weijden, 1994), and core SO90-169KL was collected during the SO90 PAKOMIN Expedition on RV Sonne (Von Rad *et al.*, 1995). For stratigraphic purposes, stable oxygen isotopes in the planktonic foraminifera *Neogloboquadrina dutertrei* were analysed with a mass spectrometer. The chronology of the NIOP cores is based on several AMS-<sup>14</sup>C datings of planktonic foraminifera *Globorotalia menardii* (NIOP489) or, due to a scarcity of foraminifera, a mixture of planktonic foraminifera (NIOP469). A -400-yr correction was applied for the age of the sea water (Bard, 1988). The elemental chemical composition of bulk samples was measured using an ICP-ES. The carbonate content was calculated from the total Ca concentration, using a correction for clay-derived Ca;  $\text{CaCO}_3 = 2.5(\text{Ca}_{\text{tot}} - (\text{Ca}/\text{Al}_{\text{clay}} \times \text{Al}_{\text{tot}}))$ , where  $\text{Ca}/\text{Al}_{\text{clay}}$  is 0.345 (Turekian and Wedepohl, 1961). The grain-size distributions of the non-carbonate (siliciclastic) fractions were measured on a Malvern 2600 laser-diffraction size analyser using a lens with 100 mm focal length.

## RESULTS AND INTERPRETATION

### *Lithology*

Core NIOP469 from the Makran continental slope shows a sedimentary succession dominated by turbidites (145 sand beds in 14 m) with intercalated hemipelagic mud intervals. Turbidite-sand-bed thickness shows an overall upward thinning between 14 and 3 metres below the sea floor (mbsf). Above 3 mbsf only a few turbidites are present. Core NIOP489 from the middle Indus Fan shows a sequence of silty-sandy turbidites (active stage channel-levee system B2; 8-10.2 mbsf) draped by a hemipelagic-mud unit (active stage channel-levee system B1 and A7-A1; 0.8-8 m) which in turn is overlain by a calcareous ooze unit (passive stage Indus Fan; above 0.8 mbsf). Within the hemipelagic mud unit a few silty-sandy turbidites occur. Core SO90-169KL from the Sindh continental slope contains a succession of partly laminated, organic-carbon-rich and partly bioturbated, organic-carbon-poor, and pteropod-rich hemipelagic muds, and contains no turbidite beds.

### *Age Model*

The sediment record in core NIOP469 (0-14 mbsf) spans the last ~20 <sup>14</sup>C ka, and the calcareous ooze-hemipelagic mud record (0-8 mbsf) in core NIOP489 spans the last ~35 ka. The  $\delta^{18}\text{O}$  records (~20-0 <sup>14</sup>C ka BP) of both cores are shown in Figure 8.2A. Both  $\delta^{18}\text{O}$  records correlate closely and record the two-step deglaciation known from many marine  $\delta^{18}\text{O}$  records (e.g. Sirocko *et al.*, 1993; Weber *et al.*, 1997) and the glacio-eustatic sea-level curve (Fairbanks, 1989, 1992; Fig. 8.2F, 8.4D). The hemipelagic mud record in core SO90-169KL spans the last ~105 ka, as indicated by its  $\delta^{18}\text{O}$  record which reveals isotope stages 1 to 5.3. The upper part (~3 mbsf; Fig. 8.3A) of the  $\delta^{18}\text{O}$  record of core SO90-169KL is correlatable with the  $\delta^{18}\text{O}$  records of cores NIOP469 and core NIOP489, i.e., the upper ~3 m in core SO90-169KL spans the interval ~20-0 <sup>14</sup>C ka BP.

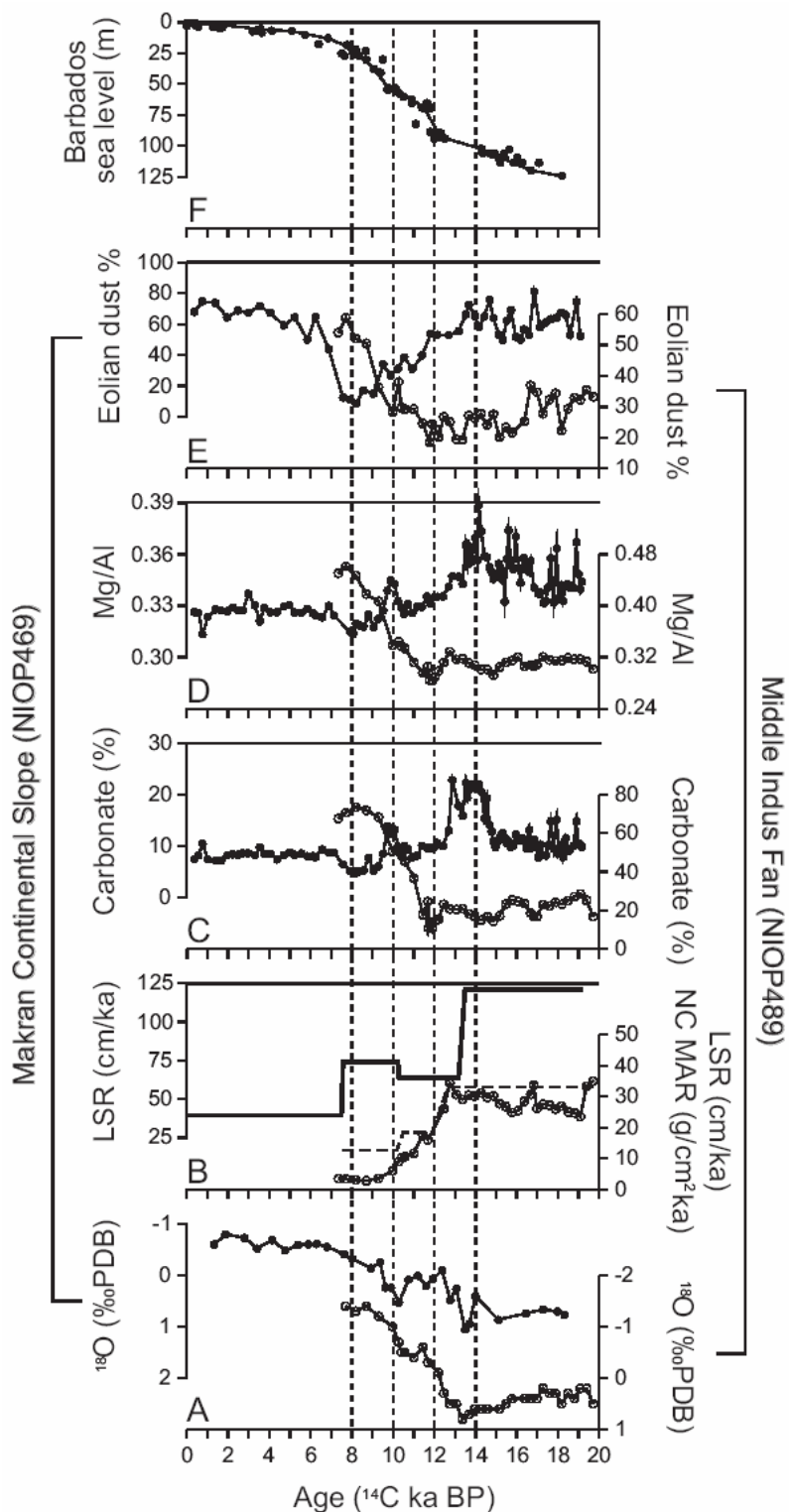


Fig. 8.2 — Sediment characteristics on the Makran continental slope (core NIOP469: filled data points) and on the middle Indus Fan (NIOP489: open data points) in relation with sea-level changes. A:  $\delta^{18}\text{O}$  of planktonic foraminifer *Neogloboquadrina dutertrei*. B: Linear sedimentation rate (LSR: NIOP469 solid line, NIOP489 dashed line) and non-carbonate ('siliciclastic') mass-accumulation rate (NC MAR: NIOP489 only). C: Carbonate content. D: Mg/Al ratio in bulk sediment. E: Contribution of eolian dust relative to fluvial mud, according to end-member modelling results of non-carbonate grain-size distributions (see Prins and Weltje, 1999; Chapter 4, 6, 7). F: Barbados sea-level curve (Fairbanks, 1989, 1992).

## Sedimentation Rates and Turbidite Frequency

Linear sedimentation rates (LSR: cm/ka) in core NIOP469 and NIOP489 were calculated between age calibration points, and the record of non-carbonate mass-accumulation rate (NC MAR: g/cm<sup>2</sup>ka) in core NIOP489 was calculated using the linear sedimentation rate, the dry-bulk density and the carbonate content (Fig. 8.2B).

LSR at site NIOP469 was at a maximum during the last glacial period (prior to ~13.5 <sup>14</sup>C ka BP ~120 cm/ka), decreased during the deglaciation period (~13.5-7.5 <sup>14</sup>C ka BP) and was at a minimum (~40 cm/ka) during the remainder of the Holocene. Turbidite deposition was most frequent during the last glacial period. Prior to ~10 <sup>14</sup>C ka BP, the frequency of turbidite deposition at site NIOP469 was 13-14 events/ka. The frequency decreased to 6-7 events/ka between ~10-7.5 <sup>14</sup>C ka BP, and to 0.4 events/ka after 7.5 <sup>14</sup>C ka BP.

At site NIOP489, the highest LSR (~33 cm/ka) is recorded prior to ~12 <sup>14</sup>C ka BP. A gradual decrease in sedimentation rate (LSR and NC MAR) appeared during the last deglaciation, directly after deposition of a thin series of turbidites (~12 <sup>14</sup>C ka BP). The decrease in sedimentation rate between ~11.5 and ~9 <sup>14</sup>C ka BP was entirely caused by a decrease in siliciclastic (non-carbonate) sediment supply. After about 10 <sup>14</sup>C ka BP the accumulation rate of pelagic carbonate, which shows only small variations around ~7 g/cm<sup>2</sup>ka throughout the studied time interval (Chapter 6), started to exceed the accumulation rate of siliciclastic material. According to the age model, the flux of the siliciclastic fraction has been reduced to ~3 g/cm<sup>2</sup>ka during the early Holocene. However, this extrapolated NC-MAR value should be regarded as a maximum value as the top of the sediment record has been affected strongly by carbonate dissolution. The oxidised (brownish) top of core NIOP489 indicates that the sediment column has been recovered completely.

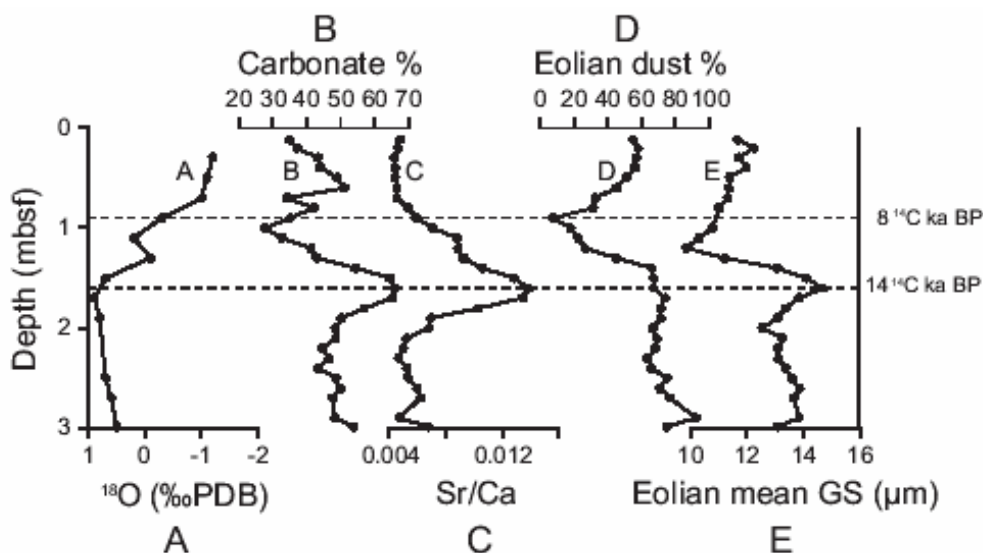


Fig. 8.3 — Sediment composition on the Sindh continental slope (core SO90-169KL). A:  $\delta^{18}\text{O}$  of planktonic foraminifer *Neogloboquadrina dutertrei*. B: Carbonate content. C: Sr/Ca ratio in bulk sediment. D: Contribution of eolian dust relative to fluvial mud. E: Mean grain size of eolian dust. (D) and (E) according to end-member modelling results of non-carbonate grain-size distributions (see Prins and Weltje, 1999; Chapter 4, 5). Compositional changes which correlate with similar changes on the Makran continental slope (NIOP469) are indicated by dashed lines; estimated AMS-<sup>14</sup>C ages of these 'events' are shown.

### Carbonate Content

Carbonate content in core NIOP469 varies between 5-23 wt% (Fig. 8.2C). Enhanced carbonate values in core NIOP469 are recorded in two discrete intervals, at  $\sim 14$  and  $\sim 10$   $^{14}\text{C}$  ka BP. These carbonate peaks coincide with enhanced Sr/Ca values from which it is inferred that an important part of the carbonate is made up of pteropods (Chapter 7), as their tests are made up of aragonite which has a higher Sr content than calcite (Sutherland *et al.*, 1984; Reichart *et al.*, 1997). Enhanced preservation of pteropods in the north-eastern Arabian Sea is related to enhanced deep convective turnover of the water column due to enhanced winter-monsoon winds (Reichart *et al.*, 1997). The independent indicator records of winter-monsoon intensity, i.e., the eolian-dust grain size records from the north-eastern Arabian Sea (e.g. SO90-169KL, Fig. 8.3E) indicate that the end of the last glacial period is characterised by maximum winter-monsoon strength (Prins and Weltje 1999; Chapter 4, 5). Correlation of enhanced carbonate (Fig. 8.3B) and Sr/Ca values (Fig. 8.3C) with maximum eolian-dust grain sizes at  $\sim 1.5$  mbsf in core SO90-169KL support the paleoclimatological interpretation of the Sr/Ca signal proposed by Reichart *et al.* (1997). Accordingly, the carbonate record of core NIOP469 mainly reflects enhanced carbonate preservation during periods of intensified winter monsoon.

Carbonate content in core NIOP489 varies between 10-74 wt% (Fig. 8.2C). The carbonate content within the hemipelagic mud unit (prior to 11.5  $^{14}\text{C}$  ka BP) varies around 20 wt% (10-30 wt%). The transition from the hemipelagic mud to the calcareous ooze unit is clearly visible in the carbonate record: carbonate content increases sharply after  $\sim 11.5$   $^{14}\text{C}$  ka BP and reaches stable values of  $\sim 70$  wt% during the Holocene. The gradual increase in carbonate content dominantly reflects a gradual decrease in siliciclastic (non-carbonate) sediment supply (Fig. 8.2B), as the accumulation rate of pelagic carbonate remained rather constant throughout the deglaciation (Chapter 6).

### Composition of Terrigenous Sediment

The geochemical composition of bulk terrigenous sediment is dependent on the grain size and provenance characteristics. Analyses of the chemical composition of selected size ranges of carbonate-free samples from cores NIOP469 and NIOP489, however, indicate that variations in the Mg/Al ratio of the bulk sediment in both cores is predominantly due to changes in the provenance of the terrigenous sediment rather than changes in the siliciclastic grain size (Chapter 6 and 7).

The Mg/Al ratio of the bulk sediment in core NIOP469 is considerably higher than the Mg/Al ratio of the siliciclastic size fractions of these sediments. In Chapter 7, we pointed out that the 'excess' Mg in the bulk sediment is present in the carbonate fraction of the sediment, most likely incorporated within detrital dolomite. Dolomite is a rather common component in the sediments of the Gulf of Oman and is supplied from the northern Arabian desert and Persian Gulf area by the north-westerly winds (Sirocko *et al.*, 1991). Sirocko *et al.* (1993) applied the abundance of dolomite in a core (last  $\sim 20$   $^{14}\text{C}$  ka) from the western Arabian Sea as a proxy of the south-eastward extent of the dolomite-rich dust plumes over the Arabian Sea, i.e., a proxy of the position of the front between the north-westerly winds and the SW summer monsoon. The Mg/Al record of core NIOP469 and the dolomite record of core 74KL from the western Arabian Sea (Sirocko *et al.*, 1993) show very similar variations through time. The Mg/Al record of the hemipelagic muds in core NIOP469 (Fig. 8.2D) thus reflects the relative contributions of eolian versus fluvial sediment input. The Mg/Al record indicates an overall high dolomite abundance during the last glacial period ( $\sim 20$ -13  $^{14}\text{C}$  ka BP) and an

overall low dolomite abundance during the Holocene (10-0  $^{14}\text{C}$  ka BP). Sirocko *et al.* (1993) suggested that the decrease of dolomite abundance on the larger glacial-interglacial scale reflects the rise of sea level during the last deglaciation by submergence of the Persian Gulf rather than an intensification of the summer monsoon. Superimposed on these large-scale trends, high-frequency changes are related to changes in the intensity of the summer monsoon. A Mg/Al maximum at  $\sim 14$   $^{14}\text{C}$  ka BP indicates maximum dust input and a weakened summer-monsoon strength at the end of the last glacial, whereas a Mg/Al minimum at  $\sim 8-9$   $^{14}\text{C}$  ka BP indicates minimum dust input and an intensified summer monsoon during the early Holocene.

From clay-mineralogical data of core NIOP489 it was inferred that prior to  $\sim 11.5$   $^{14}\text{C}$  ka BP the hemipelagic muds on the middle Indus Fan (illite- and chlorite-rich, smectite-poor) were dominantly supplied from the Indus-River source, whereas during the Holocene deposition is dominated by eolian dust (illite-, chlorite- and smectite-rich, palygorskite) supplied from the Arabian Peninsula (Chapter 6). The basin-wide dispersal of the eolian dust was caused by the north-westerly winds which prevail over the Arabian Peninsula and raise large amounts of dust from this arid region. The gradual increase in eolian-dust content between  $\sim 11.5-8$   $^{14}\text{C}$  ka BP is illustrated by an increase of the Mg/Al ratio (Fig. 8.2D). The negative correlation between the non-carbonate mass-accumulation (NC-MAR) (Fig. 8.2B) and Mg/Al records points to a gradual decrease in the supply of Indus-River-derived muds, rather than an increase in the supply of eolian dust.

#### *Grain Size of Terrigenous Sediment*

End-member modelling of the siliciclastic grain-size distributions indicates that the dominant significance of siliciclastic grain-size variation in cores NIOP469, NIOP489 and SO90-169KL is the variation in mixing of eolian dust and river-derived mud (Prins and Weltje, 1999; Chapter 4, 5, 6, 7). An increase in grain size in the hemipelagic muds in these cores implies a relative increase in eolian fraction. This thesis is supported by the mineralogical and the geochemical composition of the hemipelagic sediments. The relative contribution of eolian versus fluvial sediment in these cores is plotted in Figure 8.2E (NIOP469, NIOP489) and in Figure 8.3D (SO90-169KL).

The Makran core NIOP469 shows relatively coarse-grained muds (high eolian dust content) for the last glacial period and the late Holocene. The grain size decreased (fluvial mud content increased) gradually during the transition from the last glacial period to the Holocene interglacial period, and reached a distinct minimum during the early Holocene ( $\sim 8-9$   $^{14}\text{C}$  ka BP). Similar changes in grain size are recorded in the hemipelagic muds on the Sindh continental slope, as is illustrated by the eolian-dust record of core SO90-169KL (Fig. 8.3D). The relative contributions of eolian and fluvial sediment in the hemipelagic muds is used as an indicator of continental aridity (cf. Prins and Weltje, 1999). Correlation of the Mg/Al record and the eolian-dust record of core NIOP469 (Fig. 8.2D, E) implies a link between summer-monsoon strength and continental humidity around the Arabian Sea. The minima in both records at  $\sim 8-9$   $^{14}\text{C}$  ka BP indicate that the track of the SW summer monsoon and its associated pattern of precipitation have shifted to their northernmost position during the early Holocene (cf. Sirocko *et al.*, 1993).

The grain size in core NIOP489 shows a sharp increase around  $\sim 9$   $^{14}\text{C}$  ka BP. The relative contribution of eolian dust varies around 20-30% during the last glacial period, and increases abruptly to values of 50-60% after  $\sim 9$   $^{14}\text{C}$  ka BP. Negative correlation between the NC MAR record (Fig. 8.2B) and the carbonate, Mg/Al and eolian-dust records of core NIOP489 (Fig.

8.2C, D and E) indicates that the important change in sediment composition and texture is due to a starvation of the fluvial input to the middle Indus Fan.

### **TIMING OF TURBIDITE DEPOSITION**

The glacio-eustatic sea-level curve of Barbados (Fairbanks, 1989, 1992) is shown as a reference curve in Figure 8.2F and 8.4D. The timing of turbidite sedimentation and associated changes in the growth pattern of the Indus Fan appear strongly controlled by changes in sea level (Fig. 8.4), which is in accordance with common ideas. The initiation of channel-levee system A coincided approximately with the age of the oxygen-isotope stage 2/3 transition ( $\sim 25$   $^{14}\text{C}$  ka BP), i.e., during a sea-level fall (Chapter 6). Its building up occurred mainly during the lowstand ( $\sim$ oxygen-isotope stage 2), and gradual abandonment (inferred from e.g. decreasing NC MAR, increasing eolian dust content at site NIOP489) occurred during the sea-level rise of oxygen-isotope stage 1. Turbidite sedimentation on the middle fan ceased entirely at termination 1a ( $\sim 11.5$   $^{14}\text{C}$  ka BP), followed by a gradual decrease in fluvial mud supply between termination 1b and 1a ( $\sim 11.5$ -9  $^{14}\text{C}$  ka BP). During the sea-level highstand, i.e., after  $\sim 9$   $^{14}\text{C}$  ka BP, the Indus Fan was draped by a pelagic calcareous ooze and terrigenous sedimentation on the middle fan was dominated by eolian dust of Arabian provenance.

A comparison with turbidite sedimentation on the Makran continental slope (Fig. 8.4) indicates that changes in turbidite sedimentation in both turbidite systems were primarily controlled by the changes in sea level. However, turbidite sedimentation on the Makran continental slope sustained longer during the sea-level rise (i.e., after 11.5  $^{14}\text{C}$  ka BP) and did not cease during the sea-level highstand (i.e., after 9  $^{14}\text{C}$  ka BP). The interval of 'prolonged' turbidite sedimentation and relatively high sedimentation rates on the Makran continental slope coincides with the early Holocene humidity maximum (e.g. inferred from Mg/Al and eolian-dust records of NIOP469).

We relate this deviating pattern to the significant difference in shelf width. The Makran shelf is very narrow, not more than a few km wide, in contrast with the Sindh shelf off the Indus Delta, which is  $\sim 100$  km wide. The Indus River did not feed its coarse-grained sediment to the Indus Fan during the early highstand, and thus the canyon became disconnected from the river. During the late highstand, deposition of Indus-River-derived sediment remained restricted to the Indus Canyon and Indus Delta. In contrast, sediments discharged by the mountainous rivers on the active Makran continental margin could easily bypass the narrow and steep shelf to the deep sea during the early and late highstand. Moreover, the high rates of sediment input and continued turbidite sedimentation during the early highstand have been enhanced by enhanced river discharge as a result of the intensified summer monsoon. No explanation, as yet, is given for the few turbidite beds in the top of NIOP469 (and other cores obtained from the Makran continental slope and abyssal plain; see Chapter 7). We think that these turbidite beds originated from seismic events but further proof is lacking.

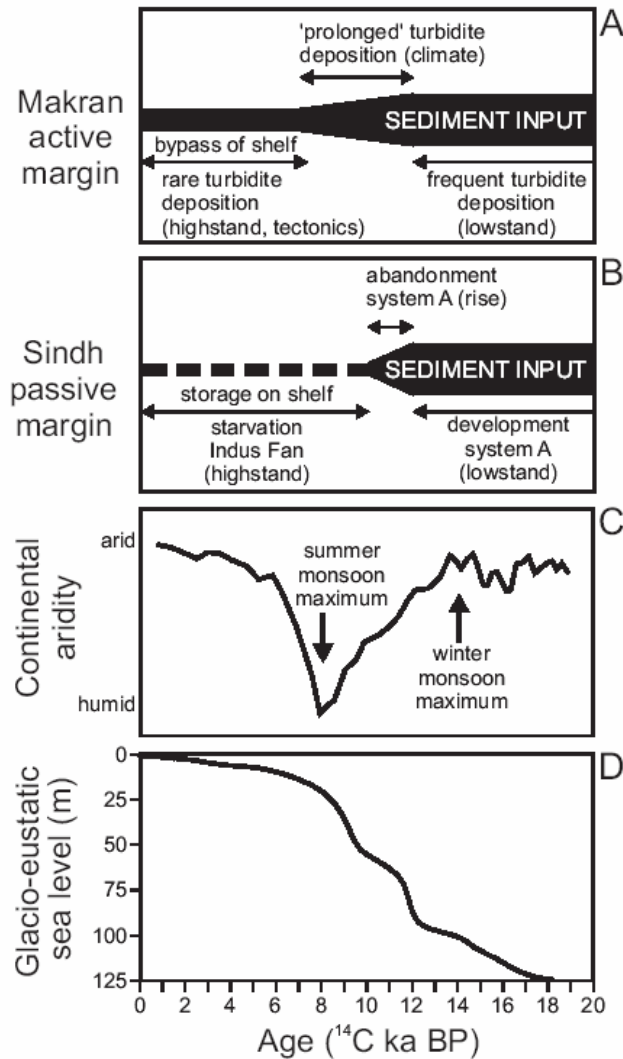


**Fig. 8.4** — Diagram showing the relation between glacio-eustatic sea-level fluctuations, climate changes and terrigenous sedimentation processes along the northern margin of the Arabian Sea. **A:** Makran continental slope (active margin); **B:** Indus Fan (passive margin); **C:** Continental-aridity proxy record (three-point moving average of contribution of eolian dust relative to fluvial mud in core NIOP469). Timing of monsoon climate extremes are indicated; **D:** Glacio-eustatic ‘Barbados sea-level curve’ (Fairbanks, 1992).

### CHANNEL-LEVEE SYSTEMS A1-A7 ON THE INDUS FAN

In the period of major feeder channel avulsion and switch from turbidite complex B to A, a period of non-channellised turbidity flow occurred as indicated by turbidite deposition at various sites (e.g. NIOP489) on the middle Indus Fan (Chapter 6). Similar turbidite intercalations in three other horizons are present in the hemipelagic mud drape in NIOP489, i.e., the distal equivalent of complex A. The rare presence of turbidites in hemipelagic drape is similarly inferred here to relate to periods of avulsion from the one channel levee system to the next (e.g. A2 to A1). The youngest series of turbidites, at  $\sim 12$   $^{14}\text{C}$  ka BP, probably belong to system A1.

The small channels A7 to A2 developed during the last glacial period, each within a time span of approximately 2 ka (between  $\sim 25$  and  $\sim 12$   $^{14}\text{C}$  ka BP). The volumes of the individual small channel-levee systems (A2-A7) are roughly similar as inferred from their geometry

seen on the GLORIA mosaic and on high-resolution seismic profiles; it seems if channels built up to a certain threshold dimension before they switched. We think that channel plugging and resultant decrease in gradient are important mechanisms that can force turbidity currents to shift to adjacent topographically low inter-channel areas. Thus the avulsion process would have been auto-cyclic. The avulsions of these channel-levee systems cannot be related to sea-level-induced changes in sediment supply, because during oxygen-isotope stage 2, the rate of sea-level change was minimal. However, millennium-scale periodicities (~2 ka) have been reported in various upwelling indices in cores from the western Arabian Sea suggesting similar periodicities in the strength of the summer monsoon (Naidu and Malmgren, 1995; Sirocko *et al.*, 1996). It is therefore very tempting to infer that avulsion frequency may have been determined by high-frequency variations in climate-induced sediment supply. However, our data are insufficient to support this hypothesis.

The youngest channel-levee system A1 is somewhat exceptional because this channel terminates into a sandy channel-mouth lobe at a relatively proximal position (Kenyon *et al.*, 1995, and our own data). This exception may be explained by its late development, beginning around ~12 <sup>14</sup>C ka BP, with diminishing supply starting at ~11.5 <sup>14</sup>C ka BP. The rapidly rising sea level resulted in a decrease in river-sediment supply causing the updip contraction of the channel-mouth lobe and eventually the abandonment of channel-levee system A. At present, we likely observe the 'fossilised' channel configuration of ~9.5 <sup>14</sup>C ka BP.

## CONCLUSIONS

Examination of turbidite systems in a tectonically active and passive region of the same basin allows to evaluate the relative importance of climate, sea level and tectonics on turbidite sedimentation. We conclude that:

1. The rise in glacio-eustatic sea level is the dominant factor in present day fan starvation for both active and passive tectonic settings, and is reflected by decreasing turbidite frequency and sediment volume;
2. The fall in sea level at the base of oxygen-isotope stage 2 caused avulsion of the main feeder channel and starvation of channel-levee system B on the Indus Fan;
3. Climate change from arid to humid and to arid again in the last 20 <sup>14</sup>C ka is recorded in both tectonic settings by the relative contribution of eolian dust to the hemipelagic intervals;
4. The increased humidity along the northern margin of the Arabian Sea during the early Holocene caused continued river-fed turbidite sedimentation on the Makran continental slope, but not in the midfan region of the Indus Fan. The difference is attributed to the difference in shelf width;
5. Channel shifting in channel-levee system A cannot be convincingly attributed to allocyclic factors and is probably autocyclic related to channel plugging.

## REFERENCES

- AGRAWAL, Y.C., MCCAVE, I.N., RILEY, J.B., 1991, Laser-diffraction size analysis, *in* Syvitski, J.P.M., ed., Principles, methods, and application of particle size analysis: Cambridge University Press, Cambridge, p. 119-128.
- ALLEN, G.P., CASTAING, P., KLINGEBIEL, A., 1971, Preliminary investigation of the surficial sediments in the Cap-Breton Canyon (southwest France) and the surrounding continental shelf – *Marine Geology*, v. 10, p. M27-M32.
- ALLEN, G.P., CASTAING, P., KLINGEBIEL, A., 1972, Distinction of elementary sand populations in the Gironde estuary (France) by R-mode factor analysis of grain-size data – *Sedimentology*, v. 19, p. 21-35.
- AN, Z., KUKLA, G.J., PORTER, S.C., XIAO, J., 1991, Magnetic susceptibility evidence of monsoon variation on the Loess Plateau of central China during the last 130,000 years – *Quaternary Research*, v. 36, p. 29-36.
- AN, Z.S. AND PORTER, S.C., 1997, Millennial-scale climatic oscillations during the last interglaciation in central China – *Geology*, v. 25, p. 603-606.
- ARTHURTON, R.S., FARAH, A., AHMED, W., 1982, The Late Cretaceous-Cenozoic history of western Baluchistan Pakistan - the northern margin of the Makran subduction complex, *in* Leggett, J.K., ed., Trench-forearc geology: sedimentation and tectonics on modern and ancient active plate margins, Geological Society Special Publication No. 10., p. 373-386.
- BARBER, B.A., 1998, Magnetic properties of modern soils and Quaternary loessic paleosols: paleoclimatic implications – *Palaeogeography, Palaeoclimatology, Palaeoecology*, v. 137, p. 25-54.
- BARD, E., 1988, Correlation of accelerator mass spectrometry <sup>14</sup>C ages measured in planktonic foraminifera: Paleoceanographic implications – *Paleoceanography*, v. 3, p. 635-645
- BAYVEL, L.P. AND JONES, A.R., 1981, Electromagnetic scattering and its applications: Applied Science, London, 289 pp.
- BCR INFORMATION, 1980, Certification report on reference materials of defined particle size. Quartz BCR no. 66, 67, 68, 69, 70. Report EUR 6825 en. Commission of the European Communities, Luxembourg.
- BEG, M.A.A., 1977, The Indus River basin and risk assessment of the irrigation system – International Working Seminar on Environmental Risk Assessment in an International Context, Tihanyi, Hungary, 13 pp.
- BISCHOF, O.F., DRESCHER, S., MERKUS, H.G., 1993, Ringonderzoek 1993: laser diffractie spectrometrie, electrical sensing zone, sedimentatie – Nederlandse Werkgroep Deeltjeskarakterisering, TU Delft, Vakgroep Chemische Procestechnologie, Sectie Deeltjestehnologie. Internal report.
- BLOEMENDAAL, J., LIU, X.M., ROLPH, T.C., 1995, Correlation of the magnetic susceptibility stratigraphy of Chinese loess and the marine oxygen isotope record: chronological and paleoclimatic implications – *Earth and Planetary Science Letters*, v. 131, p. 371-380.
- BOND, G., BROECKER, W., JOHNSON, S., MCMANUS, J., LABEYRIE, L., JOUZEL, J., BONANI, G., 1993, Correlations between climate records from North Atlantic sediments and Greenland ice – *Nature*, v. 365, p. 143-147.
- BOND, G., HEINRICH, H., BROECKER, W., LABEYRIE, L., MCMANUS, J., ANDREWS, J., HUON, S., JANTSCHIK, R., CLASEN, S., SIMET, C., TEDESCO, K., KLAS, M., BONANI, G., IVY, S., 1992, Evidence for massive discharges of icebergs into the North Atlantic ocean during the last glacial period – *Nature*, v. 360, p. 245-249.
- BOUMA, A.H., COLEMAN, J.M., STELTING, C.E., KOHL, B., 1989, Influence of relative sea level changes on the construction of the Mississippi Fan – *Geo-Marine Letters*, v. 9, p. 161-170.
- BRIDGE, J.S., 1981, Hydraulic interpretation of grain-size distributions using a physical model for bedload transport – *Journal of Sedimentary Petrology*, v. 51, p. 1109-1124.
- BRYANT, M., FALK, P., PAOLA, C., 1995, Experimental study of avulsion frequency and rate of deposition – *Geology*, v. 23, p. 365-368.
- CHAMBERS, R.L. AND UPCHURCH, S.B., 1979, Multivariate analysis of sedimentary environments using grain-size frequency distributions – *Mathematical Geology*, v. 11, p. 27-43.
- CHEN, F.H., BLOEMENDAL, J., WANG, J.M., LI, J.J., OLDFIELD, F., 1997, High-resolution multi-proxy climate records from the Chinese loess: evidence for rapid climatic changes over the last 75 kyr – *Palaeogeography, Palaeoclimatology, Palaeoecology*, v. 130, p. 323-335.
- CLARK, I.D. AND FONTES, J.-C., 1990, Paleoclimatic reconstruction in northern Oman based on carbonates from hyperalkaline groundwaters – *Quaternary Research*, v. 33, p. 320-336.
- CLEMENS, S.C., MURRAY, D.W., PRELL, W.L., 1996, Nonstationary phase of the Plio-Pleistocene Asian Monsoon – *Science*, v. 274, p. 943-948.
- CLEMENS, S.C. AND PRELL, W.L., 1990, Late Pleistocene variability of Arabian Sea summer monsoon winds and continental aridity: eolian records from the lithogenic component of deep-sea sediments – *Paleoceanography*, v. 5, p. 109-145.

- CLEMENS, S.C. AND PRELL, W.L., 1991, One million year record of summer monsoon winds and continental aridity from the Owen Ridge (site 722), northwest Arabian Sea, *in* Prell, W.L., Niitsuma, N. *et al.*, Proceedings of the Ocean Drilling Program, Scientific Results, vol. 117, p. 365-388.
- CLEMENS, S., PRELL, W., MURRAY, D., SHIMMIELD, G., WEEDON, G., 1991, Forcing mechanisms of the Indian Ocean monsoon – *Nature*, v. 353, p. 720-725.
- COLIN, C., KISSEL, C., BLAMART, D., TURPIN, L., 1998, Magnetic properties of sediments in the Bay of Bengal and the Andaman Sea: impact of rapid North Atlantic Ocean climatic events on the strength of the Indian monsoon – *Earth and Planetary Science Letters*, v. 160, p. 623-635.
- COOPER, L.R., HAVERLAND, R.L., HENDRICKS, D.M., KNISEL, W.G., 1984, Microtrac particle-size analyzer: an alternative particle-size determination method for sediment and soils – *Soil Science*, v. 138, p. 138-146.
- CURRAY, J.R., 1960, Tracing sediment masses by grain size modes – Report of the Twenty-First Session Norden, International Geological Congress, Copenhagen, p. 119-130.
- DAL CIN, R., 1976, The use of factor analysis in determining beach erosion and accretion from grain-size data – *Marine Geology*, v. 20, p. 95-116.
- DAMUTH, J.E., 1977, Late Quaternary sedimentation in the western equatorial Atlantic – *Geological Society of America Bulletin*, v. 88, p. 695-710.
- DAMUTH, J.E., FLOOD, R.D., KOWSMANN, R.O., BELDERSON, R.H., GORINI, M.A., 1988, Anatomy and growth pattern of Amazon deep-sea fan as revealed by long-range side-scan sonar (GLORIA) and high-resolution seismic studies – *American Association of Petroleum Geologists Bulletin*, v. 72, p. 885-911.
- DANSGAARD, W., JOHNSEN, S.J., CLAUSEN, H.B., DAHL-JENSEN, D., GUNDESTRUP, N.S., HAMMER, C.U., HVIDBERG, C.S., STEFFENSEN, J.P., SVEINBJORNSDOTTIR, A.E., JOUZEL, J., BOND, G., 1993, Evidence for general instability of past climate from a 250-kyr ice-core record – *Nature*, v. 364, p. 218-220.
- DAVIS, J.C., 1970, Information contained in sediment-size analyses – *Mathematical Geology*, v. 2, p. 105-112.
- DAVIS, J.C., 1986, *Statistics and data analysis in geology* (second edition): John Wiley and Sons, New York, 646 pp.
- DE BOER, G.B.J., DE WEERD, C., THOENES, D., GOOSSENS, H.W.J., 1987, Laser-diffraction spectrometry: Fraunhofer diffraction versus Mie scattering – *Particle Characterisation*, v. 4, p. 14-19.
- DICKINSON, W.R. AND SEELY, D.R., 1979, Structure and stratigraphy of forearc regions – *American Association of Petroleum Geologists Bulletin*, v. 63, p. 2-31.
- DING, Z., LIU, T., RUTTER, N.W., YU, Z., GUO, Z., ZHU, R., 1995, Ice-volume forcing of past east Asian winter monsoon variations in the past 800,000 years – *Quaternary Research*, v. 44, p. 149-159.
- DOEGLAS, D.J., 1946, Interpretation of the results of mechanical analyses – *Journal of Sedimentary Petrology*, v. 16, p. 19-40.
- DOEGLAS, D.J. AND BREZESINSKA SMITHUYSEN, W.C., 1941, De interpretatie van de resultaten van korrelgrootte-analysen – *Geologie en Mijnbouw*, v. 3, p. 273-285; v. 3, p. 291-302.
- DOWLING, J.J., 1977, A grain size spectra map – *Journal of Sedimentary Petrology*, v. 47, p. 281-284.
- DRISCOLL, M.L., TUCHOLKE, B.E., MCCAVE, I.N., 1985, Seafloor zonation in sediment texture on the Nova Scotian lower continental rise – *Marine Geology*, v. 66, p. 25-41.
- DROZ, L. AND BELLAICHE, G., 1991, Seismic facies and geologic evolution of the central portion of the Indus Fan., *in* Weimer, P. and Link, M.H., eds., *Seismic Facies and Sedimentary Processes of Submarine Fans and Turbidite Systems*: Springer-Verlag, New York, p. 383-402.
- DUPLESSY, J.C., 1982, Glacial and interglacial contrasts in the northern Indian Ocean – *Nature*, v. 295, p. 494-498.
- FAIRBANKS, R.G., 1989, A 17,000-year glacio-eustatic sea level record: influence of glacial melting rates on the Younger Dryas event and deep-ocean circulation – *Nature*, v. 342, p. 637-642.
- FAIRBANKS, R.G., 1992, Barbados sea level and Th/U <sup>14</sup>C calibration. IGBP PAGES/World data Center-A for Paleoclimatology Data Contribution Series # 92-020. NOAA/NGDC Paleoclimatology Program, Boulder CO, USA.
- FANG, X.-M., ONO, Y., FUKUSAWA, H., PAN, B.-T., LI, J.-J., GUAN, D.-H., OI, K., TSUKAMOTO, S., TORII, M., 1999, Asian summer monsoon instability during the past 60,000 years: magnetic susceptibility and pedogenic evidence from the Chinese western Loess Plateau – *Earth and Planetary Science Letters*, *in press*.
- FEELEY, M.H., T.C. MOORE JR., T.S. LOUTIT, W.R. BRYANT, 1990, Sequence stratigraphy of Mississippi Fan related to oxygen isotope sea level index – *American Association of Petroleum Geologists Bulletin*, v. 74, p. 407-424.
- FILLON, R.H. AND FULL, W.E., 1984, Grain-size variations in North Atlantic non-carbonate sediments and sources of terrigenous components – *Marine Geology*, v. 59, p. 13-50.
- FONTUGNE, M.R. AND DUPLESSY, J.C., 1986, Variations of the monsoon regime during the upper Quaternary: evidence from carbon isotopic record of organic matter in North Indian Ocean sediment cores – *Palaeogeography, Palaeoclimatology, Palaeoecology*, v. 56, p. 69-88.

## References

- FORMAN, S.L., 1991, Late Pleistocene chronology of loess deposition near Luochuan, China – *Quaternary Research*, v. 36, p. 19-28.
- FORREST, J. AND CLARK, N.R., 1989, Characterizing grain size distributions: evaluation of a new approach using multivariate extension of entropy analysis – *Sedimentology*, v. 36, p. 711-722.
- FOWLER, S.R., WHITE, R.S., LOUDEN, K.E., 1985, Sediment dewatering in the Makran accretionary prism – *Earth and Planetary Science Letters*, v. 75, p. 427-438.
- FULL, W.E., EHRLICH, R., KLOVAN, J.E., 1981, EXTENDED QMODEL - Objective definition of external end members in the analysis of mixtures – *Mathematical Geology*, v. 13, p. 331-344.
- GASSE, F., ARNOLD, M., FONTES, J.C., FORT, M., GIBERT, E., HUC, A., LI BINGYAN, LI YUANFANG, LIU QING, MELLIERES, F., VAN CAMPO, E., WANG FUBAO, ZHANG QINGSONG, 1991, A 13,000-year climate record from western Tibet – *Nature*, v. 353, p. 742-745.
- GASSE, F. AND VAN CAMPO, E., 1994, Abrupt post-glacial climate events in West Asia and North Africa monsoon domains – *Earth and Planetary Science Letters*, v. 126, p. 435-456.
- GROOTES, P.M., STUIVER, M., WHITE, J.W.C., JOHNSON, S., JOUZEL, J., 1993, Comparison of oxygen isotope records from the GISP2 and GRIP Greenland ice cores – *Nature*, v. 366, p. 552-554.
- GROUSSET, F.E., LABEYRIE, L., SINKO, J.A., CREMER, M., BOND, G., DUPRAT, J., CORTIJO, E., HUON, S., 1993, Patterns of ice-rafted detritus in the glacial North Atlantic (40-55°N) – *Paleoceanography*, v. 8, p. 175-192.
- HARMS, J.C., CAPPEL, H.N., FRANCIS, D.C., 1984, The Makran Coast of Pakistan: its stratigraphy and hydrocarbon potential, *in* Haq, B.U. and Milliman, J.D., eds., *Marine Geology and Oceanography of Arabian Sea and Coastal Pakistan*: Van Nostrand Reinhold Company, Scientific and Academic Editions, New York, p. 3-26.
- HAYTER, P.J.D., 1960, The Ganges and Indus submarine canyons – *Deep-Sea Research*, v. 6, p. 184-186.
- HEINRICH, H., 1988, Origin and consequences of cyclic ice-rafting in the northeast Atlantic Ocean, during the past 130,000 yrs – *Quaternary Research*, v. 29, p. 142-152.
- HIRLEMAN, E.D., 1987, Optimal scaling of the inverse Fraunhofer diffraction particle sizing problem: The linear system produced by quadrature – *Particle Characterisation*, v. 4, p. 128-133.
- IMBRIE, J., HAYS, J.D., MARTINSON, D.G., MCINTYRE, A., MIX, A.C., MORLEY, J.J., PISIAS, N.G., PRELL, W.L., SHACKLETON, N.J., 1984, The orbital theory of Pleistocene climate: support from a revised chronology of the marine  $\delta^{18}\text{O}$  record, *in* Berger, A., Imbrie, J., Hays, J., Kukla, G., Saltzman, B., eds., *Milankovitch and climate, Part 1*: D. Reidel, Hingham, Mass., p. 269-305.
- JANSEN, J.H.F., VAN DER GAAST, S.J., KOSTER, B., VAARS, A.J., 1998, CORTEX, a shipboard XRF-scanner for element analyses in split sediment cores – *Marine Geology*, v. 151, p. 143-153.
- JONASZ, M., 1991, Size, shape, composition, and structure of microparticles from light scattering, *in* Syvitski, J.P.M., ed., *Principles, methods, and application of particle size analysis*: Cambridge University Press, Cambridge, p. 143-162.
- JÖRESKOG, K.G., KLOVAN, J.E., REYMENT, R.A., 1976, *Geological factor analysis*. Elsevier, Amsterdam, 178 pp.
- KARLIN, R. AND LEVI, S., 1983, Diagenesis of magnetic minerals in recent hemipelagic sediments – *Nature*, v. 303, p. 327-330.
- KAZMI, A.H., 1982, Geology of the Indus Delta., *in* Haq, B.U. and Milliman, J.D., eds., *Marine Geology and Oceanography of Arabian Sea and Coastal Pakistan*: Van Nostrand Reinhold Company, Scientific and Academic Editions, New York, p. 71-84.
- KENT, D.V., 1982, Apparent correlation of paleomagnetic intensity and climatic records in deep-sea sediments – *Nature*, v. 299, p. 538-539.
- KENYON, N.H., AMIR, A., CRAMP, A., 1995, Geometry of the younger sediment bodies of the Indus Fan, *in* Pickering, K.T., Hiscott, R.N., Kenyon, N.H., Ricci Lucchi, F., Smith, R.D.A., eds., *Atlas of deep water environments: architectural style in turbidite systems*: Chapman and Hall, London, p. 89-93.
- KLEIN, G. DE VRIES, 1984, Relative rates of tectonic uplift as determined from episodic turbidite deposition in marine basins – *Geology*, v. 12, p. 48-50.
- KLOVAN, J.E., 1966, The use of factor analysis in determining depositional environments from grain-size distributions – *Journal of Sedimentary Petrology*, v. 36, p. 115-125.
- KLOVAN, J.E. AND MIESCH, A.T., 1976, EXTENDED CABFAC and QMODEL computer programs for Q-mode factor analysis of compositional data – *Computers and Science*, v. 1, p. 161-178.
- KOLLA, V. AND COUMES, F., 1987, Morphology, internal structure, seismic stratigraphy, and sedimentation on the Indus Fan – *American Association of Petroleum Geologists Bulletin*, v. 71, p. 650-677.
- KOLLA, V., HENDERSON, L., BISCAYE, P.E., 1976, Clay mineralogy and sedimentation in the western Indian Ocean – *Deep-Sea Research*, v. 23, p. 949-961.
- KOLLA, V., KOSTECKI, J.A., ROBINSON, F., BISCAYE, P.E., 1981, Distributions and origins of clay minerals and quartz in surface sediments of the Arabian Sea – *Journal of Sedimentary Petrology*, v. 51, p. 563-569.

- KOLLA, V. AND MACURDA JR., D.B., 1988, Sea-level changes and timing of turbidity-current events in deep-sea fan systems, *in* Wilgus, C.K., Hastings, B.K., Posamentier, H., Van Wagoner, J., Ross, C.A., Kendall, C.G.St.C., eds., *Sea-level changes: An Integrated Approach*, Society of Economic Palaeontologists and Mineralogists Special Publication No. 42, p. 381-392.
- KOLLA, V. AND PERLMUTTER, M.A., 1993, Timing of turbidite sedimentation on the Mississippi Fan – American Association of Petroleum Geologists Bulletin, v. 77, p. 1129-1141.
- KOLLA, V. AND SCHWAB, A.M., 1995, Indus Fan: multi-channel seismic reflection images of channel-levee-overbank complexes, *in* Pickering, K.T., Hiscott, R.N., Kenyon, N.H., Ricci Lucchi, F., Smith, R.D.A., eds., *Atlas of deep water environments: architectural style in turbidite systems*: Chapman and Hall, London, p. 100-104.
- KONERT, M. AND VANDENBERGHE, J., 1997, Comparison of laser grain size analysis with pipette and sieve analysis: a solution for the underestimation of the clay fraction – *Sedimentology*, v. 44, p. 523-535.
- KOOPMANN, B., 1981, Sedimentation von Saharastaub im subtropischen Nordatlantik während der letzten 25.000 Jahre – *Meteor Forschungs-Ergebnisse, Reihe C*, no. 35, p. 23-59.
- KRISSEK, L.A. AND CLEMENS, S.C., 1991, Mineralogic variations in a Pleistocene high-resolution eolian record from the Owen Ridge, western Arabian Sea (site 722): implications for sediment source conditions and monsoon history, *in* Prell, W.L., Niitsuma, N., *et al.*, *Proceedings of the Ocean Drilling Program, Scientific Results*, v. 117, p. 197-214.
- KUEHL, S.A., HARIU, T.M., MOORE, W.S., 1989, Shelf sedimentation off the Ganges-Brahmaputra river system: evidence for sediment bypassing to the Bengal Fan – *Geology*, v. 17, p. 1132-1135.
- KUKLA, G.J. AND AN, Z.S., 1989, Loess stratigraphy in central China – *Palaeogeography, Palaeoclimatology, Palaeoecology*, v. 72, p. 203-225.
- KUKLA, G.J., AN, Z.S., MELICE, J.L., GAVIN, J., XIAO, J.L., 1990, Magnetic susceptibility record of Chinese loess – *Transactions of the Royal Society of Edinburgh: Earth Sciences*, v. 81, p. 263-288.
- LIRER, L., SHERIDAN, M., VINCI, A., 1996, Deconvolution of pyroclastic grain-size spectra for interpretation of transport mechanisms: an application to the AD 79 Vesuvio deposits – *Sedimentology*, v. 43, p. 913-926.
- LIRER, L. AND VINCI, A., 1991, Grain-size distributions of pyroclastic deposits – *Sedimentology*, v. 38, p. 1075-1083.
- LIU, T.S. *et al.*, eds., 1985, *Loess and the environment*, China Ocean Press, Beijing.
- LOIZEAU, J.-L., ARBOUILLE, D., SANTIAGO, S., VERNET, J.-P., 1994, Evaluation of a wide range laser-diffraction grain size analyser for use with sediments – *Sedimentology*, v. 41, p. 353-361.
- MAHER, B.A. AND THOMPSON, R., 1992, Paleoclimatic significance of the mineral magnetic record of the Chinese loess and paleosols – *Quaternary Research*, v. 37, p. 155-170.
- MAHER, B.A., THOMPSON, R., ZHOU, L.P., 1994, Spatial and temporal reconstructions of changes in the Asian palaeomonsoon: a new mineral magnetic approach – *Earth and Planetary Science Letters*, v. 125, p. 461-471.
- MANLEY, P.L. AND FLOOD, R.D., 1988, Cyclic sediment deposition within Amazon deep-sea fan – *American Association of Petroleum Geologists Bulletin*, v. 72, p. 912-925.
- MARTINSON, D.G., PISIAS, N.G., HAYS, J.D., IMBRIE, J., MOORE JR., T.C., SHACKLETON, N.J., 1987, Age dating and the orbital theory of the ice ages: development of a high-resolution 0 to 300,000-year chronostratigraphy – *Quaternary Research*, v. 27, p. 1-29.
- MATTHEWS, M.D., 1991, The effect of grain shape and density on size measurement, *in* Syvitski, J.P.M., ed., *Principles, methods, and application of particle size analysis*: Cambridge University Press, Cambridge, p. 22-33.
- MCCALL, G.J.H. AND KIDD, R.G.W., 1982, The Makran, Southeastern Iran: the anatomy of a convergent plate margin active from Cretaceous to Present, *in* Leggett, J.K., ed., *Trench-forearc geology: sedimentation and tectonics on modern and ancient active plate margins*, Geological Society Special Publication No. 10., p. 387-397.
- MCCAVE, I.N., 1972, Transport and escape of fine-grained sediment from shelf areas, *in* Swift, D.J.P., Duane, D.B., Pilkey, O.H., eds., *Shelf sediment transport: process and pattern*: Hutchinson & Ross, Inc., Stroudsburg, Pennsylvania, Dowden, p. 225-248.
- MCCAVE, I.N., BRYANT, R.J., COOK, H.F., COUGHANOWR, C.A., 1986, Evaluation of a laser-diffraction-size analyzer for use with natural sediments – *Journal of Sedimentary Petrology*, v. 56, p. 561-564.
- MCCAVE, I.N., MANIGHETTI, B., ROBINSON, S.G., 1995, Sortable silt and fine sediment size/composition slicing: Parameters for palaeocurrent speed and palaeoceanography – *Paleoceanography*, v. 10, p. 593-610.
- MCCLURE, H.A., 1976, Radiocarbon chronology of late Quaternary lakes in the Arabian Desert – *Nature*, v. 263, p. 755-756.
- MCHARGUE, T.R., 1991, Seismic facies, processes, and evolution of Miocene inner fan channels, Indus Submarine Fan, *in* Weimer, P. and Link, M.H., eds., *Seismic Facies and Sedimentary Processes of Submarine Fans and Turbidite Systems*: Springer-Verlag, New York, p. 403-413.

## References

- MCHARGUE, T.R. AND WEBB, J.E., 1986. Internal geometry, seismic facies, and petroleum potential of canyons and inner fan channels of the inner Indus Submarine Fan – American Association of Petroleum Geologists Bulletin, v. 70, p. 161-180.
- MIDDLETON, G.V., 1976, Hydraulic interpretation of sand size distributions – Journal of Geology, v. 84, p. 405-426.
- MILLIMAN, J.D., QURAISSHEE, G.S., BEG, M.A.A., 1982, Sediment discharge from the Indus River to the ocean: past, present and future, *in* Haq, B.U. and Milliman, J.D., eds., Marine Geology and Oceanography of Arabian Sea and Coastal Pakistan: Van Nostrand Reinhold Company, Scientific and Academic Editions, New York, p. 65-70.
- MILLIMAN, J.D. AND SYVITSKI, J.P.M., 1992, Geomorphic/tectonic control of sediment discharge to the ocean: the importance of small mountainous rivers – Journal of Geology, v. 100, p. 525-544.
- MULDER, T. AND SYVITSKI, J.P.M., 1995, Turbidity currents generated at river mouths during exceptional discharges to the world oceans – Journal of Geology, v. 103, p. 285-299.
- MURRAY, D.W. AND PRELL, W.L., 1991, Pliocene to Pleistocene variations in calcium carbonate, organic carbon, and opal on the Owen Ridge, northern Arabian Sea, *in* Prell, W.L., Niitsuma, N. *et al.*, Proceedings of the Ocean Drilling Program, Scientific Results, v. 117, p. 343-364.
- MUTTI, E. AND NORMARK, W.R., 1987, Comparing examples of modern and ancient turbidite systems: Problems and concepts, *in* Leggett, J.K. and Zuffa, G.G., eds., Marine Clastic Sedimentology: Graham and Trotman, p. 1-38.
- NAIDU, P.D. AND MALMGREN, B.A., 1995, A 2,200 years periodicity in the Asian monsoon system – Geophysical Research Letters, v. 22, p. 2361-2364.
- NAINI, B.R. AND KOLLA, V., 1982, Acoustic character and thickness of sediments of the Indus Fan and the continental margin of western India – Marine Geology, v. 47, p. 181-195.
- NAIR, R.R., HASHIMI, N.H., PURNACHANDRA RAO, V., 1982, On the possibility of high-velocity tidal streams as dynamic barriers to longshore sediment transport: evidence from the continental shelf off the Gulf of Kutch, India – Marine Geology, v. 47, p. 77-86.
- NAIR, R.R., ITTEKKOT, V., MANGANINI, S.J., RAMASWAMY, V., HAAKE, B., DEGENS, E.T., DESAI, B.N., HONJO, S., 1989, Increased particle flux to the deep ocean related to monsoons – Nature, v. 338, p. 749-751.
- NELSON, C.H., TWICHELL, D.C., SCHWAB, W.C., LEE, H.J., KENYON, N.H., 1992, Upper Pleistocene turbidite sand beds and chaotic silt beds in the channelized, distal, outer-fan lobes of the Mississippi Fan – Geology, v. 20, p. 693-696.
- PAGE, W.D., ALT, J.N., CLUFF, L.S., PLAFKER, G., 1979, Evidence for the recurrence of large-magnitude earthquakes along the Makran coast of Iran and Pakistan – Tectonophysics, v. 52, p. 533-547.
- PORTER, S.C. AND AN, Z., 1995, Correlation between climate events in the North Atlantic and China during the last glaciation – Nature, v. 375, p. 305-308.
- POSAMENTIER, H.W. AND VAIL, P.R., 1988, Eustatic controls on clastic deposition II- Sequence and systems tract models, *in* Wilgus, C.K. *et al.*, eds., Sea-level changes: An integrated approach, Society of Economic Palaeontologists and Mineralogists Special Publication No. 42, p. 125-154.
- POSTMA, G., HILGEN, F.J., ZACHARIASSE, W.J., 1993, Precession-punctuated growth of a late Miocene submarine-fan lobe on Gavdos (Greece) – Terra Nova, v. 5, p. 438-444.
- PRINS, M.A., REICHART, G.J., VISSER, H.J., POSTMA, G., ZACHARIASSE, W.J., VAN DER LINDEN, W.J.M., CRAMP, A., 1994, Sediments recovered during NIOP cruises D1-D3, *in* Van der Linden, W.J.M. and Van der Weijden, C.H., eds., Netherlands Indian Ocean Programme Cruise Report Vol. 3, Geological study of the Arabian Sea: National Museum of Natural History, Leiden, p. 87-96.
- PRINS, M.A. AND WELTJE, G.J., 1999, End-member modeling of siliciclastic grain-size distributions: the late Quaternary record of eolian and fluvial sediment supply to the Arabian Sea and its paleoclimatic significance, *in* Harbaugh, J., Watney, L., Rankey, G., Slingerland, R., Goldstein, R., Franseen, E., eds., Numerical Experiments in Stratigraphy: Recent Advances in Stratigraphic/Sedimentologic Computer Simulations, Society of Economic Palaeontologists and Mineralogists Special Publication No. 63, *in press*.
- REA, D.K., 1994, The paleoclimatic record provided by eolian deposition in the deep sea: the geologic history of wind – Reviews of Geophysics, v. 32, p. 159-195.
- REA, D.K. AND HOVAN, S.A., 1995, Grain size distribution and depositional processes of the mineral component of abyssal sediments: Lessons from the North Pacific – Paleoceanography, v. 10, p. 251-258.
- REICHART, G.J., DEN DULK, M., VISSER, H.J., VAN DER WEIJDEN, C.H., ZACHARIASSE, W.J., 1998, A 225 kyr record of dust supply, paleoproductivity and the oxygen minimum zone from the Murray Ridge (northern Arabian Sea) – Palaeogeography, Palaeoclimatology, Palaeoecology, v. 134, p. 149-169.
- REICHART, G.J., LOURENS, L.J., ZACHARIASSE, W.J., 1997, Orbital- and suborbital-controlled variability in the oxygen minimum zone (OMZ) of the northern Arabian Sea during the last 225,000 yr, *in* Reichart, G.J., Late Quaternary variability of the Arabian Sea monsoon and oxygen minimum zone, Geologica Ultraiectina 154, p. 79-121.

- REICHART, G.J., PRINS, M.A., VISSER, H.J., 1994, Magnetic susceptibility, gamma ray transmissivity and XRF core-scanning, *in* Van der Linden, W.J.M. and Van der Weijden, C.H., eds., Netherlands Indian Ocean Programme Cruise Report Vol. 3, Geological study of the Arabian Sea: National Museum of Natural History, Leiden, p. 97-115.
- RENNER, R.M., 1993, The resolution of a compositional dataset into mixtures of fixed source compositions – Applied Statistics, *Journal of the Royal Statistical Society*, v. 42, p. 615-631.
- RENNER, R.M., 1995, The construction of extreme compositions – *Mathematical Geology*, v. 27, p. 485-497.
- ROBINSON, S.G., 1993, Lithostratigraphic applications for magnetic susceptibility logging of deep-sea sediment cores: examples from ODP Leg 115, *in* Hailwood, E.A., Kidd, R.B., eds., High resolution stratigraphy, Geological Society Special Publication, v. 70, p. 65-98.
- SARKAR, A., RAMESH, R., BHATTACHARYA, S.K., RAJAGOPALAN, G., 1990, Oxygen isotope evidence for a stronger winter monsoon current during the last glaciation – *Nature*, v. 343, p. 549-551.
- SARNTHEIN, M., 1978, Sand deserts during glacial maximum and climatic optimum – *Nature*, v. 272, p. 43-46.
- SARNTHEIN, M., TETZLAFF, G., KOOPMANN, B., WOLTER, K., PFLAUMANN, U., 1981, Glacial and interglacial wind regimes over the eastern subtropical Atlantic and North-West Africa – *Nature*, v. 293, p. 193-196.
- SARNTHEIN, M., THIEDE, J., PFLAUMANN, U., ERLLENKEUSER, H., FUTTERER, D., KOOPMANN, B., LANGE, H., SEIBOLD, E., 1982, Atmospheric and oceanic circulation patterns off northwest Africa during the past 25 million years, *in* Von Rad, U., Hinz, K., Sarnthein, M., Seibold, E., eds., *Geology of the northwest African continental margin*: Springer-Verlag, Berlin, p. 545-604.
- SASAJIMA, S. AND WANG, Y.Y., eds., 1984, *The recent research of loess in China*: Kyoto University and Northwest University, Kyoto, Japan.
- SCHULZ, H., VON RAD, U., ERLLENKEUSER, H., 1998, Correlation between Arabian Sea and Greenland climate oscillations of the past 110,000 years – *Nature*, v. 393, p. 54-57.
- SHANMUGAM, G. AND MIOLA, R.J., 1982, Eustatic control of turbidites and winnowed turbidites – *Geology*, v. 10, p. 231-235.
- SHERIDAN, M.F., WOHLTZ, K.H., DEHN, J., 1987, Discrimination of grain-size subpopulations in pyroclastic deposits – *Geology*, v. 15, p. 367-370.
- SHIMMIELD, G.B. AND MOWBRAY, S.R., 1991, The inorganic geochemical record of the northwest Arabian Sea: a history of productivity variation over the last 400 k.y. from sites 722 and 724, *in* Prell, W.L., Niitsuma, N. *et al.*, *Proceedings of the Ocean Drilling Program, Scientific Results*, vol. 117, p. 409-429.
- SHIMMIELD, G.B., MOWBRAY, S.R., WEEDON, G.P., 1990, A 350 ka history of the Indian Southwest Monsoon - evidence from deep-sea cores, northwest Arabian Sea, *in* *Transactions of the Royal Society of Edinburgh, Earth Sciences*, v. 81, p. 289-299.
- SINGER, J.K., ANDERSON, J.B., LEDBETTER, M.T., MCCAVE, I.N., JONES, K.P.N., WRIGHT, R., 1988, An assessment of analytical techniques for the size analysis of fine-grained sediments – *Journal of Sedimentary Petrology*, v. 58, p. 534-543.
- SIROCKO, F., 1991, Deep-sea sediments of the Arabian Sea: a paleoclimatic record of the Southwest-Asian summer monsoon – *Geologische Rundschau*, v. 80, p. 557-566.
- SIROCKO, F., GARBE-SCHONBERG, D., MCINTYRE, A., MOLFINO, B., 1996, Teleconnections between the subtropical monsoons and high-latitude climates during the last deglaciation – *Science*, v. 272, p. 526-529.
- SIROCKO, F. AND LANGE, H., 1991, Clay-mineral accumulation rates in the Arabian Sea during the late Quaternary – *Marine Geology*, v. 97, p. 105-119.
- SIROCKO, F. AND SARNTHEIN, M., 1989, Wind-borne deposits in the Northwestern Indian Ocean: Record of Holocene sediments versus modern satellite data, *in* Leinen, M. and Sarnthein, M., eds., *Paleoclimatology and Paleometeorology: Modern and Past Patterns of global atmospheric transport* – NATO ASI Series C 282, Kluwer, Dordrecht, Boston, London, p. 401-433.
- SIROCKO, F., SARNTHEIN, M., ERLLENKEUSER, H., LANGE, H., ARNOLD, M., DUPLESSY, J.C., 1993, Century-scale events in monsoonal climate over the past 24,000 years – *Nature*, v. 364, p. 322-324.
- SIROCKO, F., SARNTHEIN, M., LANGE, H., ERLLENKEUSER, H., 1991, Atmospheric summer circulation and coastal upwelling in the Arabian Sea during the Holocene and the last glaciation – *Quaternary Research*, v. 36, p. 72-93.
- SOLOHUB, J.T. AND KLOVAN, J.E., 1970, Evaluation of grain-size parameters in lacustrine environments – *Journal of Sedimentary Petrology*, v. 40, p. 81-101.
- STANLEY, D.J. AND WARNE, A.G., 1994, Worldwide initiation of Holocene marine deltas by deceleration of sea-level rise – *Science*, v. 265, p. 228-231.
- STEWART, R.A., PILKEY, O.H., NELSON, B.W., 1965, Sediments of the northern Arabian Sea – *Marine Geology*, v. 3, p. 411-427.

## References

- STOW, D.A.V., 1985, Deep-sea clastics: where are we and where are we going, *in* Brenchley, P.J. and Williams, B.P.J., eds., *Sedimentology, Recent Developments and Applied Aspects*: Blackwell Scientific Publications, Oxford, p. 67-94.
- STOW, D.A.V., COCHRAN, J.R., ODP LEG 116 SHIPBOARD SCIENTIFIC PARTY, 1989, The Bengal Fan: some preliminary results from ODP drilling – *Geo-Marine Letters*, v. 9, p. 1-10.
- SUKUMAR, R., RAMESH, R., PANT, R.K., RAJAGOPALAN, G., 1993, A  $\delta^{13}\text{C}$  record of late Quaternary climate change from tropical peats in southern India – *Nature*, v. 364, p. 703-706.
- SUTHERLAND, H.E., CALVERT, S.E., MORRIS, R.J., 1984, Geochemical studies of the recent sapropel and associated sediment from the Hellenic outer ridge eastern Mediterranean Sea. I: Mineralogy and chemical composition – *Marine Geology*, v. 56, p. 72-92.
- SWITHENBANK, J., BEER, J.M., TAYLOR, D.S., ABBOT, D., MCGREATH, G.C., 1977, A laser diagnostic technique for the measurement of droplet and particle size distributions, *in* Zinn, B.J., ed., *Experimental diagnostics in gas phase combustion systems – Progress in Astronautics and Aeronautics*, v. 53, p. 421-447.
- SYVITSKI, J.P.M., ed., 1991a, *Principles, methods, and application of particle size analysis*: Cambridge University Press, Cambridge, 368 pp.
- SYVITSKI, J.P.M., 1991b, Factor analysis of size frequency distributions: significance of factor solutions based on simulation experiments, *in* J.P.M. Syvitski, ed., *Principles, methods, and applications of particle size analysis*: Cambridge University Press, Cambridge, p. 249-263.
- SYVITSKI, J.P.M., LEBLANC, K.W.G., ASPREY, K.W., 1991, Interlaboratory, interinstrument calibration experiment, *in* Syvitski, J.P.M., ed., *Principles, methods, and application of particle size analysis*: Cambridge University Press, Cambridge, p. 174-193.
- TUREKIAN, K.K. AND WEDEPOHL, K.H., 1961, Distribution of the elements in some major units of the earth's crust – *Geological Society of America Bulletin*, v. 72, p. 175-192.
- UNDERWOOD, M.B. AND BACHMAN, S.B., 1982, Sedimentary facies associations within subduction complexes, *in* Leggett, J.K., ed., *Trench-forearc geology: sedimentation and tectonics on modern and ancient active plate margins*, Geological Society Special Publication No. 10, p. 357-372.
- VAN DER LINDEN, W.J.M. AND VAN DER WEIJDEN, C.H., eds., 1994, *Geological study of the Arabian Sea. Netherlands Indian Ocean Programme Cruise Report Vol. 3*: National Museum of Natural History, Leiden, 136 pp.
- VANDENBERGHE, J., AN, Z., NUGTEREN, G., LU, H., VAN HUISSTDEN, K., 1997, New absolute time scale for the Quaternary climate in the Chinese loess region by grain-size analysis – *Geology*, v. 25, p. 35-38.
- VISHER, G.S., 1969, Grain size distributions and depositional processes – *Journal of Sedimentary Petrology*, v. 39, p. 1074-1106.
- VON RAD, U., RÖSCH, H., BERNER, U., GEYH, M., MARCHIG, V., SCHULZ, H., 1996, Authigenic carbonates derived from oxidized methane vented from the Makran accretionary prism off Pakistan – *Marine Geology*, v. 136, p. 55-77.
- VON RAD, U., SCHULZ, H., SONNE 90 SCIENTIFIC PARTY, 1995, Sampling the oxygen minimum zone off Pakistan: glacial-interglacial variations of anoxia and productivity (preliminary results, Sonne 90 cruise) – *Marine Geology*, v. 125, p. 7-19.
- VON RAD, U. AND TAHIR, M., 1997, Late Quaternary sedimentation on the outer Indus shelf and slope (Pakistan): evidence from high-resolution seismic data and coring – *Marine Geology*, v. 138, p. 193-236.
- WEBER, M.E., WIEDICKE, M.H., KUDRASS, H.R., HÜBSCHER, C., ERLLENKEUSER, H., 1997, Active growth of the Bengal Fan during sea-level rise and highstand – *Geology*, v. 25, p. 315-318.
- WEIMER, P., 1990, Sequence stratigraphy, facies geometries, and depositional history of the Mississippi Fan, Gulf of Mexico – *American Association of Petroleum Geologists Bulletin*, v. 74, p. 425-453.
- WELLS, J.T. AND COLEMAN, J.M., 1982, Deltaic morphology and sedimentology, with special reference to the Indus River Delta, *in* Haq, B.U. and Milliman, J.D., eds., *Marine Geology and Oceanography of Arabian Sea and Coastal Pakistan*: Van Nostrand Reinhold Company, Scientific and Academic Editions, New York, p. 85-100.
- WELTJE, G.J., 1994, Provenance and dispersal of sand-sized sediments: Reconstruction of dispersal patterns and sources of sand-sized sediments by means of inverse modelling techniques – *Geologica Ultraiectina* 121, 208 pp.
- WELTJE, G.J., 1995, Unravelling mixed provenance of coastal sands: the Po delta and adjacent beaches of the northern Adriatic Sea as a test case, *in* Oti, M.N. and Postma, G., eds., *Geology of deltas*: Balkema, Rotterdam, p. 181-202.
- WELTJE, G.J., 1997a, End-member modelling of compositional data: Numerical-statistical algorithms for solving the explicit mixing problem – *Journal of Mathematical Geology*, v. 29, p. 503-549.

- WELTJE, G.J., 1997b, Construction of predictive regions in ternary diagrams: towards statistically rigorous provenance studies. Internal report with computer programs, Department of Geology, Faculty of Earth Sciences, Utrecht University, 28 pp.
- WELTJE, G.J. AND DE BOER, P.L., 1993, Astronomically induced paleoclimatic oscillations reflected in Pliocene turbidite deposits of Corfu (Greece): Implications for the interpretation of higher order cyclicity in fossil turbidite systems – *Geology*, v. 21, p. 307-310.
- WHITE, R.S., 1982, Deformation of the Makran accretionary sediment prism in the Gulf of Oman (north-west Indian Ocean), *in* Leggett, J.K., ed., *Trench-forearc geology: sedimentation and tectonics on modern and ancient active plate margins*, Geological Society Special Publication No. 10, p. 357-372.
- WILLIAMS, M.A.J. AND CLARKE, M.F., 1984, Late Quaternary environments in north-central India – *Nature*, v. 308, p. 633-635.
- WILLIAMS, M.A.J. AND ROYCE, K., 1982, Quaternary geology of the middle Son valley, north central India: implications for prehistoric archaeology – *Palaeogeography, Palaeoclimatology, Palaeoecology*, v. 38, p. 139-162.
- WOHLETZ, K.H., SHERIDAN, M.F., BROWN, W.K., 1989, Particle size distributions and the sequential fragmentation/transport theory applied to volcanic ash – *Journal of Geophysical Research*, v. 94, no. B11, p. 15703-15721.
- XIAO, J., PORTER, S.C., AN, Z., KUMAI, H., YOSHIKAWA, S., 1995, Grain size of quartz as an indicator of winter monsoon strength on the Loess Plateau of central China during the last 130,000 yr – *Quaternary Research*, v. 43, p. 22-29.
- XINGMIN, M., DERBYSHIRE, E., KEMP, R.A., 1997, Origin of the magnetic susceptibility signal in Chinese Loess – *Quaternary Science Reviews*, v. 16, p. 833-839.
- ZHOU, D., CHEN, H., LOU, Y., 1991, The logratio approach to the classification of modern sediments and sedimentary environments in northern South China Sea – *Mathematical Geology*, v. 23, p. 157-165.